

Analysis and Optimization of Springback in Sheet Metal Forming

Abdulaziz Hosain Alghtani

Submitted in accordance with the requirements for the degree of
Doctor of Philosophy

The University of Leeds
School of Mechanical Engineering

July 2015

The candidate confirms that the work submitted is his own, except where work which has formed part of jointly authored publications has been included. The contribution of the candidate and the other authors to this work has been explicitly indicated below. The candidate confirms that appropriate credit has been given within the thesis where reference has been made to the work of the others.

During the PhD study, the candidate wrote a conference paper by his own and presented an oral presentation of the 9th European LS-DYNA conference hold in 2013 in Manchester , UK about “Springback Analysis and Optimization in Sheet Metal Forming”. In this study, the numerical analysis of springback and optimisation approach described in Chapters 7 and 8 are similar to the published conference paper.

This copy has been supplied on the understanding that it is copyright material and that no quotation from the thesis may be published without proper acknowledgement.

© 2015 The University of Leeds and Abdulaziz Hosain Alghtani

The right of Abdulaziz Hosain Alghtani to be identified as Author of this work has been asserted by him in accordance with Copyright, Designs and Patents Act 1988

Acknowledgements

I would like to express my special appreciation and thanks to my advisors Professor David Barton and Dr. Peter Brooks , you have been tremendous mentors for me. I would like to thank you for encouraging my research and for allowing me to grow as a research scientist. Your advice on both research as well as on my career has been priceless. I also want to thank you for letting my defense be an enjoyable moment, and for your brilliant comments and suggestions, thanks to you. I would also like to thank Professor Yoshida and his group at Hiroshima University for their generous support and help. I also would like to thank Dr Richard Chittenden and Mr Tony Wiese at Mechanical Engineering Laboratory of Leeds University in their support of the experimental part of this thesis. I also give thanks and appreciate the generous support from Jaguar LandRover company in the UK, for the materials they delivered.

A special thanks to my family. Words cannot express how grateful I am to my father for all of the sacrifices that you've made on my behalf. Your prayer for me was what sustained me thus far. I would also like to thank all of my friends who supported me in writing, and incentivised me to strive towards my goal. At the end I would like express appreciation to my beloved wife Wasayf who spent sleepless nights with me and was always my support in the moments when there was no one to answer my queries.

Abstract

Sheet metal forming processes are widely used in the automotive industry to fabricate many components such as body panels, the structural members of the chassis and so on. The forming process involves many stages. There are many defects that might occur on a work piece during or after each set of processes and one of the most challenging of these is associated with the phenomenon of springback; that is, the distortion in specimen geometry due to the elastic recovery and other effects. The integration of springback into the design of the forming process represents a significant challenge due to difficulties associated with its prediction.

There are several factors that control the magnitude and direction of component distortion causing by springback. The primary aim of the present study is to evaluate the influence exerted on springback by the main parameters that affect the forming process. This will provide guide lines to create new CAE methods that can be used to predict the amount of springback within sheet metal forming processes. Two common forming processes will be investigated within this work, the so called L-bending and U-drawing processes, since these underpin many of the more complex forming operations. A forming test rig has been designed and manufactured that replicates each of these processes under controlled and repeatable conditions. Process parameters that can be controlled are the die and punch profile radii and clearance between the punch and die, and the normal clamp load applied on the work piece by the blank holder. In parallel, finite element models capable of simulating the L-bending and U-drawing bending processes were developed and validated for four different blanks materials: high and low strength steel, and high and low strength aluminium alloy.

Material characterization for four different blanks was conducted to derive required parameters for the simulation analysis. Also, friction coefficients were measured between each blank material and the forming tools using a pendulum tribometer.

Mesh sensitivity studies were firstly conducted to provide a mesh that represents an appropriate compromise between accuracy and consuming time. Results from the numerical analysis were compared to those from the experiments and good

agreement was generally found, except for the high strength steel where the galvanised coating (not modelled in the analysis) affected the results.

The model was then used to conduct parametric studies on the effect of certain parameters on the amount of the springback i.e. the blank holder load, die and punch radii and the radial clearance. Finally, an optimisation scheme was developed to derive the optimum combination of parameters to minimise springback. These results and the general methodology could form the basis of a reliable CAE system to control springback in common metal forming operations.

Table of Contents

CHAPTER 1: INTRODUCTION	1
1.1 Overview	1
1.2 Aims and objectives of the Research.....	2
1.2.1 Overall aim	2
1.2.2 Objectives.....	2
1.3 Thesis outlines	3
CHAPTER 2: BACKGROUND AND LITERATURE REVIEW.....	5
2.1 Introduction	5
2.2 Plasticity in sheet metal forming	8
2.2.1 Isotropic hardening	9
2.2.2 Kinematic hardening	9
2.3 Yoshida-Uemori model.....	11
2.4 Identification of the Yoshida-Uemori model parameters.....	16
2.5 Numerical modelling of springback.....	19
2.5.1 Comparison of material models	19
2.5.2 Comparison of numerical schemes.....	24
2.6 Design of Experiments and optimisation techniques in sheet metal forming	28
2.7 Summary of the findings and implication for the current study.....	29
CHAPTER 3: DERIVATION OF THE MECHANICAL PROPERTIES OF THE BLANKS MATERIALS	32
3.1 Introduction	32
3.2 Machine description.....	33
3.3 Specimen preparation	33
3.4 Uniaxial tensile test to failure	36
3.4.1 Methodology	36
3.4.2 Results	38
3.4.3 Discussion	47
3.5 Cyclic tension test	49
3.5.1 Methodology	49
3.5.2 Results	51

3.5.3 Discussion	54
3.6 Anisotropy test.....	54
3.6.1 Methodology	55
3.6.2 Results	55
3.6.3 Discussion	57
3.7 Cyclic tension-compression tests.....	57
3.7.1 Methodology	57
3.7.2 Results	58
3.7.3 Discussion	61
3.8 Summary.....	61
CHAPTER 4: METAL FORMING AND MEASUREMENT APPARATUS	62
4.1 Introduction	62
4.2 Die and blank holder design	65
4.2.1 Preliminary die and blank holder design	65
4.2.2 Final die and blank holder design	67
4.2.3 Die and blank holder assembly	69
4.3 Punch design	71
4.4 Metal forming experiment set up	73
4.5 Specification of Instron machine	75
4.6 Kemco 400 CMM machine	77
4.7 Summary.....	78
CHAPTER 5: MEASUREMENT OF FRICTION COEFFICIENT.....	79
5.1 Introduction	79
5.2 Apparatus.....	79
5.3 Metal forming lubrication	82
5.4 Experimental set-up.....	83
5.4.1 Specimen preparation.....	83
5.4.2 Experimental procedure.....	88
5.5 Results and discussion.....	90
5.5.1 Steel blank materials	90
5.5.2 Aluminium blank materials	93
5.6 Summary of friction coefficient experiments	95
CHAPTER 6: L-BENDING SHEET METAL FORMING PROCESS	96
6.1 Introduction	96
6.2 L-bending experiments.....	97

6.2.1	Experimental method.....	97
6.2.2	Experimental results	100
6.3	Numerical analysis of L-bending process and subsequent springback.....	109
6.3.1	Finite element model	109
6.3.2	Mesh sensitivity study	113
6.3.3	The effect of the degradation of Young's modulus	114
6.3.4	Comparison of numerical and experimental results.....	116
6.4	Parametric study	121
6.4.1	The effect of the die radius	121
6.4.2	The effect of clearance	123
6.4.3	The effect of the punch radius.....	125
6.4.4	The effect of the blank holder force (BHF)	126
6.4.5	The effect of the blank thickness.....	127
6.5	Discussion.....	129
6.6	Summary.....	133
CHAPTER 7: U-DRAWING SHEET METAL FORMING EXPERIMENTS AND SIMULATION.....		134
7.1	Introduction	134
7.2	U-drawing experiments.....	135
7.2.1	Experimental method.....	135
7.2.2	Punch load behaviour during the U- drawing process	137
7.2.3	Springback after the U-drawing process	142
7.3	Numerical analysis of U-drawing process and subsequent springback.....	145
7.3.1	Finite element model	145
7.3.2	Results of the mesh sensitivity study	149
7.3.3	The effect of the degradation of Young's modulus	153
7.4	Comparison of numerical and experimental results	155
7.5	Summary.....	158
CHAPTER 8: PARAMETRIC STUDY AND MINIMISATION OF SPRINGBACK AFTER U-DRAWING		159
8.1	Introduction	159
8.2	Parametric study	159
8.2.1	The effect of the blank thickness.....	159
8.2.2	The effect of the die radius	163

8.2.3 The effect of the punch radius.....	165
8.2.4 The effect of clearance	168
8.3 Design of experiment and optimisation analysis	170
8.4 Summary.....	181
CHAPTER 9: CONCLUSIONS AND FUTURE WORK	183
9.1 Conclusions.....	183
9.2 Recommendations for future work.....	188

List of Tables

Table 3.1 Chemical composition of the CPLA10414 material [52]	45
Table 3.2 Strain gauge specification [54]	50
Table 3.3 Young's modulus parameters for the four different materials	53
Table 3.4 Ra in rolling, 45 ⁰ and 90 ⁰ orientations for the DP600 material (Plastic strain : 0.1).....	55
Table 3.5 Ra in rolling, 45 ⁰ and 90 ⁰ orientations for the DX54D material (Plastic strain : 0.1).....	56
Table 3.6 Ra in rolling, 45 ⁰ and 90 ⁰ orientations for the CPLA100K38 material (Plastic strain : 0.1).....	56
Table 3.7 Ra in rolling, 45 ⁰ and 90 ⁰ orientations for the CPLA10414 material (Plastic strain : 0.1).....	56
Table 3.8 Yoshida-Uemori model parameters for the four different materials.....	60
Table 4.1 Compression spring specification [57]	68
Table 4.2 Description of the components used in both L-bending and U-drawing experiments.....	71
Table 5.1 The average static and dynamic friction coefficients under dry and lubricated condition during the first 22 seconds of the test	95
Table 6.1 The relationship between the yield and ultimate stresses and the corresponding punch force for the steel blank materials.....	105
Table 6.2 The relationship between the yield and ultimate stresses and the corresponding punch force for the aluminium blank materials.....	105
Table 6.3 The springback angle after L-bending process for all materials.....	108
Table 6.4 Dimensions of the L-bending model (all dimensions in mm).....	110
Table 6.5 Static and dynamic friction coefficients assumed for the four materials.....	112
Table 6.6 Experimental and numerical springback angle after L-bending process for all 4 materials.....	119
Table 7.1 Experimental springback results for the four blank materials.....	144
Table 7.2 Dimensions of the U-drawing finite element model	147
Table 7.3 Effect of different element size for the 3D model of the blank in U-drawing springback predictions (red box indicates converged results).....	150
Table 7.4 Experimental and numerical springback results for the four blank materials.....	157
Table 8.1 Optimum and simulation results of the springback after U-drawing for the DP600 blank for the two design variables	175
Table 8.2 Springback predictions after U-drawing for all blanks for the initial and optimised designs.	181

List of Figures

Figure 2.1 V and U bending sheet metal forming [9]	5
Figure 2.2 L-bending (wiping-die bending) sheet metal forming.....	6
Figure 2.3 U- drawing sheet metal forming	7
Figure 2.4 A drawing sheet metal forming process for a complex product [9].....	7
Figure 2.5 Schematics of the yield surface expands assuming isotropic hardening [14].....	9
Figure 2.6 Schematics of the yield surface (a) translation of the surface assuming kinematic hardening (b) stress-strain curve showing shifted yield stress in compression [14].....	10
Figure 2.7 Stress–strain curve of tension-compression experiment [15].....	11
Figure 2.8 Yoshida-Uemori model consisting of two surfaces [15].....	12
Figure 2.9 Schematic of the surface of g in the stress space when (a) $R = 0$ and (b) $R > 0$ [5, 15].....	15
Figure 2.10 The motion of a) the yield surface and b) the bounding surface under uniaxial forward-reverse deformation according to the Y-U model [5]	17
Figure 2.11 Normalized of experimental transient stress offset versus reverse plastic strain for different C values, for low and high strength steel (SPCC and SPFC respectively) [5]	18
Figure 2.12 The influence of the parameter h on the simulation of the cyclic responses of stress-strain (a) $h= 0.1$ and (b) $h= 0.9$ according to the Y-U model [5].....	19
Figure 2.13 Stress-strain curve for two cyclic tension compression of high strength steel sheet for four different model [15].....	21
Figure 2.14 The NUMISHEET'93 benchmark problem for the DP600 blank (a) sketch of the problem (b) tip deflection definition of springback(c) tip deflection magnitude for different hardening models and with or without considering the degradation of the Young's modulus [3]	22
Figure 2.15 (a) Schematic of U-drawing experimental set-up and (b) side wall curl after springback for different die radii simulated using different four models [15].....	24
Figure 2.16 The influence of (a) die radius and (b) clearance on the springback after L-bending [37].....	27
Figure 2.17 Springback of three different materials after U-drawing [38].....	27
Figure 3.1 Shimadzu tensile test machine at Hiroshima University – Japan.....	33
Figure 3.2 Specimen types A and B (all dimensions in mm)	34
Figure 3.3 Specimen type A geometry- all dimensions in mm.....	35

Figure 3.4 Specimen type B geometry- all dimensions in mm.....	35
Figure 3.5 Loading fixture for specimen type B prior to the cyclic tension-compression test.....	36
Figure 3.6 Clamped specimen type A with the extensometer	37
Figure 3.7 Stress-strain curve for DP600.....	39
Figure 3.8 Yield and ultimate stress for the DP600 at different orientations	40
Figure 3.9 Elongation of the DP600 at different orientations	40
Figure 3.10 Stress-strain curve for the DX54D	41
Figure 3.11 Yield and ultimate stress for the DX54D at different orientations.....	42
Figure 3.12 Elongation of the DX54D at different orientations	42
Figure 3.13 Stress-strain curve for the CPLA100K38.....	43
Figure 3.14 Yield and ultimate stress for the CPLA100K38 at different orientations	44
Figure 3.15 Elongation of the CPLA100K38 at different orientations	44
Figure 3.16 Stress-strain curve for CPLA10414	45
Figure 3.17 Yield and ultimate stress for the CPLA10414 at different orientations.....	46
Figure 3.18 Elongation of the CPLA10414 at different orientations.....	46
Figure 3.19 Stress-strain curves for 4 different materials	47
Figure 3.20 Yield and ultimate stress for the four materials at different orientations to the rolling orientation.....	48
Figure 3.21 Elongation of the four materials at different orientations to the rolling orientation.....	48
Figure 3.22 The relationship between the tensile strength and the elongation of different materials [53].....	49
Figure 3.23 Cyclic tension test set up	50
Figure 3.24 Loading and unloading stress-strain curves for four different materials.....	51
Figure 3.25 Loading and unloading stress-strain curves for the DP600 material.....	52
Figure 3.26 Unloading modulus degradation with effective plastic strain for the four different materials	53
Figure 3.27 Cyclic tension-compression test on specimens type B at Hiroshima University in Japan.....	57
Figure 3.28 Stress-Strain curve for two cyclic tension compression test for the four different materials	59
Figure 3.29 Comparison between experimental result and Y-U model for four different materials.....	60
Figure 4.1 Sheet metal forming concept for L-bending (a) prior to forming (b) end of the process (c) the final L-shape showing springback	63
Figure 4.2 Sheet metal forming concept for U-drawing (a) prior to forming (b) end of the process (c) the final U-shape showing springback.....	64

Figure 4.3 Preliminary die design.....	65
Figure 4.4 (a) Preliminary design of blank holder and (b) the distribution of pressure shown using FujiFilm sheet between the blank holder and the die after the four bolts had been tightened.....	66
Figure 4.5 Final design of the (a) die and (b) blank holder	67
Figure 4.6 Bolts and springs on the blank holder.....	68
Figure 4.7 Die and blank holder design assembly for (a) L-bending and (b) U-drawing (springs not shown for simplicity).....	70
Figure 4.8 Punch design assembly	72
Figure 4.9 Design assembly of (a) L-bending (b) U-drawing test rig (springs not shown for simplicity).....	74
Figure 4.10 Forming test rig set up	75
Figure 4.11 INSTRON tensile test machine at University of Leeds.....	77
Figure 4.12 Kemco CMM 400 machine set up to measure the L shape springback angle.....	77
Figure 5.1 (a) The pendulum tribometer apparatus (b) front view (c) side view.....	80
Figure 5.2 The relationship between the arm angle (β) and the transducer voltage	82
Figure 5.3 Picture of (a) blank ring (b) blank holder (c) assembly.....	83
Figure 5.4 Free body diagram for the forces acting on the ball arm.....	85
Figure 5.5 The ball after wear showing the dimensions and surface finish of the wear scar.....	87
Figure 5.6 The friction pendulum apparatus concept (a) front (b) side view of the apparatus (c) free body diagram at position A (d) free body diagram at position B.....	90
Figure 5.7 Friction coefficient for DP600 under dry conditions	91
Figure 5.8 Friction coefficient for DP600 under lubricated conditions	92
Figure 5.9 Friction coefficient for DX54D under dry conditions	92
Figure 5.10 Friction coefficient for DX54D under lubricated conditions.....	93
Figure 5.11 Friction coefficient for CPLA10414 under dry and lubricated condition	94
Figure 5.12 Friction coefficient for CPLA100k38 under lubricated condition.....	94
Figure 6.1 L-bending process (a) prior to the forming process (b) end of the forming process (c) final product with springback	96
Figure 6.2 Blank dimensions for L-bending process.....	98
Figure 6.3 The process of forming the blank (a) on the die (b) clamped by holder (c) fully formed L-part.....	99
Figure 6.4 Unloading process for L-bending (a) fully formed L-part (b) middle of punch reverse (c) fully removed punch.....	100

Figure 6.5 Punch load versus displacement for the high strength steel (DP600) during L-bending	101
Figure 6.6 Punch load versus displacement for the low strength steel (DX54D) during L-bending	102
Figure 6.7 Punch load versus displacement for the high strength aluminium (CPLA100k38) during L-bending	102
Figure 6.8 Punch load versus displacement for the low strength aluminium (CPLA10414) during L-bending	103
Figure 6.9 Comparison of punch load versus displacement between DP600 and DX54D steel during L-bending.....	104
Figure 6.10 Comparison of punch load versus displacement between CPLA100k38 and CPLA10414 aluminium alloy during L-bending.....	104
Figure 6.11 The specimens after the L-bending experiments	107
Figure 6.12 Kemco CMM 400 machine set up to measure the L shape profile after springback	107
Figure 6.13 Measurement of springback after the L-bending process, showing approximation location of measurement points (θ_L is the measured springback angle).....	108
Figure 6.14 L-bending model.....	109
Figure 6.15 Flow chart for the numerical analysis of the L-bending and U-drawing forming processes and springback (B.C. here denotes boundary conditions....	111
Figure 6.16 Typical finite element mesh showing high mesh density around the bend area of the blank	113
Figure 6.17 Number of elements used in the blank model versus the springback for DP600 steel.....	113
Figure 6.18 The L-angle after the springback with and without consideration of elastic stiffness degradation for steel materials.....	115
Figure 6.19 The L-angle after the springback with and without consideration of elastic stiffness degradation aluminium materials.	115
Figure 6.20 Experimental and numerical punch load versus displacement curves for the high strength steel (DP600).....	116
Figure 6.21 Experimental and numerical punch load versus displacement curves for the high strength steel (DX54D)	117
Figure 6.22 Experimental and numerical punch load versus displacement curves for the high strength aluminium (CPLA100k38).....	117
Figure 6.23 Experimental and numerical punch load versus displacement curves for the high strength aluminium (CPLA10414)	118
Figure 6.24 The effect of galvanised steel coating thickness on the springback after V bending [70].....	120

Figure 6.25 Comparison of the experimental and numerical analysis of the springback after L-bending for copper alloy with nickel coating compared with uncoated alloy [71].....	120
Figure 6.26 The effective plastic strain distribution within the DP600 blank for three different die radii (a) 4 mm (b) 6 mm and (c) 8 mm.....	122
Figure 6.27 The effect of the die radius on the springback angle after L-bending for the different materials	123
Figure 6.28 The effective plastic strain distribution on the DP600 blank for three different clearness (a) 0.2mm (b) 0.4 mm and (c) 0.9 mm	124
Figure 6.29 The effect of the clearance on the springback angle after L-bending for the different materials	125
Figure 6.30 The effect of the punch radius on the springback angle after L-bending for the different materials	125
Figure 6.31 The effective plastic strain distribution on the DP600 blank for two different blank holder loads (a) 0.6 kN and (b)1.2 kN.....	126
Figure 6.32 The effect of BHF on the springback angle after L-bending for the different materials.....	127
Figure 6.33 The effective plastic strain distribution within the CPLA100k38 blank for three different blank thicknesses (a) 1.6 mm (b) 2 mm and (c) 2.5 mm	128
Figure 6.34 The effect of the blank thickness on the springback angle after L-bending for the different materials	129
Figure 6.35 Simplified beam model representing the gap and the punch and die radii as distance (l_1 or l_2)	130
Figure 6.36 A general schematic of elastic-plastic stress strain curve	131
Figure 6.37 Springback angle versus maximum plastic strain for the DP600 steel which were at mixed of different design parameters	132
Figure 6.38 Springback angle versus maximum plastic strain for the CPLA100k38 aluminium which were for three different blank thicknesses	132
Figure 7.1 U-drawing process: (a) prior to the forming process, (b) end of the forming process and (c) final product with springback	134
Figure 7.2 U-drawing rig mounted on Instron test machine	135
Figure 7.3 Blank dimensions for U- drawing bending process	136
Figure 7.4 The experimental U-drawing process (a) prior to forming (b) during the forming (c) fully formed part (d) after removing the tools (showing springback).....	137
Figure 7.5 (a) Punch load versus displacement for the high strength steel (DP600) during U-drawing (b) the forming tools at the end of the forming process.....	139
Figure 7.6 Punch load versus displacement for the high strength steel (DX54D) during U-drawing.....	140

Figure 7.7 Punch load versus displacement for the high strength aluminium (CPLA100k38) during U-drawing.....	140
Figure 7.8 Punch load versus displacement for the low strength aluminium (CPLA10414) during U-drawing.....	141
Figure 7.9 Comparison of average punch load versus displacement between the DP600 and DX54D steels during U- drawing	141
Figure 7.10 Comparison of average punch load versus displacement between the CPLA100k38 and CPLA10414 aluminium alloys during U-drawing.....	142
Figure 7.11 The specimens showing springback after the U- drawing process	143
Figure 7.12 Kemco CMM 400 machine set up to measure the U shape profile	143
Figure 7.13 Measurement of springback angles after the U-drawing process, showing approximate location of measurement points of a blank.....	144
Figure 7.14 Theoretical model of U-drawing process	146
Figure 7.15 Blank discretisation for the U-drawing bending 2D modelling	147
Figure 7.16 The 3D shell element model of U-drawing process.....	148
Figure 7.17 Blank discretisation for the 3D shell element model of the U-drawing process.....	149
Figure 7.18 Comparison between experimental and 2D numerical modelling of punch force versus displacement curves in U- drawing for different blank mesh densities for DP600 steel	151
Figure 7.19 3D U-drawing simulation for DP600 and equivalent plastic strain distribution in the blank (a) whole assembly, (b) to (g) snapshots during the process, (i) after springback.....	152
Figure 7.20 Comparison between experimental and numerical punch force versus displacement curves in U- drawing process for DP600.....	153
Figure 7.21 Springback after U-drawing process for all materials included and exclude the elastic modulus degradation in comparison with experiment (a) θ_1 and (b) θ_2	154
Figure 7.22 Punch load versus displacement for the low strength steel (DX54D) during U- drawing.....	155
Figure 7.23 Punch load versus displacement for the low strength aluminium (CPLA10414) during U-drawing.....	156
Figure 7.24 Punch load versus displacement for the high strength aluminium (CPLA100k38) during U-drawing process	156
Figure 8.1 Predicted springback after U–drawing for different blank thickness for all tested materials (a) θ_1 and (b) θ_2	161
Figure 8.2 A mid-plane cross section for the U-deformed part	162
Figure 8.3 Maximum principal strain on upper and lower surfaces for three different CPLA100k38 blank thicknesses (a) full data (b) data zoomed into zones II, III and IV.	162

Figure 8.4 Predicted springback after U –drawing for different die radii for all four materials (a) θ_1 and (b) θ_2	164
Figure 8.5 Maximum principal strain on upper and lower surface, for three different die radii for DP600 blank.....	165
Figure 8.6 Maximum principal strain on upper and lower surface for three different punch radii for DP600 blank.....	166
Figure 8.7 Predicted springback after U –drawing for different punch radii for all four materials (a) θ_1 and (b) θ_2	167
Figure 8.8 Predicted springback after U –drawing for different clearance for all four materials (a) θ_1 and (b) θ_2	169
Figure 8.9 Maximum principal strain on upper and lower surface for two different clearances for CPLA100k38 blank.....	170
Figure 8.10 stages of Design of Experiment and optimisation procedures	172
Figure 8.11 Build and validation DoE points	173
Figure 8.12: Response surface showing predicted θ_1 springback angle for the DP600 blank.....	174
Figure 8.13: Response surface showing predicted θ_2 springback angle for the DP600 blank.....	174
Figure 8.14 Final stage of U –drawing and the subsequent springback for the DP600 blank for (a) the initial design (b) the optimum design.....	176
Figure 8.15 Maximum principal strain on upper and lower surfaces for initial and optimum designs for DP600 blank	177
Figure 8.16 Final stage of U–drawing and the subsequent springback for the DX54D blank for (a) the initial design (b) the optimum design.....	178
Figure 8.17 Maximum principal strains on upper and lower surfaces for initial and optimum designs for DX54D blank	178
Figure 8.18 Final stage of U-drawing process for CPLA100k38 aluminium blank	179
Figure 8.19 Final stage of U –drawing and the subsequent springback for the CPLA100k38 blank for (a) the initial design (b) the optimum design	180
Figure 8.20 Final stage of U –drawing and the subsequent springback for the CPLA10414 blank for (a) the initial design (b) the optimum design	180

Nomenclature

$\bar{\sigma}$	the effective Von Mises stress
σ_y	the yield stress
α	back stress
Y	the yield surface radius
D^p	the rate of plastic deformation
$\dot{\gamma}$	plastic deformation increment
β	the bounding surface centre
β_o	the kinematic hardening of the bounding surface at the point of reverse stress
B	initial size of the bounding surface
R	Isotropic hardening stress
\dot{P}	the effective plastic strain rate
C	a material parameter that controls the rate of the kinematic hardening
R_{sat}	the saturated value of the isotropic hardening stress R at large plastic strain
m	a material constant which controls the rate of isotropic hardening
b	a material parameter
q	the centre of the g surface
r	the radius of the g surface
h	a material parameter
E	Young's modulus
E_o	Young's modulus for the original elastic region
E_a	the Young's modulus for the plastic region

γ	a material constant
ε^p	plastic strain
σ_{eng} and σ_T	Engineering and true stress respectively
ε_{eng} and ε_T	Engineering and true strain respectively
P	the instantaneous tensile
A_0	the original gauge cross-sectional area of the specimen
ΔL and L_0	load the displacement and the gauge length of the specimen respectively
r_a	the anisotropy coefficient
ε_2 and ε_3	the strains in the width and thickness directions
R_a	the normal anisotropy coefficient
E^*	The equivalent elastic modulus
ν	Poisson's ratio
μ	friction coefficient
W	dimensionless load parameter
θ_1 and θ_2	Springback angles after U-drawing process
θ_l	Springback angle after L-bending process

CHAPTER 1: INTRODUCTION

1.1 Overview

There is considerable interest in reducing fuel consumption in aeroplanes and automobiles. Light weight materials of high strength are one of the key ways in which to reduce vehicle weight in order to decrease the fuel consumption and improve performance, handling and comfort [1-3]. In the past, the design of the metal forming tools was based on the experience of manufacturing engineers and trial and error experiments. These methods are very costly and time-consuming as stated in [4] and there is a need for development and use of more systematic and scientific methods.

Many defects are known to occur during or after sheet metal forming processes. Springback is one of these defects and occurs when, after releasing the forming tools from the formed part, the part attempts to return to its original shape. The presence of springback is more pronounced among the new high strength materials than for materials of low strength that were previously used.

The quality of springback prediction depends on the accuracy of the material model that describes the behaviour of the sheet material as it undergoes large deformation bending and unbending that are a characteristic of such metal forming processes. In the past many researchers have investigated the behaviour of elastic-plastic materials and have proposed many models, but usually only with small deformations. In contrast, sheet metal forming usually involves a large deformation followed by an attempt by the material to return to its original shape, which gives rise to the springback phenomena.

In recent years, researchers have realised that for a precise prediction of springback, the Bauschinger effect, which is characterised by early re-yielding during reverse deformation, should be taken into the account [5]. Some researchers have investigated experimentally large-strain cyclic plasticity [6], while other papers have been published on reverse deformation after plastic deformation [7, 8].

In 2003, Yoshida et al. [5] succeeded in the production of an appropriate material model that arose from a series of cyclic tension-compression deformation experiments which deformed sheet metal at large strains. This led to the development of the widely used Yoshida-Uemrio model for large strain cyclic plasticity. The impact of this study is an improved predictive tool that enhanced the quality of the manufactured products.

1.2 Aims and objectives of the Research

1.2.1 Overall aim

The overall aim of this project is to investigate the extent to which advanced CAE techniques can be used to predict springback in sheet metal forming processes and to develop numerical optimisation procedures in order to control the springback to an acceptable level.

1.2.2 Objectives

1. To conduct a literature review of the analysis of sheet metal forming, springback prediction and related optimisation techniques.
2. To design a test rig and conduct experiments for L and U-drawing processes in order to measure the springback phenomenon and validate the numerical methods for a range of materials commonly used in the automotive industry.
3. To develop suitable numerical models of the simple L and U-drawing processes in order to predict the springback.
4. To conduct parametric studies using the validated numerical models, to investigate the influence of the main parameters on springback.
5. To develop appropriate optimisation techniques to minimise the springback in simple sheet metal forming operations.

1.3 Thesis outlines

The thesis is structured as follows:

Chapter 1: Introduction

This chapter introduces a summary of the area of research, the aim and objectives of this work and the structure of the thesis.

Chapter 2: Literature Review

This chapter gives an overview of sheet metal forming and the plasticity theory that explains the material behaviour under such circumstances. It defines the Yoshida-Uemori model and the definition of the necessary model parameters for different materials. The chapter also reviews literature relevant to the present work in springback analysis and design optimisation.

Chapter 3: Derivation of the mechanical properties of the blank materials

This chapter presents the experiments conducted to acquire the mechanical properties of the research materials and Y-U model parameters. Also it reports the degradation of the Young's modulus during reverse plastic deformation for each material. The sheet materials used in this project were provided by Jaguar Land Rover, in the UK. Two of them were high strength materials (steel and aluminium alloy) and the remaining two were low strength materials (steel and aluminium alloy).

Chapter 4: Metal forming and measurement apparatus

This chapter explains the evolution of design of the metal forming rig for both the L- bending and U-drawing forming operations.

Chapter 5: Measurement of friction coefficient

This chapter describes the pendulum tribometer apparatus which was used to measure both the static and dynamic coefficient of friction between the blank materials and representative steel tool material. Also, it explains in detail the specimen preparation and experimental technique. Finally, measured friction coefficients for all blank materials are reported.

Chapter 6: L-bending sheet metal forming process

This chapter discusses the experimental methods and results for the L-bending process. Moreover, it describes the 2D finite element simulation and compares the experimental and numerical results. Finally, it discusses the influence of important parameters on the springback level.

Chapter 7: U- drawing sheet metal forming experiments and simulation

This chapter discusses the experimental methods and results for the U-drawing process. Moreover, it describes both 2D and 3D finite element simulations and compares the experimental and numerical prediction from the 2D and 3D models.

Chapter 8: Parametric study and the minimisation of springback after a U-drawing process

This chapter discusses the influence of important parameters on the springback level after the U-drawing process. It describes the use of a design of experiments technique to select 30 combinations of points within a design space. It also shows how a response surface for the springback is generated within the design of space. Finally, it delivers a set of optimum design variables that lead to minimal springback after the U-drawing process.

Chapter 9: Conclusions and Future Work

This chapter presents the conclusions of the current research which in turn leads to suggestions and recommendations for future work.

CHAPTER 2: BACKGROUND AND LITERATURE REVIEW

2.1 Introduction

Sheet metal forming is a process in which a thin sheet of metal is formed into a desired shape. In most sheet metal forming processes, the forming apparatus consists of rigid components which normally include a die that has the final required shape, a punch to push the metal sheet into the die cavity and a holder to clamp the specimen during the forming process. However in some sheet metal forming processes, there is no need for the holder and this is known as air bending such as V-bending and U-drawing as shown in Figure 2.1.

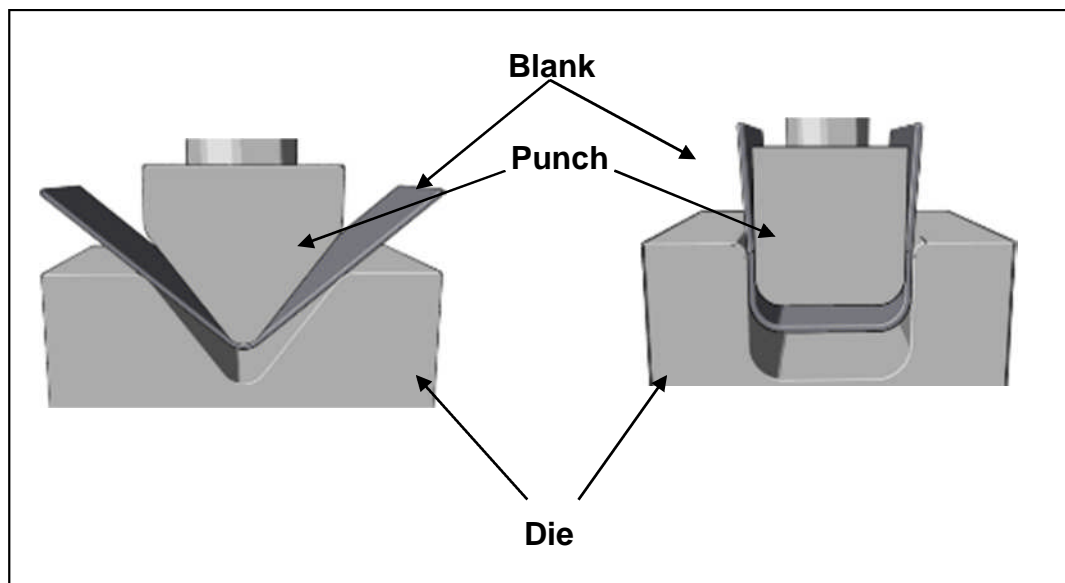


Figure 2.1 V and U bending sheet metal forming [9]

Sheet metal forming processes are widely used by the automotive and aerospace industries. More than 55% of sheet metal components are produced by press-brake bending in these industries [10].

Press-brake bending is a sheet metal forming process where the sheet is subjected to a bending load and can perform different operations such as V-bending, U-drawing, channel die bending and wiping-die bending which is also known as L-bending. It is operated by placing the metal sheet (a blank) over a die and the punch then travels down, pressing the blank into the die cavity. In this thesis, wiping-die bending is termed L-bending.

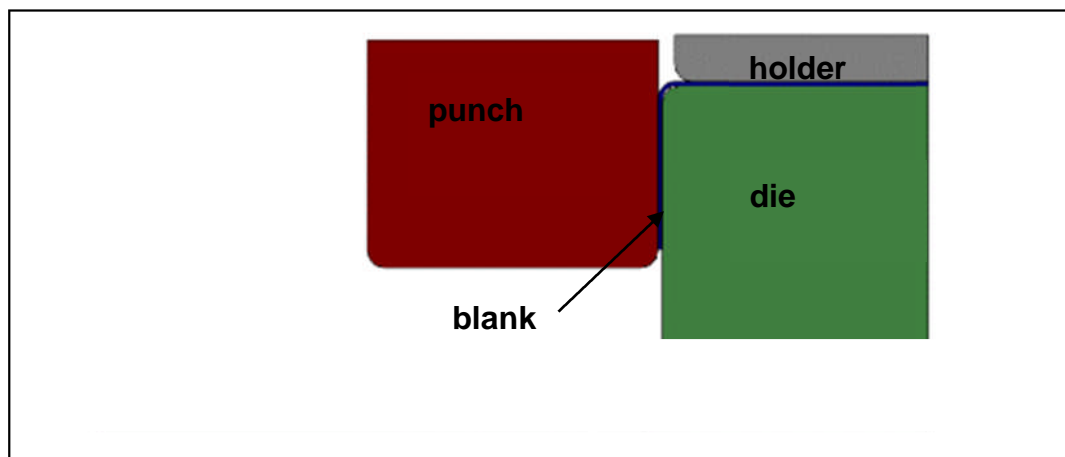


Figure 2.2 L-bending (wiping-die bending) sheet metal forming

Sheet drawing-forming is another kind of sheet metal forming process. In this operation, the sheet is subjected to a drawing (stretching) force in addition to the bending force, due to a holder that clamps the specimen. Figure 2.3 illustrates the principle of the U-drawing sheet metal forming process. Figure 2.4 shows an example of the drawing sheet forming process for a complex part. The current project investigates springback after the common L-bending and U-drawing processes. This is because both processes involve severe deformation of a blank and secondly only one metal forming rig is required to study both processes.

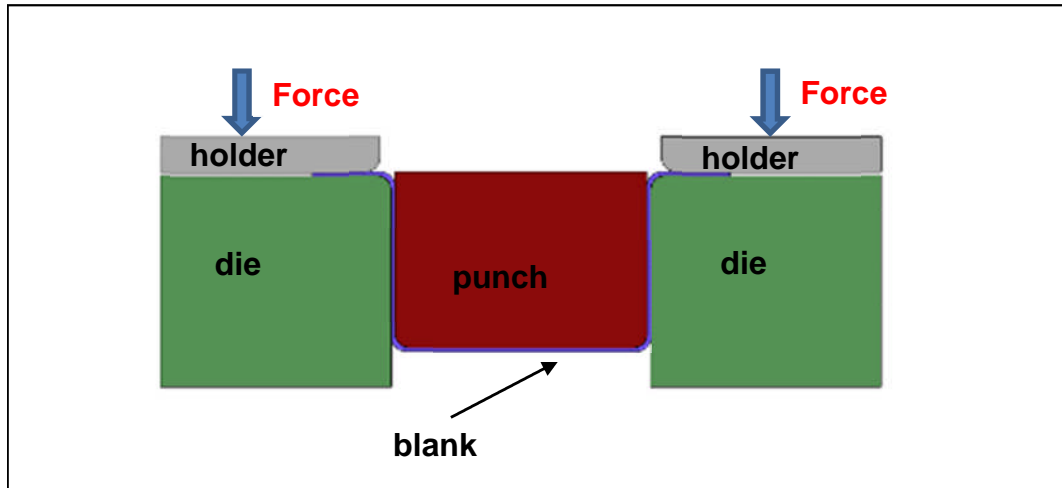


Figure 2.3 U- drawing sheet metal forming

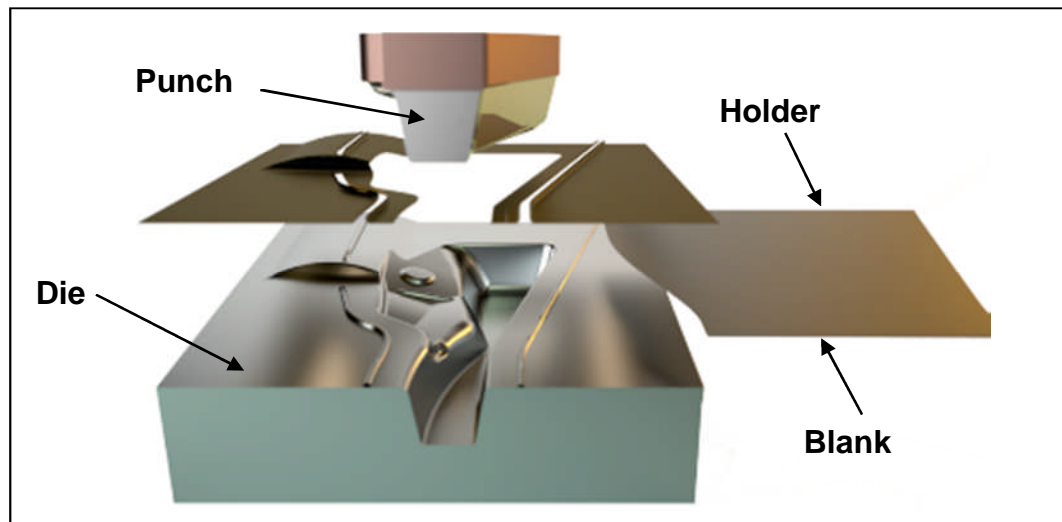


Figure 2.4 A drawing sheet metal forming process for a complex product [9]

As a result of the need to reduce fuel consumption for economic and environmental purposes, the automotive industry has made a considerable effort to replace the conventional sheet materials with high strength aluminium and steel. This leads to a decrease in vehicle weight which in turn reduces the CO₂ emissions. However, the often low formability and/or substantial springback of high strength material are technical difficulties that the manufacturing engineers must overcome. The springback affects the quality of the final product, making the designing of forming tools more difficult and expensive.

One way to eliminate such problems is to provide an accurate prediction of high strength sheet metal forming, both during the forming process and after releasing the forming tools. Therefore, in this chapter the theory of plasticity during sheet forming processes is discussed. An advanced material model well suited for such studies is identified and extensively explained. Finally, technical methods of reducing the springback after sheet metal forming including appropriate optimisation techniques are explored.

2.2 Plasticity in sheet metal forming

During the forming process of a sheet metal, the deformed regions have different stress and strain behaviour; some regions remain elastic whilst others have yielded and are therefore plastically deformed. The constrained plastic flows that result makes the equations that describe the stress-strain relation difficult to solve for such problems. A simple case in the metal forming process is to assume a rectangular beam, so the bending moment M_e at the limit of elastic deformation can be calculated by:

$$M_e = \frac{\sigma_y w h^2}{6} \quad (2.1)$$

where w and h denote the beam cross-section dimensions and σ_y is the yield stress of a material. For an elastic-perfectly plastic material, the fully plastic bending moment M_p is given by:

$$M_p = 1.5 M_e \quad (2.2)$$

However, the difficulty of defining the material behaviour during the forming process provides a challenge in developing constitutive equations to describe more realistic behaviour [11]. Three main aspects should be considered to describe a material that undergoes a plastic forming process: a yield criterion, a strain hardening model and a plastic flow rule [12]. Also the degradation of the Young's modulus that follows plastic deformation is reported to influence the accuracy of springback prediction [2, 3, 5, 13].

Several constitutive equations are available to describe the initial yielding and its evolution during subsequent plastic deformation such as isotropic hardening and kinematic hardening models [2, 3].

2.2.1 Isotropic hardening

Isotropic hardening can be assumed when materials experience monotonous and proportional deformation where the initial yield surface expands uniformly during the deformation as shown in Figure 2.5. Under this assumption, the yield surface can be defined by:

$$f(\sigma) = \bar{\sigma} - \sigma_y = 0 \quad (2.3)$$

in which, $\bar{\sigma}$ denotes the effective Von Mises stress and σ_y is the yield stress.

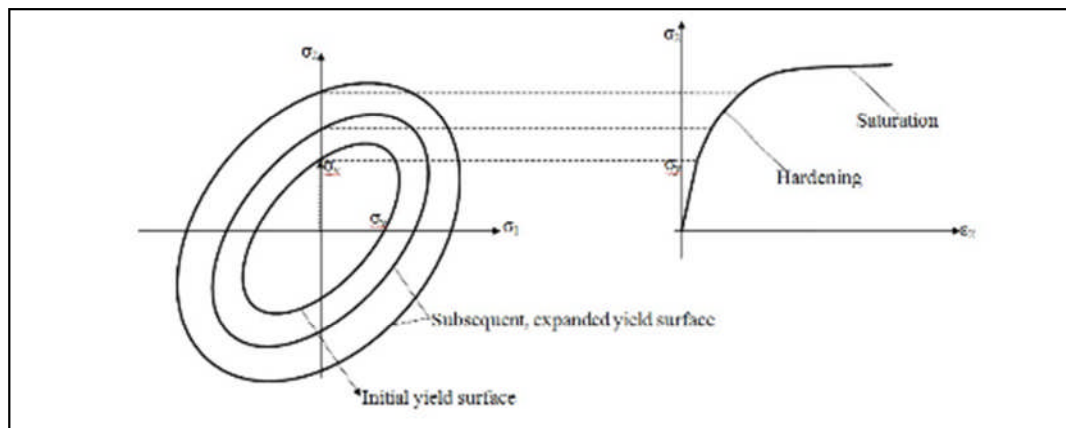


Figure 2.5 Schematics of the yield surface expands assuming isotropic hardening [14]

2.2.2 Kinematic hardening

When a material undergoes non-monotonic deformation, the isotropic assumption is often not sufficiently accurate to describe the material behaviour. For instance, in sheet metal forming processes, when the deformed part is removed from the tools, the material experiences elastic unloading leading to the springback phenomenon.

This is affected by translation of the yield surface due to the Bauschinger effect and the yield function becomes:

$$f(\sigma - \alpha) - \sigma_y = 0 \quad (2.4)$$

where α is the back stress.

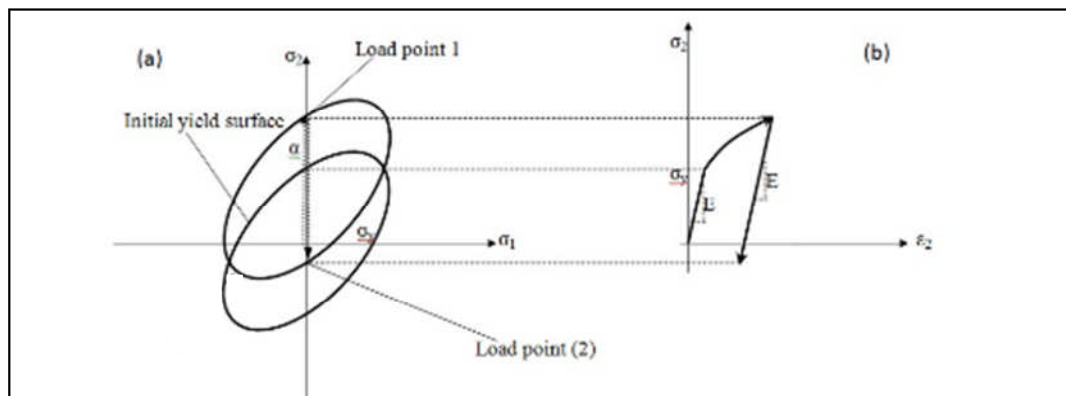


Figure 2.6 Schematics of the yield surface (a) translation of the surface assuming kinematic hardening (b) stress-strain curve showing shifted yield stress in compression [14]

Sheet metal forming involves large deformations followed by an attempt of the material to return to its natural shape leading to springback. The quality of springback prediction depends on the accuracy of the material model that describes the behaviour of the sheet material as it undergoes the large deformation associated with the bending and unbending processes. In the past many researchers have investigated the behaviour of elastic-plastic deformation and have proposed many models but usually this is within the limits of small deformation theory. In contrast, sheet metal forming is characterised by large deformations and then followed by the deformed material attempting to return to its original shape, known as springback. More recently, some researchers have recognised that for a more precise prediction of springback, the Bauschinger effect should be taken into account which is characterised by early re-yielding during reverse deformation as shown in Figure 2.7 [5].

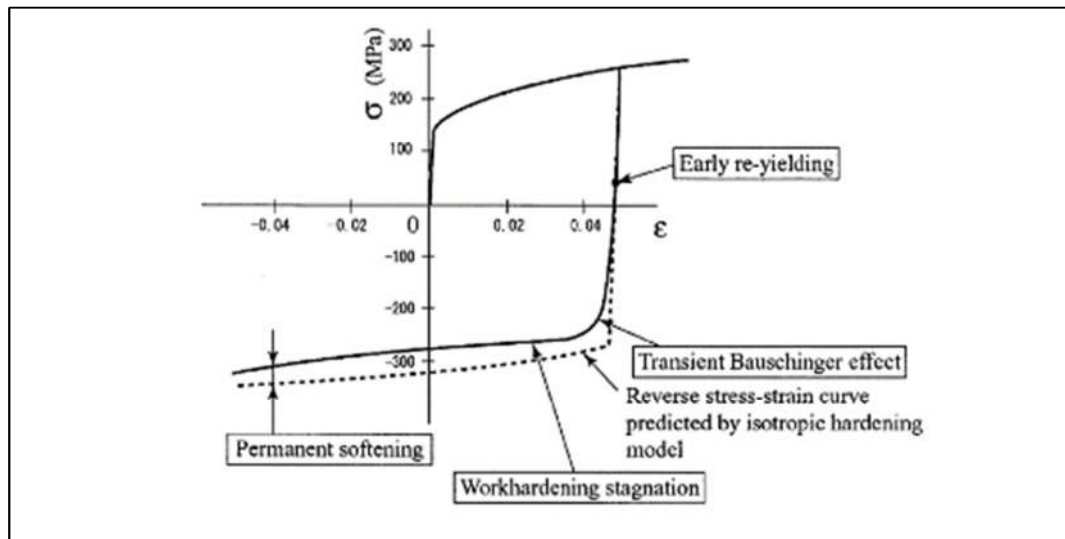


Figure 2.7 Stress–strain curve of tension-compression experiment [15]

A few researchers have investigated experimentally large-strain cyclic plasticity [6], while a number of papers have been published on reverse deformation after plastic loading [7, 8]. In 2003, Yoshida et al. succeeded in performing cyclic tension-compression deformation experiments for sheet metal at the large levels of strain that are typically encountered in such processes [5]. They described the important behaviour as comprising the Bauschinger effect, permanent elastic softening and work-hardening stagnation. The resulting material model, known as the Yoshida-Uemori (Y-U) model is described below.

2.3 Yoshida-Uemori model

This model consists of three different surfaces: a yield surface (f), a bounding surface (F) and an additional surface (g) which is a non-isotropic hardening surface. The yield surface of kinematic hardening is surrounded by a bounding surface of mixed isotropic-kinematic hardening as illustrated in Figure 2.8. The yield surface is fixed in its size but its centre moves with the deformation while the bounding surface is allowed to change in both size and location [5, 15].

The bounding surface illustrates the global work-hardening associated with the formation of stable dislocations. It is defined as follows:

$$F = \phi(\sigma - \beta) - (B + R) = 0 \quad (2.8)$$

where β is the bounding surface centre, B is its initial size with R being associated with isotropic hardening.

The position of the centre of the yield surface f relative to the centre of the bounding surface F is given by the vector α_* which is defined in (2.9):

$$\alpha_* = \alpha - \beta \quad (2.9)$$

Under a uniaxial stress state, the evolution of back stress is expressed by:

$$\dot{\alpha}_* = C \left(\left(\frac{a}{Y} \right) (\sigma - \alpha) - \sqrt{\frac{a}{\dot{\alpha}_*}} \alpha_* \right) \dot{P} \quad (2.10)$$

where,

$$\dot{P} = \sqrt{\left(\frac{2}{3} \right) D^P : D^P}, \quad \dot{\alpha}_* = \phi(\alpha_*), \quad a = B + R - Y$$

Here \dot{P} and D^P denote the effective plastic strain rate and plastic deformation rate respectively and C is a material parameter that controls the rate of the kinematic hardening. Equation (2.10) shows that the yield surface moves within the bounding surface e.g. when the current stress at point a is on the yield surface, it moves towards point A on the bounding surface as shown in Figure 2.8.

Therefore, under the uniaxial stress state, equation (2.10) becomes:

$$\dot{\alpha}_* = Ca \left(\dot{\epsilon}^P - \text{sgn}(\alpha_*) \sqrt{\frac{|\alpha_*|}{a}} |\dot{\epsilon}^P| \right) \quad (2.11)$$

where, $\dot{\epsilon}^p$ represents plastic strain rate and $\text{sgn}(\alpha_*)$ is a function where:

$$\begin{aligned}\alpha_* > 0, & \quad \text{sgn}(\alpha_*) = 1 \quad (\text{tension}) \\ \alpha_* < 0, & \quad \text{sgn}(\alpha_*) = -1 \quad (\text{compression}) \\ \alpha_* = 0, & \quad \text{sgn}(\alpha_*) = 0\end{aligned}$$

In the Y-U model, the bounding surface is assumed to expand and move during the deformation. Therefore, the isotropic hardening of the bounding surface is expressed by (2.12):

$$\dot{R} = m(R_{\text{sat}} - R)\dot{P} \quad (2.12)$$

where R_{sat} is the saturated value of the isotropic hardening stress R at large plastic strain and m is a material constant which controls the rate of isotropic hardening.

The kinematic hardening of the bounding surface is assumed as in (2.13):

$$\dot{\beta} = m\left(\frac{2}{3}bD^p - \beta\dot{P}\right) \quad (2.13)$$

where b represents a material parameter [5, 15].

The permanent softening and work-hardening stagnation occur due to the dissolution of dislocation cell walls preformed during forward deformation and the formation of new dislocation microstructures during reverse deformation [5, 15]. These phenomena are described by the kinematic hardening of the bounding surface and the additional surface (g) as shown in Figure 2.9 and defined in (2.14):

$$g = \phi(\sigma - q) - r = 0 \quad (2.14)$$

where q and r are the centre and the radius of the g surface respectively.

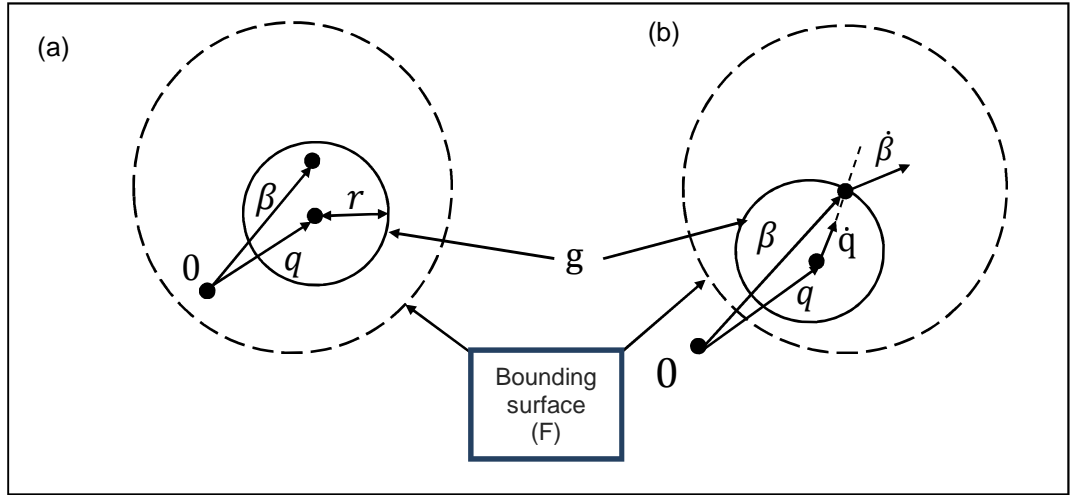


Figure 2.9 Schematic of the surface of g in the stress space when (a) $\dot{R} = 0$ and (b) $\dot{R} > 0$ [5, 15]

It is assumed that the centre of the bounding surface at distance β from the origin is either inside the g surface as shown in Figure 2.9 (a) or on the g surface as shown in Figure 2.9 (b). Isotropic hardening of the bounding surface takes place when the centre of the bounding surface remains on the g surface, as shown in Figure 2.9 (b): In other words, $\dot{R} > 0$ when,

$$g = \sqrt{\frac{3}{2}} \|\beta - q\| - r = 0 \quad \text{and} \quad \frac{\partial g}{\partial \beta} : \dot{\beta} > 0 \quad (2.15)$$

and $\dot{R} = 0$ otherwise, see Figure 2.9 (a)

The kinematic motion of the g surface is expressed by:

$$\dot{q} = \mu(\beta - q) \quad (2.16)$$

Assuming the consistency condition that the centre of the bounding surface should be either on or inside the surface of g , the following two parameters are defined:

$$\mu = \frac{(1-h)\Gamma}{r} \quad \text{and} \quad \Gamma = \frac{3(\beta - q) : \dot{\beta}}{2r} \quad (2.17)$$

$$\begin{aligned} \dot{r} &= h\Gamma, & \text{when } \dot{R} > 0 \\ \dot{r} &= 0, & \text{when } \dot{R} = 0 \end{aligned} \quad (2.18)$$

where h is a material parameter varying from 0 to 1 that controls the expansion rate of the g surface. High values of the h parameter mean a rapid expansion of the g surface.

Also in the Yoshida-Uemori model, the effect of plastic strain on the Young's modulus is taken into account using the following equation.

$$E = E_o - (E_o - E_a)(1 - e^{-\gamma p}) \quad (2.19)$$

where E is the current Young's modulus and E_o and E_a are the Young's modulus for the original elastic region and for the plastic region, respectively and γ and p represent a material constant and the level of plastic strain respectively.

2.4 Identification of the Yoshida-Uemori model parameters

Section 2.3 has shown that the Y-U model requires a total of 7 material parameters (Y , B , R_{sat} , b , m , C , and h). These can be determined experimentally with the use of constitutive equations. Each of the seven parameters is explained below.

As mentioned above, Y is the radius of the yield surface which represents the elastic limit as shown in Figure 2.10 (a). The stress-strain curves of the tension-compression (forward-reverse) experiment are essential to determine the parameters of the Y-U model.

The bounding stress-strain curve under tension load is described as $\sigma_{bound}^{(fow)}$ which is the (b)-(c) line of the stress-strain curve shown in Figure 2.10 (b). By fitting the (b)-(c) line and use of equation (2.20) which comes from the evolution equation for the mixed isotropic-kinematic hardening of the

bounding surface B , R_{sat} , b and m can be determined. From Figure 2.10 (b) it can be seen that B can be found by obtaining the stress at $\varepsilon^p = 0$:

$$\sigma_{bound}^{(fow)} = B + R + \beta = B + (R_{sat} + b)(1 - e^{-m\varepsilon^p}) \quad (2.20)$$

Here R is the isotropic hardening stress and R_{sat} is the saturated value of R at large plastic strain. m denotes a material parameter that controls the rate of isotropic hardening. b is also a material parameter. ε^p is plastic strain.

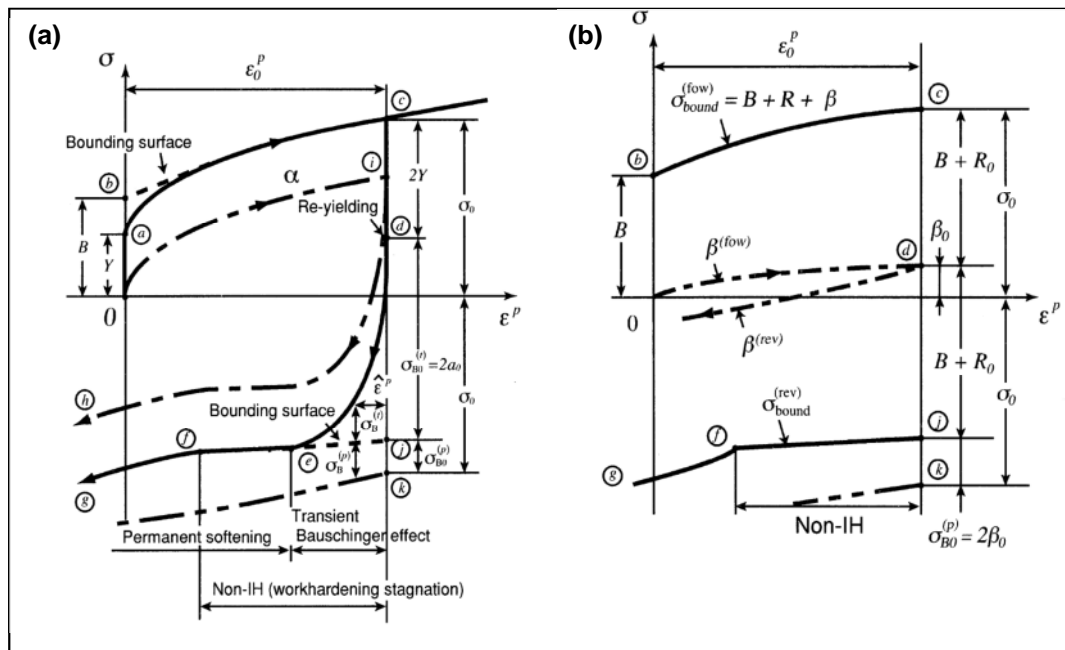


Figure 2.10 The motion of a) the yield surface and b) the bounding surface under uniaxial forward-reverse deformation according to the Y-U model [5]

The parameter b is calculated using equation (2.21):

$$\sigma_{B0}^{(p)} = 2\beta_0 = 2b(1 - e^{-m\varepsilon_0^p}) \quad (2.21)$$

where β_0 is the kinematic hardening of the bounding surface at the point of reverse stress as shown in Figure 2.10 (b). ε_0^p denotes the plastic prestrain. Given that the parameter m is calculated by equation (2.20), then it is easy to find the parameter b by using equation (2.21)

From equation (2.11) and from the stress-strain curve of the transient Bauschinger deformation as shown in Figure 2.10, the parameter C is determined using:

$$C \approx \frac{2}{\varepsilon^p} \left[(1 + \ln 2) - \sqrt{\frac{|\alpha_*|}{a}} + \ln \left(1 + \operatorname{sgn}(\alpha_*) \sqrt{\frac{|\alpha_*|}{a}} \right) \right] \quad (2.22)$$

The transient stress offset is $\sigma_B^{(t)} = a + \alpha_*$ where

$$\frac{\alpha_*}{a} \approx \frac{\sigma_B^{(t)}}{a_o} - 1 = 2 \left(\frac{\sigma_B^{(t)}}{\sigma_{Bo}^{(t)}} \right) - 1, \quad a_o = \frac{1}{2} \sigma_{Bo}^{(t)} = \sigma_o - Y - \frac{1}{2} \sigma_{Bo}^{(p)}$$

The simulation of the relationship between the transient stress offset and the reverse plastic is obtained by varying the parameter C , see Figure 2.11.

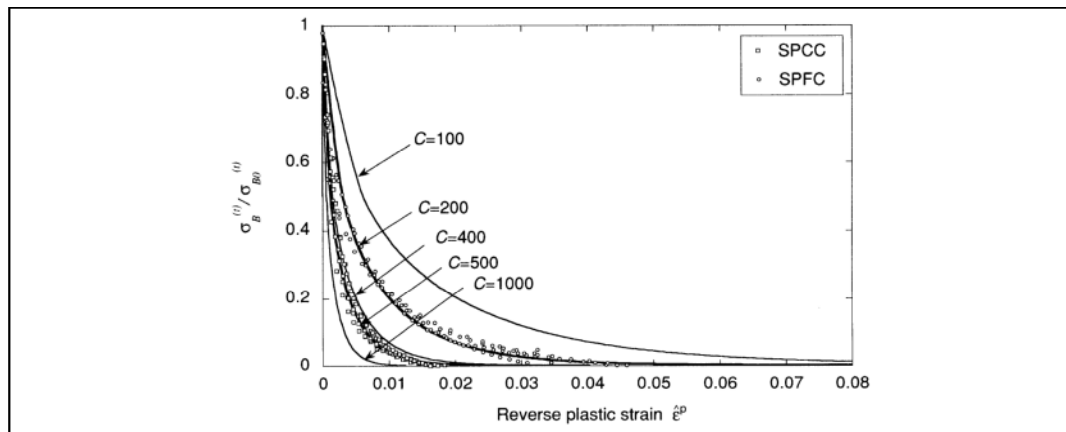


Figure 2.11 Normalized of experimental transient stress offset versus reverse plastic strain for different C values, for low and high strength steel (SPCC and SPFC respectively) [5]

The h parameter is determined by simulation of the stress-strain response and is varied from 0 to 1 to obtain the best fit to the corresponding experimental curves, see Figure 2.12.

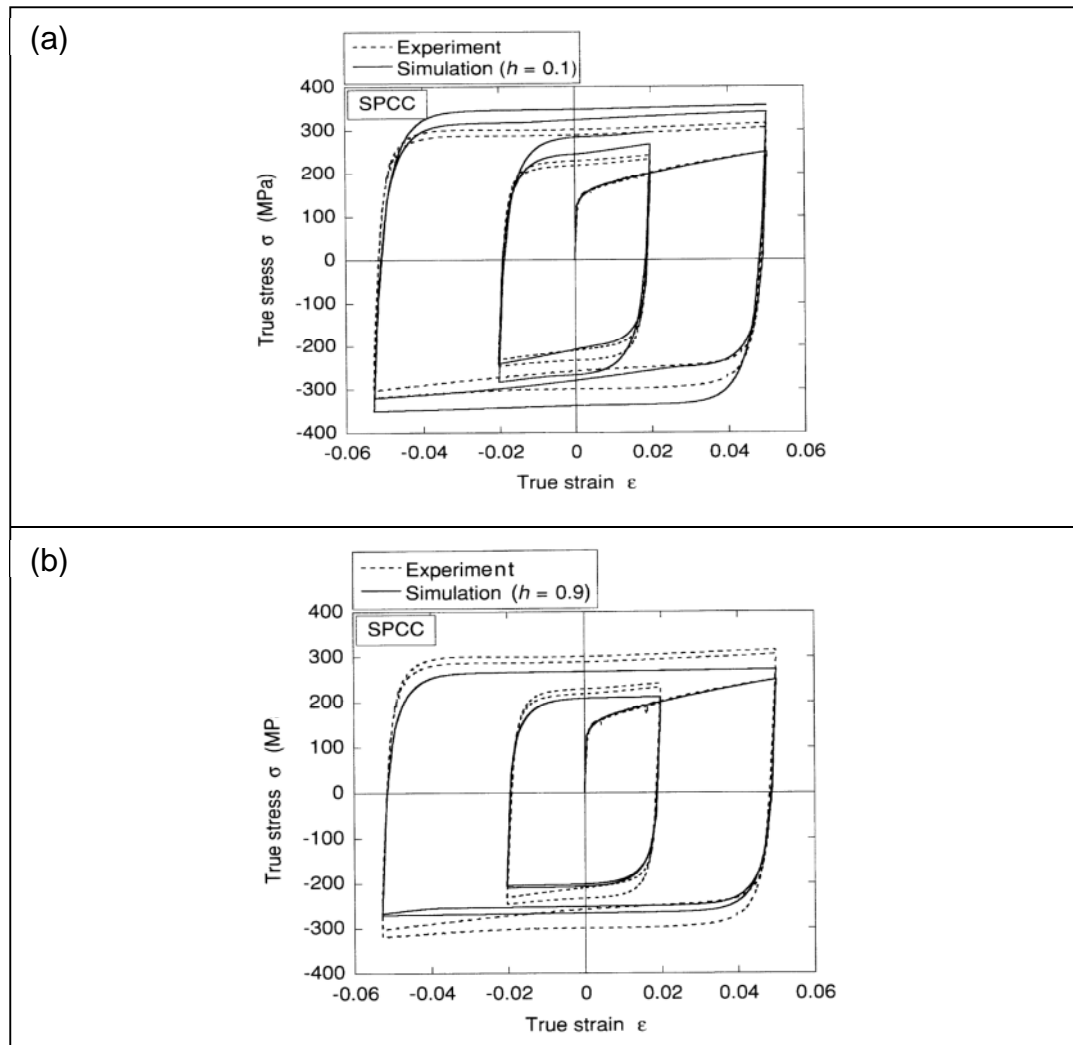


Figure 2.12 The influence of the parameter h on the simulation of the cyclic responses of stress-strain (a) $h = 0.1$ and (b) $h = 0.9$ according to the Y-U model [5]

2.5 Numerical modelling of springback

2.5.1 Comparison of material models

In the past many researchers have investigated the behaviour of elastic-plastic deformation and proposed suitable models but within the limits of small deformation theory. However, in sheet metal forming, a blank material undergoes severe distortion and a subsequent attempting of the deformed blank to return to the undeformed shape described as the springback phenomenon.

Many commercial FE codes contain constitutive models to simulate the mechanical behaviour of different materials. One such model is the mixed isotropic-kinematic hardening model. However, these models have limitations in predicting some aspects of material behaviour. For example such models often exclude the Bauschinger effect, work hardening stagnation, when the rate of work hardening during large deformations is almost zero, and the reduction in Young's modulus following unloading from large plastic strains [5].

Although various researchers [5, 16-20] have concluded that for a precise prediction of springback, the Bauschinger effect should be taken into account, few researchers have investigated large-strain cyclic plasticity experimentally [6]. While some papers have been published on reverse deformation after the plastic loading [7, 8], Yoshida was the first to successfully conduct cyclic tension-compression deformation experiments for typical sheet material at large strains [5].

Some researchers have suggested constitutive models which describes both the Bauschinger effect and work hardening stagnation [21]. However, they do not pay much attention to the stress-strain response in the small scale re-yielding region which is essential to predict springback [5]. The plastic anisotropy has a positive correlation with the springback which increases with the increase of this plastic anisotropy [22-25].

Yoshida and Uemori [15] compared their model (Y-U model) with several other models such as the isotropic hardening (IH) model, the linear kinematic hardening (LK) model and the nonlinear kinematic hardening (NLK) model of Armstrong–Frederick (AF). Figure 2.13 shows a comparison of a two cycle stress-strain curve for high strength steel between the four models and experimental data. It is clear from Figure 2.13 that both the AF and Y-U models are in good general agreement with the experimental results but the Y-U model has slightly better fit to the experimental data. This is due to the fact that the Y-U model is able to predict the Bauschinger effect much better than the AF model [5, 15]

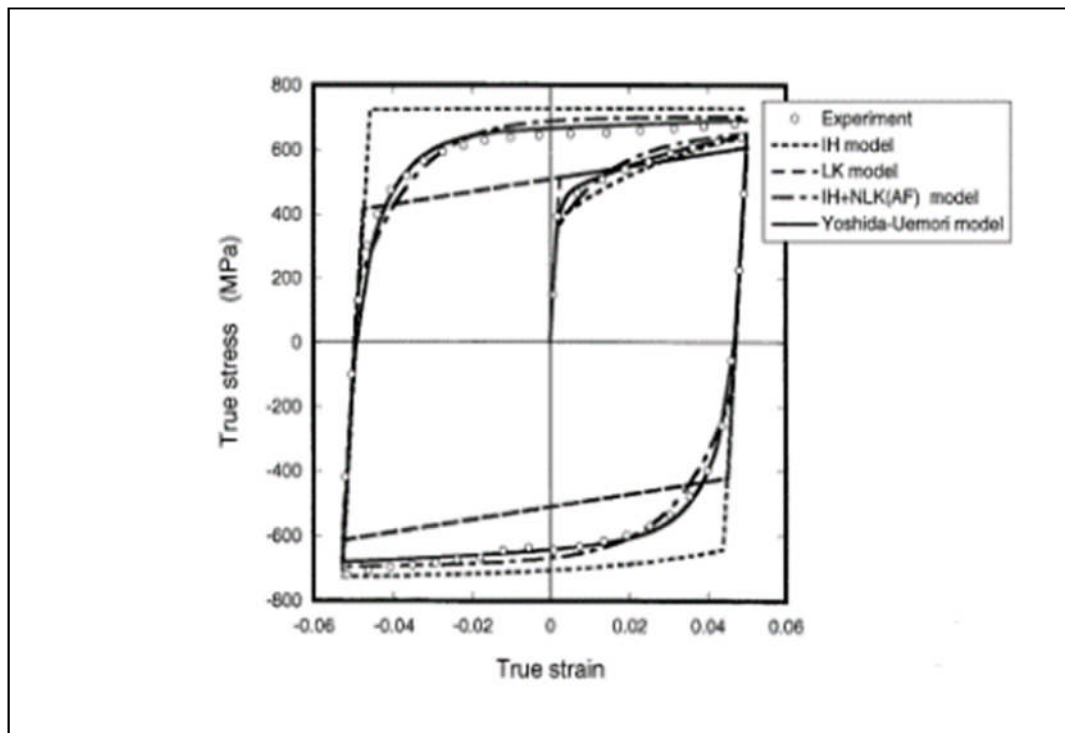


Figure 2.13 Stress-strain curve for two cyclic tension compression of high strength steel sheet for four different model [15]

Eggertsen and Mattiasson [3, 26] investigated the following five hardening models: isotropic, mixed isotropic -kinematic, Geng-Wagoner, Armstrong-Frederick and Yoshida-Uemori hardening models. They used the NUMISHEET'93 benchmark problem as illustrated in Figure 2.14 (a) for a DP600 high strength steel blank. Also, the degradation of the Young's modulus during reverse stress was examined. Figure 2.14 shows the springback prediction after the forming process for a DP600 blank for the five hardening modelling mentioned above, with or without assuming a reduction in the Young's modulus. From this figure, it is clear that the Geng-Wagoner and Yoshida-Uemori hardening models are predicting the springback very well and that the reduction of the Young's modulus must be considered for accurate results.

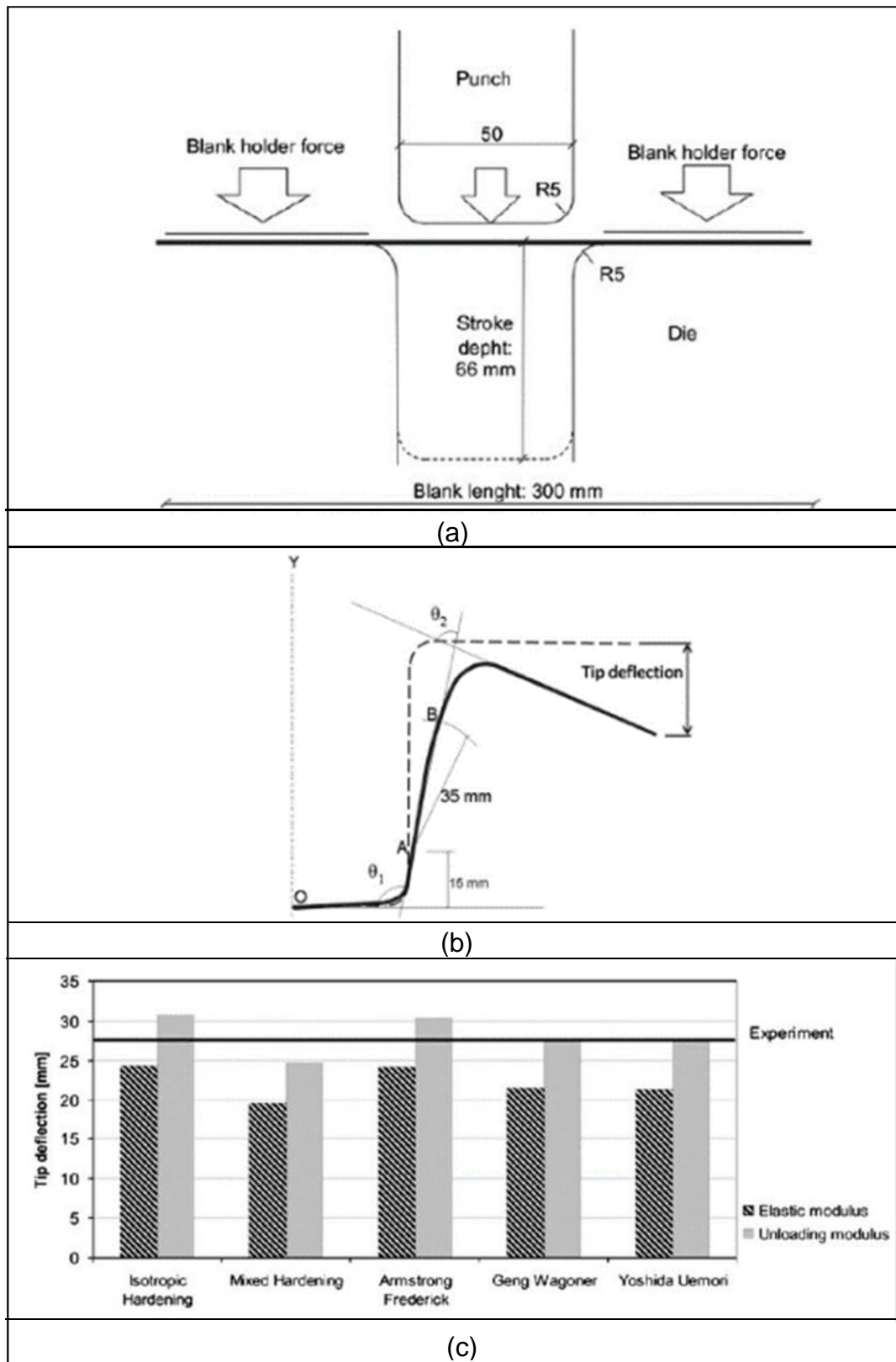


Figure 2.14 The NUMISHEET'93 benchmark problem for the DP600 blank (a) sketch of the problem (b) tip deflection definition of springback(c) tip deflection magnitude for different hardening models and with or without considering the degradation of the Young's modulus [3]

Chongthairungruang et al. [27] conducted experiments on a modified S-rail forming ring using dual phase steel DP780 to investigate springback with respect to the pre-strain effect and material orientation. Finite element analysis was carried out using several material models: Hill's 1948 plasticity model, Barlat–Lian's 1989 model, and the Yoshida–Uemori kinematic hardening material model. It was found that the best springback prediction was when the Y-U model was used, followed by Barlat–Lian's model. Also, it was found that the higher the pre-strain of the deformed part, the higher the springback that resulted.

Chongthairungruang et al. [28] also investigated springback in the U-drawing process for three different steels: one was mild strength steel (JSC270C) and two were high strength steels (JSC590R and JSC780Y). Finite element analysis was conducted using Hill's 1948 model, Barlat's 2000 model and the Yoshida–Uemori model for the three materials. They found that the higher the strength of the material, the higher the springback. They also found that the Y-U model gave more precise prediction of the springback than the other models especially for the high strength steels.

Yoshida and Uemori [15] studied the springback occurring in a high strength steel after the U-drawing process illustrated in Figure 2.15 (a). The investigation compared the springback by measuring the side wall curl using the four different models explained above. Also four different radii were used to demonstrate the influence of the die radius on the level of the springback. Figure 2.15 (b) shows clearly the robustness of the Y-U model in predicting the springback after the U-drawing process. Also it shows the significant influence of the die radius on the magnitude of the springback.

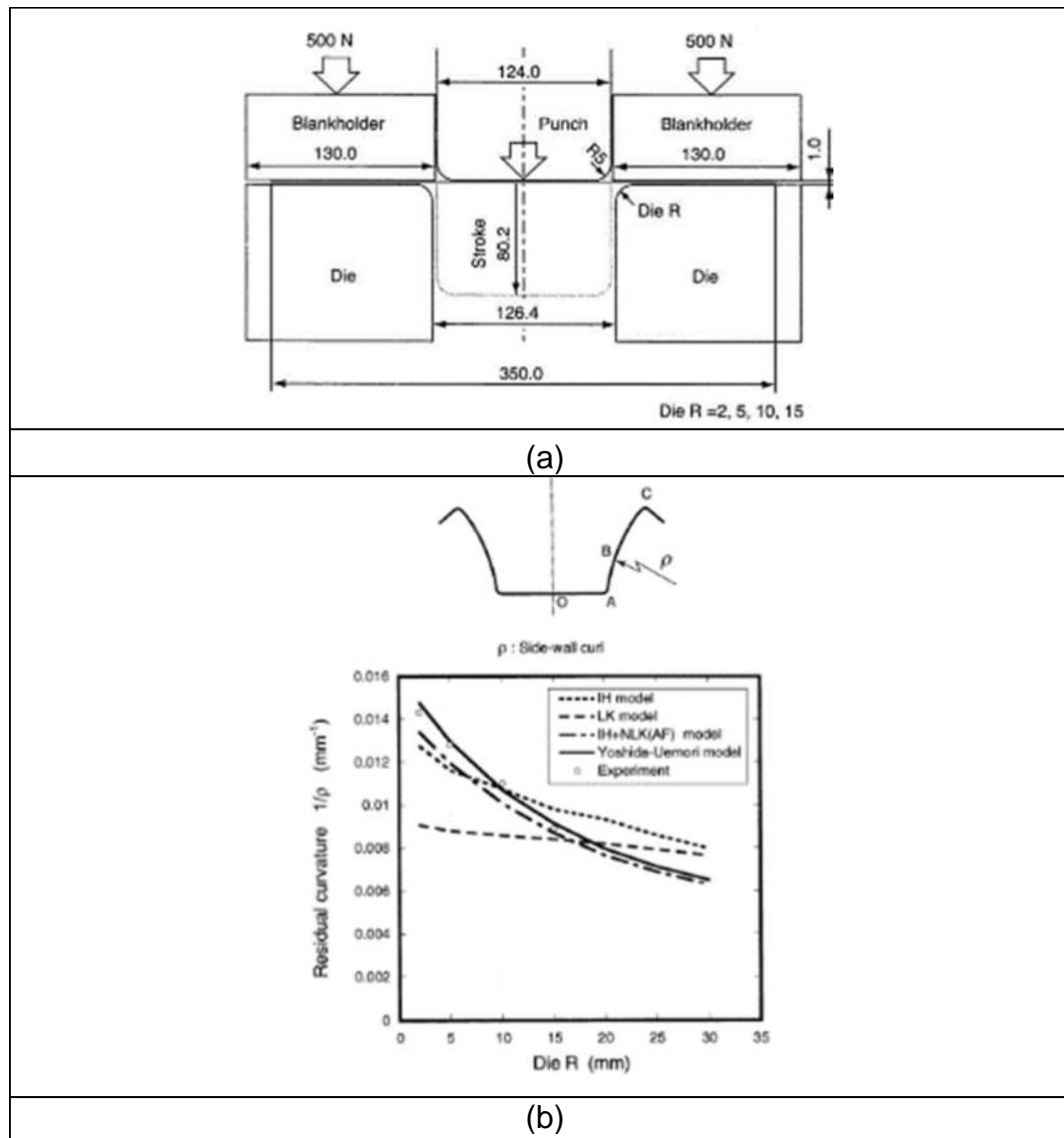


Figure 2.15 (a) Schematic of U-drawing experimental set-up and (b) side wall curl after springback for different die radii simulated using different four models [15]

2.5.2 Comparison of numerical schemes

There are two main approaches used to solve a dynamic equilibrium equation at every time step. Firstly, the explicit method proceeds by predicting the solution at time $t+\Delta t$ by using the solution at time t without iterating to check the convergence of the solution and hence it requires a relatively small time step to obtain accurate results. Secondly, the implicit method can obtain the solution at time $t+\Delta t$ based on this time and using the

solution obtained at time t but with an iteration procedure to give the required level of accuracy. A large time step can be applied for the implicit method [29].

The implicit finite element method has been applied by Prior [30] to analysis 2D forming problems, the advantage being the ability to analyse static and quasi-static problems easily. However, the disadvantages of this method are that it requires a large memory and computational time due to the problems of high nonlinearities such as the friction behaviour and contact changes during the sheet metal forming process. Furthermore, there may be convergence difficulties due to changes in contact conditions and, for 3D complex metal forming problems, convergence is often not achievable. On the other hand, the advantages of the explicit method when analysing large three dimensional contact problems in metal forming processes are the low memory requirements and run times compared with the implicit technique [30].

Sun et al. [31] investigated the difference between implicit and explicit integration methods for a dynamic problem. Fast and slow linear contacts were investigated. They concluded that the explicit method is much less computationally expensive than the implicit one for the fast contact problem. On the other hand, the implicit scheme is appropriate for the slow contact problems

Karafillis and Boyce [32] investigated 3D simulation of a forming process followed by springback calculation using two different approaches: implicit-implicit and explicit-implicit. The implicit scheme for the forming analysis requires a high computational time and it is very difficult to predict the required computation time due to convergence difficulties [30, 32]. However, the explicit method gave lower computational time with good agreement with experiment. Narasimhan and Lovell [33] utilized the explicit technique for the forming process analysis and the implicit procedure for the springback calculation. The springback predictions showed good agreement with the experimental results.

The U-drawing process of the NUMISHEET'93 benchmark problem shown in Figure 2.14 (a) was selected to investigate numerical parameters that

influence the prediction of springback using the explicit scheme for the forming analysis followed by the implicit method for springback calculation by Lee et al. [34]. The parameters investigated were contact damping, penalty method parameter, blank element size, element size around tool corner and punch velocity. It was found that the element size in the blank and around the tool corner have significant influence on the springback prediction.

Lee et al. [35] investigated a U-drawing process where the blank was drawn by an elliptical tool using the explicit method for the forming process and the implicit method for the springback calculation. The results explained the bi-directional springback phenomenon which occurs in the manufacture of the part [35].

Wang et al. [10] investigated springback in sheet metal forming using the U-drawing process as a benchmark. It was found that greater strength and lower Young's modulus material results in higher springback angle. Other researchers have investigated the influence of die radius and clearance on springback for steel sheet. They found that springback increases with increasing die radius as well as with clearance [36, 37].

Chen and Ko investigated the influence of the die radius and the clearance on springback after the L-bending process [37]. They found that an increase in the die radius and clearance both increased the springback as shown in Figure 2.16 (a) and (b) respectively.

Samuel [38] studied springback after U-drawing for three different materials: mild steel, stainless steel and aluminium alloy. He utilised the MARC FEM package to develop 2-D plane-strain models to investigate the springback in U-drawing of the three materials. The springback was greater for the stainless steel, then for the aluminium alloy, whilst the mild steel blank showed trivial springback as shown in Figure 2.17. Also parameters such as plastic anisotropy, friction coefficient, die radius, punch radius and blank holder force were investigated. It was found that the springback increases with the increase of the punch radius and plastic anisotropy. However, the increase of the blank holder force and friction coefficient caused a reduction in the springback level.

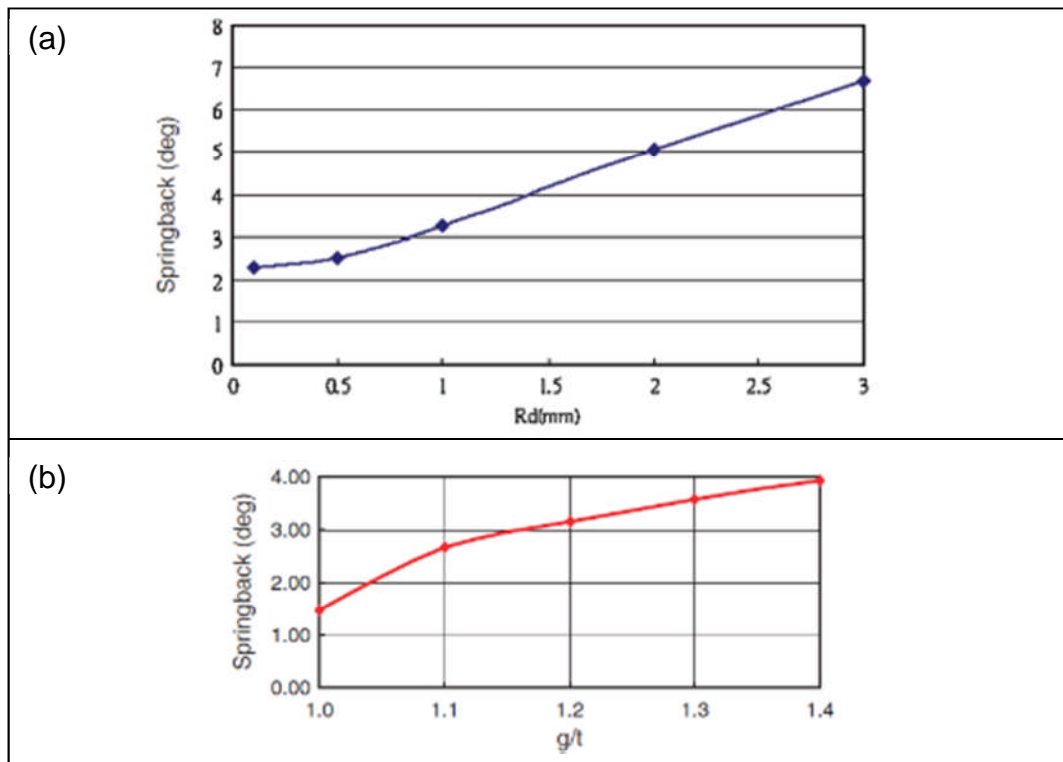


Figure 2.16 The influence of (a) die radius and (b) clearance on the springback after L-bending [37]

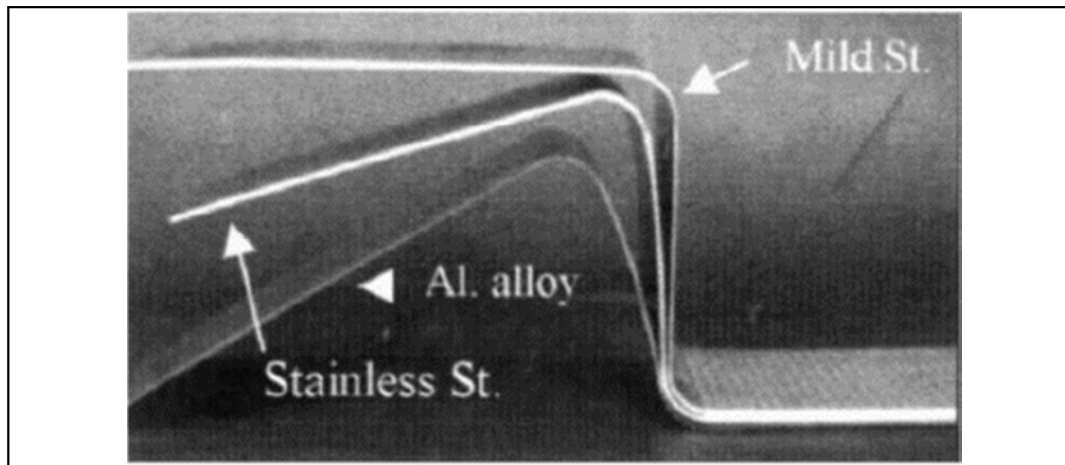


Figure 2.17 Springback of three different materials after U-drawing [38]

The springback in a deep drawing process was investigated by Padmanabhan et al. [39] using a 3D implicit finite element technique. The isotropic hardening behaviour with plastic anisotropy as described by Hill's 1948 material model was considered for a ASIS 304 stainless steel blank.

The influence of three parameters, die radius, blank holder force and friction coefficient, on springback was investigated using the Taguchi method. It was found that the die radius is the most important factor that controls the springback followed by the friction coefficient and then the blank holder force.

Wenjuan et al. [40] employed an artificial neural network (ANN) and genetic algorithm (GA) to predict springback. It was found that the springback is reduced by selecting a smaller die radius, larger height of the deformed part, larger clearance and thicker metal sheet as well as a material with a higher Young's modulus and lower yield strength.

2.6 Design of Experiments and optimisation techniques in sheet metal forming

The process of finding the best solution under a set of given conditions is called optimisation. In practice engineers have to make decisions about the design, maintenance, cost etc. of many kinds of engineering systems. The goal of the decision making is defined by an objective function which is used to minimise or maximise a certain parameter [41].

Optimisation methods based on empirical rule adjustment are not applicable to complex geometries or materials without large databases. Therefore, the time to undertake an optimisation process can be very large. The response surface method (RSM) is deemed to be a reliable method to reduce this time [42]. The RSM evaluates an objective function at several points in the design space to gain a good approximation [43].

Mkaddem and Bahloul [43] applied the RSM to two parameters (clearance and die radius) to investigate the mechanical behaviour of a sheet metal forming process. The numerical simulation results showed good agreement with experiment [43]. Furthermore, the RSM was applied to evaluate the maximum bending during the metal forming process and to investigate the influence of both die radius and clearance as design variables. A cubic

polynomial function was used to gain good prediction of optimal die radius and clearance[43].

Hino et al. [44] designed an optimum blank size for sheet metal forming using the interaction of high- and low-fidelity optimisation methods. The main purpose behind this approach was to reduce computing times since the low-fidelity method is much less time consuming than the high-fidelity method. The corrected low-fidelity method is used in the iterative optimisation procedure while the high-fidelity method is used to correct the results of the low-fidelity method and to validate the final solution. It was found that this optimisation procedure was both quick and accurate [44].

Gassara et al. [45] designed an optimisation technique to minimise springback in L-bending. They developed a Gauss-Newton technique by coupling the Abaqus/standard code with Python. Three process parameters were optimised in this study: die radius, clearance and the blank holder force. The objective function was defined as the difference between the desired value of the springback angle and the simulated value of this angle [45].

2.7 Summary of the findings and implication for the current study

This chapter has illustrated several important aspects of sheet metal forming processes such as plasticity theory, material modelling and numerical modelling of the processes.

Many researchers have investigated elastic-plastic deformation and proposed different models, but usually within the limits of small deformation. A blank material is exposed to large deformation under sheet metal forming processes such as U-drawing. The deformed part then attempts to return to its original shape which is known as the springback phenomenon. Most commercial FE codes possess constitutive models to simulate the mechanical behaviour of different materials. However, these models have

limitations in predicting some aspects of material behaviour such as the large deformation cyclic plasticity which is a common occurrence in sheet metal forming. For example the Bauschinger effect, work hardening stagnation (when the rate of work hardening during large deformation is almost zero) and the reduction in Young's modulus in the case of unloading are not adequately considered by many models.

Researchers have investigated a number of hardening models: principally the isotropic, mixed isotropic-kinematic, Geng-Wagoner, Armstrong-Frederick and Yoshida-Uemori hardening models.

Many have used the NUMISHEET'93 U-drawing benchmark problem for a DP600 high strength steel blank because it results in significant springback. Also, the degradation of the Young's modulus during reverse stress has been examined by various researchers. They concluded that the Geng-Wagoner and Yoshida-Uemori hardening models predict the springback to an acceptable level of accuracy and the reduction of the Young's modulus should also be considered for accurate results.

In the current study the Y-U model was used for the following reasons:

1. Most researchers who have used this model have obtained an accurate prediction of the springback that occurs after sheet metal forming processes.
2. The Y-U model parameters for the materials in the present work could be derived using the Yoshida and Uemori laboratory and facilities in Hiroshima University in Japan.
3. The Y-U model is implemented in the Ls-Dyna software which is available at Leeds University.

Also based on the literature review, explicit and implicit finite element methods were utilised for the forming and the springback analysis respectively since together this represents a computationally efficient approach.

It was found from the literature that many researchers have investigated springback after the U-drawing utilising the NUMISHEET 93 benchmark problem. The blank materials used do not necessarily have the same properties or are formed under the same conditions e.g. of friction

coefficient. Therefore, the current study will design an appropriate metal forming rig which is able to perform the two forming processes: L-bending and U-drawing processes using the same tools. Also, the rig will be able to vary parameters such as the die radius, clearance and blank holder force.

Furthermore, most of the researchers assumed the static and dynamic friction coefficients to be the same which, in reality, is not the case. Therefore, both static and dynamic friction coefficients were measured in the present work for the four blank materials sliding against a typical tool surface.

Although 2D plane strain modelling of the U-drawing process is computationally faster, many researchers investigating such processes have used 3D thin shell quadratic elements. Therefore, this research has investigated the differences between the two approaches.

Design of experiment and optimisation analysis have been found by some researchers to be an appropriate approach to minimise springback. Several researchers minimise the springback after U-drawing or L-bending processes by varying two design variables such as die radius and clearance or die radius and blank holder force. However, in the current study a parametric study was conducted using suitable ranges for important parameters that might control the magnitude of springback. Based on the results obtained from the parametric studies, the most influential factors on the springback were selected for use in a new approach to optimisation analysis for metal forming problems involving springback.

CHAPTER 3: DERIVATION OF THE MECHANICAL PROPERTIES OF THE BLANKS MATERIALS

3.1 Introduction

This chapter describes the experiments that have been undertaken to derive the mechanical properties of the material samples required for the Y-U material model. These experiments were carried out using a Shimadzu tensile test machine located in the elasto-plasticity laboratory in the Mechanical Engineering Department at the University of Hiroshima in Japan.

In order to identify the properties of the test sheet materials, two kinds of specimens were cut at different angles to the rolling direction (0° , 45° and 90°) and sets of uniaxial tension and tension-compression tests were conducted. The sheet materials used in this project were provided by Jaguar Land Rover, in the UK. Two of them were high strength materials (steel and aluminium) and the remaining were low strength materials (steel and aluminium). They were as follows:

- DP600 (high strength steel) at a thickness of 1.6 mm.
- DX54D (low strength steel) at a thickness of 1.6 mm.
- CPLA100K38 (high strength aluminium alloy) at a thickness of 2.5 mm.
- CPLA10414 (low strength aluminium alloy) at a thickness of 2.5 mm.

Specimen preparation and the experimental methodology are explained in the following sections. The principal objective of this study was to use the results of the experiments to identify the following for each material:

- Bulk mechanical properties including the yield stress (Y), the ultimate stress (U) and the elongation (EL) in the three in-plane directions.
- The degree of anisotropy which provides the normal anisotropy coefficient by determining the r_0 , r_{45} and r_{90} parameters

- The degradation of the Young's modulus at large plastic strains (E_0 , E_a and ζ)
- The Y-U model parameters (Y , B , C , b , m , R_{sat} and h)

These findings will be used to define the parameters of the Y-U material model within the numerical simulation of the forming process and the subsequent springback.

3.2 Machine description

A Shimadzu tensile test machine was used for all the experimental work and this is shown in Figure 3.1. This machine has a load capacity of 50 kN. The cross-head velocity can be varied from 0.0005 to 1000 mm/min within ± 0.1 %. A dedicated computer, installed with specialist testing software, controls the machine functions and captures the data required [46].

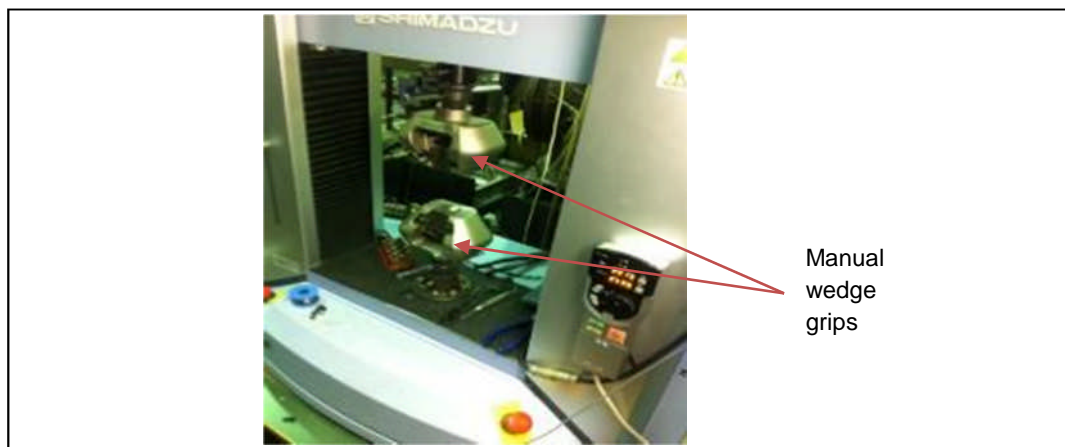


Figure 3.1 Shimadzu tensile test machine at Hiroshima University – Japan

3.3 Specimen preparation

In order to characterise the mechanical properties of the material samples required for the Y-U material model of the selected sheet materials, two types of standardised samples (A and B) were designed and cut at different angles to the rolling direction (0° , 45° and 90°). The specimen dimensions are shown in Figure 3.2.

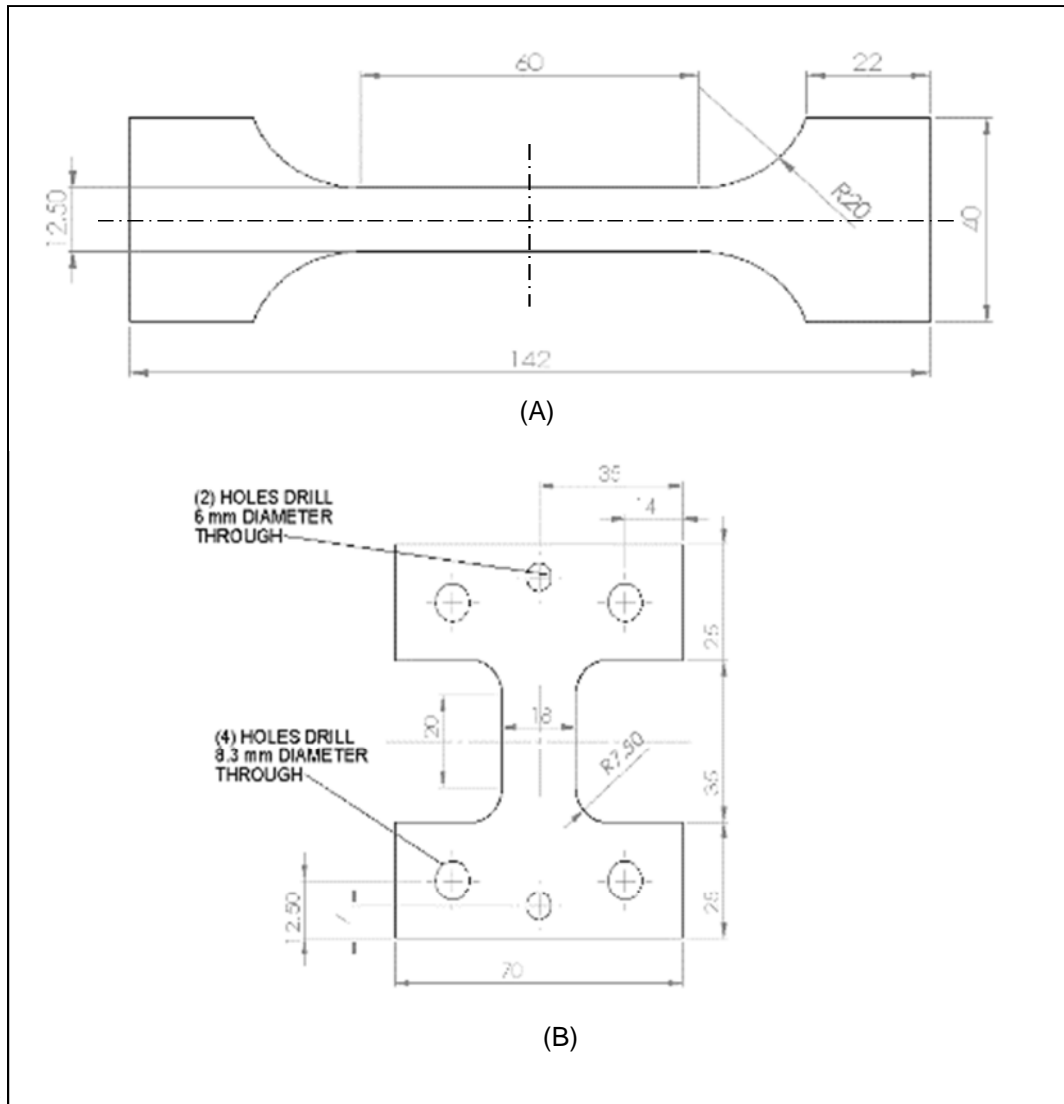


Figure 3.2 Specimen types A and B (all dimensions in mm)

The specimens were produced by wire cutting. The total required number of samples for both kinds of specimen is 16. The experimental method of Yoshida requires the use of two samples of specimen B, that are cut in the rolling direction. In addition, 14 samples from specimen type A were produced as follows: 6 samples at 0° , 4 samples at 90° , and other 4 at 45° to the rolling direction of the specimen. After wire cutting, the samples were cleaned from impurities, that may have stuck on their surfaces, using ethanol. The samples were then measured in width and thickness by a micrometer prior to testing.

The measurement was taken at three points, one on the centre and two on each end of the gauge length as can be seen in Figure 3.3, from which the average dimensions were calculated. The specimen type A was marked as shown in Figure 3.3 to aid extensometer location. If a strain gauge was used it was mounted at the centre of the specimen as shown in Figures 3.3 and 3.4. Specimen type A has a gauge length of 50 mm and width of 12.5 mm.

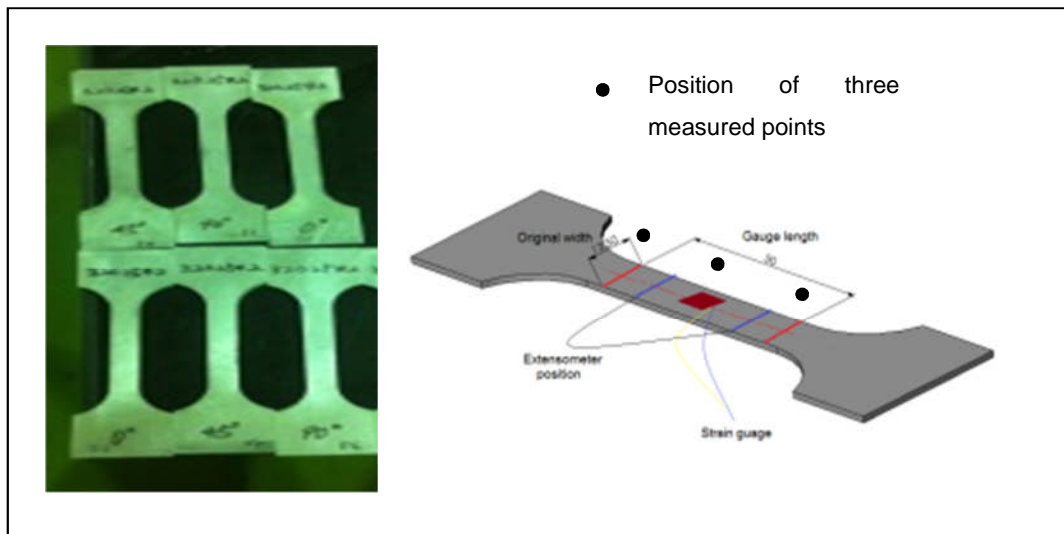


Figure 3.3 Specimen type A geometry- all dimensions in mm

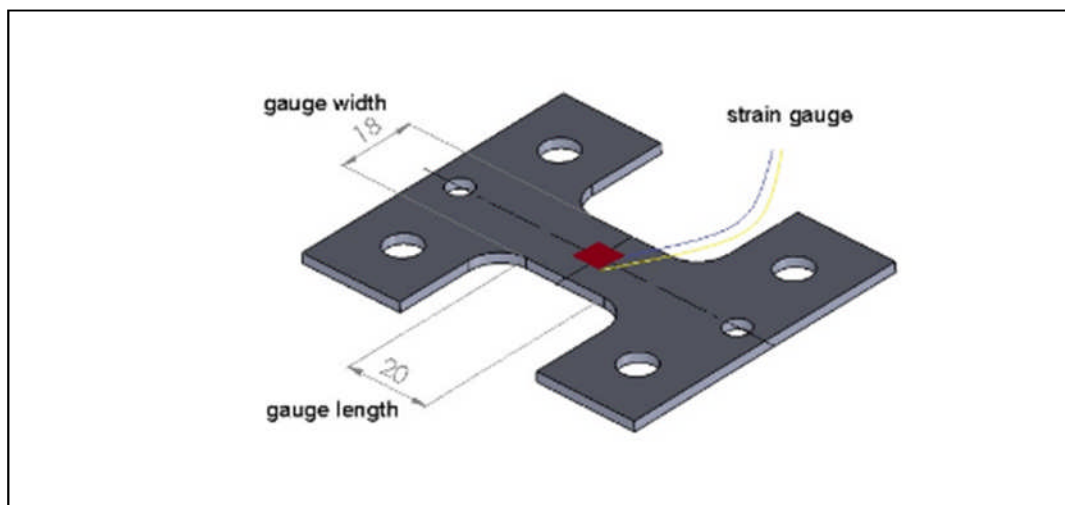


Figure 3.4 Specimen type B geometry- all dimensions in mm

A special loading fixture was used for the specimen type B, which is used to perform the cyclic tension-compression tests. This specimen has a gauge length of 20 mm and a width of 18 mm and was clamped by a special device that consisted of two plates parallel to each other attached by coil-springs as shown in Figure 3.5. This was to prevent the sheet material from buckling. Also, two sheets of Teflon were placed between the specimen and the special device to reduce the friction as much as possible.

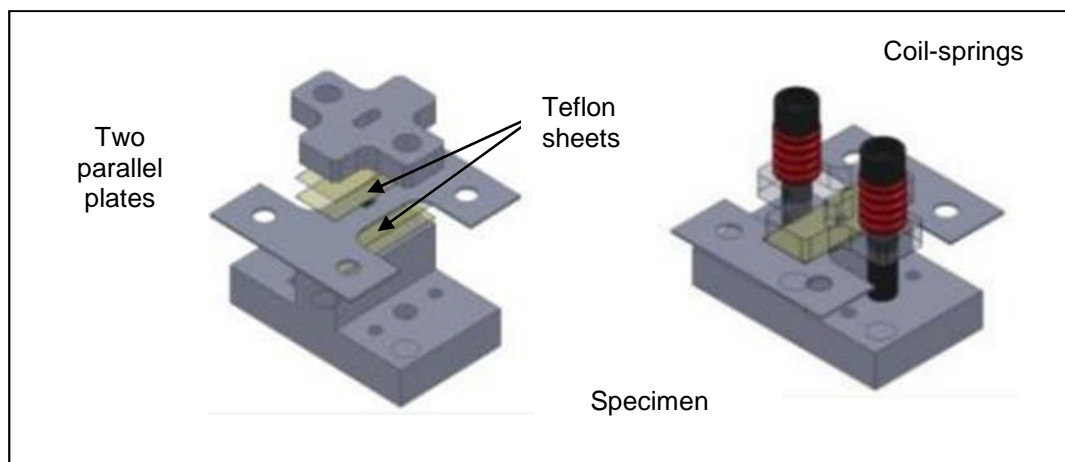


Figure 3.5 Loading fixture for specimen type B prior to the cyclic tension-compression test

3.4 Uniaxial tensile test to failure

3.4.1 Methodology

The uniaxial tensile test was performed on two samples of type A taken parallel, transverse and diagonal to the rolling direction. The experiments were conducted using the Shimadzu tensile test machine described in section 3.2. The main purpose of this test was to identify the mechanical properties (yield, ultimate stress and elongation at break) of the materials. It was also used to set-up the cyclic tension, degree of anisotropy and cyclic compression-tension tests.

The uniaxial tensile test was conducted as follows: After the specimen had been prepared as derived in section 3.3, the sample was clamped and an extensometer was attached to the specimen for conducting strain measurements as shown in Figure 3.6. The specimen was then subjected to tensile load with a constant cross-head speed of 0.5 mm/min until it reached the ultimate stress and subsequently failed.

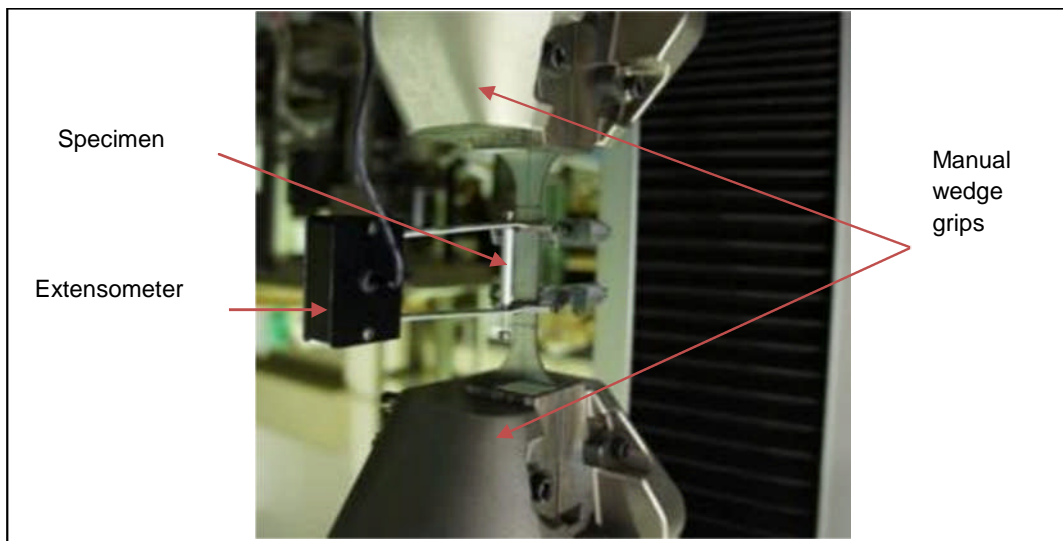


Figure 3.6 Clamped specimen type A with the extensometer

The test was performed for two samples each cut at 0° , 45° and 90° to the rolling direction to determine the stress-strain curve for the material in the different directions. The data obtained was manipulated in order to determine the engineering stress and strain using equations (3.1) and (3.2) :

$$\sigma_{\text{eng}} = \frac{P}{A_0} \quad (3.1)$$

$$\varepsilon_{\text{eng}} = \frac{\Delta L}{L_0} \quad (3.2)$$

Here, P and A_0 denote the instantaneous tensile load and the original gauge cross-sectional area of the specimen. Also ΔL and L_0 represent the displacement and the gauge length of the specimen. By considering the

usual constant volume assumption during plastic deformation, the true stress and strain were calculated using equations (3.3) and (3.4) :

$$\sigma_T = \sigma_{eng}(1 + \varepsilon_{eng}) \quad (3.3)$$

$$\varepsilon_T = \ln(1 + \varepsilon_{eng}) \quad (3.4)$$

The yield stress was obtained from the stress-strain curves at a strain offset of 0.002 as recommended by the ASTM E-8 code [47]. The Young's modulus was determined as the slope of the stress-strain curve within the elastic region.

3.4.2 Results

Using the data exported from the PC of the Shimadzu tensile test machine and the above equations, the stress-strain curves for the DP600 material were obtained as shown in Figure 3.7, in the rolling, transverse and diagonal directions. This shows that the stress-strain curves are almost identical in the different orientations.

Figure 3.7 confirms the consistency in the material behaviour for each direction with respect to the rolling orientation. It can be observed that the specimens cut at 90⁰ experience slightly lower stresses than the other specimens. Also the behaviour of the 0⁰ and 45⁰ specimens were almost indistinguishable to each other.

Figures 3.8 and 3.9 summarise the mechanical properties of the DP600 material in terms of the yield stress (Y), ultimate stress (U) and elongation at failure (EL) in the three directions. These figures represent the average of the results for the two tested specimens at each orientation. Also, they illustrate the variation in the results through the error bar. Overall the figures show that there is no significant variation in the results between specimens.

It is apparent from Figure 3.8 that the 0⁰ specimens gained maximum yield and ultimate stress which were 405.7 and 655.5 MPa respectively. Likewise,

the minimum stress was found for the 90° specimens where the yield stress and the ultimate stress were 378.7 MPa and 646.2 MPa respectively. From Figures 3.8 and 3.9, it can be seen that the higher the yield stress the lower the elongation of the material. For example, the lowest elongation was found for the 0° specimens that displayed maximum yield stress. On the other hand, the minimum yield stress was found for the 90° specimens which had maximum elongation.

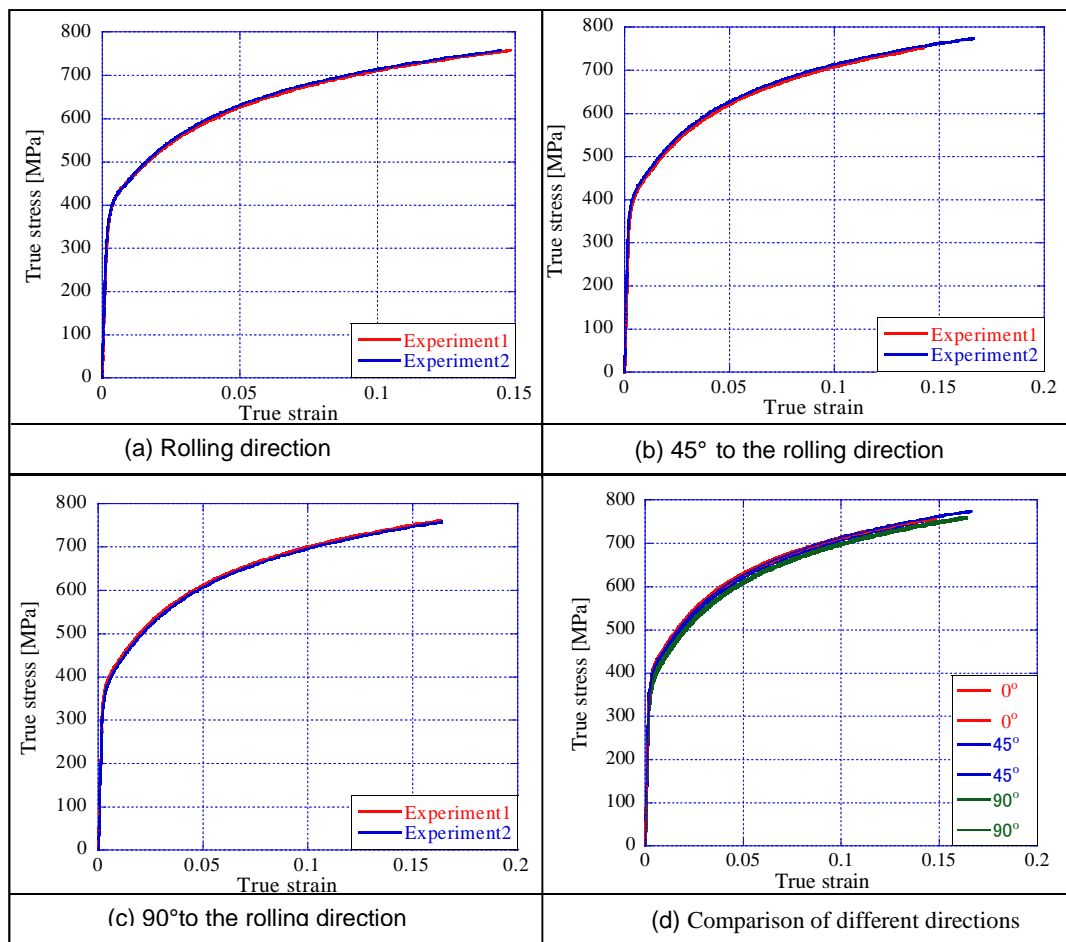


Figure 3.7 Stress-strain curve for DP600

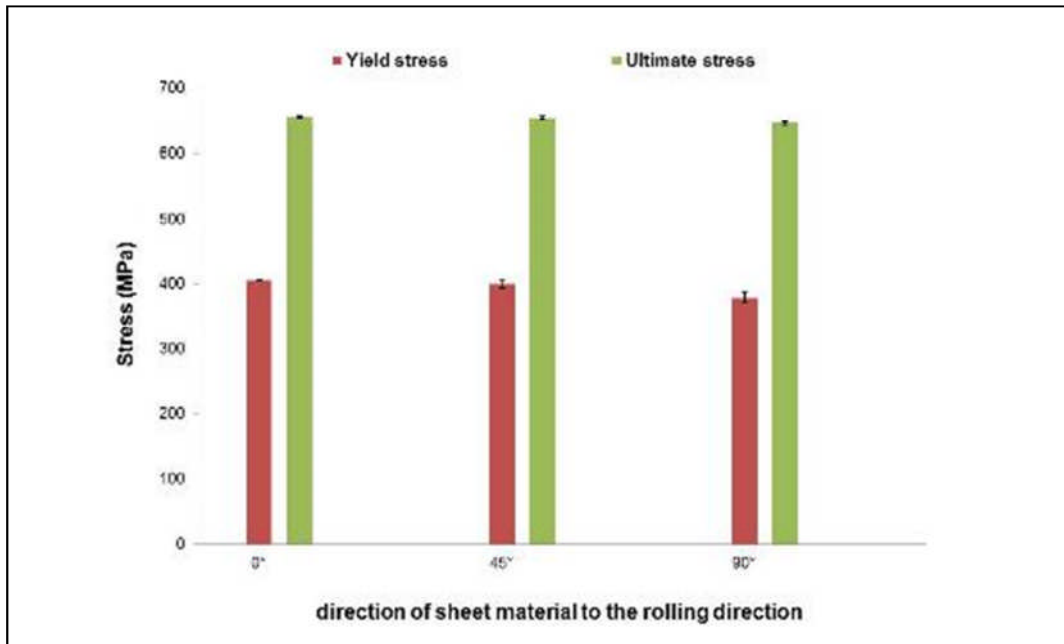


Figure 3.8 Yield and ultimate stress for the DP600 at different orientations

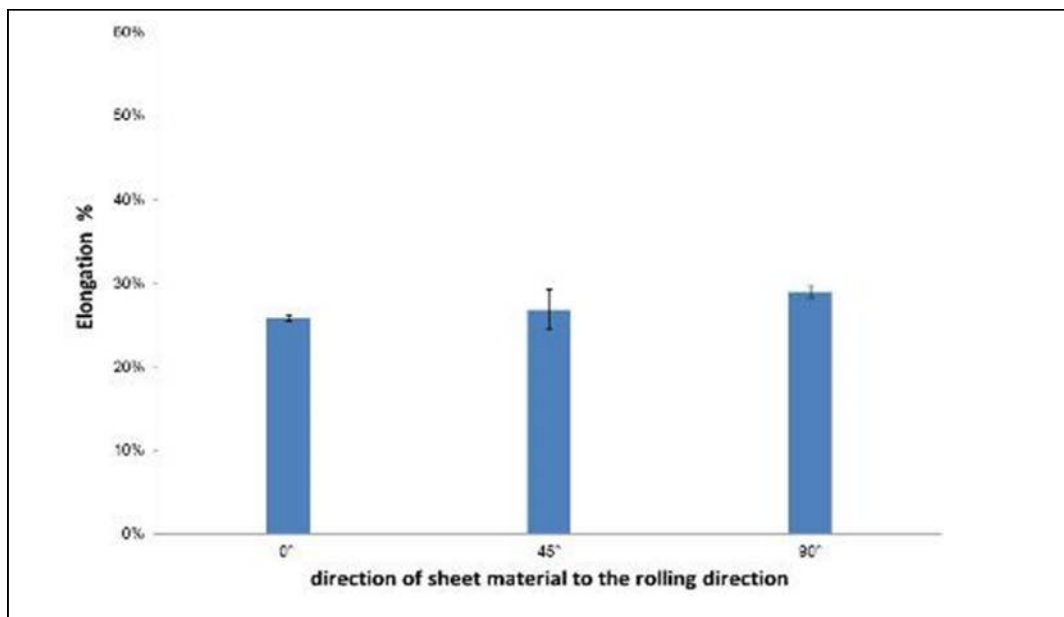


Figure 3.9 Elongation of the DP600 at different orientations

The stress-strain curves for the DX54D material are shown in Figure 3.10 in the rolling, 45 degree and 90 degree directions. The similarity of the stress-strain curves in each direction is apparent. Also Figure 3.10 (d) shows a visible difference in the stress-strain curve especially for the 45° specimens,

where the stress is the highest for a given strain. However, there is no significant difference between the stress-strain curves of the 0° and 90° material samples.

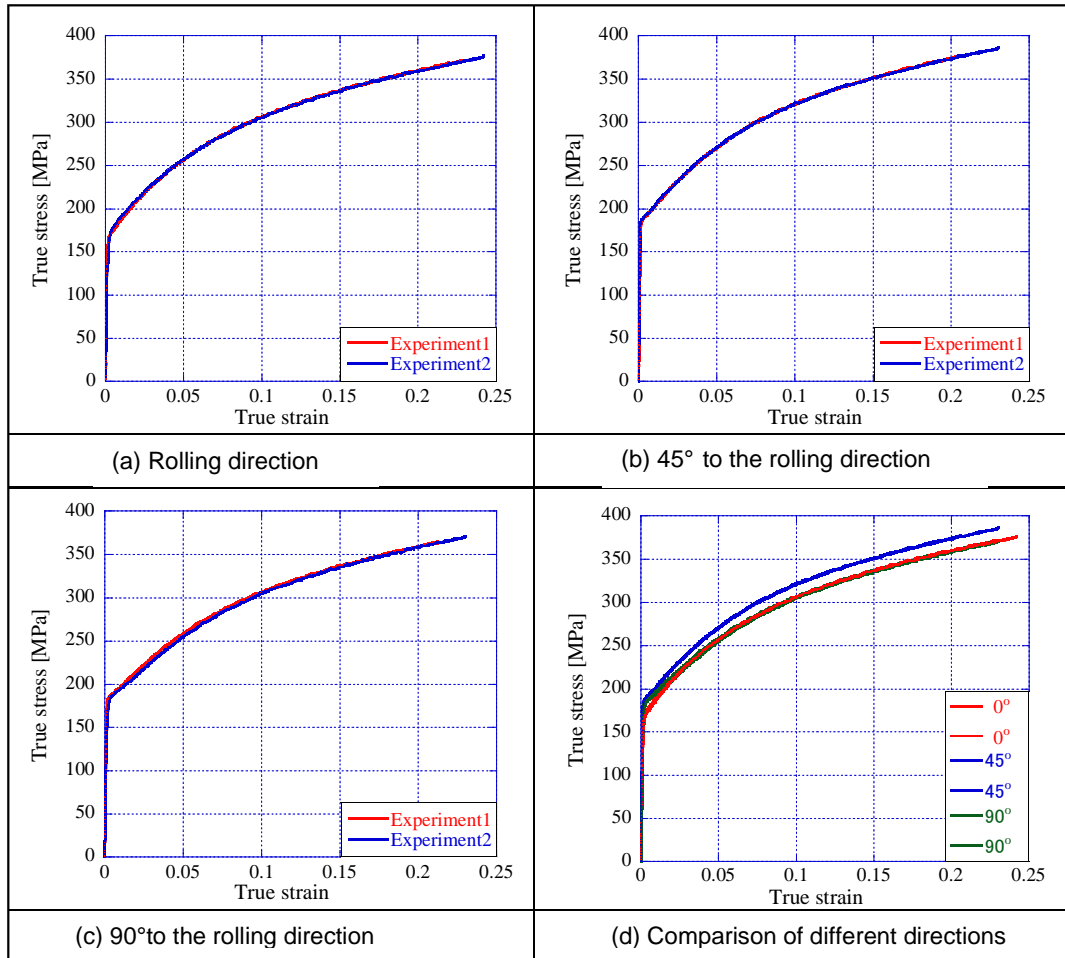


Figure 3.10 Stress-strain curve for the DX54D

The mechanical properties for the DX54D material such as yield stress (Y), ultimate stress (U) and elongation at break (EL) in the three directions are shown in Figures 3.11 and 3.12. The maximum yield and ultimate stress were found for the specimen cut diagonal to the rolling directions where the mean values were about 189 MPa and 307 MPa respectively. On the other hand the minimum yield stress was found for the 0° specimens as shown in Figure 3.11.

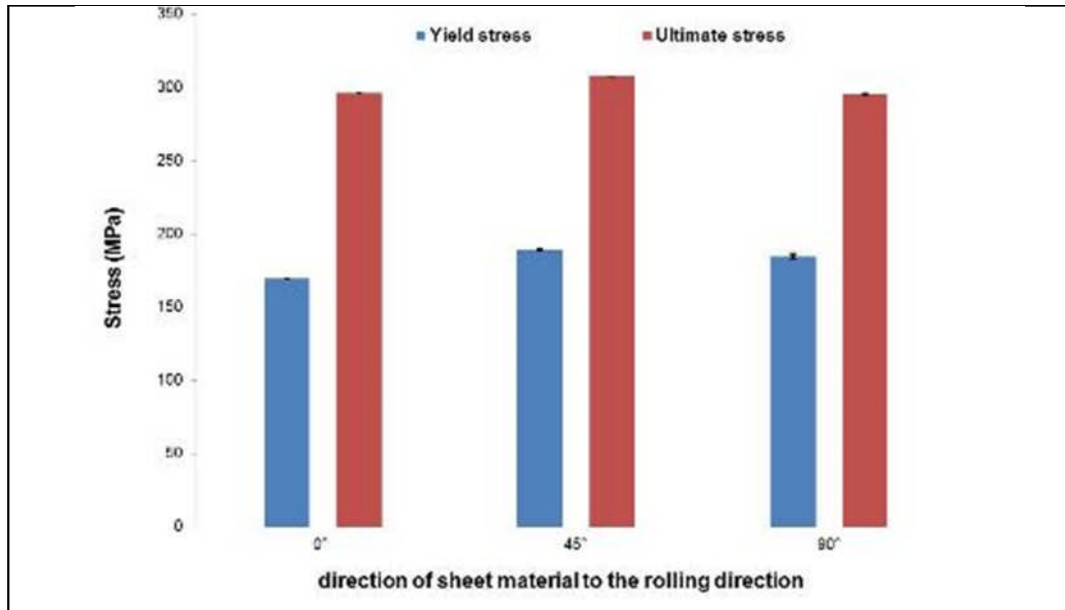


Figure 3.11 Yield and ultimate stress for the DX54D at different orientations

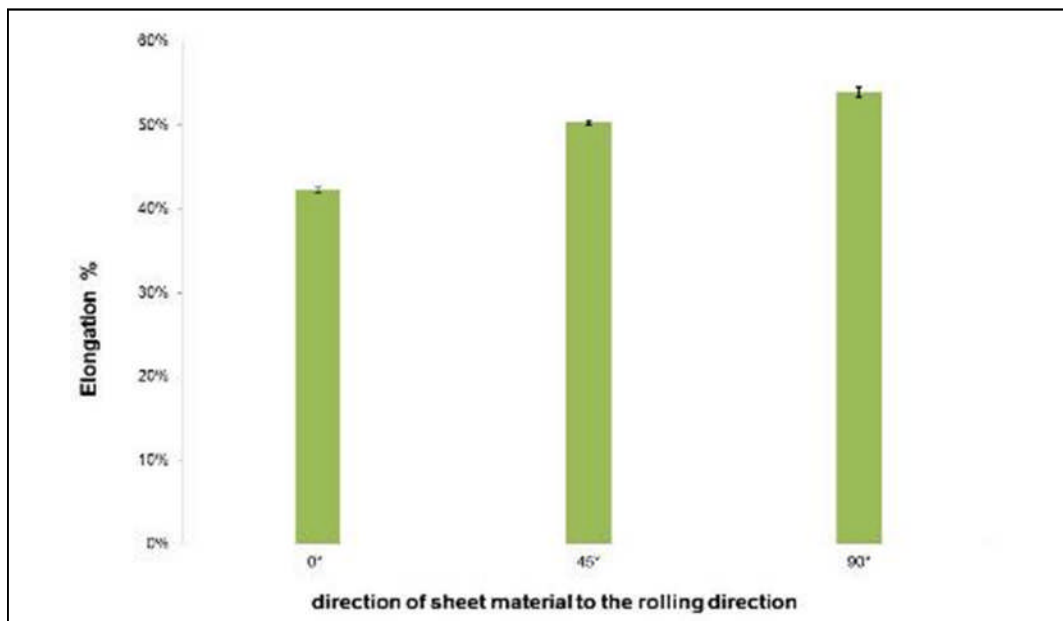


Figure 3.12 Elongation of the DX54D at different orientations

The stress-strain curves for the CPLA100K38 material are shown in Figure 3.13 for the rolling, 45° and 90° directions. It can be seen that the stress-strain curves observed from the different orientation of the specimens were almost equal in each direction. Figure 3.13 (d) shows that the 0°

specimens experience somewhat higher stresses for a given strain than the other specimens whilst the stress-strain curves of the 45° and 90° specimens are very similar.

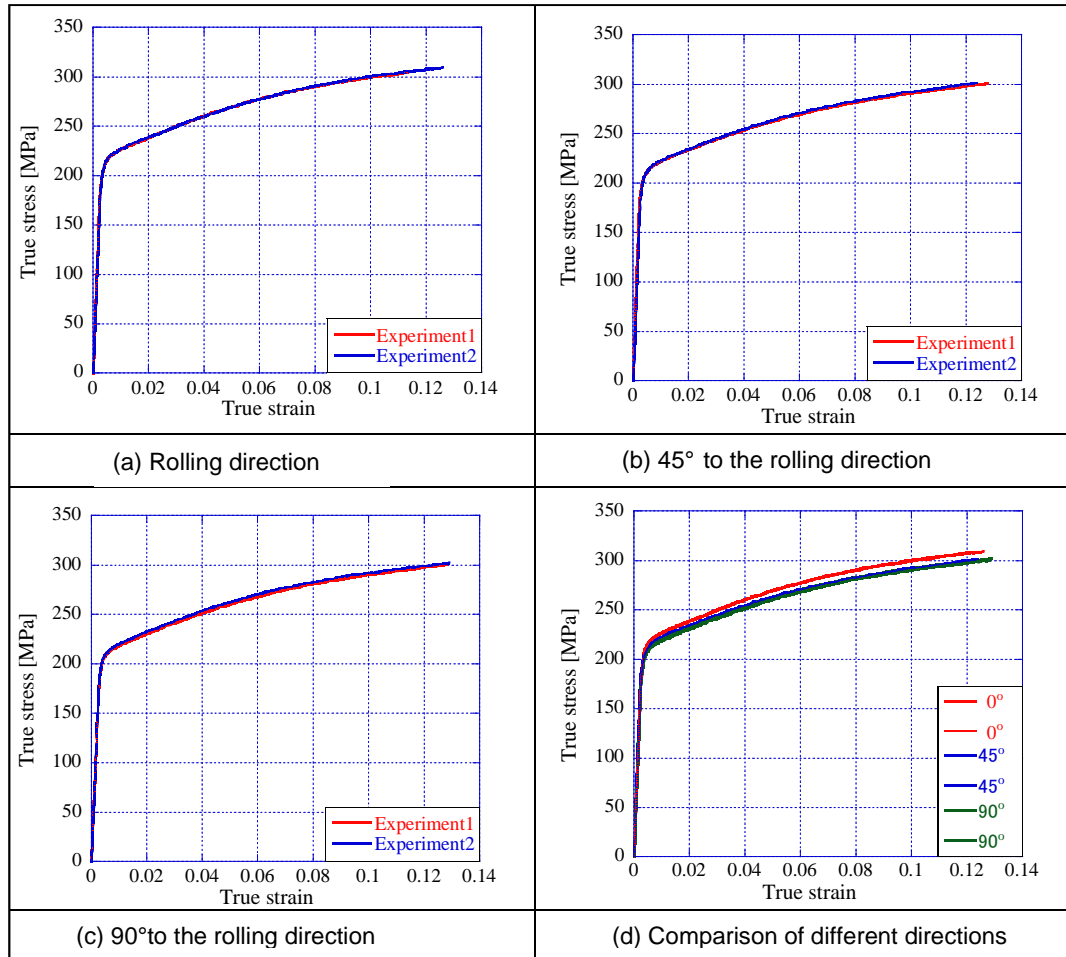


Figure 3.13 Stress-strain curve for the CPLA100K38

The mechanical properties for the CPLA100K38 material such as yield stress (Y), ultimate stress (U) and elongation (EL) in the three directions are shown in Figures 3.14 and 3.15. Although Figure 3.13 (d) shows that the specimen cut parallel to the rolling orientation experienced higher stresses than the other specimens, the maximum yield stress was found for 45° specimens as shown in Figure 3.14. The highest ultimate stress was found for specimens cut transverse to the rolling direction. Moreover there was no significant difference of the material elongation in each orientation as can be seen in Figure 3.15.

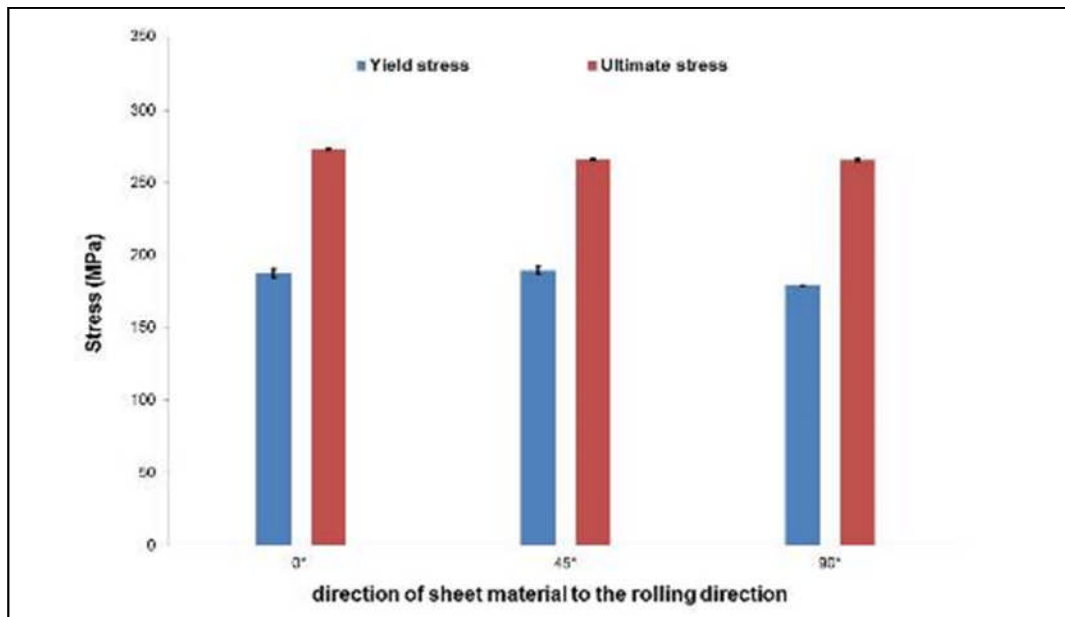


Figure 3.14 Yield and ultimate stress for the CPLA100K38 at different orientations

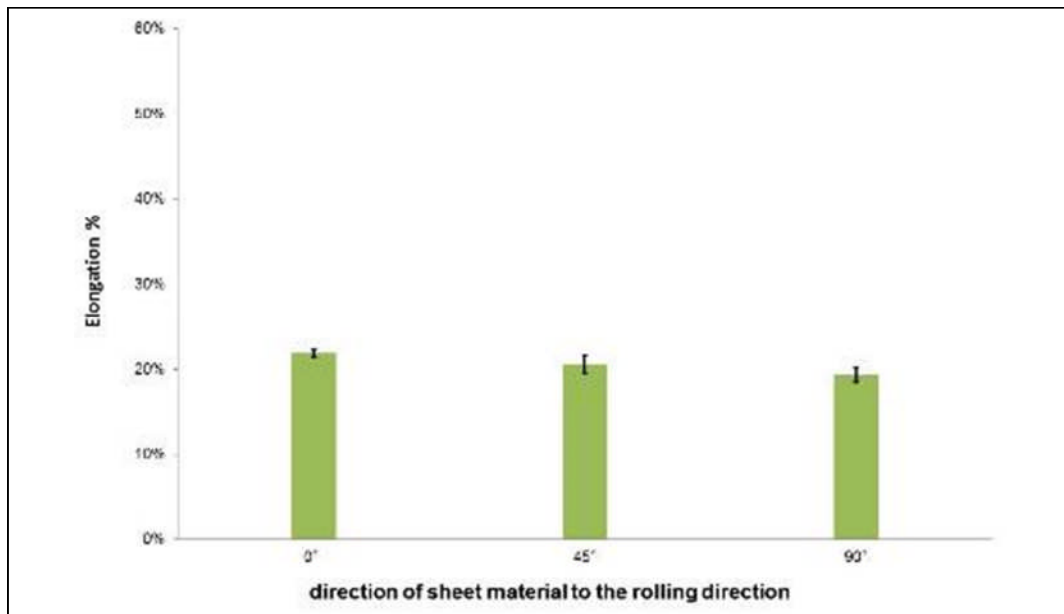


Figure 3.15 Elongation of the CPLA100K38 at different orientations

The stress-strain curves for the CPLA10414 aluminium alloy are shown in Figure 3.16 for the rolling, 45° and 90° direction of the sheet. Interestingly, this figure shows unstable stress-strain curve due to the so-called serration or Portevin–Le Chatelier (PLC) effect which is common in Al Mg alloys [48-50]. This is due to the interaction between solute atoms and mobile

dislocations which is known as dynamic strain aging [49-51] and results in inhomogeneous deformation with a number of localisation bands. These are undesirable as they can affect the formability of the material [51]. The chemical composition of the CPLA 10414 alloy is summarised in Table 3.1 from which it can be seen that the Mg content is relatively high [52]. Figure 3.16 shows that the stress-strain curves were almost identical for each of the two 45° and 90° specimens whilst they were more varied for the 0° specimens.

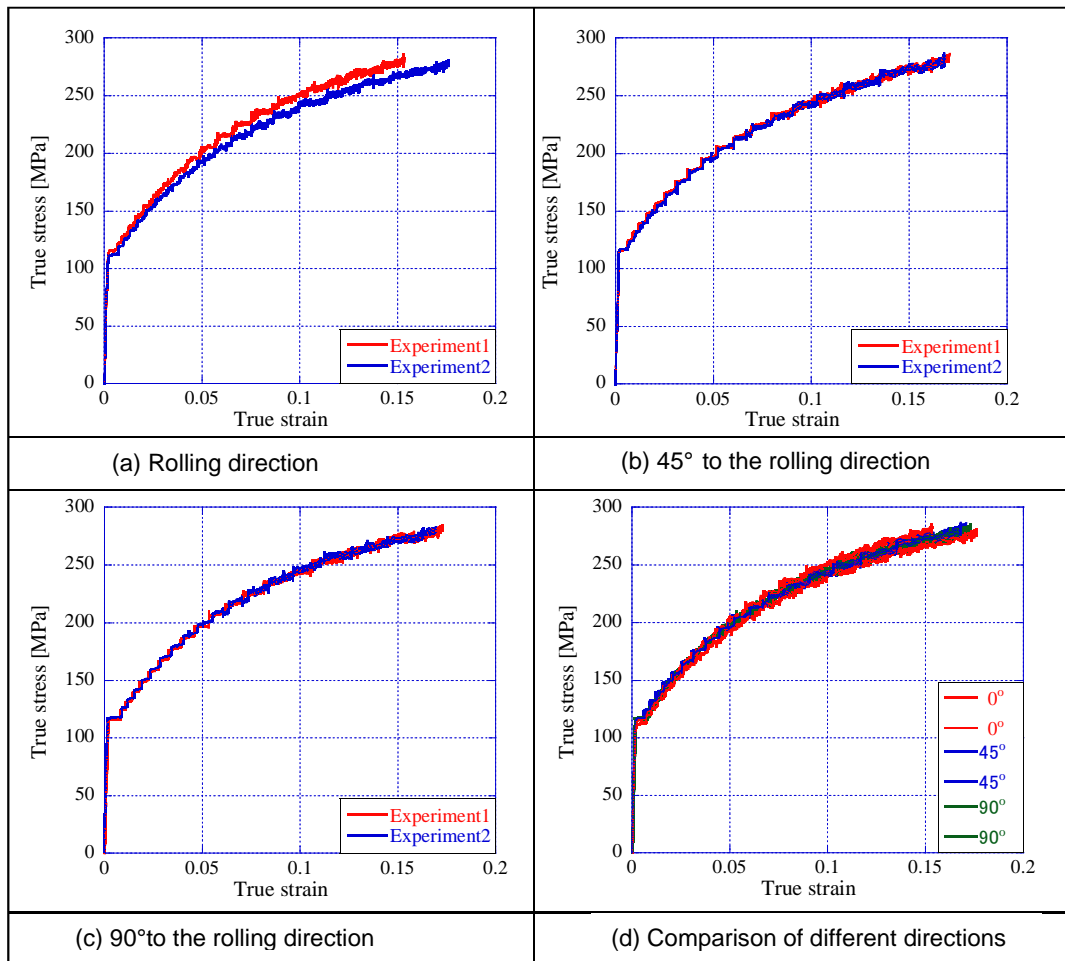


Figure 3.16 Stress-strain curve for CPLA10414

Table 3.1 Chemical composition of the CPLA10414 material [52]

Element	Manganese (Mn)	Iron (Fe)	Magnesium (Mg)	Silicon (Si)	Aluminium (Al)
% Present	0.50 (Typical)	0.40 (Typical)	2.60 - 3.20	0.40 (Typical)	Balance

Figure 3.16 (d) shows minor variations in the stress-strain curves for the same material in the three directions. Figures 3.17 and 3.18 show the mechanical properties for the CPLA10414 alloy such as yield stress (Y), ultimate stress (U) and elongation (EL) in the three directions. It is apparent from these figures that there was no significant variation in the yield and ultimate stress or in the elongation of the CAPLA10414 material in the three orientations despite the presence of the PLC effect.

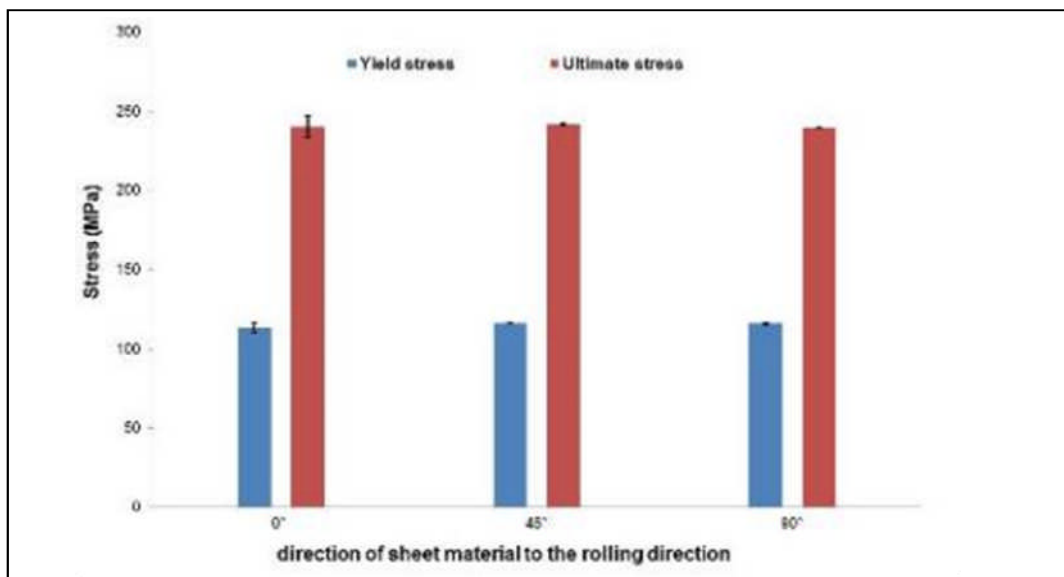


Figure 3.17 Yield and ultimate stress for the CPLA10414 at different orientations

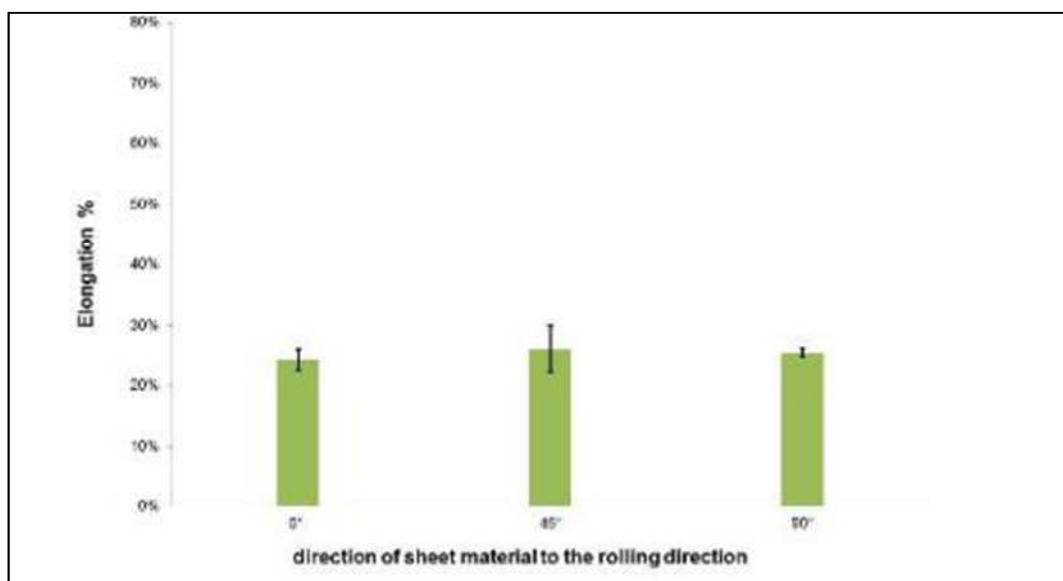


Figure 3.18 Elongation of the CPLA10414 at different orientations

3.4.3 Discussion

The differences between the stress-strain curves obtained for the selected tested materials were significant as shown in Figure 3.19. The highest yield stress was obtained for the high strength steel material (DP600) and this was about 400 MPa. The lowest yield stress was around 115 MPa measured for the low strength aluminium (CPLA10414) as can be seen from Figure 3.20. However, coincidentally, there was no significant differences between the yield stress of the low strength steel (DX54D) and the high strength aluminium (CPLA100K38) as shown in Figure 3.19. Moreover, the elongation was greater for the low strength materials than the higher strength ones as would be expected. The highest elongation was found for the DX54D steel cut at 90° to the rolling direction and this was about 54% as can be seen from Figure 3.21. Figure 3.22 shows similar observations from the literature that the higher strength material has lower elongation at failure [53]. In addition, there is a noticeable difference in the elongation between the high and low strength steel. However, elongation of the high and low strength aluminium was very similar despite the difference in their strength.

Furthermore, elongation of the highest strength aluminium (CPLA100K38) was less than the high strength steel (DP600), although the yield strength of the DP600 is higher than the high strength aluminium as can be seen in Figures 3.20 and 3.21.

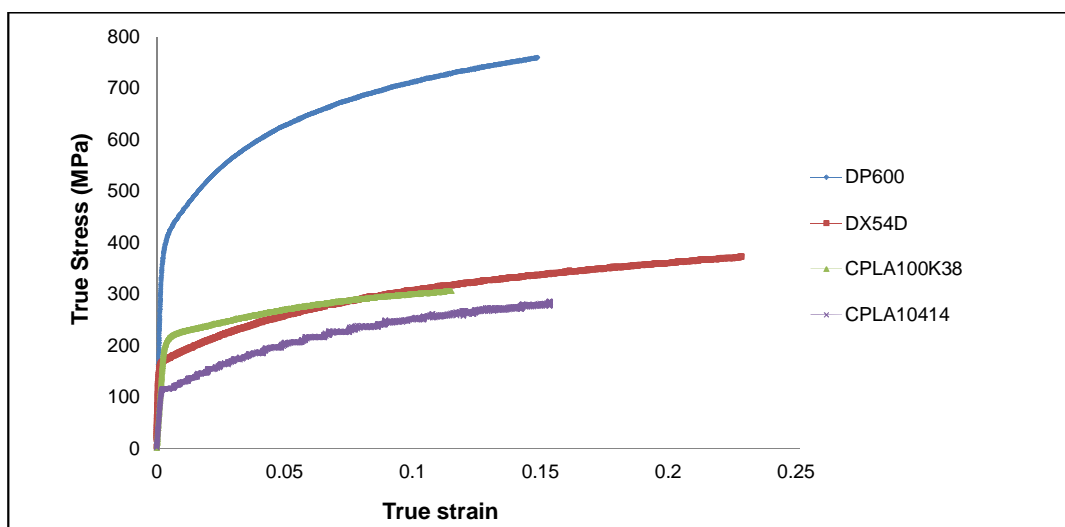


Figure 3.19 Stress-strain curves for 4 different materials

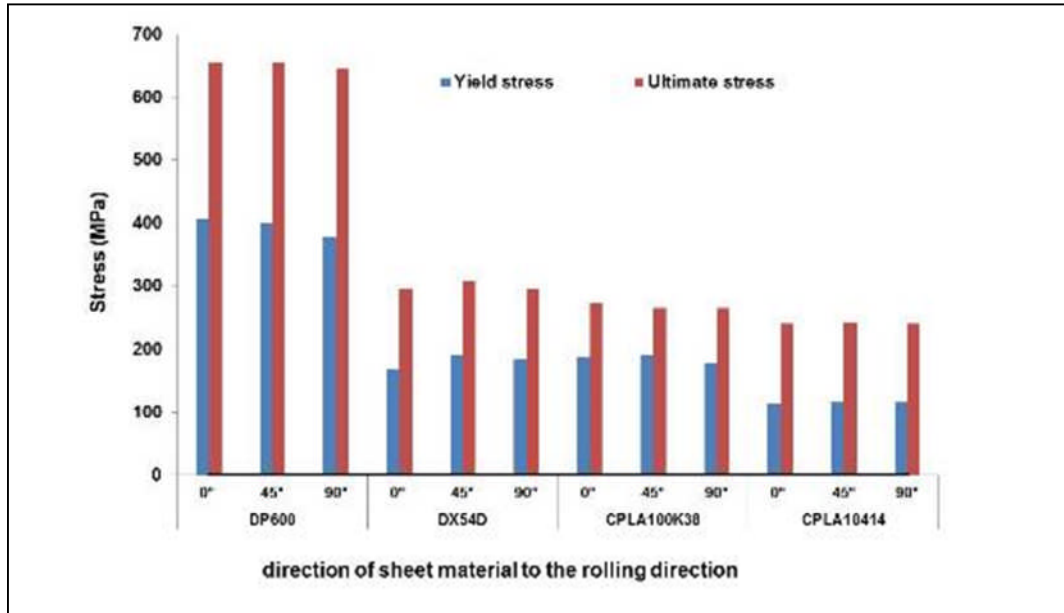


Figure 3.20 Yield and ultimate stress for the four materials at different orientations to the rolling orientation

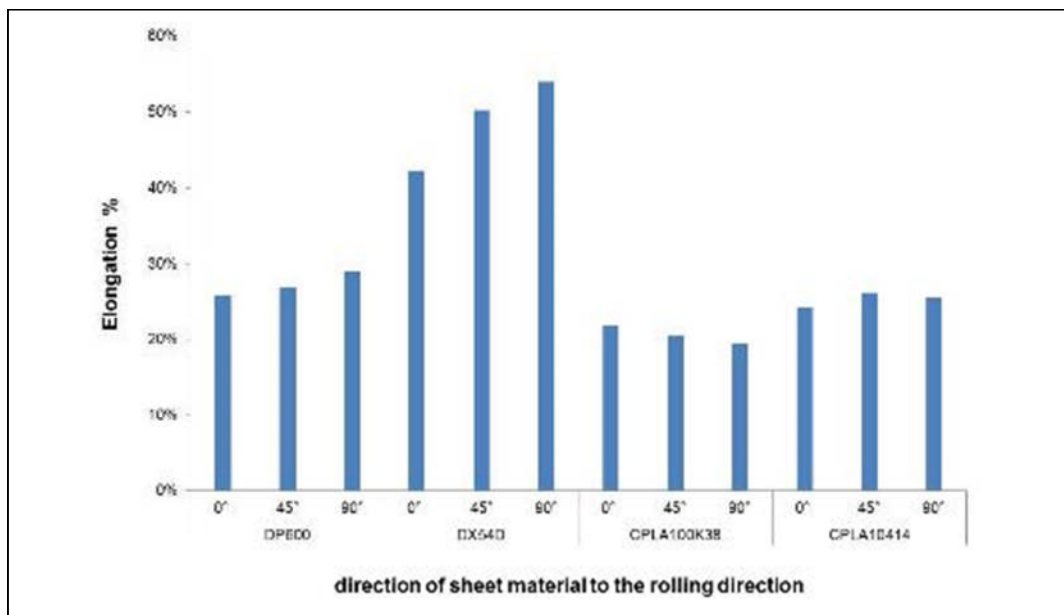


Figure 3.21 Elongation of the four materials at different orientations to the rolling orientation

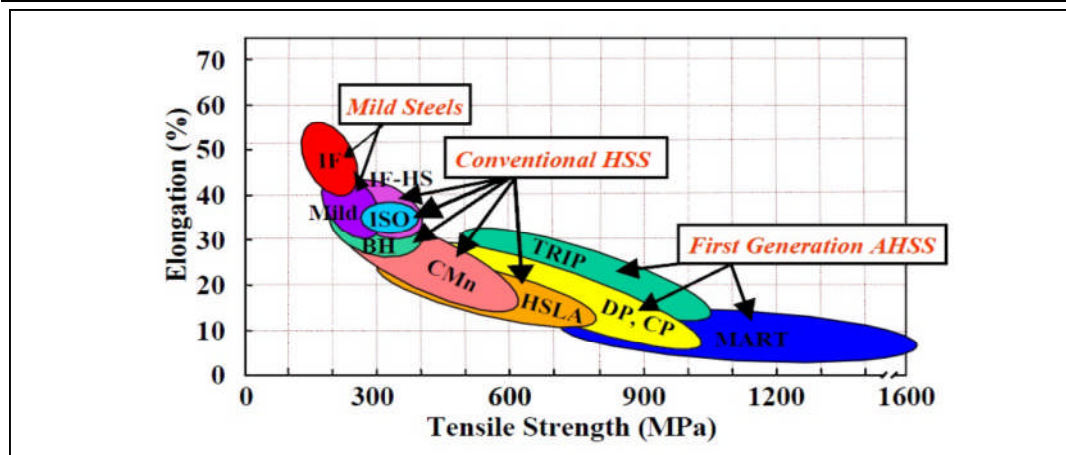


Figure 3.22 The relationship between the tensile strength and the elongation of different materials [53]

3.5 Cyclic tension test

3.5.1 Methodology

A series of uniaxial tensile tests were conducted on type A samples taken parallel to the rolling direction in order to investigate the evolution of the Young's modulus during the plastic deformation.

The samples were prepared as described in section 3.3 and the experiments were again performed at Hiroshima University. The specimen was subjected to uniaxial loading and unloading at several displacements to represent bending and unbending operations at large deformation that typically occur for sheet material undergoing metal forming processes including U-drawing. Therefore, the specimen was subjected to tension to a certain level of load and then the load was removed to perform the unloading situation. In this experiment, it was necessary to attach a strain gauge to the centre of specimen surface as shown in Figure 3.23. The strain gauge type was YEFLA-2 provided by Tokyo Sokki Kenkyujo Co, Ltd and its specification is summarised in Table 3.2.

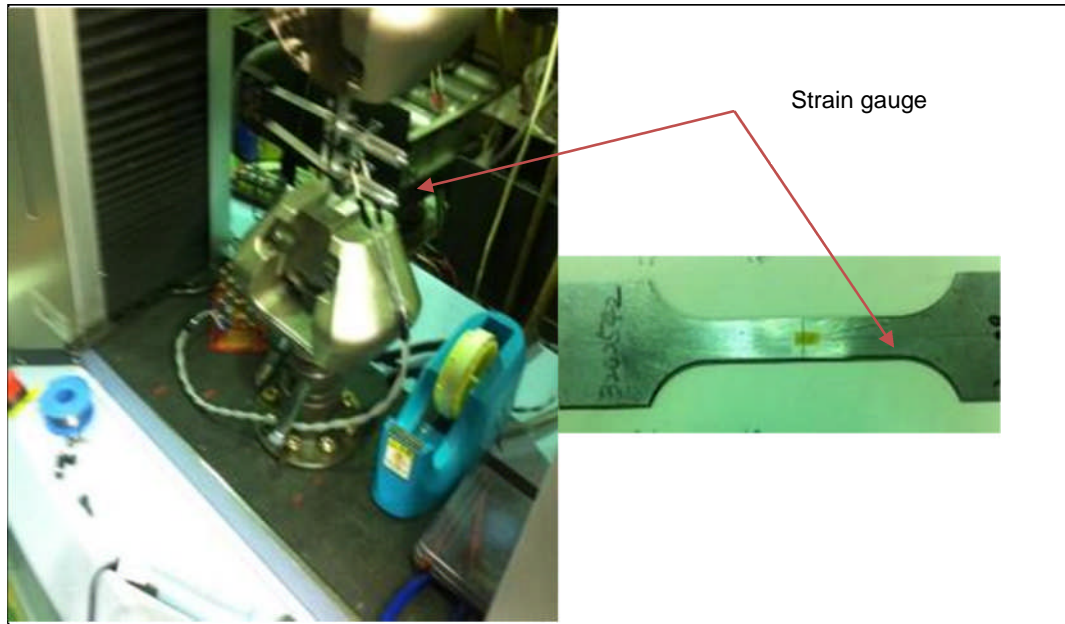


Figure 3.23 Cyclic tension test set up

Table 3.2 Strain gauge specification [54]

Gauge Size (mm)		Backing (mm)		Resistance (Ω)	Strain Limit
Length	Width	Length	Width	120	10 ~ 15%
2	1.8	7.5	4		

This experiment was performed according to the following sequence. First, the sample was clamped and was then subjected to 80% of the tension load which had caused initial yield. The cross-head was then reversed to perform the unloading situation. The sample was then subjected to a further load, up to a certain displacement, after which the machine was reversed again to achieve the unloading behaviour. Subsequently, this process was repeated a number of times at higher displacements.

The measured data was manipulated in order to plot the stress-strain curve using equations (1) to (4) as explained in section 3.4. Subsequently the Young's modulus was calculated by determining the slope of stress-strain curve in the elastic region and in the plastic regions for each unloading

situation. Consequently, the degradation of the Young's modulus with effective plastic strain was calculated using equation (2.19):

$$E = E_o - (E_o - E_a)(1 - e^{-\gamma p}) \quad (2.19)$$

Here, E_o and E_a denote Young's modulus for the elastic and large plastic strain respectively and γ and p stand for material constant and the effect of plastic strain. This test was performed for two samples in the rolling direction of the metal sheet for each of the four materials.

3.5.2 Results

Figure 3.24 shows the loading and unloading stress-strain curves at several displacements for the four different materials.

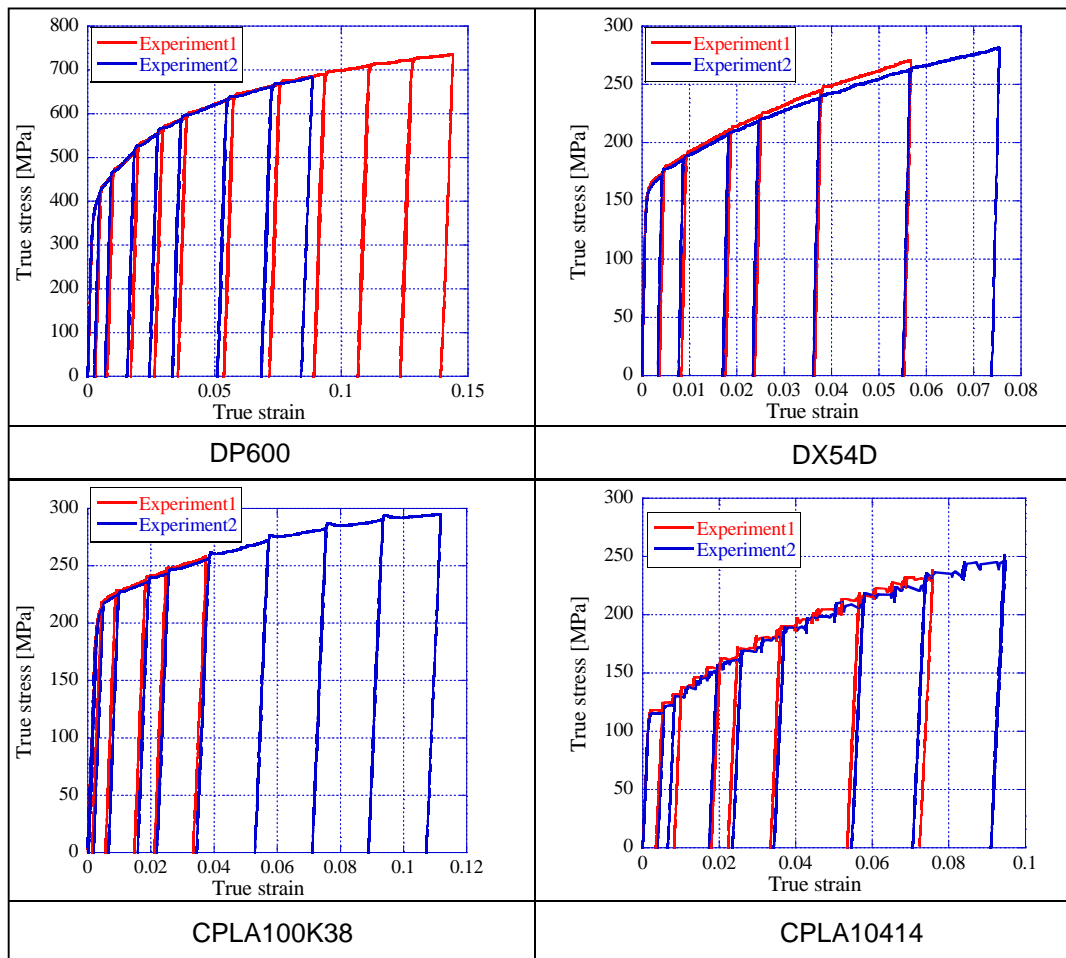


Figure 3.24 Loading and unloading stress-strain curves for four different materials

The Young's modulus was calculated by determining the unloading slope of the stress-strain curve for purely elastic loading and at several strain levels within the plastic region as shown in Figure 3.25. This figure shows part of the whole curves shown in Figure 3.24, and illustrates how the first unloading curve (in the elastic region) is used to calculate the Young's modulus.

Figure 3.25 also shows how the first and second Young's modulus in the plastic region is measured by determining the unloading slope at each stage. The degradation of the Young's modulus with effective plastic strain was calculated using equation (8) as discussed in section 3.5.1. Figure 3.26 shows that the Young's modulus decreases with relatively small plastic strain and then remains almost constant up to relatively large plastic deformations. Strong evidence of the degradation of the Young's modulus during the plastic deformation was observed for all the tested materials. Similar observations have been widely noted by many researchers [3, 13, 27].

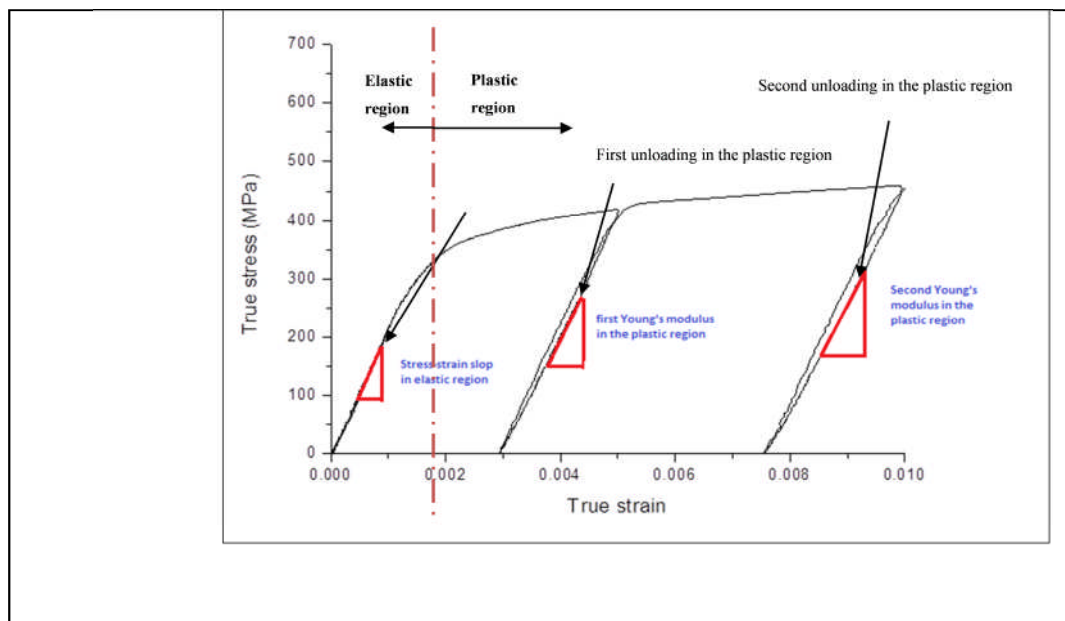


Figure 3.25 Loading and unloading stress-strain curves for the DP600 material

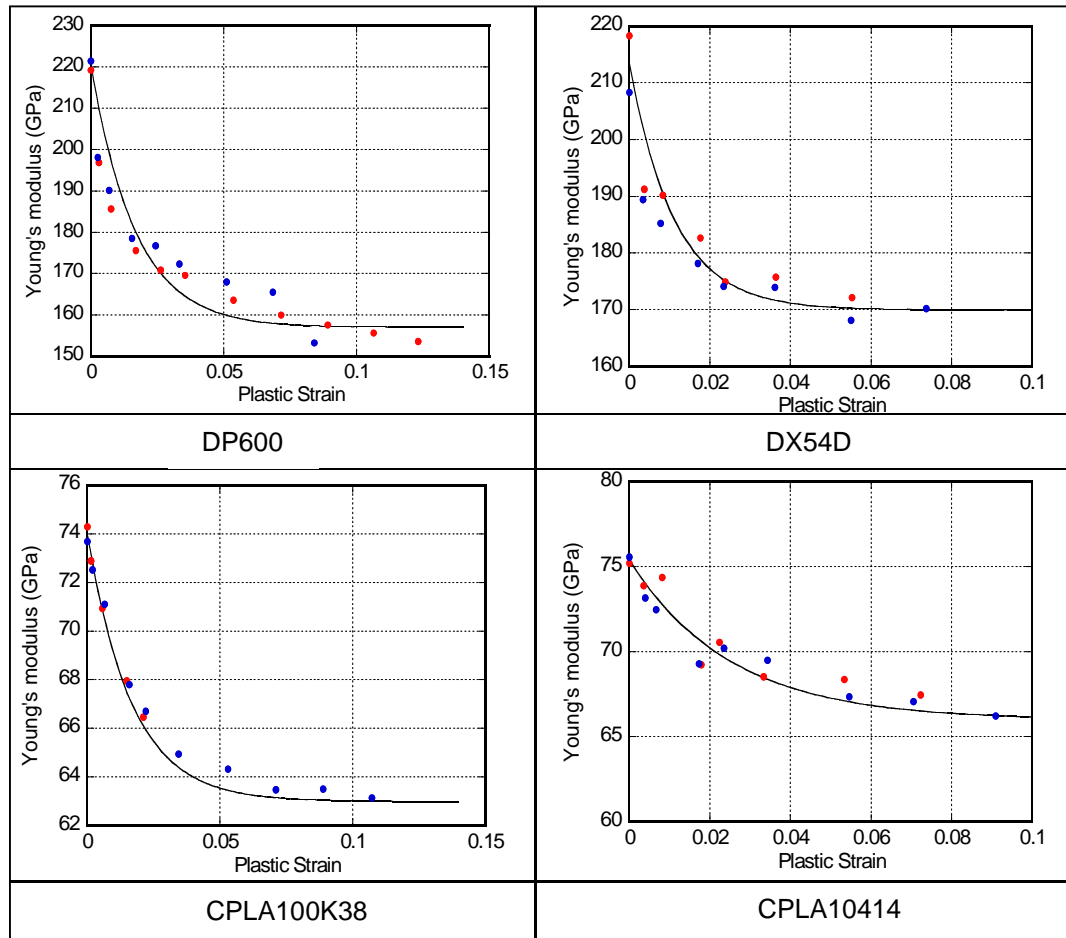


Figure 3.26 Unloading modulus degradation with effective plastic strain for the four different materials

Table 3.3 summarises the Young's modulus parameters for all the tested materials to be used for the numerical analyses reported in Chapter 6, 7 and 8.

Table 3.3 Young's modulus parameters for the four different materials

	DP600	DX54D	CPLA100K38	CPLA10414
E_o [GPa]	220.3	213.3	74.0	75.4
E_a [GPa]	157.0	170.0	63.0	66.0
γ	60.0	90.0	60.0	40.0
Reduction %	28.7%	20.3%	14.9%	12.5%

3.5.3 Discussion

Degradation of Young's modulus was found to occur in each tested material but at different levels. In each case the Young's modulus decreased with relatively small plastic strain and then remained almost constant after relatively large deformation. The single most striking observation to emerge from the data comparison was that the highest reduction of the Young's modulus was for the high strength materials. The degradation of the modulus was the highest for DP600 material at 28.7% of the initial value. However, there was no significant difference in the decrease of the modulus for the two aluminium materials. The lowest Young's modulus reduction was found for the CPLA10414 aluminium at 12.5% of the original value as illustrated in Table 3.3.

3.6 Anisotropy test

Plastic anisotropy occurs when a metal experiences a plastic deformation that may vary with the direction of loading (rolling, 45⁰ and 90⁰). Consequently, properties of the metal become non-homogeneous [55]. Plastic anisotropy is defined by the anisotropy coefficient:

$$r_a = \frac{\varepsilon_2}{\varepsilon_3} = \frac{\varepsilon_w}{\varepsilon_t} = -\frac{\varepsilon_w}{(\varepsilon_w + \varepsilon_l)} \quad (3.5)$$

Here ε_2 and ε_3 are the strains in the width and thickness directions respectively as shown in Figure 3.3. The strain in the thickness direction (ε_t) can be defined by adding the strain in width and length of the specimen; (ε_w and ε_l) respectively. It is apparent from this equation that if the r_a is more than one, the material is strained more in the width than in the thickness direction which is called the 'thinning resistance'. However if the r_a is less than 1, there is a risk of the sheets getting thinner which could lead to premature failure.

The main purpose of this test is to identify the degree of anisotropy of the material which may affect the metal forming process, especially the springback.

3.6.1 Methodology

The tensile test was performed as explained above in section 3.4 where the specimen type A was subjected to up to 0.1 mm of displacement and the test stopped. The sample was then removed and the current width and length was measured at three positions and the average was taken. The plastic anisotropy for a certain direction was determined using equation (3.5). Subsequently, the normal anisotropy coefficient was obtained using equation (3.6) [55]:

$$R_a = \frac{r_0 + 2r_{45} + r_{90}}{4} \quad (3.6)$$

3.6.2 Results

The plastic anisotropy (r-value) at 0° , 45° and 90° directions and the normal anisotropy coefficient R_a of the sheet materials investigated for this project are listed in Tables 3.4 to 3.7. The difference in the normal anisotropy between the materials is obvious from these tables. Both steel materials have R_a greater than one. However the aluminium alloys have values lower than the unity value of normal isotropy. Also, from these data, it can be seen that the high strength materials resulted in the lowest value of the normal anisotropy for both steel and aluminium samples.

Table 3.4 R_a in rolling, 45° and 90° orientations for the DP600 material (Plastic strain : 0.1)

Orientation	No of samples	r_a	average	R_a
0°	1	1.18	1.24	1.28
	2	1.30		
45°	1	1.26	1.29	
	2	1.32		
90°	1	1.28	1.30	
	2	1.32		

**Table 3.5 R_a in rolling, 45° and 90° orientations for the DX54D material
(Plastic strain : 0.1)**

Orientation	No of samples	r_a	average	R_a
0°	1	2.18	2.07	1.83
	2	1.95		
45°	1	1.41	1.42	
	2	1.43		
90°	1	2.38	2.39	
	2	2.40		

**Table 3.6 R_a in rolling, 45° and 90° orientations for the CPLA100K38
material (Plastic strain : 0.1)**

Orientation	No of samples	r_a	average	R_a
0°	1	0.81	0.79	0.56
	2	0.78		
45°	1	0.43	0.43	
	2	0.43		
90°	1	0.56	0.59	
	2	0.62		

**Table 3.7 R_a in rolling, 45° and 90° orientations for the CPLA10414
material (Plastic strain : 0.1)**

Orientation	No of samples	r_a	average	R_a
0°	1	0.84	0.81	0.75
	2	0.78		
45°	1	0.71	0.70	
	2	0.70		
90°	1	0.81	0.80	
	2	0.80		

3.6.3 Discussion

The anisotropy tests show that the normal anisotropy for the steel materials is greater than one. However, the normal anisotropy was lower than one for the aluminium alloy tested materials. Moreover, the results show that for the same material, the high strength material produced lower normal anisotropy than the low strength materials. Therefore, it could be argued that the high strength materials have a greater risk of thinning due to the normal anisotropy in addition to other effects such as the inelastic recovery which gives rise to springback. Since the sheet metal that undergoes U-drawing is subjected to plastic deformation in only one direction, the anisotropy test could help to select an appropriate cutting direction of the sheet metal. For instance, the r_a of the CPLA100K38 material cut parallel to the rolling direction displayed greater normal anisotropy than for the other directions.

3.7 Cyclic tension-compression tests

3.7.1 Methodology

This test was performed to define the deformation behaviour of the four materials under large strain cyclic plasticity such as the Bauschinger effect and work hardening stagnation. The specimen type B was clamped in the special loading fixture and the strain gauge was connected as shown in Figure 3.27.

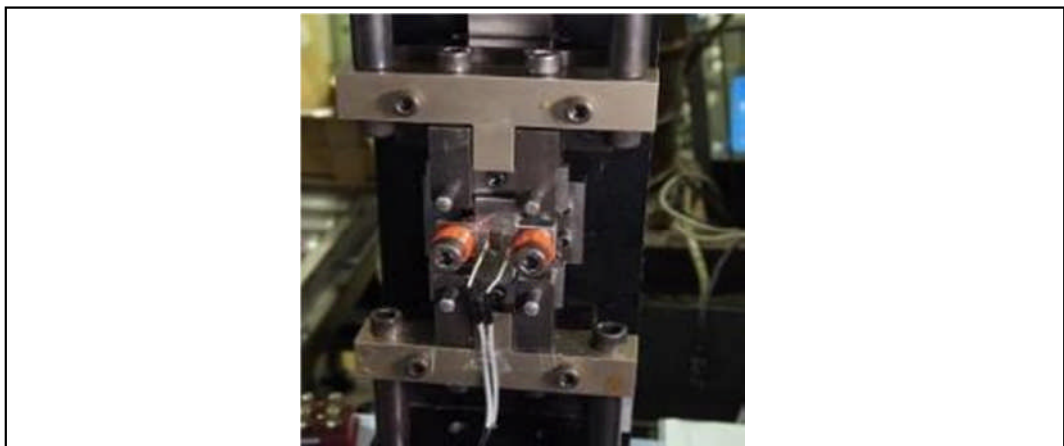


Figure 3.27 Cyclic tension-compression test on specimens type B at Hiroshima University in Japan

This test was performed for two tension-compression cycles. For the first cyclic tension-compression, the specimen was subjected to the load up to 0.025 true strain then unloaded followed by compression up to -0.025 true strain then unloaded. For the second cyclic tension-compression, the tension force was applied to the sample up to 0.05 true strain followed by unloading and then it was compressed up to -0.05 true strain followed by unloading to the end of the test. The stress-strain curve was calculated in the same way as explained for the standard experiment in section 3.4. This test was performed for two samples in the rolling direction only for each sheet.

3.7.2 Results

The load and displacement data was utilised as described in section 3.4 to determine the stress-strain curve for the two cyclic tension-compression tests for the two high strength materials (steel and aluminium) and the two low strength materials (steel and aluminium) as shown in Figure 3.28.

The figure shows that the stress-strain curves are almost identical for each material which is a good evidence of the repeatability of the test. It is apparent from this figure that the Bauschinger effect is demonstrated by the early re-yielding during the reverse loading for all the tested materials. This was more noticeable in the high strength materials (DP600 and CPLA100K38) than the low strength materials (DX54D and CAPLA1414). Furthermore, the work hardening stagnation is not visible for the high strength steel. However, it is visible for the other three materials. These findings are consistent with other published results [5, 56]. According to the current study and these published results, the Bauschinger effect is observed by early re-yielding under reverse stress and the work hardening stagnation is more noticeable for low strength materials than for higher strength materials.

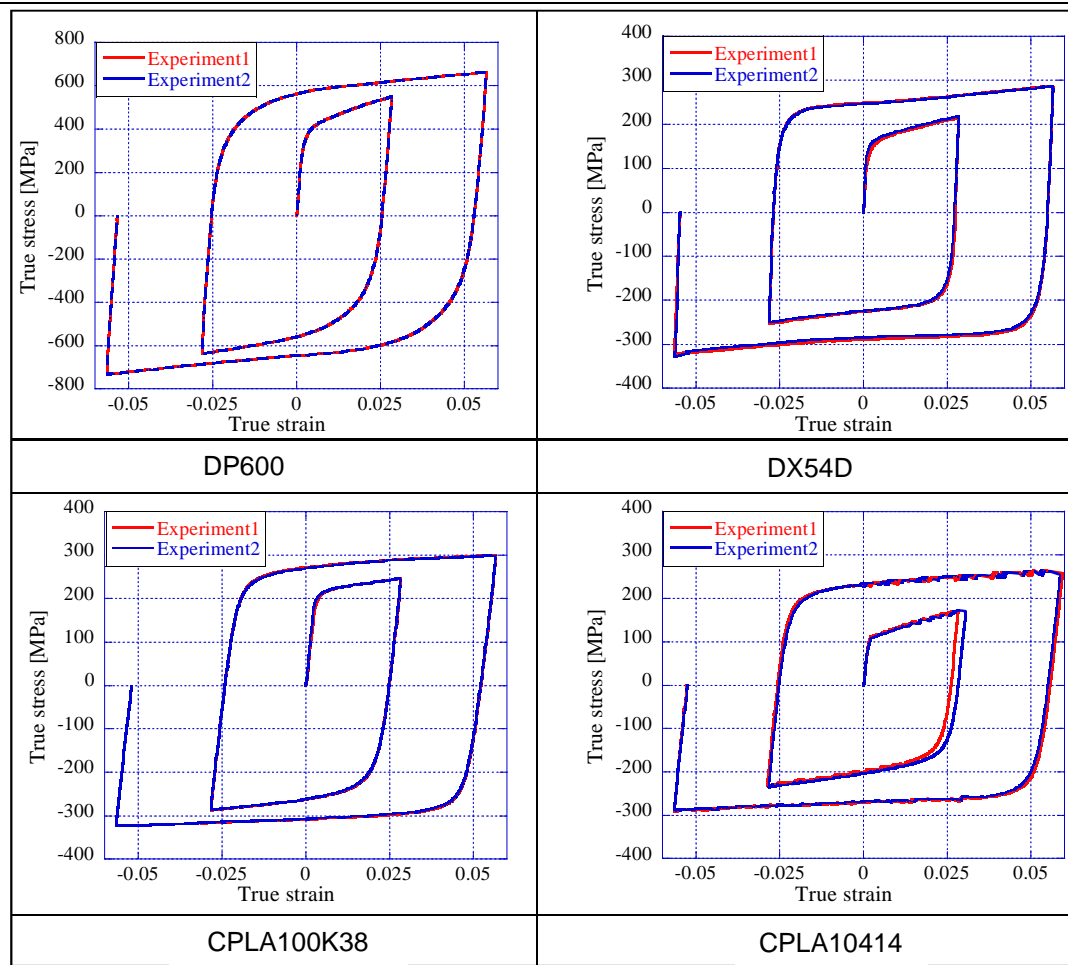


Figure 3.28 Stress-Strain curve for two cyclic tension compression test for the four different materials

The results of these experiments were used to identify parameters of the Y-U model using the Mata-Para Software available in the elasto-plasticity laboratory in the Mechanical Engineering Department in Hiroshima University, Japan. This software finds the best fit of the variable parameters of the model to experimental data. Figure 3.29 illustrates the comparison between stress-strain curves from the experiments of the tension-compression and the Yoshida-Uemori (Y-U) model. This figure shows only minor variations between the experimental and Y-U model results.

The 7 Y-U parameters obtained for the tested materials from these tests are summarized in Table 3.8. What is interesting in this data is that the yield stress for each material has a lower value than the one measured at a strain offset of 0.002 in a single cycle test.

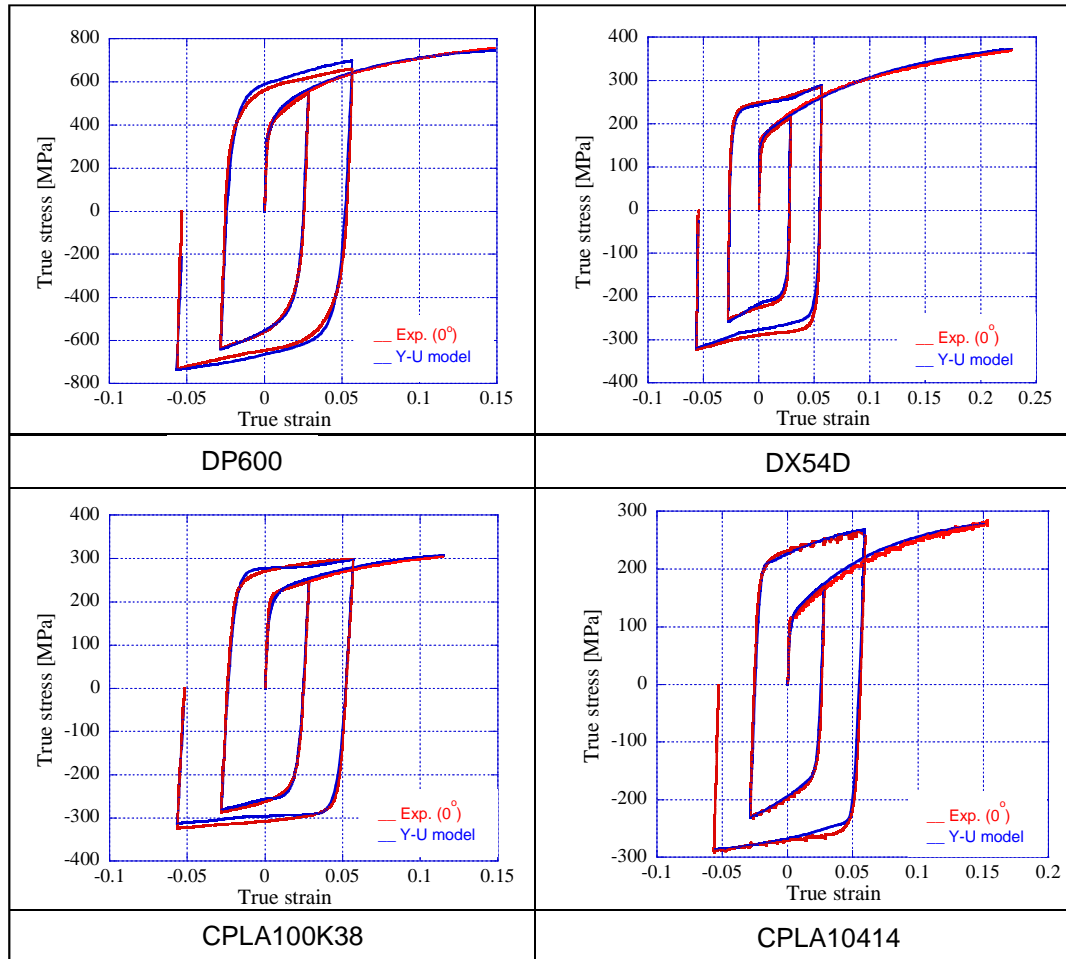


Figure 3.29 Comparison between experimental result and Y-U model for four different materials

Table 3.8 Yoshida-Uemori model parameters for the four different materials

Yoshida Parameters	Y (MPa)	B (MPa)	C	b (MPa)	m	R _{sat} (MPa)	h
DP600	326	143	400	120	17	188	0.3
DX54D	145	30	650	60	9	170	0.5
CPLA100K38	150	75	650	10	15	95	0.5
CPLA10414	60	60	1500	30	15	150	0.1

3.7.3 Discussion

The cyclic tension-compression test results show that the Bauschinger effect occurs in each material tested for this project. The single most striking observation to emerge from Figure 3.28 is that the high strength materials start re-yielding earlier than the low strength materials which may be one of the reasons for a significant level of springback for high strength materials as mentioned in the literature [3]. Moreover, the work-hardening stagnation was clear for all materials tested in this project except for the DP600 steel where it was not visible. This is due to the fact that the high strength steel has naturally lower isotropic hardening than the low strength steel [5]. Figure 3.29 shows that the Y-U model accurately predicts the cyclic tension-compression behaviour of the materials tested for this project and Table 3.8 summarises the Y-U model parameters. These parameters will be used for the numerical analyses described in Chapters 6 to 8.

3.8 Summary

In this chapter, the experiments undertaken to derive the mechanical properties of the material samples required for the Y-U material model have been explained. The experimental methodology was clarified including the specimen preparation, the test machine used and the experimental set up.

The stress-strain curves for all tested material behaved normally except for the CPLA10414 aluminium alloy which experienced a serrated stress-strain curve due to the so-called PLC effect. This phenomenon is common in Al Mg alloys [48-50] and is undesirable as it affects the formability of the material [51]. It has also been shown that the Bauschinger effect is quite obvious for all the tested materials. Furthermore, work-hardening stagnation was more visible in the two aluminium alloys and the low strength steel than in the high strength steel. Also, the results show the clear degradation of the Young's modulus during cyclic plasticity loading for all the tested materials. These results emphasise the need to utilise the Y-U model to accurately simulate metal forming operations which include large scale cyclic plastic deformation such as in the L-bending and U-drawing operations studied in this thesis.

CHAPTER 4: METAL FORMING AND MEASUREMENT APPARATUS

4.1 Introduction

This chapter outlines the design of the metal forming rig used to perform the U-drawing and L-bending sheet metal forming experiments. In sheet metal forming processes a number of different defects may occur in the formed parts, whether during or after the process, including rupture, wrinkling, galling and springback as mentioned in chapter 2. Springback is the most complex and challenging issue in the sheet metal industry; this is because it is influenced by a number of parameters which should all be embodied within the forming rig concept. These parameters are the die corner radius, clearance and blank holder force as mentioned in the literature review, Chapter 2. Therefore, the main purpose of this test rig is to validate the numerical analysis so that the real influence of these factors on the phenomenon of springback can be studied. The design of the forming test rig has therefore taken into the account the need to vary the die radius, clearance and blank holder force.

The forming test rig was to be installed on an Instron 5985 Dual Column Floor Model machine which is located in the Strength of Materials Laboratory in the School of Mechanical Engineering at the University of Leeds, so the features of this machine were taken into consideration in the design of the rig. The rig consists of 6 main components: the base plate, die, blank, blank holder, punch and punch holder. The design concept can permit the same assembly to perform either of the two metal forming operations studied in this thesis: L-bending as shown in Figure 4.1 and U-drawing bending shown in Figure 4.2. The following sections describe an appropriate design for the two metal forming processes, taking into account simplicity in manufacture, cost and accuracy required, so that the tools produced could be used for both types of experiment.

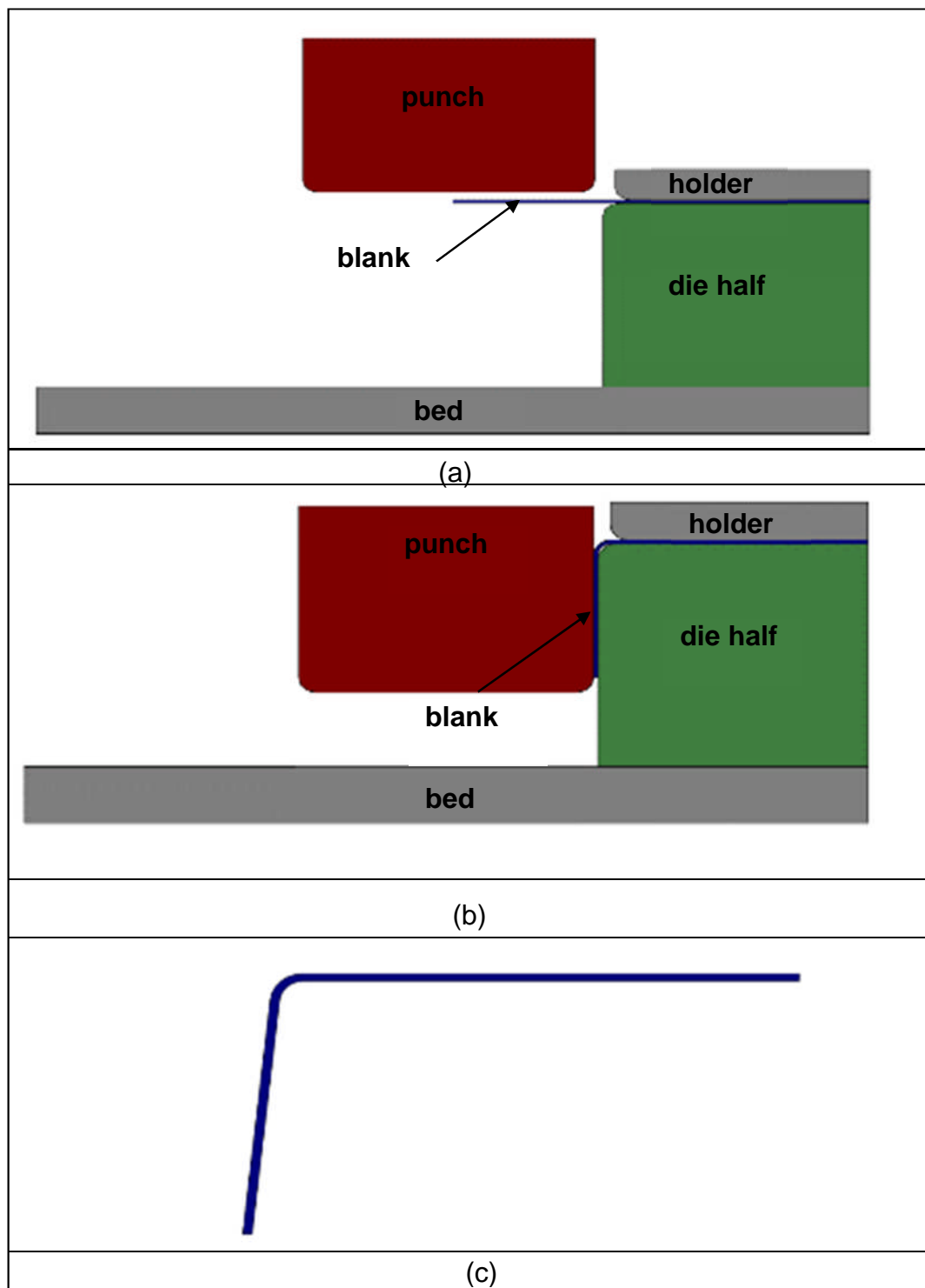


Figure 4.1 Sheet metal forming concept for L-bending (a) prior to forming (b) end of the process (c) the final L-shape showing springback

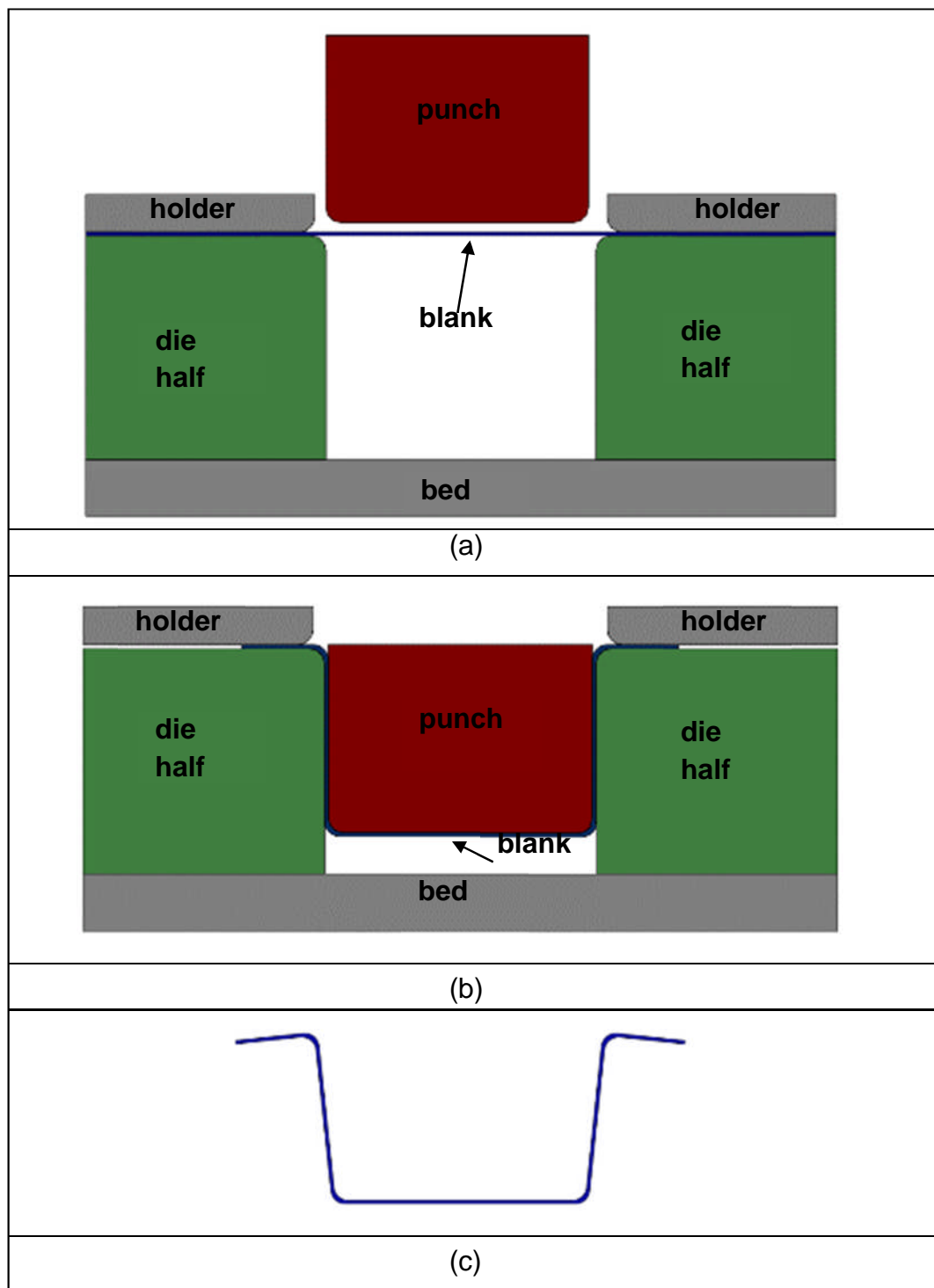


Figure 4.2 Sheet metal forming concept for U-drawing (a) prior to forming (b) end of the process (c) the final U-shape showing springback

4.2 Die and blank holder design

The die must represent the shape of the final formed product. In this study two main products will be formed: U and L shapes. Therefore, the die is made in two symmetrical halves; one on the left and another on the right hand side of the rig. The main reason of making two identical parts for the die is to allow L-bending or U-drawing to proceed in the same test rig.

4.2.1 Preliminary die and blank holder design

The design of the die and blank holder began with an initial design. Figure 4.3 illustrates the preliminary design of one half of the die. As mentioned above, the principal design variables are the die radius and clearance. A series of interchangeable corner radius inserts were designed from 1 to 4 mm to permit control over the magnitude of the corner radius employed in the experimental work. The control of the clearance is explained below. Four M10 bolts passing through holes on the top of the die surface were used to fasten the blank holder, thereby applying the blank holder force.

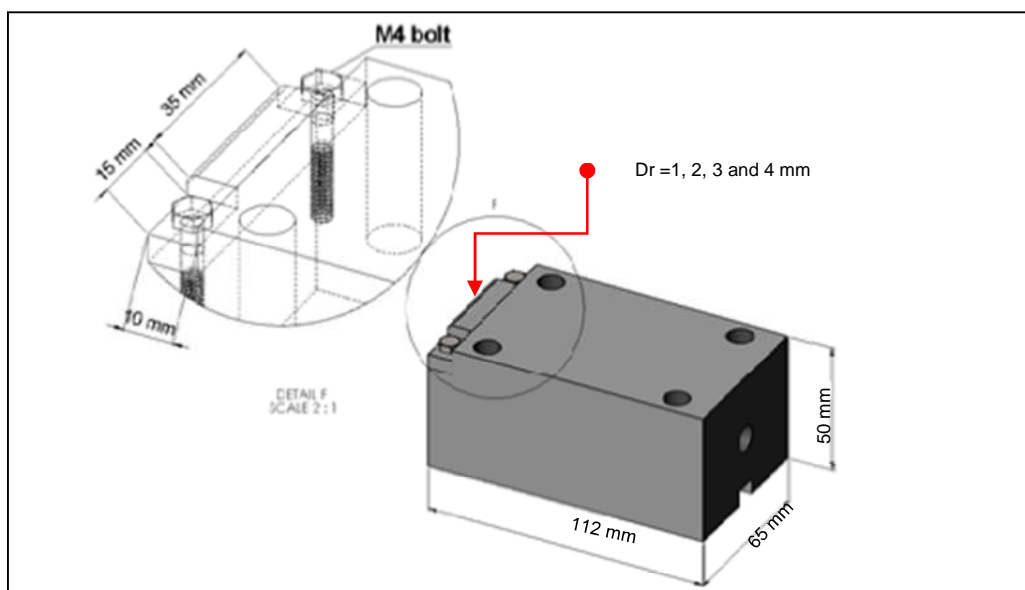


Figure 4.3 Preliminary die design

One M10 hole was machined on the side of the die to support the die half and to control the clearance as discussed below. A groove was machined on the middle of the bottom die surface of 10mm width and 6 mm depth to support and guide the die half on the bed as explained below.

The blank holder was designed to apply a near uniform pressure to the blank. Initially a rectangular plate with four 10 mm clearance holes was specified. The bottom of the blank holder contained a shallow channel of 0.5 mm depth with the same width as the blank. This was to ensure that the blank was correctly aligned during the metal forming process. Also, the channel depth was smaller than the blank thickness in order to be able to pressurise the blank. The pressure loading was achieved by tightening the 4 M10 bolts on either side of the blank to a specific torque. Figure 4.4 (a) illustrates initial the blank holder design.

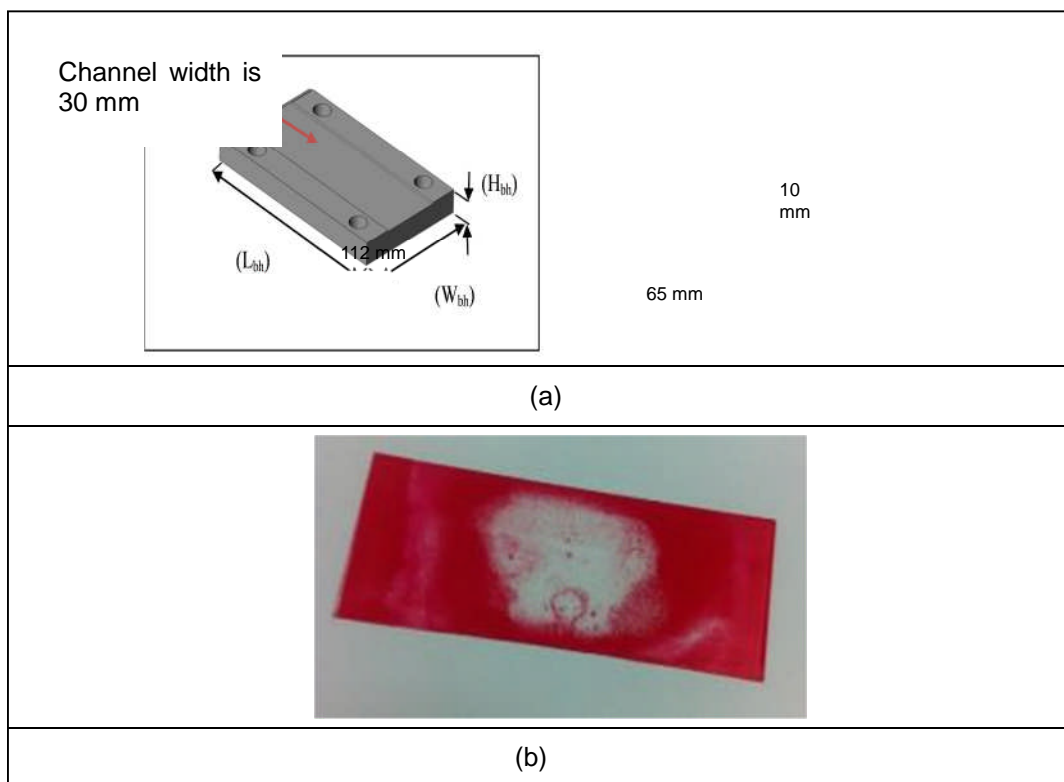


Figure 4.4 (a) Preliminary design of blank holder and (b) the distribution of pressure shown using FujiFilm sheet between the blank holder and the die after the four bolts had been tightened

Prior to the metal forming experiments, a pressure sensitive film was inserted between the blank and the blank holder to check the uniformity of the pressure distribution. After applying a certain torque to the bolts, it was found that the distribution of the pressure applied to the blank was not uniform as shown in Figure 4.4 (b). From this figure, the pressure sensitive film indicates that the lowest pressure was in the middle whereas the red coloration indicates high pressures near to the location of the bolts. This is due to the fact that the central area is further away from the effect of the bolt loads. Furthermore, it was realised that when the blank had been drawn away from the influence of the load from the two bolts located at the outer edge of the die, the load on the blank holder reduced. Therefore, further development of the design was required in order to overcome such issues.

4.2.2 Final die and blank holder design

The design of the die was developed by adding two additional M10 bolts equidistant between the existing bolts to improve the pressure distribution and make sure that blank is firmly clamped during the U-drawing operation. The new die and blank holder design is shown schematically in Figure 4.5.

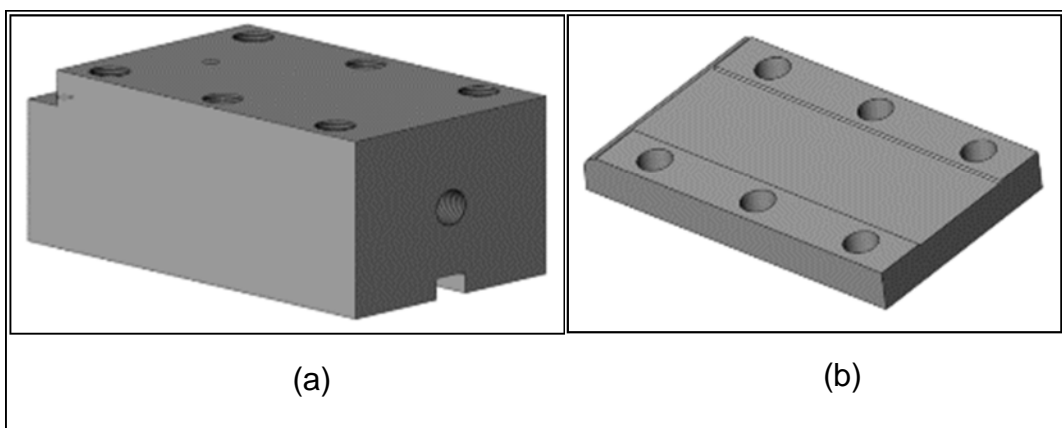


Figure 4.5 Final design of the (a) die and (b) blank holder

The blank holder force is one of the main parameters in the current study and this can be applied in several ways. This study has used bolts fitted with springs of known stiffness; as the bolts rotate, they progressively compress the springs which in turn generate the clamp load that is applied to the blank holder. The springs were placed between the top surface of the blank holder and the bottom surface of the bolt head as shown in Figure 4.6. Also, washers were used between the bolt head and the top of the spring. The specification of the springs according to the supplier is shown in Table 4.1. To ensure the reliability of these springs, the Instron machine was used to measure the spring stiffness. It was found that the spring compressed 1 mm for 70 N of applied axial load as stated by the company which supplied the springs [57]. Therefore, the blank holder force was generated by screwing each bolt by two full rotations to produce 3.0 mm spring compression which equates, to a compressive spring load of 210 N per spring, giving a total load of 1260 N.

Table 4.1 Compression spring specification [57]

Outside diameter (mm)	Wire diameter (mm)	Free length (mm)	Spring rate (N/mm)	Max safe load (N)
25.4	4.06	31.75	70.54	429.45



Figure 4.6 Bolts and springs on the blank holder

4.2.3 Die and blank holder assembly

A die bed (1) was designed to combine the two halves of the die for the U-drawing experiments as shown in Figure 4.7. The bed is in the form of a rectangular block which has the same width as the two die halves and sufficient length to carry the other components. A square section groove (2) is machined into the top surface of the die bed and on to the bottom surface of the die keys (3), as illustrated in Figure 4.7. The test fixes the die in all degrees of freedom except translation along the axis of the groove. There are two possible methods to vary the clearance between the punch and die halves. The first technique is simply to vary the punch width. The second method uses an end piece (4), designed to control the separation of the two halves of the die through shims located between the end piece and the die as shown in Figure 4.7. The drawback of the first option is that it allows only limited clearance variation, as well as being costly as a new punch has to be made for each clearance. Therefore the second approach has been chosen for this experiment because of its low cost and its flexibility in varying the clearance. Figure 4.7 illustrates how the die and the blank holder are assembled using the die bed and end piece. Table 4.2 explains the function of the main components of this assembly in more detail.

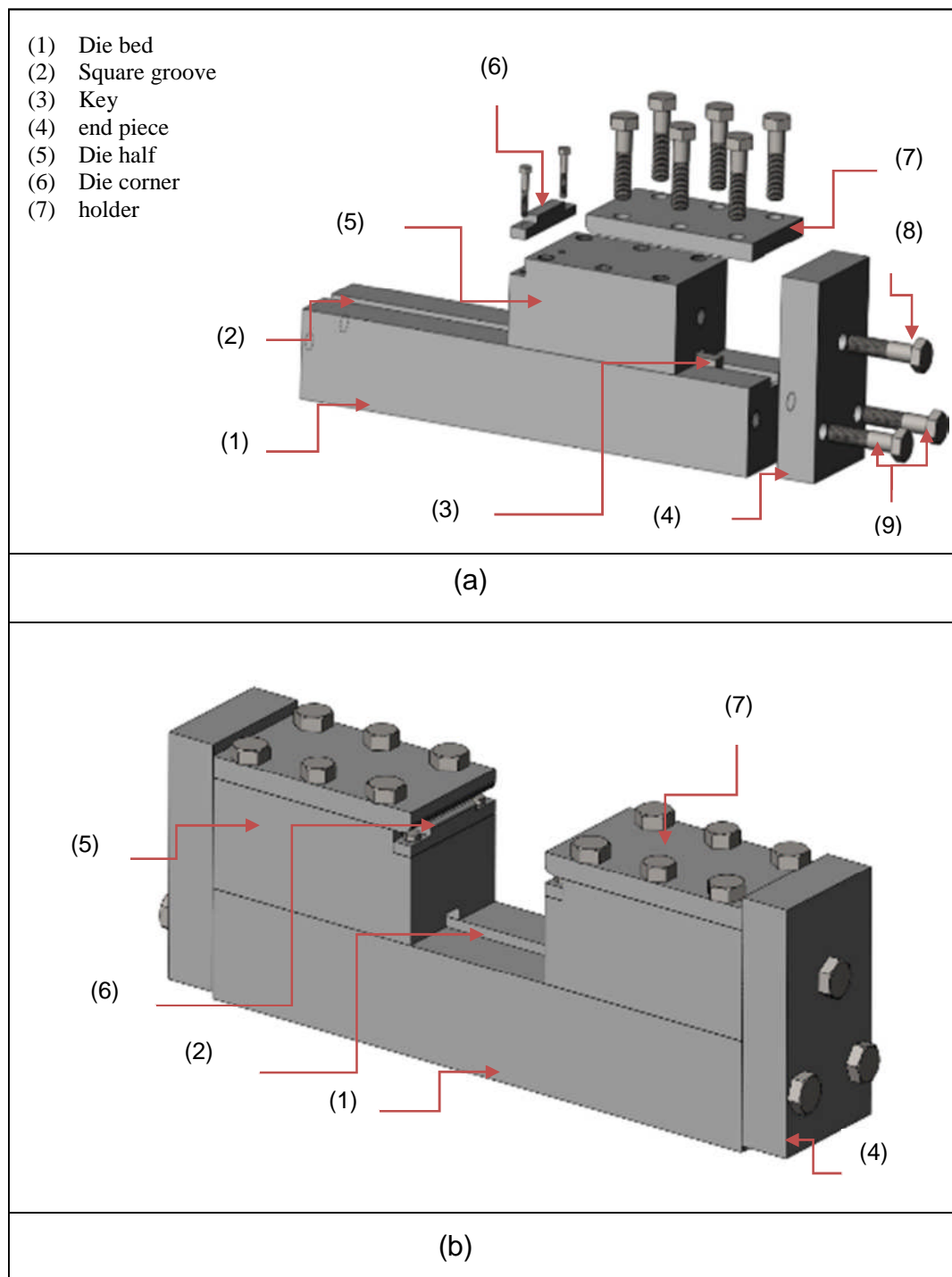


Figure 4.7 Die and blank holder design assembly for (a) L-bending and (b) U- drawing (springs not shown for simplicity)

Table 4.2 Description of the components used in both L-bending and U-drawing experiments

Part	Function
(1) Die bed	To combine the two halves of the die for the U-drawing experiments
(2) Square groove	To allow the use of the key mentioned in (3)
(3) Key	To fix the die in all degree of freedom except transition along the axis of the groove
(4) end piece	To control the separation of the two halves
(5) Die half	One half for L-bending and two halves for U-drawing experiments
(6) Die corner	To represent changeable die radii
(7) holder	To apply certain load on the blank
(8) M10 bolt	To vary the clearance between the punch and die halves
(9) 2 M10 bolts	To fix the end piece on the die bed

4.3 Punch design

Figure 4.8 illustrates the design of the punch assembly for both the L-bending and U-drawing experiments. The punch assembly is divided into five parts: the main punch (1), punch holder (2), top adaptor (3), two cylindrical pillars (4) and cross bar (5). The punch is manufactured from an EN8 steel block with radiused edges on its bottom face that engages with the blank. The punch is attached to the punch holder by a central pin (6) and two screws on the top edges to ensure alignment.

Two vertical pillars are fixed down on to the test rig base (9) and the pillars locate a horizontal cross bar (5) through which the punch holder is able to vertically slide via the brass bushes (7). The punch is therefore fixed in all degrees of freedom except for the vertical direction. The top of the punch assembly is rigidly attached to the cross-head of the Instron machine by means of the top adapter (3).

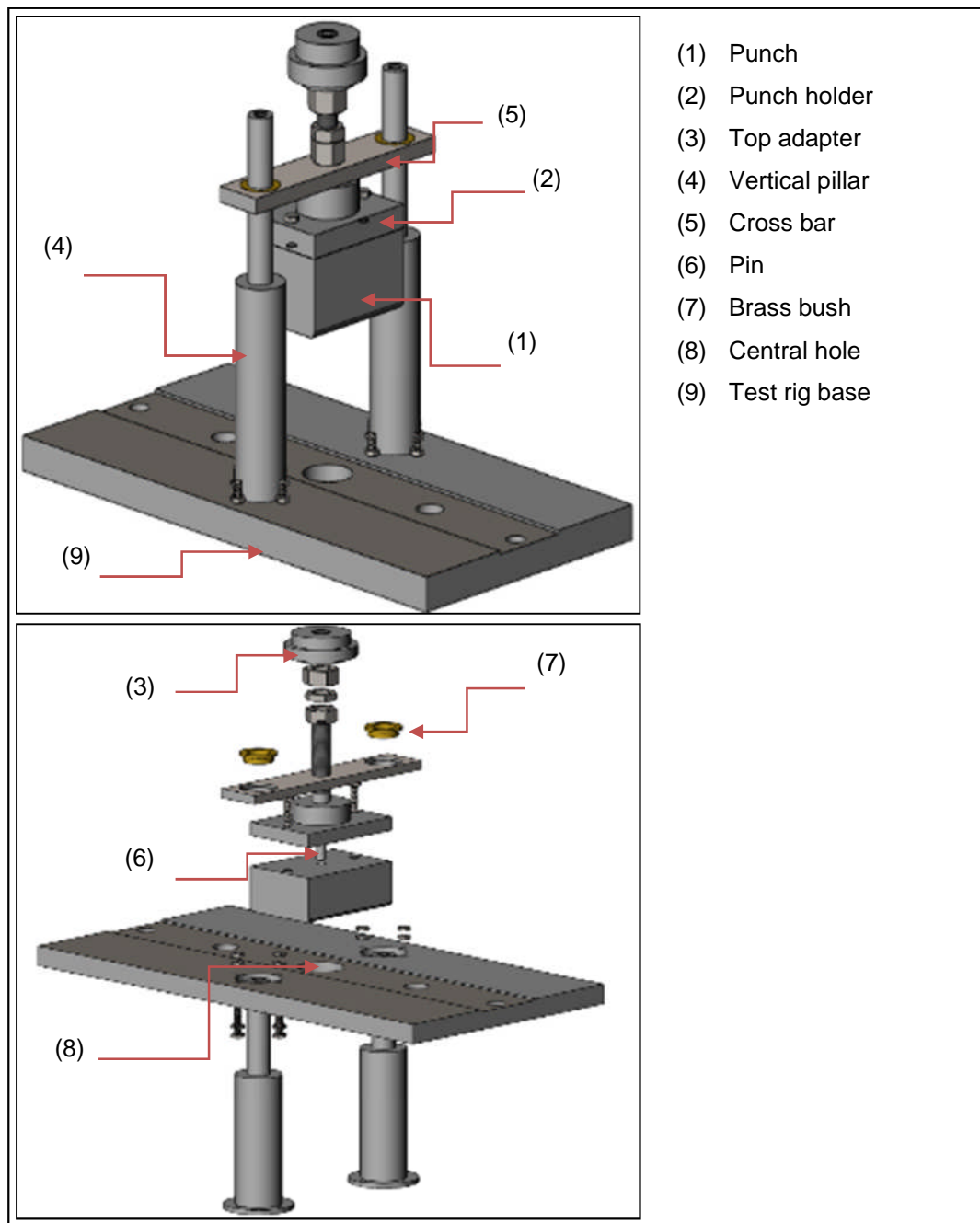


Figure 4.8 Punch design assembly

4.4 Metal forming experiment set up

The complete assembly (punch and die) used for both the L-bending and U-drawing experiments is shown in Figure 4.9. The forming test rig was installed on a universal Instron machine. Therefore, the two subassemblies have been designed to locate on the cross-head and the bed of the test machine. First, the top adapter (3) shown in Figure 4.8 was designed to hold the punch in the cross-head of the machine. Second, the test rig base plate shown in Figure 4.9 was designed to attach the whole assembly to the centre of the base plate of the Instron as shown in Figure 4.10. The base plate was fixed into the centre of the machine base using two bolts with nuts on the edges of the base plate as can be seen in Figure 4.10. Also, the base plate has a rectangular groove along its upper surface to precisely locate the die components at the centre of the main machine base as shown in Figure 4.9. This ensured correct alignment of the punch sub-assembly (attached to the Instron cross head) with the die sub-assembly on the Instron base plate.

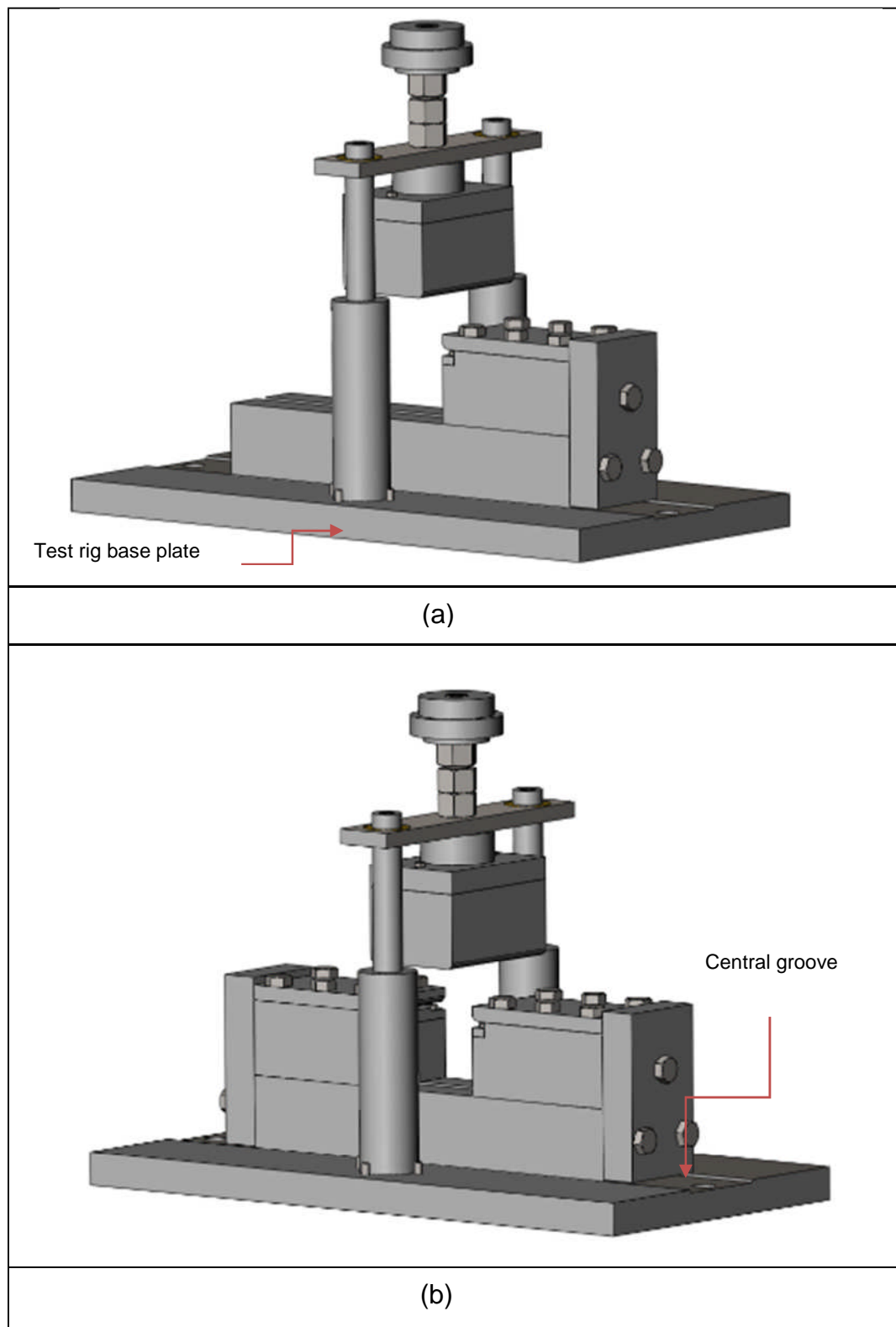


Figure 4.9 Design assembly of (a) L-bending (b) U-drawing test rig (springs not shown for simplicity)

Figure 4.11 shows the main features of the machine, which consists of a fixed base plate with machined slots and a cross-head which is free to move vertically at a programmed rate. A dedicated computer installed with specialist testing software (Instron Bluehill 2) controls the machine functions and captures the data required. The machine has the following features [58]:

- Load capacity is up to 250 kN
- Cross-head speed 0.0001 to 508 mm/min
- PC data acquisition rate up to 1 kHz simultaneously on load, extension, and strain channels
- Position measurement accuracy: ± 0.01 mm or 0.05% of crosshead displacement (whichever is greater)
- Cross-head speed accuracy (zero or constant load): $\pm 0.05\%$ of set speed
- Load measurement accuracy: $\pm 0.4\%$ of reading down to 0.01 of load cell capacity with 2525, 2530, or 2580 Series load cell; $\pm 0.5\%$ of reading down to 0.004 of load cell capacity with 2525 or 2530 Series load cell; $\pm 0.5\%$ of reading down to 0.002 of load cell capacity with 2580 Series load cell
- Strain measurement accuracy: $\pm 0.5\%$ of reading down to 0.2 of full range with ASTM E83 class B or ISO 9513 class 0.5 extensometer
- PC with Bluehill materials testing software package with a universal testing capability. In this project, the Bluehill software was used to export data from the machine such as cross-head load and its displacement.

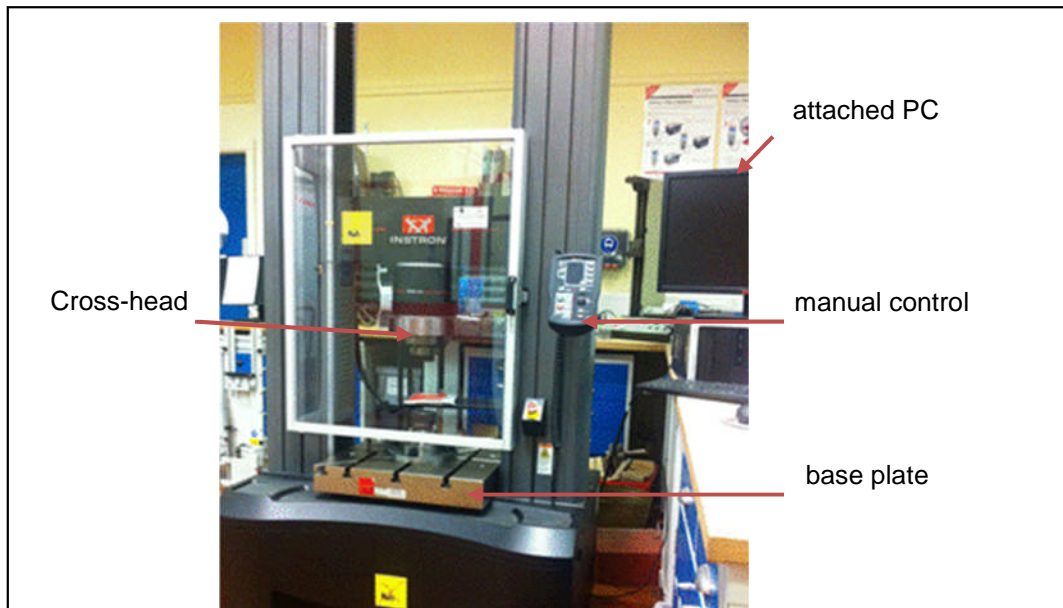


Figure 4.11 INSTRON tensile test machine at University of Leeds

4.6 Kemco 400 CMM machine

A co-ordinate measurement machine (CMM; Kemco 400) as shown in Figure 4.11 was used to measure the deformed specimens either after the L-bending or U-drawing processes to evaluate the magnitude of the springback. Two steel blocks were used to hold the specimen on the machine base plate as shown in Figure 4.12. The machine resolution is 0.001 mm which is sufficient for this kind of application. The machine was calibrated prior to each test to eliminate measurements errors.



Figure 4.12 Kemco CMM 400 machine set up to measure the L shape springback angle

4.7 Summary

In this chapter, the design of the L-bending and U-drawing forming apparatus was explained in detail, considering the features of the Instron machine and the design variables such as the die radius and clearance. Also, the means of applying a measurable and consistent blank holder force was considered. Finally, the CMM machine used to measure springback after completion of the forming processes was described

CHAPTER 5: MEASUREMENT OF FRICTION COEFFICIENT

5.1 Introduction

In a metal forming process, the workpiece experiences friction due to the contact between the workpiece and the tool surfaces. This can dominate the strain patterns and performance of many forming processes [59, 60]. In this project, especially the U-drawing process, the blank is subjected to large plastic deformation in addition to the friction force which resists the movement of the blank into die the cavity. This could influence the punch load required to form the part. Also the surface of the tools and the formed part could be adversely affected by the amount of friction that occurs during the process. This chapter reports experiments undertaken to measure the friction coefficient for the four different blank materials used in this project under dry and lubricant conditions. Subsequently, the results were utilised in the numerical analysis for more precise prediction of the metal forming process.

5.2 Apparatus

The apparatus used to measure both the static and dynamic friction coefficient was a special machine developed by Leeds University called a pendulum tribometer. Figure 5.1 illustrates the main features of this instrument which consists of two identical halves. The experiments can be conducted under either dry or lubricated conditions. This machine essentially consists of a disc (2) fixed on an inclinable frame (7), a lubricant reservoir (1), a ball arm (4) and motor (8). The purpose of the disc is to hold a ring which represents one of the surfaces of interest, in this case the blank material.

The ball arm holds the ball which represents the tool material. Also, a further function of the pin arm is to read the angle β , which is essential to measure the friction coefficient, and to carry an additional load if required. The lubricant tank may be filled with any kind of liquid lubricant and it can be adjusted to match the drop of the disc specimen.

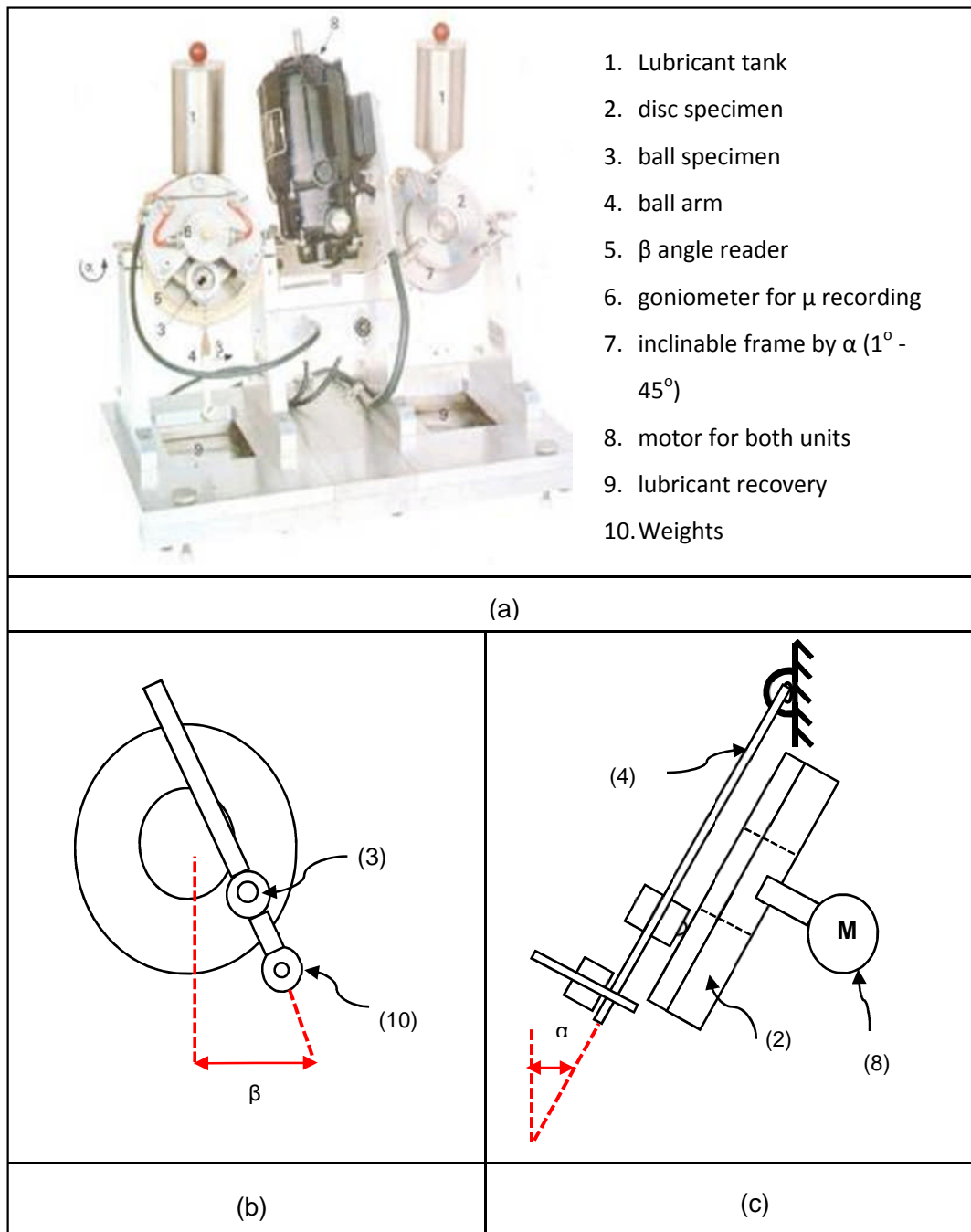


Figure 5.1 (a) The pendulum tribometer apparatus (b) front view (c) side view

The pendulum tribometer works by using the motor (8) as shown in Figure 5.1 to rotate the disc (2) either clockwise or anticlockwise via drive belts and pulleys. The disc contains the blank material specimen. The ball is in contact with the blank through the ball arm (4). The contact pressure at the ball-blank interface depends on the contact area and the magnitude of the load. The normal load can be controlled by adding additional weights to the ball arm or by changing the angle of inclination α .

As a result of the disc rotating, the ball attempts to slide along the specimen causing an increase in the pendulum angle β . At a certain point, assuming there is a difference between the static and dynamic friction coefficients, the ball will reach a 'sticking' point where the relative velocity between the two test pieces is zero. At this point, the gravitational force, resulting from the pendulum angle, is equal to the driving force of the rotating specimen. The ball then slips back to a lower angle and the process is repeated. The pendulum angle is measured by a capacitance voltage rotation transducer.

The machine was calibrated by determining the relationship between the angle of the arm (β) and the corresponding voltage from the transducer. For example, at zero degrees of arm angle, the system will show zero volts and with an increase in the angle the voltage will increase. The angle was set to different values (0° , 5° , 10° , 15° , 25° , 30°) and the corresponding voltage was obtained. This test was repeated for three times and the relationship between the angle and the voltage was plotted as shown in Figure 5.2. It shows only minor differences in the results for the repeated tests which indicates the consistency of the experiment and also the linearity of the transducer.

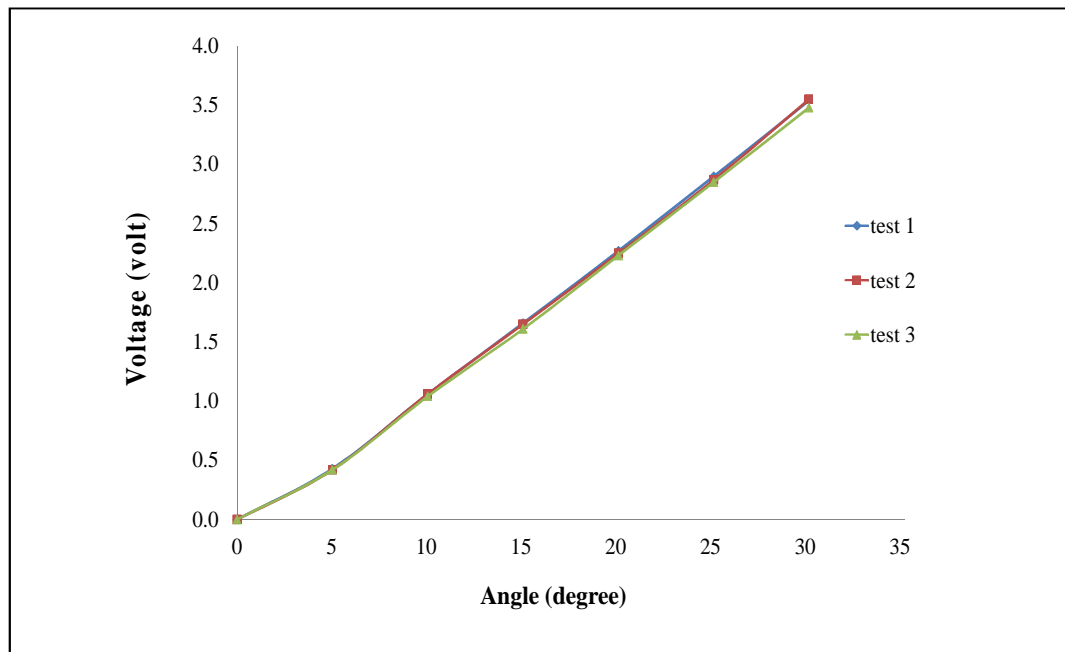


Figure 5.2 The relationship between the arm angle (β) and the transducer voltage

One of the advantages of this device is the simplicity with which friction coefficient tests can be conducted. Further, this machine can conduct two experiments simultaneously, using the two identical halves. Also, several contact geometries can be used, such as flat-on-flat and ball-on-flat. Furthermore, it is flexible in changing the ball-on-disc contact angle by adjusting the inclination angle α as shown in Figure 5.1 (c).

5.3 Metal forming lubrication

ULTAFORM 1030 supplied by Rocol Company [61] is a mixture of mineral oil and chlorinated paraffin which is formulated as a cold metal forming lubricant, suitable for many ferrous and non-ferrous metals. It was applied between the blank materials and a representative tool forming surface to investigate the influence of lubrication on the friction coefficient.

5.4 Experimental set-up

5.4.1 Specimen preparation

Two essential components have to be manufactured prior to the test: holders (discs) made from steel and second rings made from the blank sheet materials. The holder was made to hold the ring on the inclinable frame as seen in Figure 5.1. 6 rings for each sheet material were produced by a wire cutting machine for the aluminium materials and by a laser cutting machine for the steel materials. The inner and outer diameters for both the holder and blank ring were 35 mm and 66 mm respectively. Both holder and rings were cleaned using acetone and then attached together using special glue. Figure 5.3 shows the holder and the ring assembly when they have been glued together

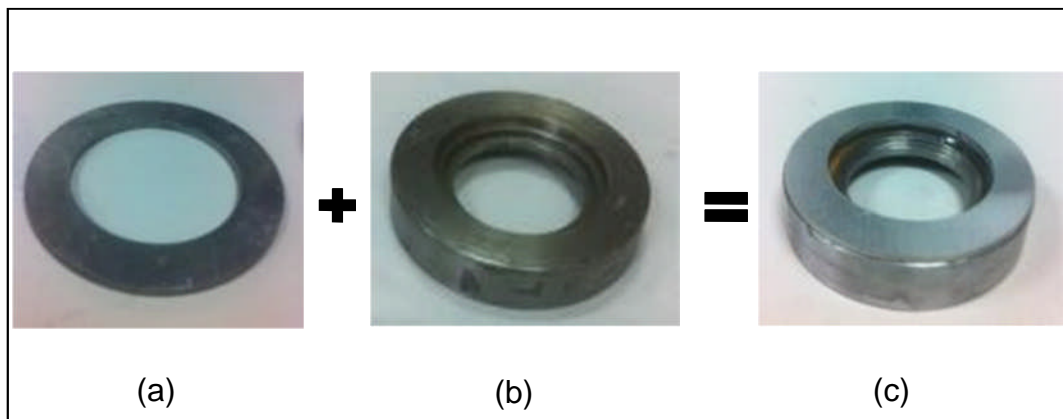


Figure 5.3 Picture of (a) blank ring (b) blank holder (c) assembly

The ball represents the tool material which in the forming test rig described in Chapter 4 was EN8 steel. It proved difficult to obtain EN8 balls in the required quantity. Consequently, balls manufactured from an appropriate material having similar properties to EN8 were sourced. The most important mechanical parameters that dominate the friction coefficient between two materials are the hardness of each material and the surface finish.

It was found that 316 stainless steel has comparable hardness to the EN8 steel as could be seen in [62, 63] and the required roughness was achievable via surface conditioning carried out in the tribology laboratory in Leeds University. This conditioning is discussed later in this section

The friction test must experience similar operational conditions such as contact pressure, surface roughness and sliding velocity to those in the forming rig. The average contact pressure applied on the blank holder in the metal forming experiments was calculated to be 0.3 MPa. The punch velocity of 2 mm/s in the metal forming operation was set as the sliding velocity in the friction test. The tools of the metal forming rig were manufactured to a surface roughness Ra of about 0.15 μm . This value was similar to that obtained for the ball after it had been modified. The ball modification to reach similar contact pressures to these occurring in the metal forming rig is described below.

The contact between the ball and the blank surface is characterised as a sphere in contact with a plate. Therefore, according to Hertzian contact theory, the maximum pressure that can be generated from pressing the ball on to the blank materials is calculated using equation (5.1):

$$P_{max} = \frac{E^*}{2\pi} (3W)^{\frac{1}{3}} \quad (5.1)$$

where E^* denotes the equivalent elastic modulus and W is a dimensionless load parameter calculated using the following equations:

$$\frac{1}{E^*} = \frac{1}{2} \left(\frac{(1 - \nu_A^2)}{E_A} + \frac{(1 - \nu_B^2)}{E_B} \right) \quad (5.2)$$

$$W = \left(\frac{F}{E^* R_e^2} \right) \quad (5.3)$$

Here, ν denotes the Poisson's ratio, F is the contact load and R_e is the equivalent radius of curvature.

R_e is calculated using equation (5.4):

$$\frac{1}{R_e} = \frac{1}{R_1} + \frac{1}{R_2} \quad (5.4)$$

The contact force F was calculated taking into account the arm load, ball load and the additional weights and how they act on the contact point (C) as shown in Figure 5.4. By taking a summation of total moments around the joint of the bar (point D), the unknown contact force F can be defined using expression (5.5):

$$\sum M_D = 0 \quad (5.5)$$

$$\begin{aligned} &-(m_w \cdot g) \sin \alpha \cdot (117.71) - (m_a \cdot g) \cdot \sin \alpha \cdot (65.17) \\ &- (m_b \cdot g) \cdot \sin \alpha \cdot (28) + F \cdot (28) = 0 \end{aligned} \quad (5.6)$$

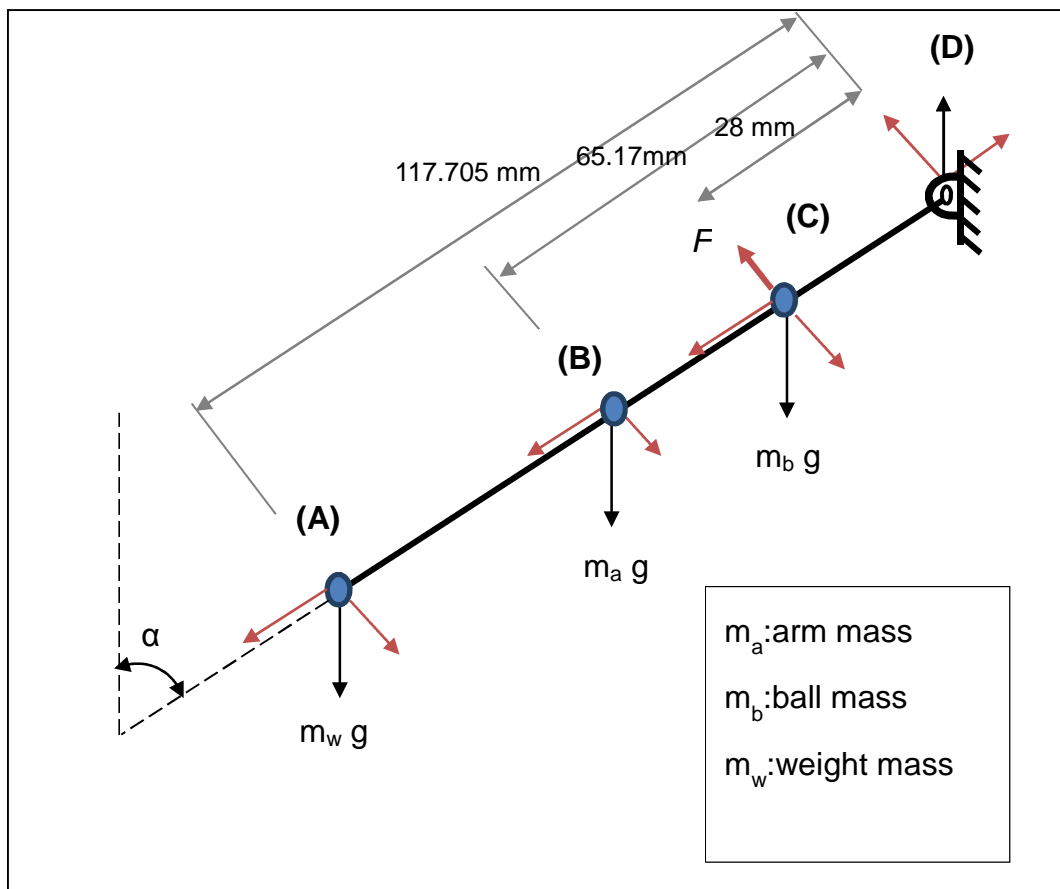


Figure 5.4 Free body diagram for the forces acting on the ball arm

Two discs, each of mass 164.23 grams, were used as additional forces acting on point (A) as shown in Figure 5.4. The ball arm and the ball mass are 28.56 grams and 3.8 grams respectively. The dimensions from each applied load to the point D are shown in Figure 5.4 and the α angle is assumed to be 45° . From the above considerations, the contact force acting on the blank surface (F) was calculated to be 5.2 N. As the contact type is a sphere on a flat surface, the R_e is calculated as follows:

$$\frac{1}{R_e} = \frac{1}{R_b} + \frac{1}{\infty} \quad (5.7)$$

$$\therefore R_e = R_b = 6.35 \text{ mm}$$

The equivalent elastic modulus for the ball and blank material was calculated from equation (5.8):

$$\frac{1}{E^*} = \frac{1}{2} \left(\frac{(1 - \nu_b^2)}{E_b} + \frac{(1 - \nu_B^2)}{E_B} \right) \quad (5.8)$$

where ν_b and ν_B are the Poisson's ratio for the ball and blank materials respectively and assumed to be 0.3 for both and E_b and E_B denote the Young's modulus for the ball and blank materials respectively. The elastic modulus of the steel ball material is assumed to be 206 GPa; however the modulus differs for each of the blank materials as reported Chapter 3. In this sample calculation, only one of the blank materials is considered for simplicity. Thus the DP600 steel was assumed to have an elastic modulus of 220.3 GPa, as mentioned in Chapter 3, from which E^* was calculated to be 234 GPa from equation (5.8).

By substituting the contact force determined by equation (5.6), the R_e value found by (5.7), and the equivalent Young's modulus, the W parameter was calculated from equation (5.3) to be 4.8×10^{-08} . The maximum pressure is calculated by using equation (5.1) to be 195.7 MPa, which is significantly higher than the pressure produced by the blank holder pressure that was set at 0.3 MPa for both L-bending and U-drawing experiments.

Consequently, the ball was subjected to contact against a flat steel surface and polished to achieve surface roughness close to that of the tools. As a result, an almost circular flat surface was produced with a diameter of about 2 mm as shown in Figure 5.5. Therefore, the contact pressure was recalculated by dividing the contact force calculated by equation (5.5) to be 5.2 N, by the new area which is a circle of 2 mm diameter. The pressure calculated was 1.66 MPa which is still higher than the desired pressure (0.3 MPa) but very much closer than the original value for the perfectly spherical ball of 442 MPa.

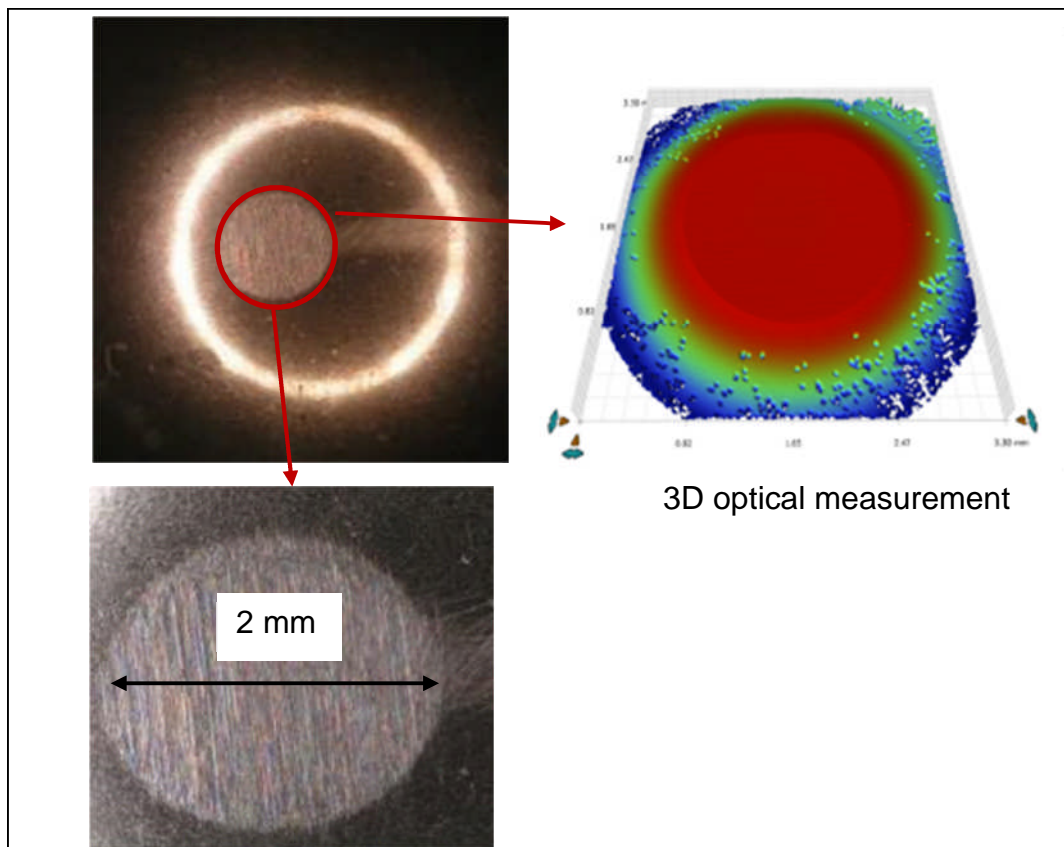


Figure 5.5 The ball after wear showing the dimensions and surface finish of the wear scar

A further way to reduce the contact pressure is to reduce the contact force by decreasing the inclined frame angle (α) or reducing the additional weights. Any variance in the α angle will change the surface topography.

Therefore, reducing the additional weight was the best achievable option. The minimum additional weight available in this study was a disc of 17.5 gram. Using this weight, the contact force was recalculated to be 0.97 N giving a contact pressure of 0.3 MPa which is the same level as in the forming rig.

5.4.2 Experimental procedure

The idea of the friction coefficient experiment is to allow the surfaces of interest to slide against each other. Here, the pendulum tribometer device allows a ball to contact a ring surface while the ring is rotated. Consequently, the ball will momentarily be stationary on the ring surface at the top of the stroke, which represents the static friction condition, and will then fall back which represents the dynamic friction condition.

Figure 5.6 illustrates the theory of measuring the friction coefficient through the sliding process of the tribometer device. The ball was attached to the pin arm by a special mechanism and the voltage transducer was set to zero. The disc was then rotated clockwise which causes the ball to slide over the disc. However, due to the static friction, the ball will 'stick' at a certain angle β_s with the vertical as shown in Figure 5.6. At some point, the ball will no longer resist the gravity force and be pulled down to a lower angle β_d . This behaviour was observed to occur throughout the experiment run time which was 60 seconds. The data obtained was manipulated in order to measure the static and dynamic friction coefficients as described below.

The friction coefficient was calculated as the ratio of the friction force (F) and the normal load (N):

$$\mu = \frac{F}{N} \quad (5.9)$$

In the pendulum tribometer apparatus, the friction force is a function of the pendulum angle and inclined frame angle. The gravitational ball load on the blank was analysed at two positions as indicated in Figure 5.6:

1. At point A, the ball was placed in contact with the blank ring top surface prior to the rotation of the arm, where β angle is zero. Therefore, the α angle alone controls the normal force and the tangential force.

Figure 5.6 (c) illustrates the free body diagram for the ball load, with respect to the inclined frame angle (α). The load on the ball was divided into two components; one is the normal reaction $mg \sin \alpha$ which acts perpendicular to the blank surface (N) as shown in equation (5.9) and the other is the force $mg \cos \alpha$ that acts tangential to the surface

2. When the ball is at position B the total ball load $mg \cos \alpha$ was again divided to two components: the tangential component is $mg \cos \alpha \sin \beta$ and normal component is $mg \cos \alpha \cos \beta$.

Here, the important tangential component of the ball force is $mg \cos \alpha \sin \beta$ which represents the friction force to be used in equation (5.9). Therefore, using equations (5.9), the friction coefficient can be expressed by equation (5.10):

$$\mu = \frac{mg \cos \alpha \sin \beta}{mg \sin \alpha} = \frac{\sin \beta}{\tan \alpha} \quad (5.10)$$

Here, β is the arm angle when it rotates and α represents the inclinable frame angle which could be set between 0° and 45° . In the current investigation, the angle α was set to 45 degrees for all experiments. Also, the contact pressure and sliding velocity applied were 0.3 MPa and 2 mm/s respectively. Also the friction coefficient between the blank materials and the representative forming tool surface were measured under both dry and lubricated conditions.

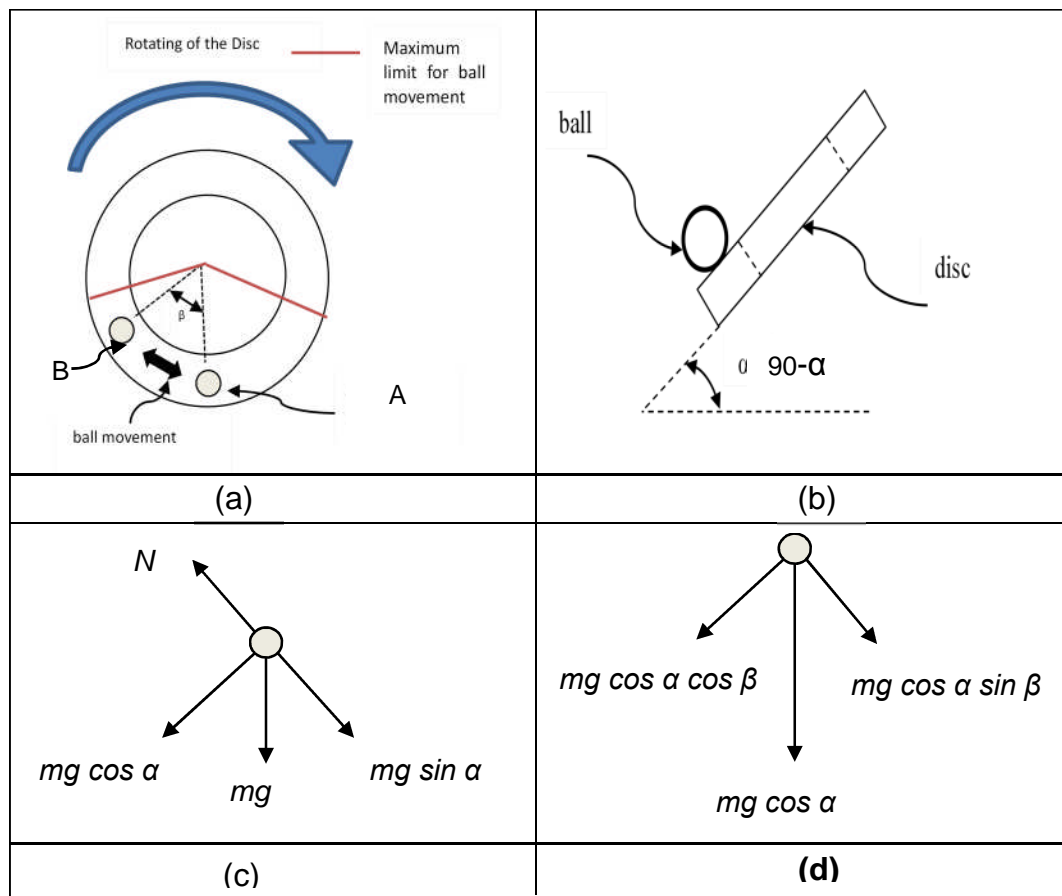


Figure 5.6 The friction pendulum apparatus concept (a) front (b) side view of the apparatus (c) free body diagram at position A (d) free body diagram at position B

5.5 Results and discussion

5.5.1 Steel blank materials

Figures 5.7 to 5.10 illustrate the variation of the friction coefficient for the contact of the steel ball against the steel blank materials. These figures depict that the amplitude of oscillations in the coefficient of friction for dry conditions is higher than in the lubricated condition, which could be attributed to the existence of a stick–slip phenomenon such as occurs when the static friction coefficient is greater than the dynamic one.

The static friction coefficient was measured by selecting the highest values of the friction coefficient from the full data, and an average line was plotted. However, the dynamic friction coefficient was determined by averaging the whole data set.

Figures 5.7 and 5.9 show the high amplitude of friction coefficient oscillations under dry conditions for the high and low strength steel (DP600 and DX54D) respectively. The oscillations in friction coefficient for both materials were reduced remarkably under lubricated conditions as shown in Figures 5.8 and 5.10. Moreover, it can be seen that the static friction coefficient was higher than the dynamic friction coefficient, especially under dry conditions. However, there was not much difference between the static and dynamic friction coefficient under lubricated conditions. Also, it can be seen that the magnitude of the friction coefficient decreases with time possibly due to plastic deformations that might occur at the asperities of the surfaces during the course of the experiment.

Despite using the lubricant in testing the friction coefficient for the DP600, some oscillations appeared at certain times of the test run as shown in Figure 5.8. This was thought to be due to the existence of some scratch marks on the surface of the tested material which are unavoidable.

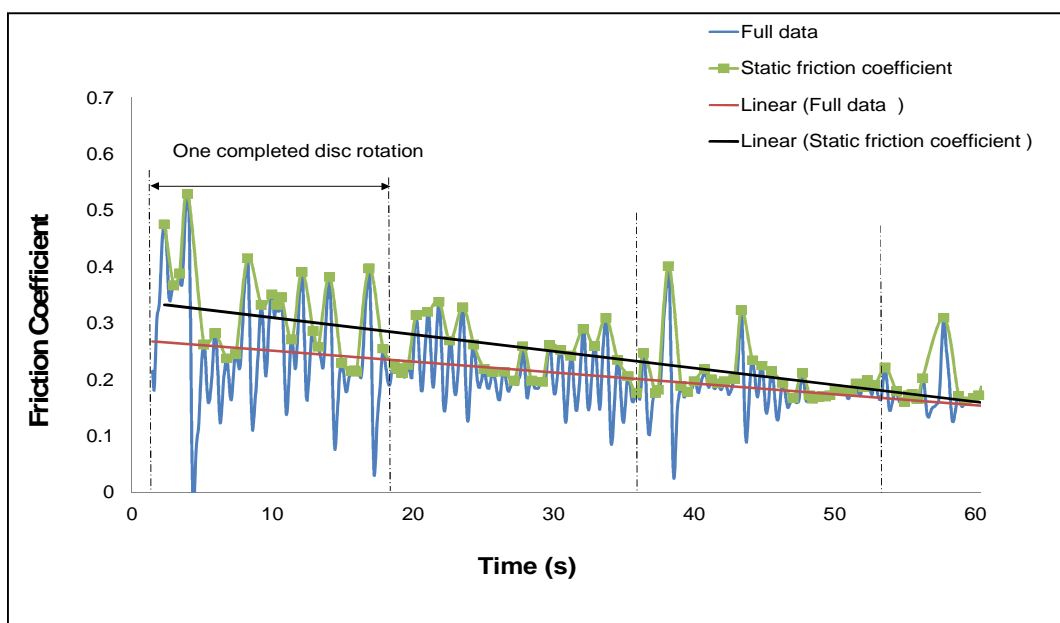


Figure 5.7 Friction coefficient for DP600 under dry conditions

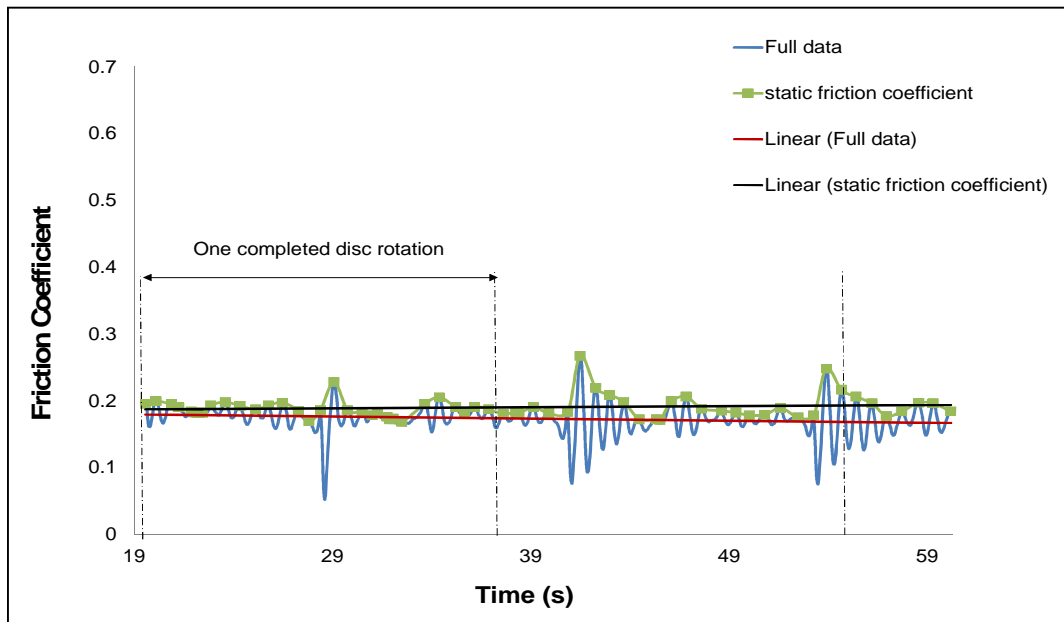


Figure 5.8 Friction coefficient for DP600 under lubricated conditions

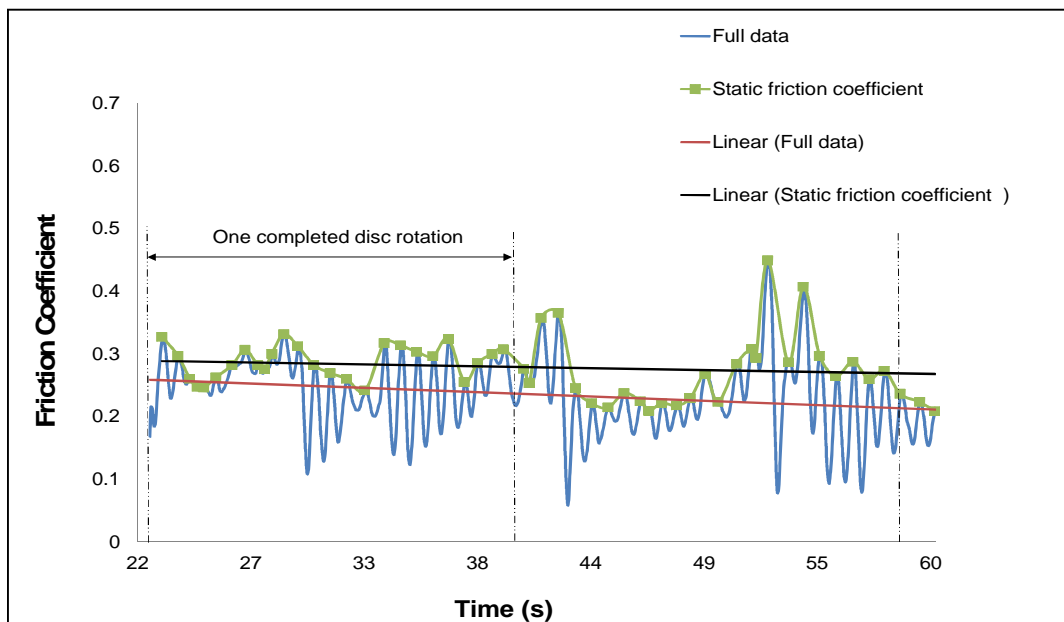


Figure 5.9 Friction coefficient for DX54D under dry conditions

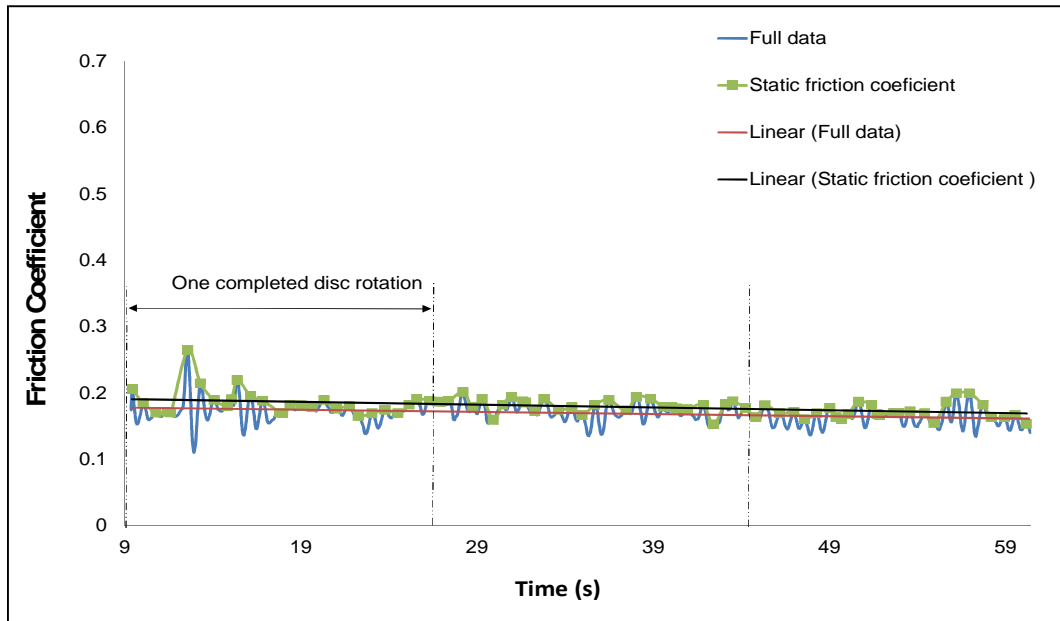


Figure 5.10 Friction coefficient for DX54D under lubricated conditions

5.5.2 Aluminium blank materials

The friction coefficient for a steel-aluminium contact under dry conditions was difficult to be obtained; the steel ball tended to adhere to the aluminium disc throughout the rotation of the disc until it reached the maximum angle β as illustrated in Figure 5.6. Then the ball dropped at certain times when the ball arm hit the barrier which determines the maximum angle β . In fact, no results could be obtained for either of the aluminium alloys under dry conditions because the friction coefficient is so high that it exceeded the limit of the machine. The reason for this is thought to be that the differences in hardness of the two materials in contact might cause ploughing; the hard material asperities of the steel surface plough into the soft aluminium material [64]. This means that plastic deformation occurs, which increases the frictional force.

Although the same lubricant used between the two steel surfaces was also used for the steel-aluminium friction tests, the variation of the friction coefficient was higher for the aluminium alloys than for the steel materials. This indicates that the applied load was still high, relatively, to the hardness of the tested aluminium materials, which can result in plastic deformation of the asperities through the contact.

According to Hamrock [65], high load and low hardness under lubricated condition may cause plastic deformation, known as plasto-hydrodynamic lubrication. Figure 5.12 shows the high amplitude of oscillations in the friction coefficient under lubricated conditions. Also, this figure shows a general reduction in the magnitude of friction coefficient during the process because of asperity deformation leading to a generally flatter (and therefore smoother) surface.

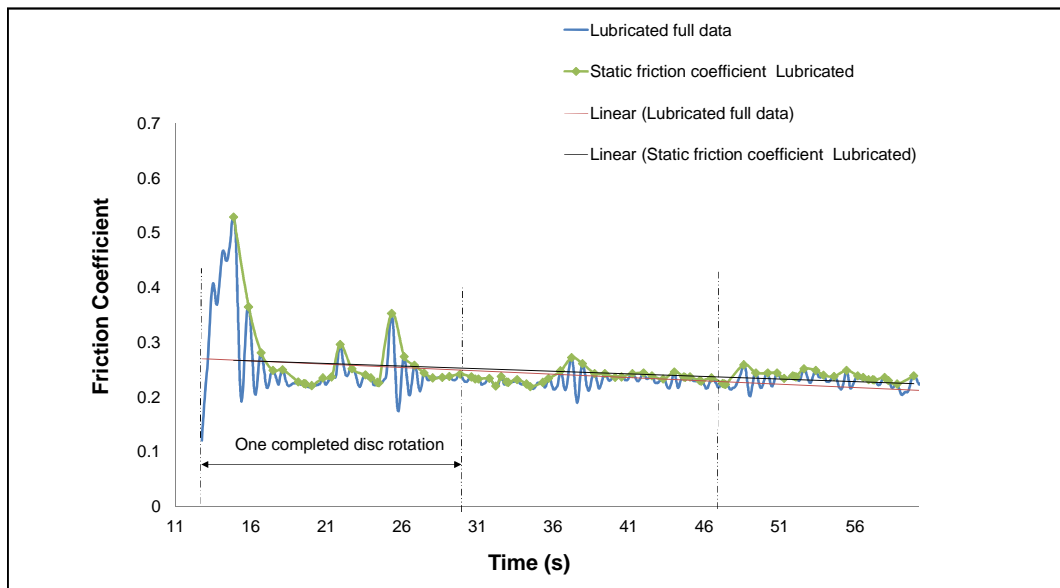


Figure 5.11 Friction coefficient for CPLA10414 under dry and lubricated condition

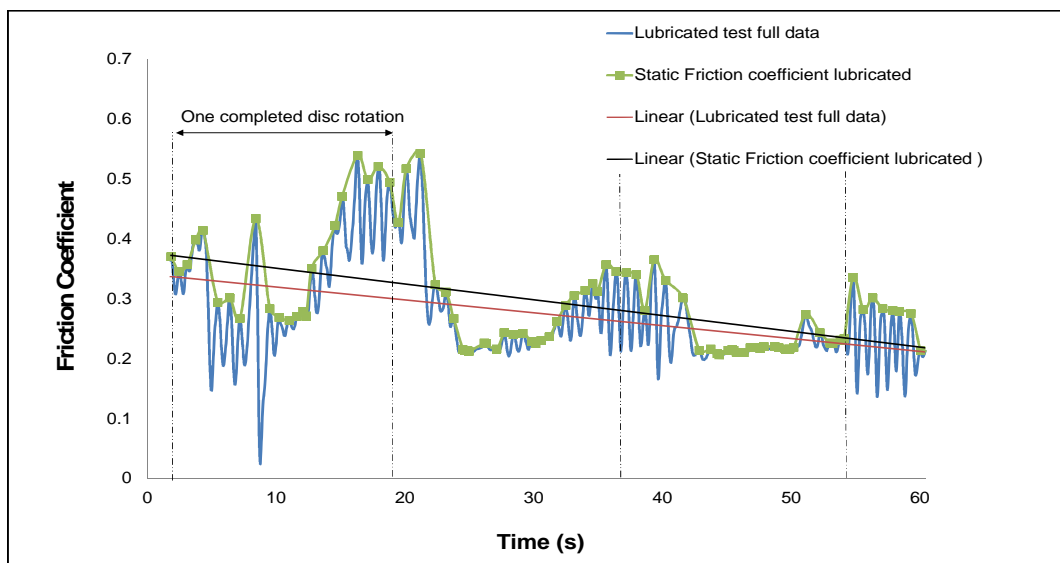


Figure 5.12 Friction coefficient for CPLA100k38 under lubricated condition

Table 5.1 summarises the static and dynamic friction coefficients measured under both dry and lubricated conditions for the four blank materials. As stated above each test was run for 60 seconds. However, the forming experiments in this project were run for 22 seconds. Therefore, only the first 22 seconds of the friction coefficient experimental results were considered in the calculation of the friction coefficients shown in Table 5.1.

Table 5.1 The average static and dynamic friction coefficients under dry and lubricated condition during the first 22 seconds of the test

Materials	Friction coefficient under dry conditions		Friction coefficient under lubricated conditions	
	Static	Dynamic	Static	Dynamic
DP600	0.31	0.25	0.20	0.17
DX54D	0.29	0.26	0.18	0.17
CPLA100k38	--	--	0.37	0.34
CPLA10414	--	--	0.27	0.27

5.6 Summary of friction coefficient experiments

This chapter outlines the experimental methodology for the friction coefficient test. It explains the apparatus, the experimental set-up, the parameters used and the test conditions. It also illustrates how the contact ball surface was modified to simulate the sliding situation that occurs in the U-drawing process. The contact pressure and linear velocity applied were 0.3 MPa and 2 mm/s, respectively. Each test lasted for 60 seconds and the friction coefficient results were obtained. Both dry and lubricated condition tests were conducted. Finally, the static and dynamic friction coefficients under both dry and lubricated conditions for the four blank materials were derived. These were utilized in the numerical analysis of the L-bending and U-drawing metal forming processes as described in Chapters 6, 7 and 8.

CHAPTER 6: L-BENDING SHEET METAL FORMING PROCESS

6.1 Introduction

This chapter investigates the springback that occurs after the L-bending process described in Chapter 4 for the four blank materials used in this project. The main components and concept of the L-bending process are illustrated in Figure 6.1. The blank is clamped by the blank holder as shown in Figure 6.1(a). The punch is moved to form the blank around the die as shown in Figure 6.1(b). Finally the tools are released from the formed specimen with the possibility of springback as shown in Figure 6.1 (c).

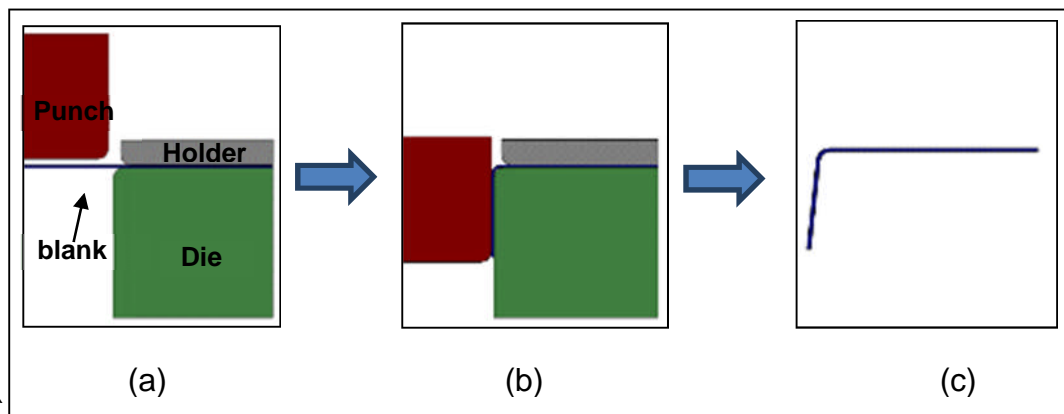


Figure 6.1 L-bending process (a) prior to the forming process (b) end of the forming process (c) final product with springback

In this chapter, experimental investigations for one set of parameters, the die radius (4 mm), punch radius (4 mm) and the die/punch gap (3.5 mm), for all four materials are reported. The influence of mechanical properties of the blank material during the forming process (punch force vs. displacement) and after the process (the springback) is investigated.

Four different blank materials were used: two steel materials and two aluminium alloy materials. These materials and their mechanical properties were introduced in Chapter 3.

The finite element method (FEM) was utilised to simulate the forming and springback processes, and validation of the modelling was investigated for all four materials. The blank materials were modelled using the Yoshida-Uemori model parameters which were derived in Chapter 3. HyperMesh v11.0 was used to build the model (creating the geometry and the mesh, specifying the material properties and the boundary conditions). Subsequently, the explicit version of Ls-Dyna_971 was employed to run the model to simulate the forming process. The Dyna file which contains the stresses and strains of the blank at the end of the forming process was then imported into Hypermesh to activate the implicit analysis mode for the springback calculation conducted using the implicit version of Ls-Dyna_971. Ls-Dyna_971 was used also as the postprocessor to display results such as the punch load and displacement, stresses and strains in the blank, blank thickness reduction and angle after the springback. A parametric study was carried out to investigate the effects of the punch radius, die radius, the clearance and the blank thickness on the degree of springback.

6.2 L-bending experiments

6.2.1 Experimental method

In order to perform the L-bending experiments, a metal forming press was designed, manufactured and installed on an Instron universal test machine as described in Chapter 4. The four blank materials provided by Jaguar Land Rover were laser cut into rectangular strips of 150 × 30 mm as shown in Figure 6.2. The die and punch radii were both 4 mm; the blank thickness was 1.6 mm for the steel materials and 2.5 mm for the aluminium materials.

The clearance was calculated by measuring the gap between the forming tools (the die and the punch) as shown in Figure 6.3 (c) and subtracting the blank thickness from this measured gap. The clearance was set at values of 1.9 mm and 1.0 mm for steel and aluminium blanks respectively, using a gauge plate at the start of each series of experiments.

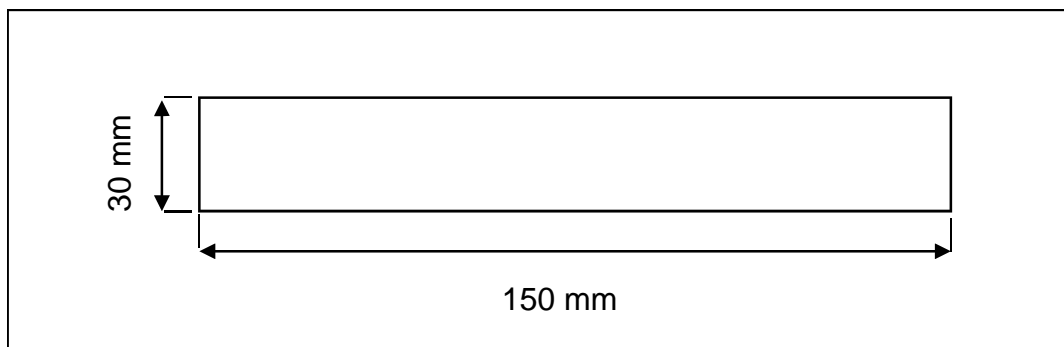


Figure 6.2 Blank dimensions for L-bending process

Prior to the test, the tools and the required blank materials were cleaned using acetone to remove impurities. The blank was then placed on the die as shown in Figure 6.3 (a). The holder was placed over the blank in such a way that the shallow channel described in Chapter 4 fitted closely around the blank to ensure that the blank was correctly aligned during the metal forming process.

Six bolts, fitted with springs, were used to apply the clamp force to the blank holder. The springs were located between the top surface of the blank holder and the bottom surface of bolt head as shown in Figure 6.3 (b). Washers were used between the head of the bolt and top of the spring to help distribute the load. The specification of the springs is explained in Chapter 4. To ensure the reliability of these springs, the Instron machine was used to measure the spring rate. It was found that the spring compressed by 1 mm for 70 N applied force as stated by the springs' manufacturer. Applying a known force on the blank holder is achieved simply by screwing each bolt to a certain level of spring compression.

One full rotation of the bolt head leads to 1.5 mm spring compression which means that for one rotation, the spring produces about 105 N of axial force. In the current study, two full rotations of each bolt were made giving a total blank holder force of 1.26 kN .

Figure 6.3 (b) shows the blank has been clamped and the punch set approximately 3.5 mm above the top surface of the blank. At this position, the Bluehill 2 software, mentioned in chapter 4, was utilised to zero the load and displacement readings of the transducers. This program was also used to specify the punch speed and final displacement which were 2 mm/s and 48 mm respectively.

The punch was moved at constant speed to just before the die bottom to form the blank, making an L-shape as shown in Figure 6.3 (c). The punch was then returned back to its original position during the unloading process as shown in Figure 6.4. It is clear that springback occurred during raising of the punch. The blank holder force was removed by releasing the bolts and the formed part was carefully removed. The test was carried out three times for each material under the same conditions to assess the repeatability of the experiments.

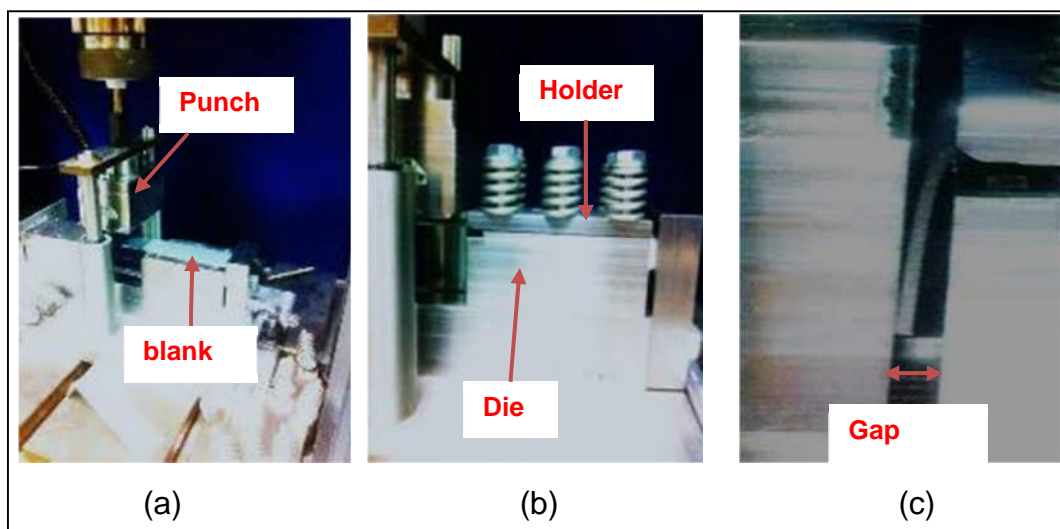


Figure 6.3 The process of forming the blank (a) on the die (b) clamped by holder (c) fully formed L-part

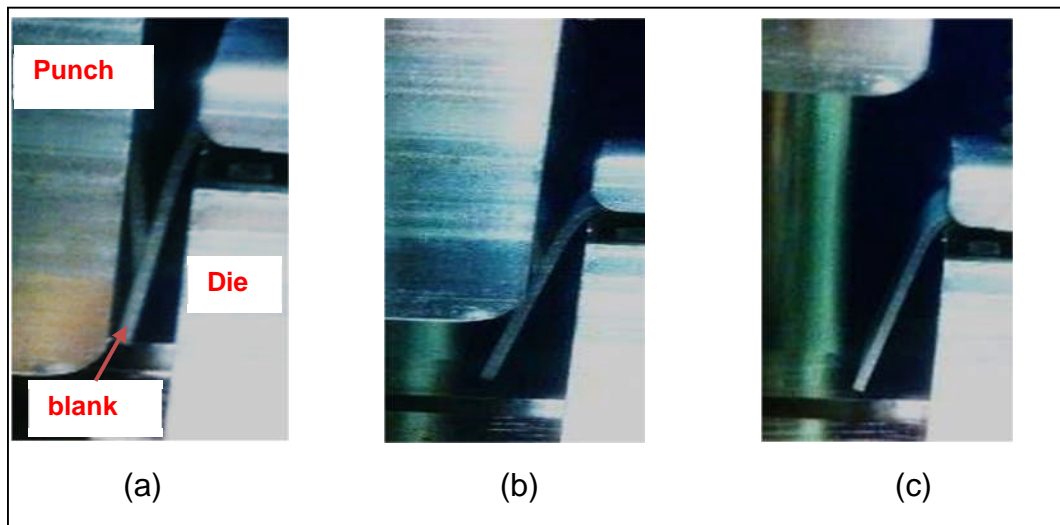


Figure 6.4 Unloading process for L-bending (a) fully formed L-part (b) middle of punch reverse (c) fully removed punch

6.2.2 Experimental results

6.2.2.1 Punch load behaviour during the L-bending process

Figures 6.5 to 6.8 show the punch load vs displacements plots as read by the Bluehill software for the four blank materials. A similar trend of the punch force versus displacement curves were seen for all four blank materials. Also, the results of the three experiments for each material confirm the consistency in the blank behaviour during these L-bending metal forming experiments. Therefore, for simplicity the punch force behaviour is described in detail for the DP600 material only as shown in Figure 6.5 where, the punch force-displacement curve is divided into four regions; I, II, III and IV. Pictures of the blank at the end of each of regions II, III and IV were taken for clarification and are shown in Figure 6.5. In the first region the punch force increases as the blank is bent around the die radius. In the second region II, a further increase in the punch load was seen due to increasing friction force between the punch and the blank which leads to further bending of the blank. In region III, the punch force falls dramatically as deformation of the blank material has been mostly undertaken within the first two regions of the operation.

The force finally levels off to an almost constant value as the influence of friction between the punch and the blank remains essentially unchanged up to the end of the process as shown in region IV of Figure 6.5.

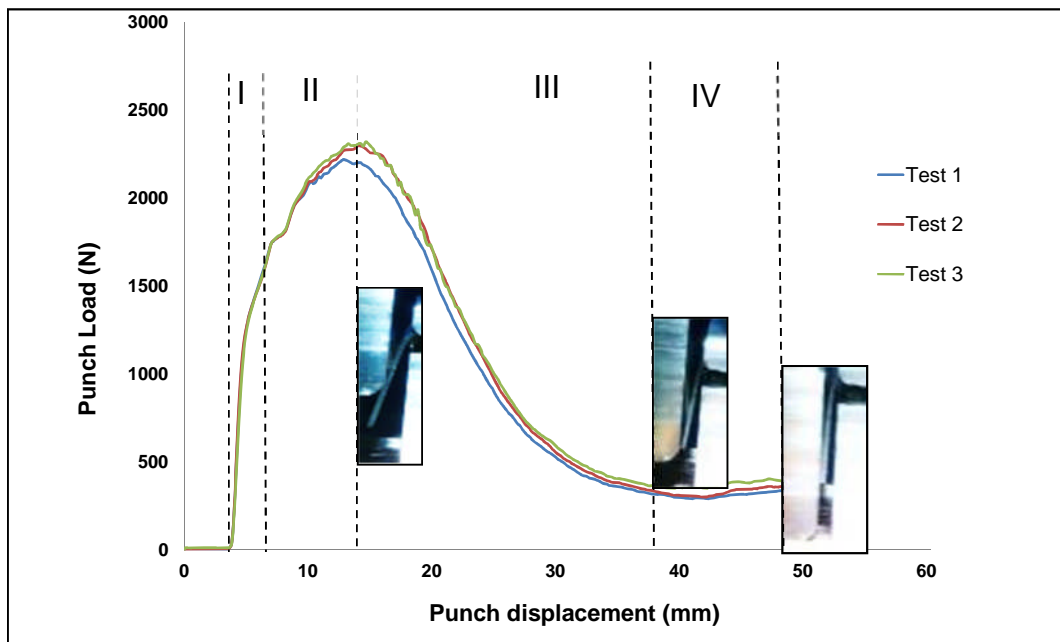


Figure 6.5 Punch load versus displacement for the high strength steel (DP600) during L-bending

Similar behaviour of punch load versus displacement was observed for the other three materials as shown in Figures 6.6 to 6.8 for the DX54D, CPLA100k38 and CPLA10414 blanks respectively. The mean maximum punch load required to form each material is reported in Table 6.1.

Figures 6.9 and 6.10 show the mean punch load versus displacement curves for the steel and aluminium materials respectively. It is observed that the differences are much higher between the two steel materials shown in Figure 6.9 than between the two aluminium alloys shown in Figure 6.10. It was found that the maximum punch load required to form the DP600 was about 2.5 times higher than that required to form the low strength steel (DX54D). However, the maximum punch force measured during the forming of the high strength aluminium (CPLA100k38) was only 1.65 greater than that for the lower strength alloy (CPLA10414) as seen in Figure 6.10.

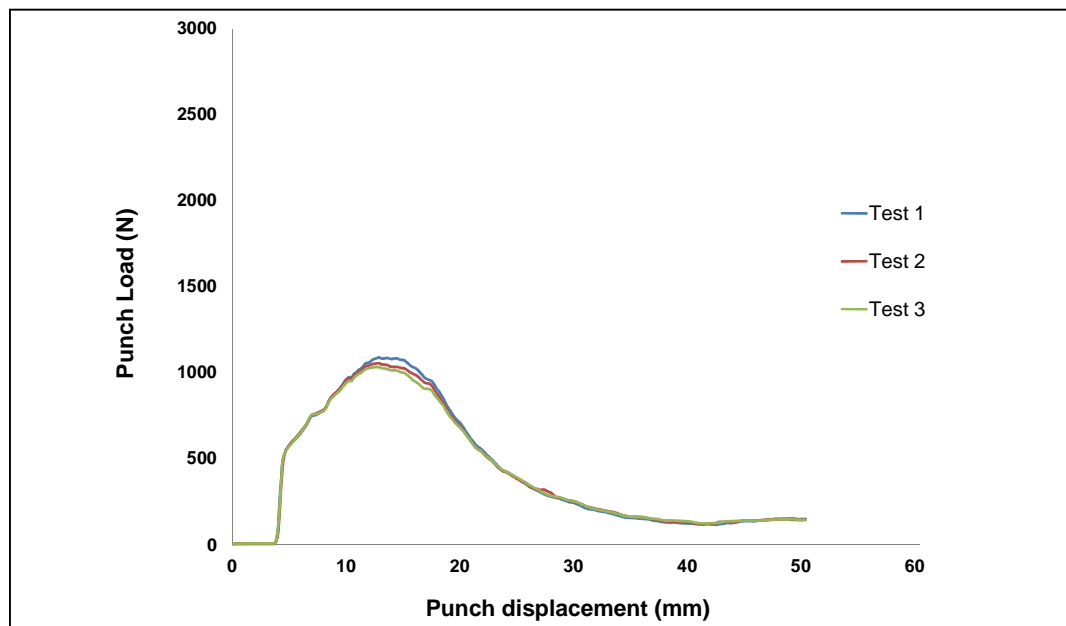


Figure 6.6 Punch load versus displacement for the low strength steel (DX54D) during L-bending

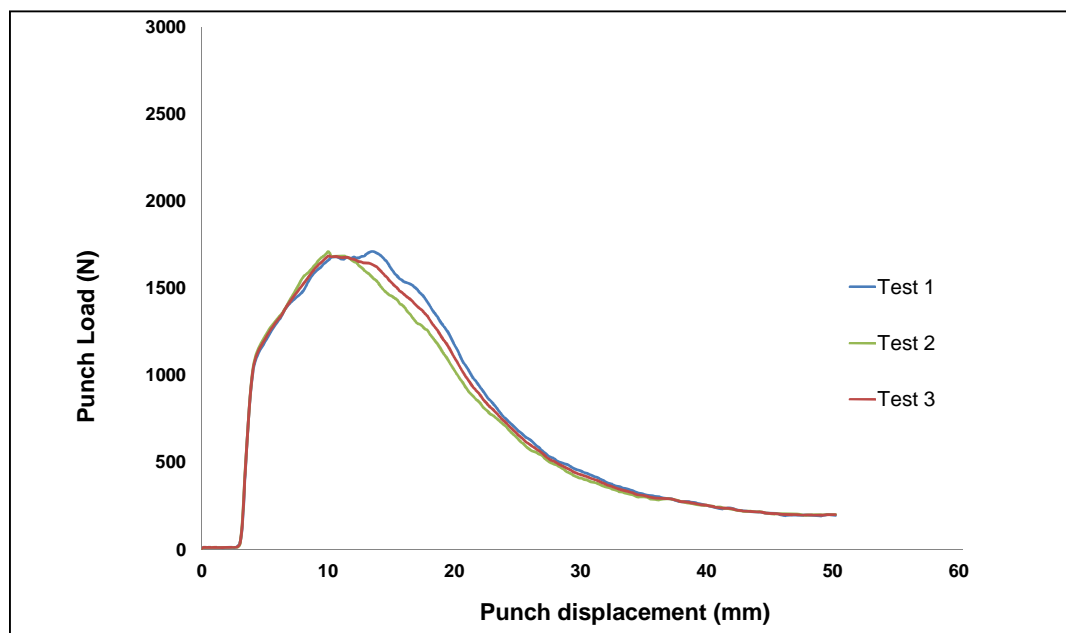


Figure 6.7 Punch load versus displacement for the high strength aluminium (CPLA100k38) during L-bending

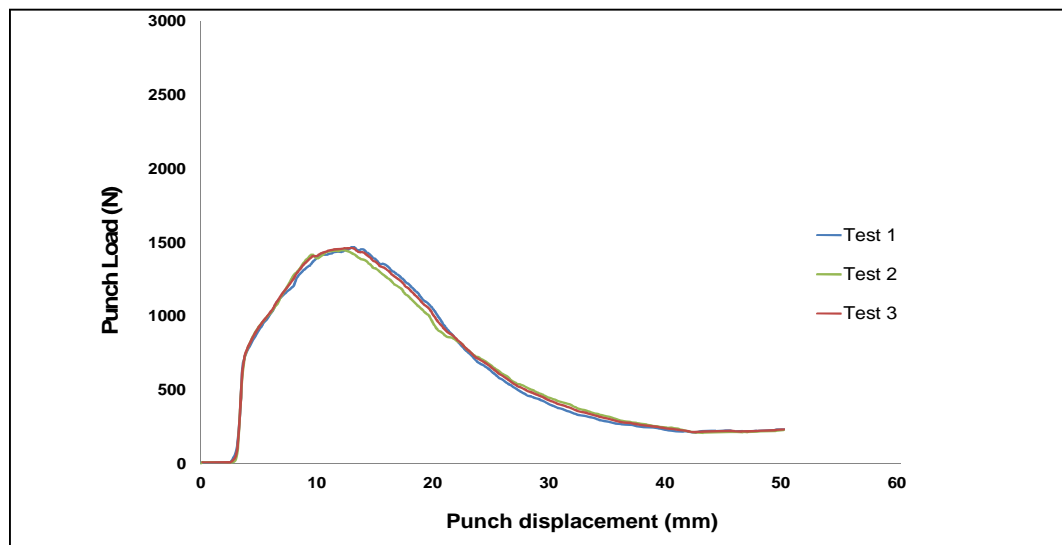


Figure 6.8 Punch load versus displacement for the low strength aluminium (CPLA10414) during L-bending

To understand the difference between the punch load behaviour during the L-bending process of the two material groups, two critical points (A,a and B,b) on each curve in Figures 6.9 and 6.10 were defined. A capital letter is related to the high strength material and the lower case is for the low strength material. The points (A,a) were defined as the first deviation from linear behaviour and the points (B,b) as the maximum point of the punch force curve. Values of the punch load at these points are shown in Tables 6.1 and 6.2 for steel and aluminium materials respectively. From the data in Chapter 3 where the mechanical properties of the materials have been reported, it was found that there is strong relationship between the points (A,a) and the yield stress and between points (B,b) and the ultimate stress. The difference between the yield stresses of the high strength material and the lower one is almost the same as the variance between the punch force at point A and at point a. Similarly, the variance between punch force at point B and b is almost equal to the difference between the ultimate stress of the high strength materials and the low strength ones as illustrated in Tables 6.1 and 6.2.

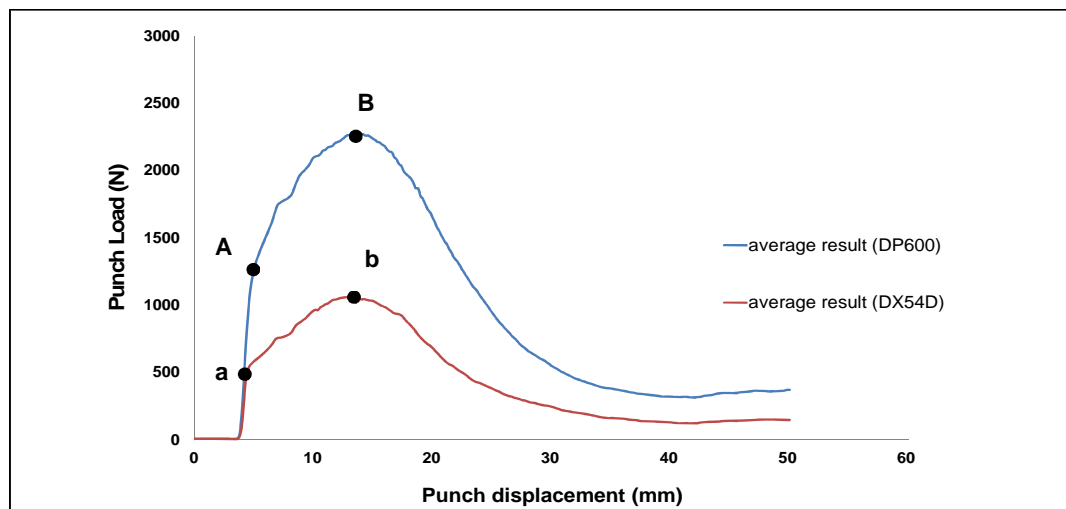


Figure 6.9 Comparison of punch load versus displacement between DP600 and DX54D steel during L-bending

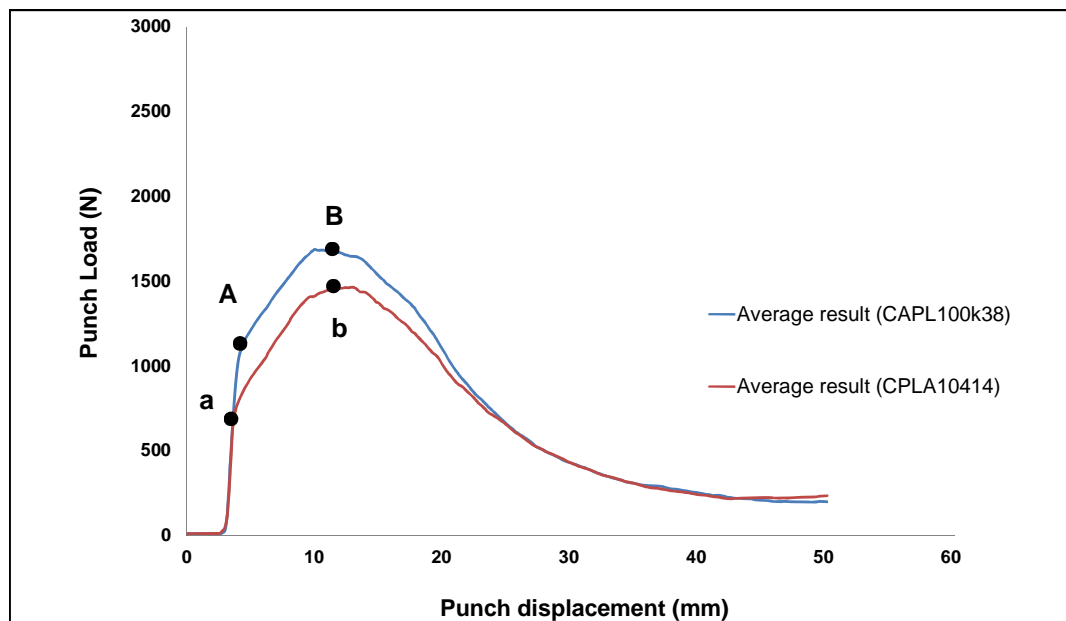


Figure 6.10 Comparison of punch load versus displacement between CPLA100k38 and CPLA10414 aluminium alloy during L-bending

Table 6.1 The relationship between the yield and ultimate stresses and the corresponding punch force for the steel blank materials

Criteria	Materials		Ratio of stresses (high/low)	Punch force (N)		Punch force ratio (A/a or B/b)
	High strength	Low strength				
	DP600	DX54D				
Yield stress (MPa)	405.7	169.5	2.39	A	a	
				1311.3	538.3	2.43
Ultimate stress (MPa)	656.5	296.4	2.21	B	b	
				2269.6	1058.6	2.14

Table 6.2 The relationship between the yield and ultimate stresses and the corresponding punch force for the aluminium blank materials

Criteria	Materials		Ratio of stresses (high/low)	Punch force (N)		Punch force ratio (A/a or B/b)
	High strength	Low strength				
	CPLA100k38	CPLA10414				
Yield stress (MPa)	187.4	113.3	1.65	A	a	
				1089.3	646.6	1.68
Ultimate stress (MPa)	273	240.3	1.14	B	b	
				1686.6	1462.8	1.15

6.2.2.2 Springback after the L-bending process

After each L-bending experiment, the deformed part was removed carefully from the forming rig. Figure 6.11 shows one specimen for each material after removal. It is obvious that much greater springback occurs in the high strength steel specimen compared to the low strength steel. However, it

seems that there is no significant difference in the springback between the high and low strength aluminium deformed parts.

All specimens were carefully measured using the coordinate machine (CMM; Kemco 400) described in Chapter 4. The Kemco machine resolution is 0.001 mm which is sufficient for this kind of application. First the machine was calibrated prior to the measurement. Second, the deformed part was placed and fixed to the platform of the machine as shown in Figure 4.12. Three points were carefully selected for each side of the L-shape by touching a ruby ball on the side of the specimen as shown in Figure 4.12.

Figure 6.13 illustrates an approximate L-shape and the three points that were selected from each side of the sample; straight lines were plotted through these three points for each specimen. Subsequently, the springback angle (θ_L) was measured by determining the angle between line AB and line CD.

The springback results for each specimen are reported in Table 6.3. It can be seen that the variation in the experimental results between specimens was small for each material; for instance, θ_L for the three DP600 specimens was 101.32° , 101.07° and 101.20° respectively. This illustrates the consistency of the experiments. From this table, it is also clear that the amount of springback was much higher for the high strength materials than for the lower strength materials. The highest springback was found for the DP600 (high strength steel), whilst DX54D (low strength steel) had the lowest springback. For the aluminium alloys, although the CPLA10414 is classified as a low strength material, it produced relatively high springback in comparison to the CPLA100k38 (high strength material). The average values of the springback angle for the CPLA10414 and the CPLA100k38 alloys were around 97° and 99° respectively.

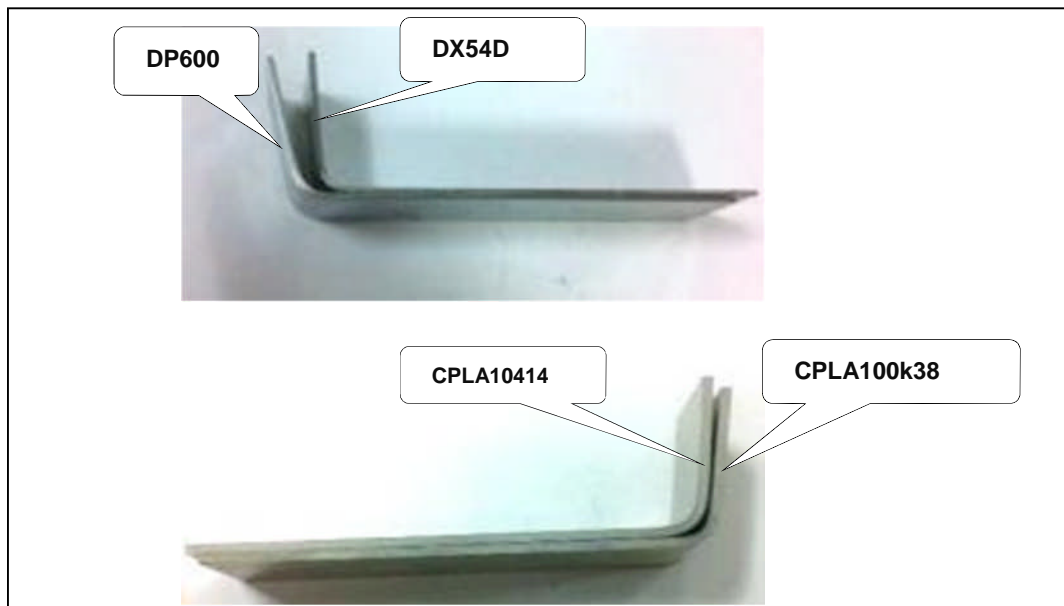


Figure 6.11 The specimens after the L-bending experiments

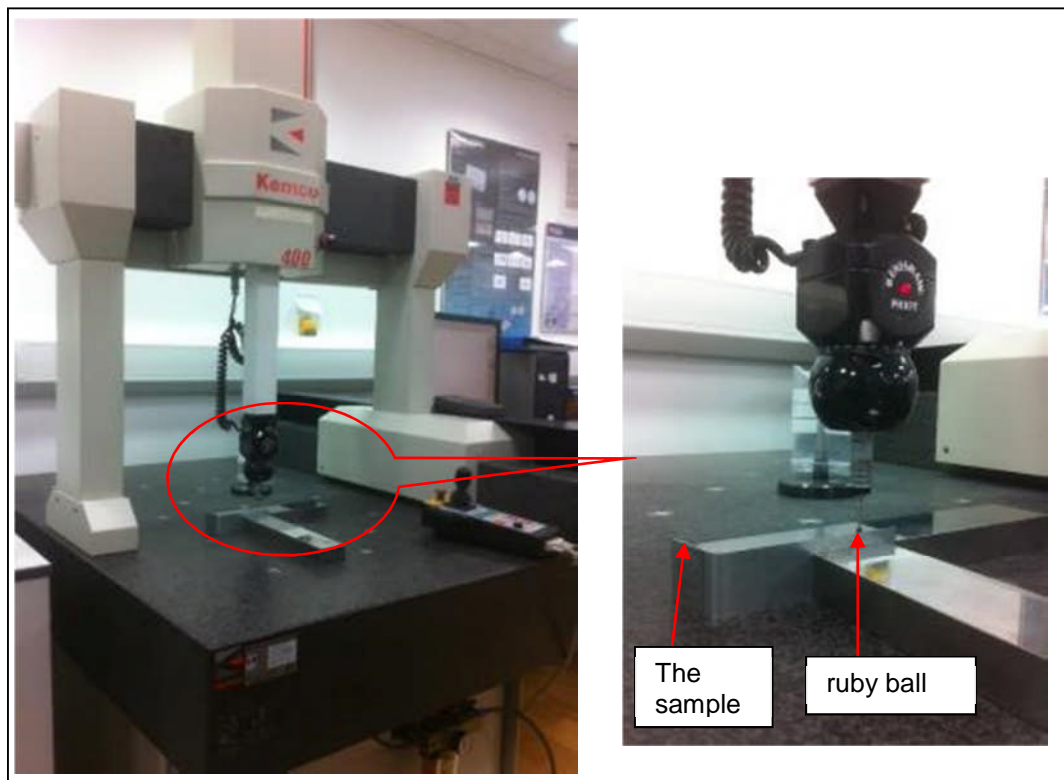


Figure 6.12 Kemco CMM 400 machine set up to measure the L shape profile after springback

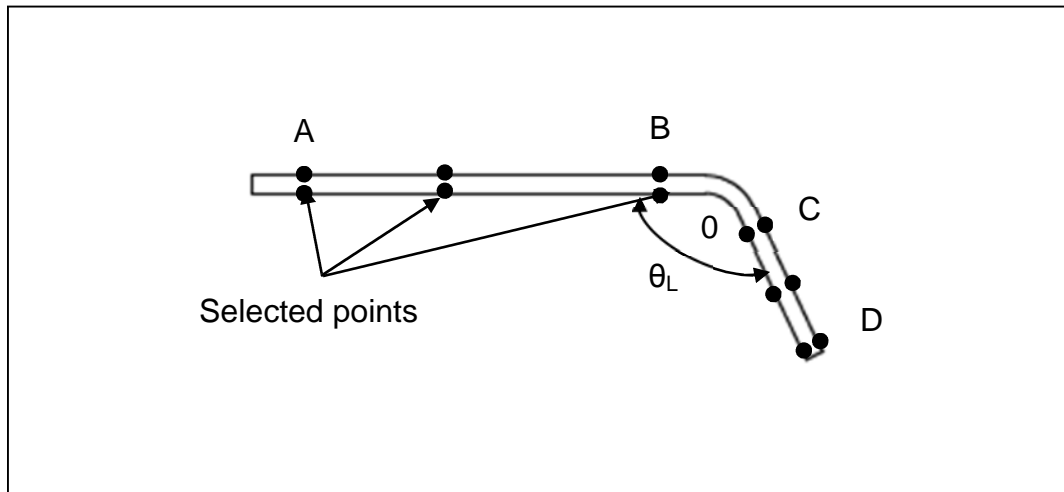


Figure 6.13 Measurement of springback after the L-bending process, showing approximation location of measurement points (θ_L is the measured springback angle)

Table 6.3 The springback angle after L-bending process for all materials

Material	Angle after springback (degrees)	
	Individual	Average
DP600	101.3	101.2
	101.1	
	101.2	
DX54D	93.7	93.7
	93.7	
	93.7	
CPLA100k38	99.4	99.0
	98.7	
	98.9	
CPLA 10414	97.0	96.8
	96.6	
	96.7	

6.3 Numerical analysis of L-bending process and subsequent springback

6.3.1 Finite element model

The L- bending process requires the use of a punch, die, blank and blank holder. As the blank width is much larger than its thickness, the process is modelled using 2D plane strain quadratic shell elements as shown in Figure 6.14. The assumption here is that the strain in the transverse (Z) direction is negligible compared with strains in the in-plane (X-Y) directions.

The punch, die and blank holder were considered to be rigid bodies, while the blank was considered to be a deformable body modelled as a homogenous sheet material (uncoated) with properties as per the Y-U model described in Chapter 3. The geometric parameters listed in Table 6.4 represent the actual geometry utilised in the experiments.

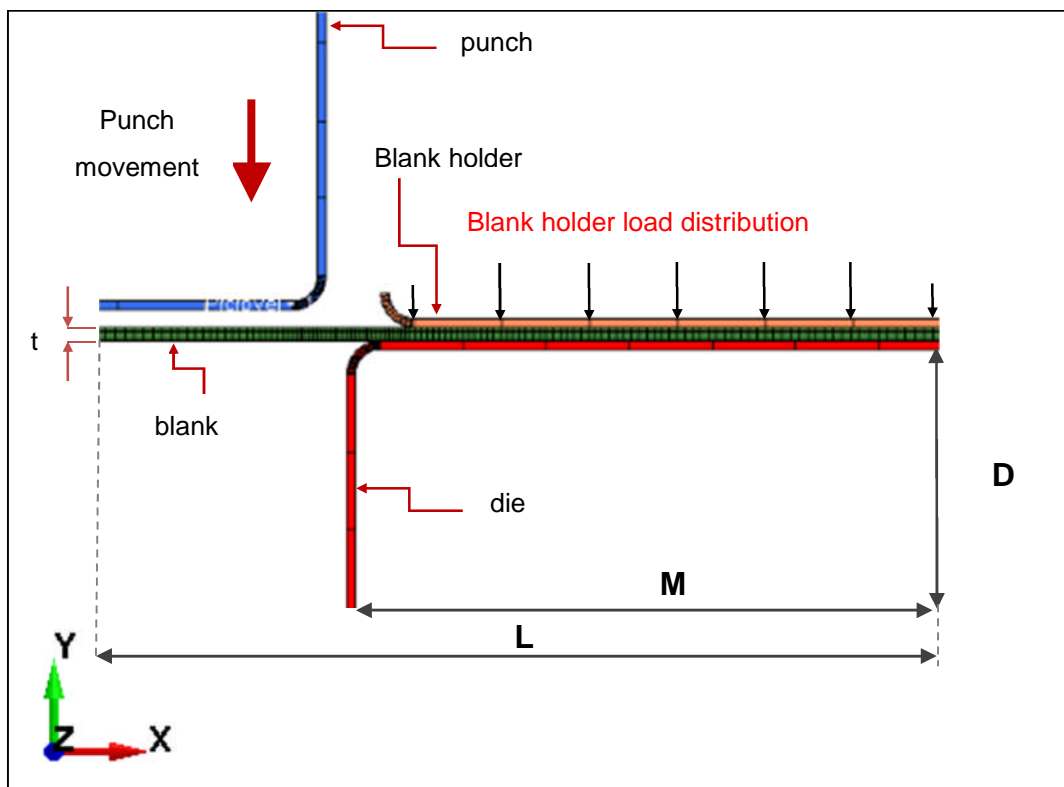


Figure 6.14 L-bending model

Table 6.4 Dimensions of the L-bending model (all dimensions in mm)

Geometrical Parameters	L	D	M	Die and punch radii	Gap	Material	Blank thickness
Dimension (mm)	150	50	112	4	3.5	steel	1.6
						aluminium	2.5

The analysis of springback after the L-bending process requires two sequential operations: loading and unloading. The loading process is initiated as the blank sheet is clamped by the blank holder. Then, the punch is moved down to bend the blank sheet into an L-shape. Subsequently, the unloading process is initiated when the tools are removed from the workpiece. In this study, as mentioned in Chapter 2, the explicit finite element method incorporated in the Ls-Dyna software was used to analyse the L-bending forming process. Then the implicit mode of Ls-Dyna was utilised to calculate the springback that occurs in the blank during the unloading process. In the implicit springback analysis, all constraints were removed from the workpiece leaving it completely free to take up its final deformed shape. Figure 6.15 illustrates the overall numerical methodology used in the current studies for both L-bending and U-drawing process (Chapter 7).

The boundary conditions for analysis of the L-bending process as indicated in Figure 6.14 are:

- The punch is constrained in all rotations and displacement in the X direction but free in the Y -direction.
- The blank holder is constrained in all rotations and displacement in the X direction but free in the Y -direction.
- The die is fixed in all degrees of freedom

The punch was moved at a velocity of 2 mm/s in the Y-direction, producing up to 48 mm of punch displacement. A distributed normal constant force of 1.26 kN was applied to the blank holder in the Y-direction as shown in Figure 6.14. A 2D surface-to-surface contact was used to define the interaction between the punch, die, blank and blank holder components. In this contact definition, the blank holder, punch and die were considered to be the master surfaces and the blank was treated as the slave surface.

The static and dynamic coefficients of friction were as derived from the experimental observations in Chapter 5, under dry or lubricated conditions when the steels or aluminium alloys were simulated as listed in Table 6.5. The material model used was the Y-U model available as material type 125 in Ls-Dyna, with parameters for the four material as defined in Table 3.8.

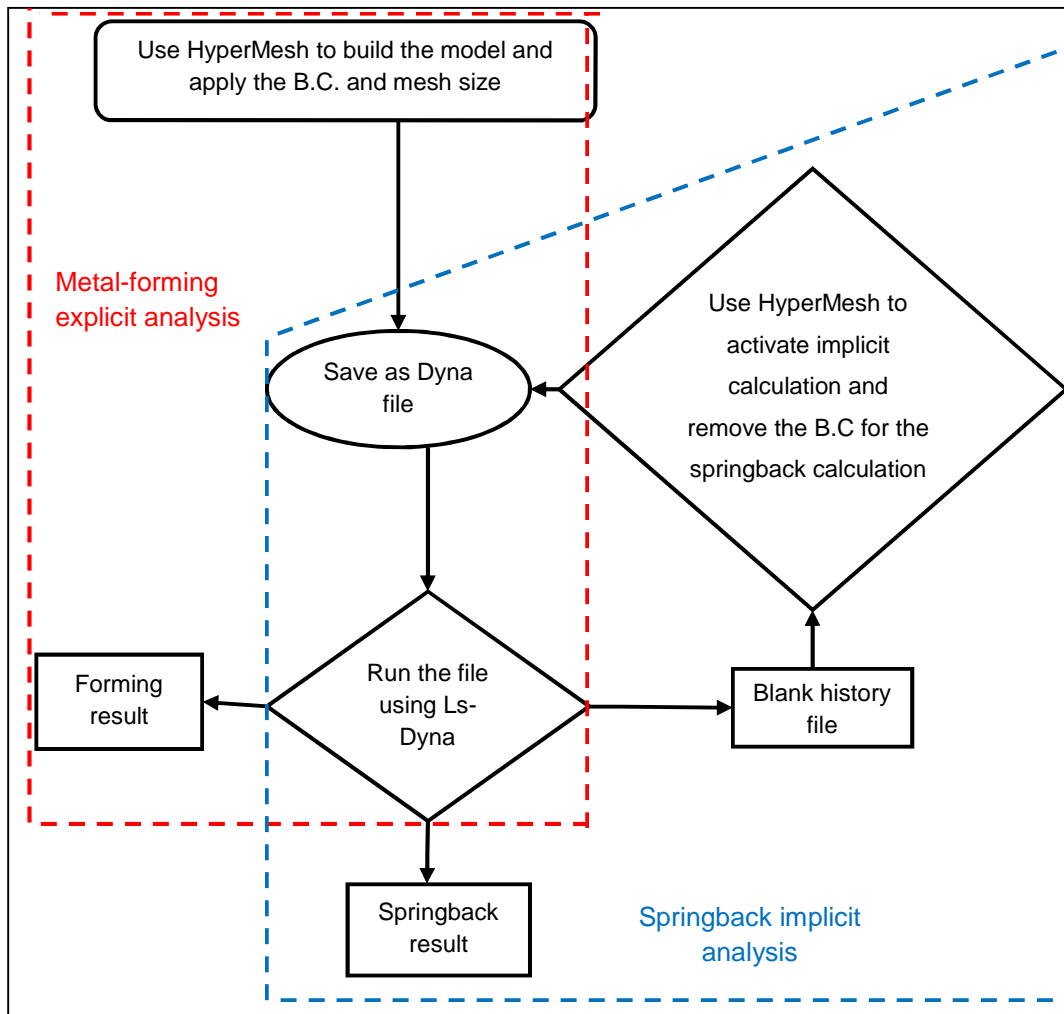


Figure 6.15 Flow chart for the numerical analysis of the L-bending and U-drawing forming processes and springback (B.C. here denotes boundary conditions)

Table 6.5 Static and dynamic friction coefficients assumed for the four materials

Materials	Friction coefficient	
	Static	Dynamic
DP600	0.31	0.25
DX54D	0.29	0.26
CPLA100k38	0.37	0.34
CPLA10414	0.27	0.27

In any finite element analysis, the mesh density is an important parameter to consider when assessing the quality of results produced by a model. A small element size for discretisation of the blank provides more precise results. On the other hand, a finer mesh leads to increased computation time. During the L-bending process, only a certain area of the blank in the region of the bend experiences severe stress, whilst the remainder of the blank is relatively stress-free.

Therefore, this study has developed a blank model for the L-bending process as shown in Figure 6.16. The most important region in the blank is the one that undergoes severe material distortion due to the bending around the die corner. Therefore, constant and small elements sizes were created along a 15 mm section of the blank length that undergoes this severe bending as shown in Figure 6.16. The element size was then gradually increased away from the bend region as there is much less blank material deformation in these regions. Each type of blank material had its blank mesh model validated by comparison with the experimental results as explained below.

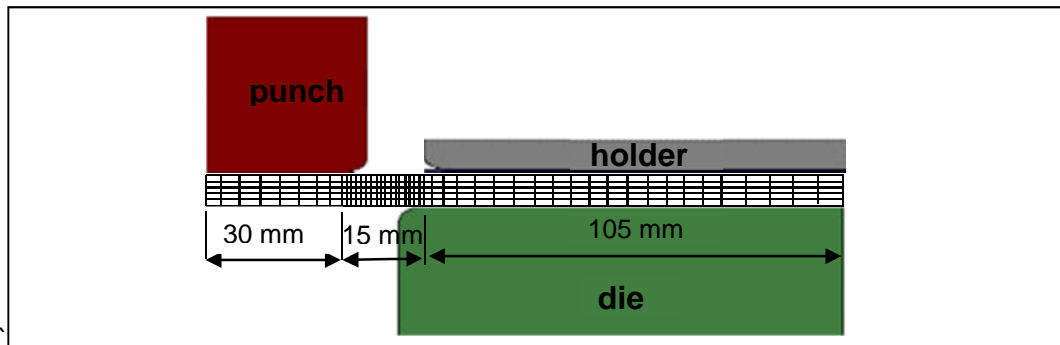


Figure 6.16 Typical finite element mesh showing high mesh density around the bend area of the blank

6.3.2 Mesh sensitivity study

A mesh sensitivity study was carried out by increasing the number of blank elements, taking into account the basic blank mesh model shown in Figure 6.16. Two aspects were considered to verify the numerical results: the punch force versus displacement curve during the forming process and the springback after the forming process. Each material behaved differently; for instance, for the steel material, 2340 elements were sufficient to achieve a converged springback result as shown in Figure 6.17. The element size in the 15 mm length section of the blank was 0.25×0.25 mm and this mesh was used for all the subsequent investigations for both steel materials.

However, for the aluminium materials, more elements (5369 elements) were required to achieve converged results with an element size of 0.25×0.25 mm in the bend region.

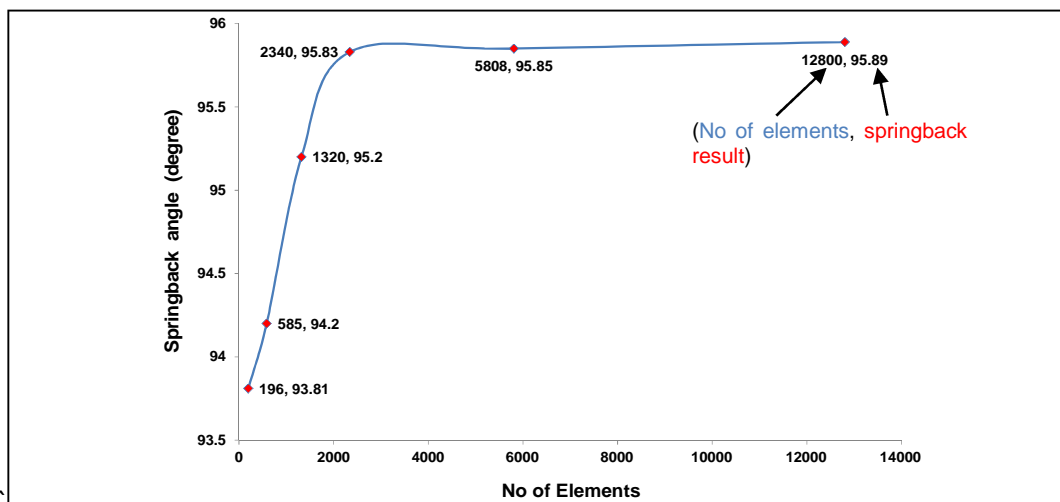


Figure 6.17 Number of elements used in the blank model versus the springback for DP600 steel

6.3.3 The effect of the degradation of Young's modulus

As has been reported in [66], the Young's modulus is degraded after application of a reverse plastic stress for most metals and alloys. Therefore, in this project two kinds of numerical analysis were considered; one assumed a constant Young's modulus equal to the initial value and the second assumed a decreasing Young's modulus. The degradation of the Young's modulus with effective plastic strain was determined using the following expression introduced in Chapter 3:

$$E = E_o - (E_o - E_a)(1 - e^{-\gamma p}) \quad (6.1)$$

in which E_o and E_a denote Young's modulus for the elastic and large plastic strain regimes respectively and γ is a material constant. In the current study the L-bending model was run assuming both a constant and a varying Young's modulus. The Young's modulus reduction parameters listed in Table 3.3 for each material were used in the current study.

Figure 6.18 shows the predicted and measured springback with and without the degradation of the Young's modulus for the steel materials. Although there was a significant difference between the experimental and numerical prediction of the springback for the coated DP600 high strength steel as explained below, there was a clear difference in the springback when a reduction of the Young's modulus was assumed and when it was constant. However, the difference for the low strength steel was much less.

On the other hand, Figure 6.19 shows there was a significant difference when a reduction of the Young's modulus was assumed and when this effect was ignored for the aluminium materials. Very much better agreement between the experimental and numerical results of the springback for the aluminium blanks was obtained when a reduction in modulus was assumed.

Other researchers have investigated the influence of the reduction of material stiffness on the springback prediction using similar numerical models. They achieved good agreement between the numerical and experimental results [67] when a reduction of Young's modulus was

assumed. This shows the importance of including the reduction of the Young's modulus in the numerical analysis of springback after the L-bending process. Therefore, the degradation of the Young's modulus was taken into account for all four materials in all subsequent simulations of the L-bending process.

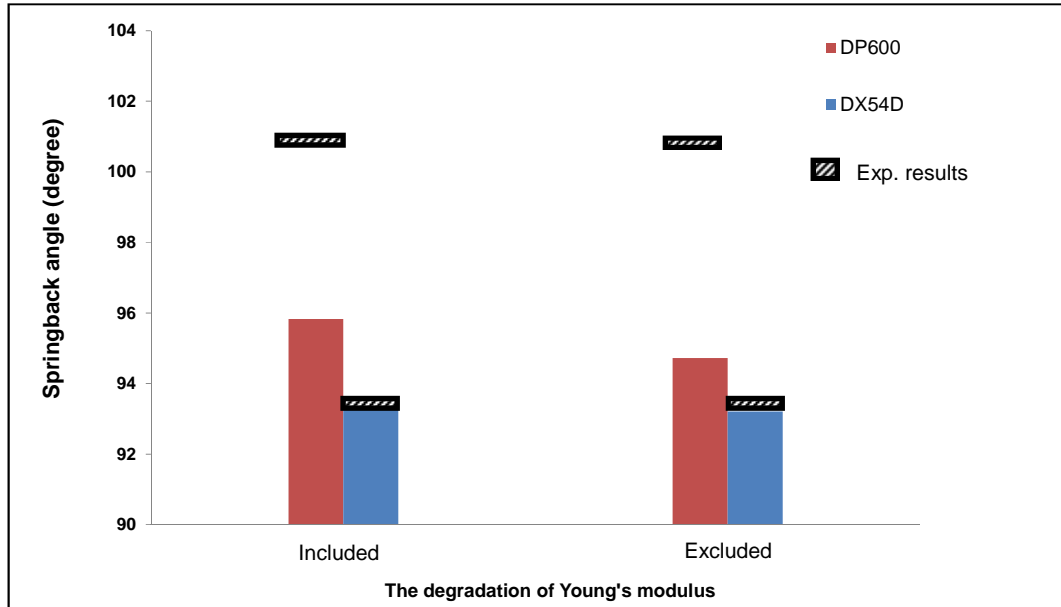


Figure 6.18 The L-angle after the springback with and without consideration of elastic stiffness degradation for steel materials.

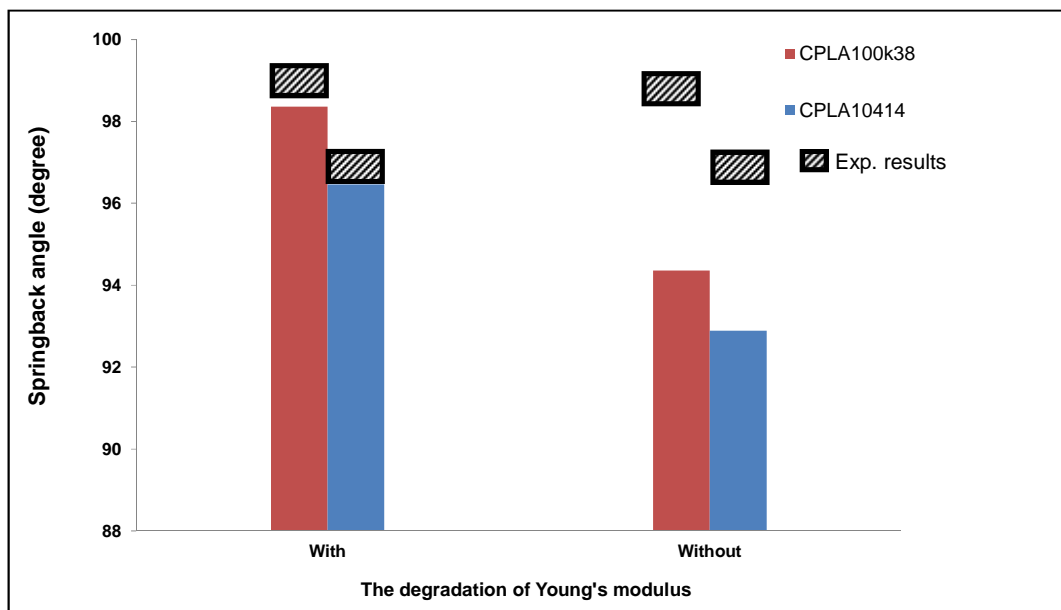


Figure 6.19 The L-angle after the springback with and without consideration of elastic stiffness degradation aluminium materials.

6.3.4 Comparison of numerical and experimental results

The numerical and experimental punch force against displacement curves during the L-bending process for all four materials are compared in Figures 6.20-6.23. Figure 6.20 illustrates a significant difference between the experimental and numerical punch force-displacement curves for the DP600 steel. The difference in behaviour was thought to be due to the thin coating of zinc that was present on the samples of the DP600 used in the experiments. The presence of the coating stiffens the blank but the coating was not modelled in the simulation. The influence of the coating on the DP600 blank maximum load is further explained below. However, for the other three blank materials, the numerical results were in very good agreement with experiment as shown in Figures 6.21 to 6.23.

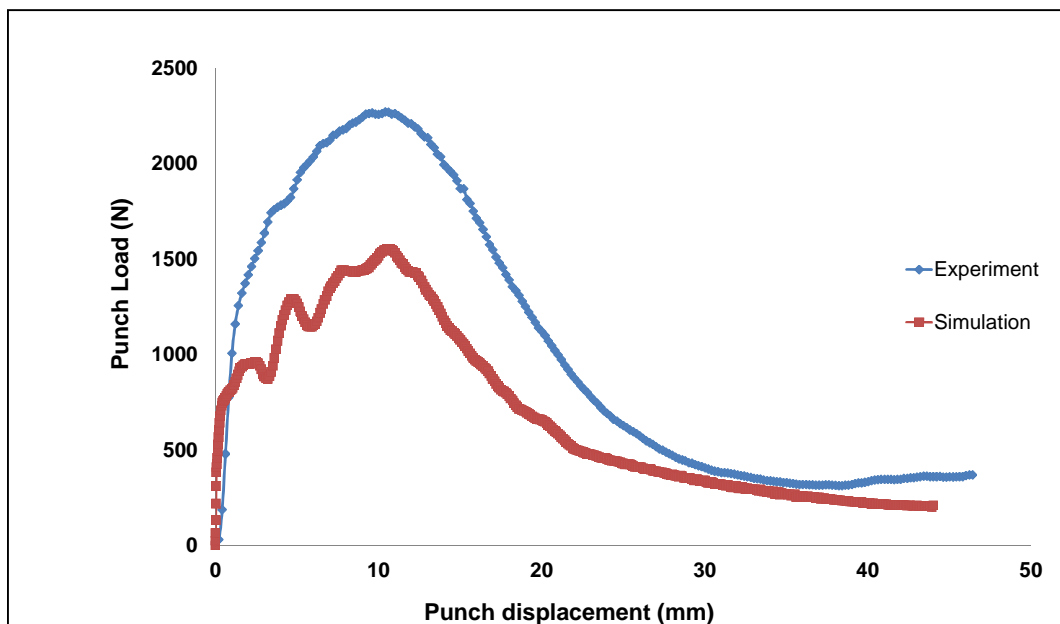


Figure 6.20 Experimental and numerical punch load versus displacement curves for the high strength steel (DP600)

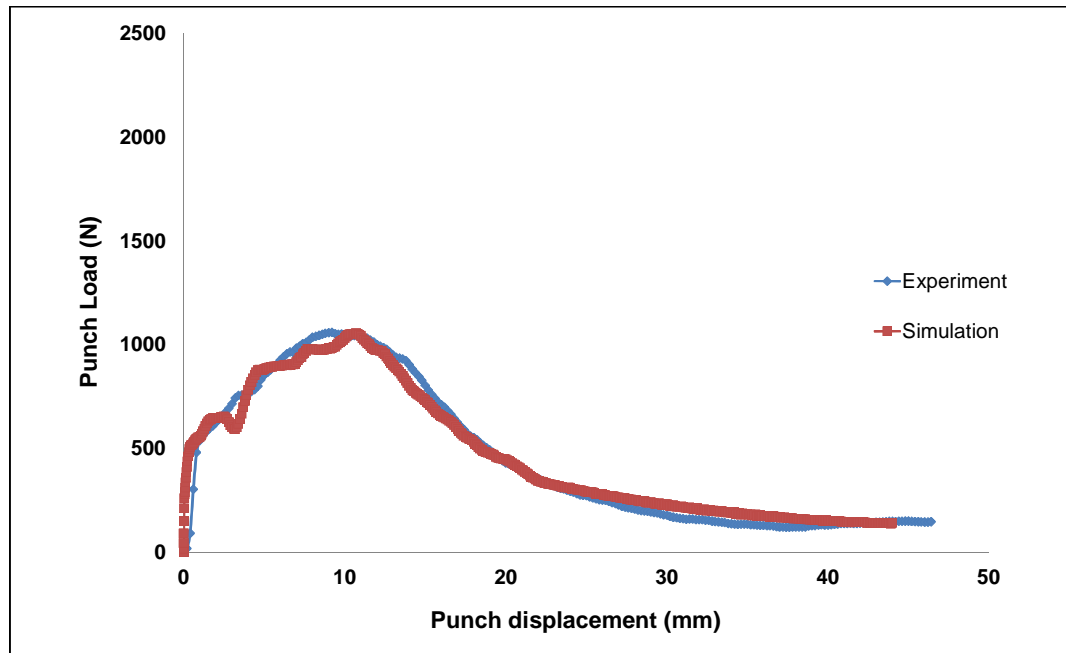


Figure 6.21 Experimental and numerical punch load versus displacement curves for the high strength steel (DX54D)

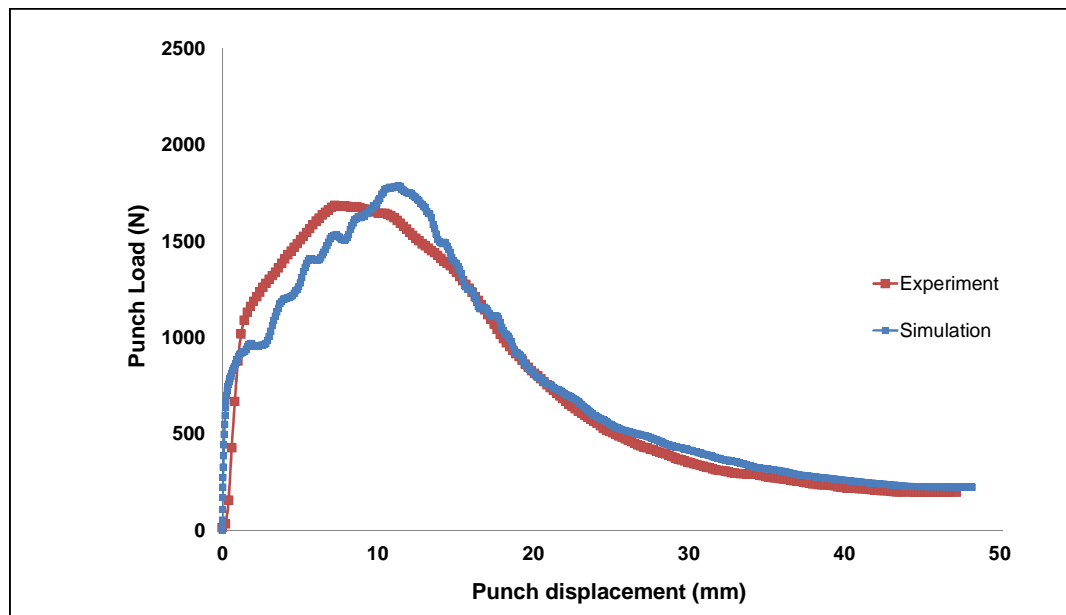


Figure 6.22 Experimental and numerical punch load versus displacement curves for the high strength aluminium (CPLA100k38)

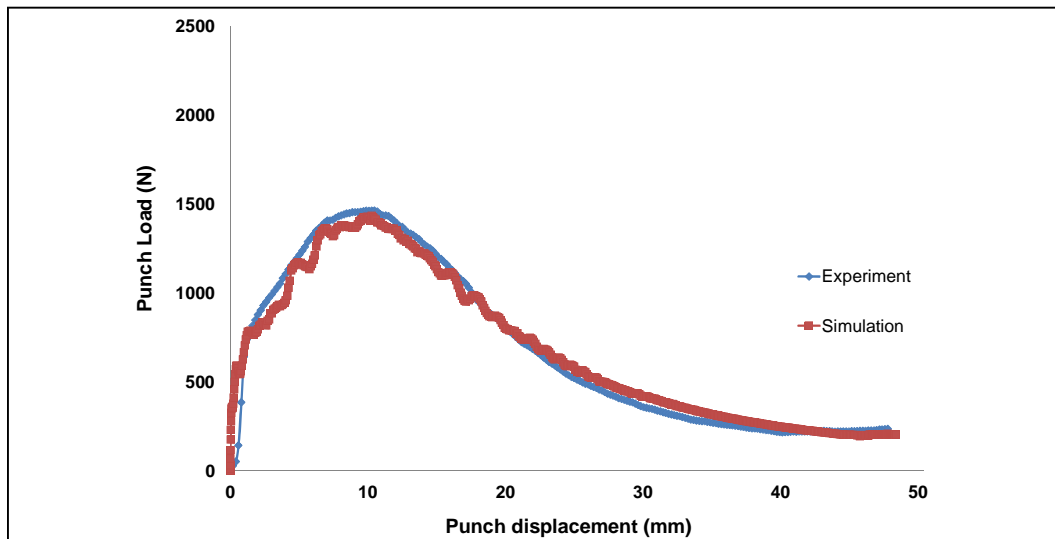


Figure 6.23 Experimental and numerical punch load versus displacement curves for the high strength aluminium (CPLA10414)

Table 6.6 contains the experimental and numerical results of the springback angle after L-bending for each material. The error between the experimental and numerical results was calculated using equation (6.2):

$$\text{Error} = \left(\frac{\theta_{LExp} - \theta_{LNum}}{\theta_{LExp}} \right) \times 100\% \quad (6.2)$$

where θ_{LExp} and θ_{LNum} are the experimental and numerical springback angles respectively.

It can be seen from Table 6.5 that the maximum error was found for the DP600 steel for reasons explained below. The aluminium parts achieved good correlation between the experimental and the numerical results, with errors of only around 0.2%.

The large difference between the experimental and the simulation springback angles for the DP600 specimens is thought to be due to the effect of the hot dipped galvanised zinc coating present on this material. In [68], it was stated that a zinc coated steel experiences plastic instability, fracture and formation of cracks within the coating and a lack of adherence between the coating and the substrate. The hot dipped galvanised zinc

coating was found to have a significant influence on the strain path when the coated steel undergoes large plastic bending due to the presence of the zinc coating on the surface which is brittle [68, 69]. This effect is not apparent in the tensile tests conducted to measure the parameters of the Y-U model but its effect is much more significant in the L-bending tests where the outer surface layers of the DP600 specimens are subjected to the maximum strain.

Table 6.6 Experimental and numerical springback angle after L-bending process for all 4 materials

Material	Angle after springback (degrees)		Error (%)
	Experiment	Simulation	
DP600	101.2	95.8	5.3
DX54D	93.7	93.4	0.4
CPLA100k38	99.0	98.8	0.2
CPLA 10414	96.8	96.5	0.2

The mechanical properties of hot dipped galvanised zinc coated steel have been investigated in [69]. It was found that the yield strength of the coated layer is higher than the uncoated steel and its effect varies with the coating thickness. Furthermore it was found [70] that the springback after the V-bending process increases with the increase of the coating thickness as shown in Figure 6.24.

The difference in the springback angle after L-bending between experimental and numerical prediction was also measured in [71] for KLF125 copper alloy with a nickel coating as shown in Figure 6.25. The above explanation of the influence of the hot dipped galvanised zinc coating on the springback after L-bending process suggests a further investigation of how to model the behaviour of the coating layer with the substrate. However, this was considered to be outside the scope of the present work.

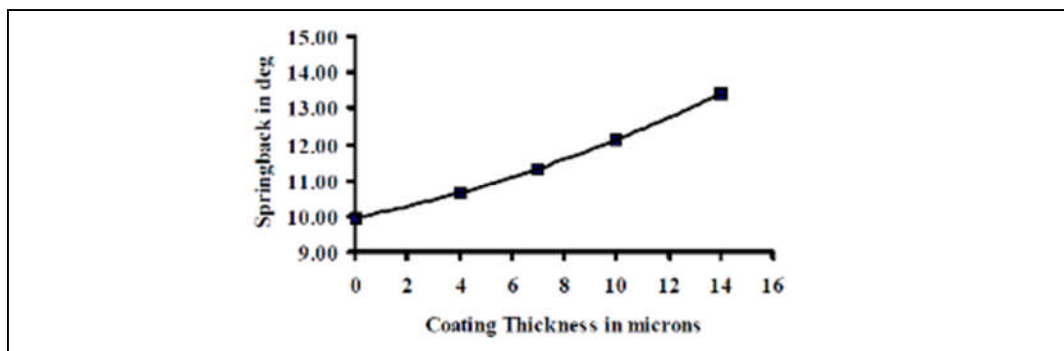


Figure 6.24 The effect of galvanised steel coating thickness on the springback after V bending [70]

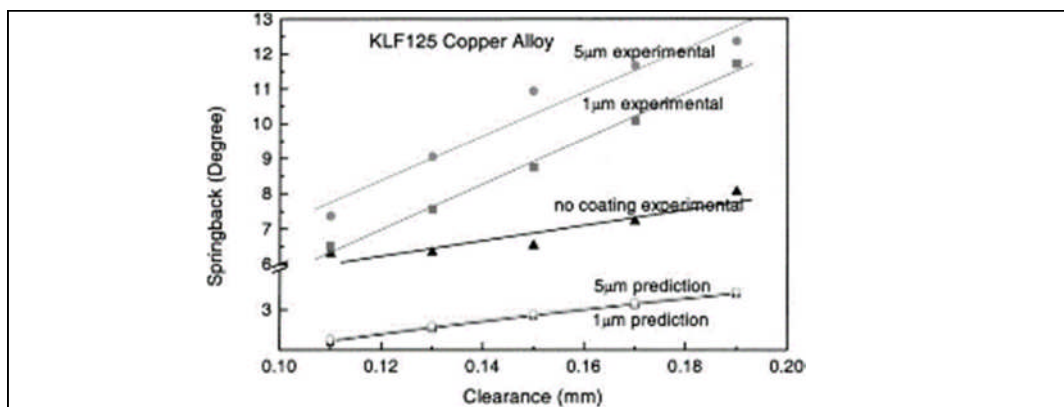


Figure 6.25 Comparison of the experimental and numerical analysis of the springback after L-bending for copper alloy with nickel coating compared with uncoated alloy [71]

6.4 Parametric study

As mentioned in the literature review, there are a number of factors that influence the degree of springback after the L-bending process. In this project, important parameters such as die radius, punch radius, clearance, blank holder force, and blank thickness were investigated as described below. The baseline values of the geometric parameters were the same as listed in Table 6.4 . Only one parameter was varied at a time with other parameters remaining as defined in Table 6.4.

6.4.1 The effect of the die radius

In this study the die radius was varied at five levels of 4, 6, 8, 10 and 12 mm for each of the four materials. Figure 6.27 shows that for all tested materials the smaller the die radius, the lower the springback that occurs after the L-bending process. This is due to the fact that deformation occurring around the bend area is larger for the minimum die radius. This is shown in Figure 6.26 which illustrates the plastic strain distribution within the bent zone for the DP600 blank. This figure shows that the maximum plastic strain occurred in the blank when the die radius was 4 mm.

Figure 6.27 shows that the springback angle for the DP600 increases from 95.8 to almost 98.5 degrees for increase of die radius from 4 to 10 mm. However, there was much lower increases in springback for DX54D where the springback angles were 93.4 and 93.8 degrees for die radii of 4 and 12 mm respectively.

The springback for the aluminium materials behaved quite similarly; here the springback angle increased significantly with increase of the die radius of 4 to 8 mm but then increased only slightly as the die radius was increased up to 12 mm as shown in Figure 6.27. Therefore, in conclusion, the minimum springback for all materials occurs when die radius is set at the minimum value considered of 4 mm.

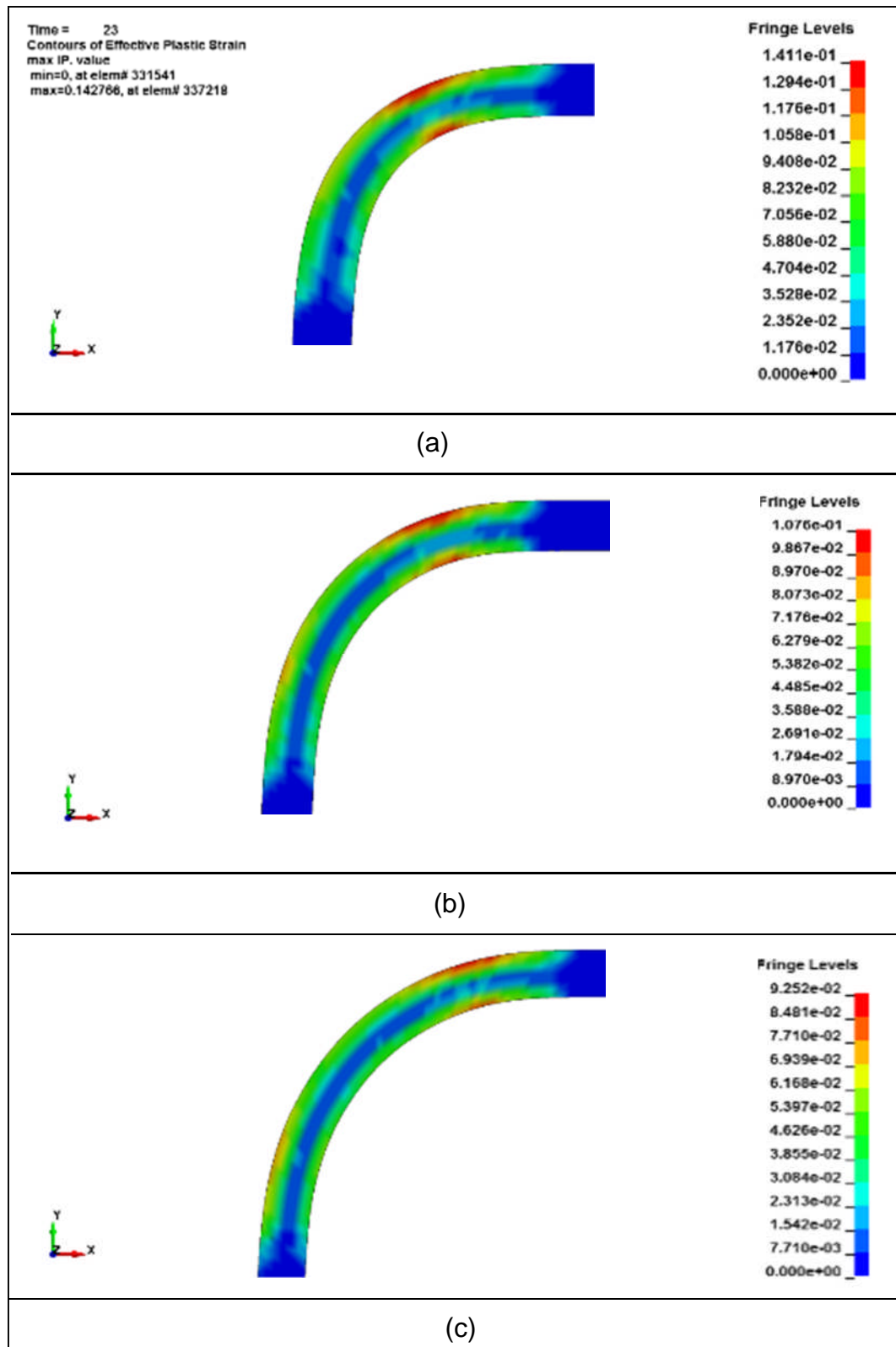


Figure 6.26 The effective plastic strain distribution within the DP600 blank for three different die radii (a) 4 mm (b) 6 mm and (c) 8 mm

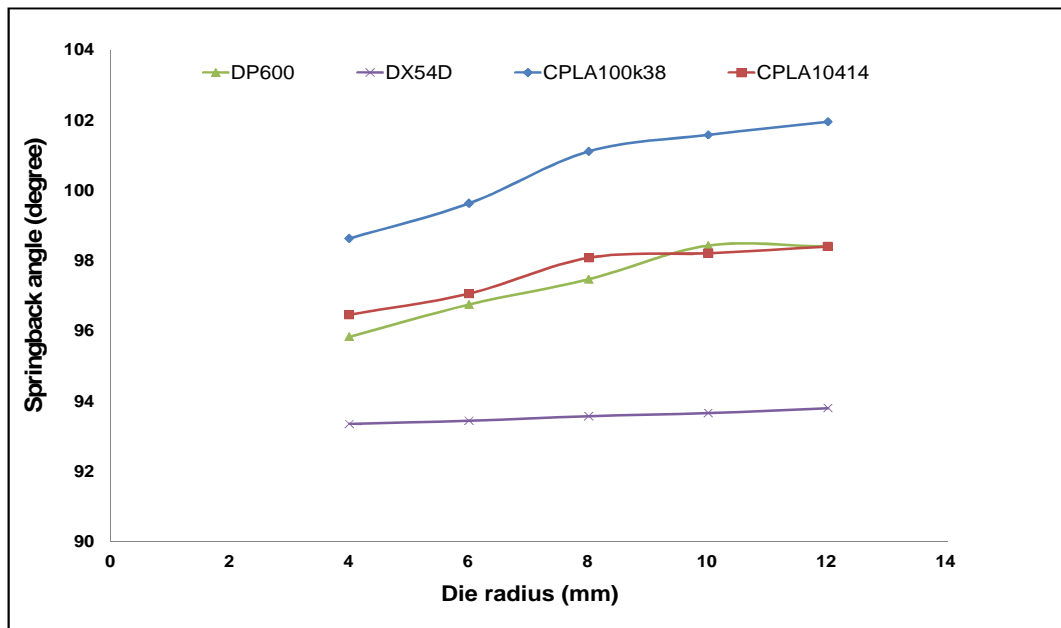


Figure 6.27 The effect of the die radius on the springback angle after L-bending for the different materials

6.4.2 The effect of clearance

For the steels, the gap between the forming tools was varied from 1.8 to 3.5 mm which gave a clearance varying from 0.2 to 1.9 mm. On the other hand the gap for the aluminium specimens was varied from 2.8 to 4 mm which gave a clearance varying from 0.3 to 1.5 mm. Figure 6.29 shows that the springback angle increases approximately linearly with increase in clearance for all tested specimens. However, for the aluminium samples, the rise was linear until 1 mm of clearance and then increased only slightly up to 1.5 mm of clearance. The minimum springback angle was only slightly greater than the target angle of 90° , for DX54D at a clearance of 0.2 mm as shown in Figure 6.29. However, for the other materials the minimum springback angle varied from 92.86° for DP600 to 96.85° for CPLA100k38 at the minimum clearance. Figure 6.28 illustrates the plastic strain distribution within the bend area of the DP600 blank. The figure clearly shows that the maximum plastic strain was associated with the minimum clearance although the differences in the value of the maximum strains predicted were quite small.

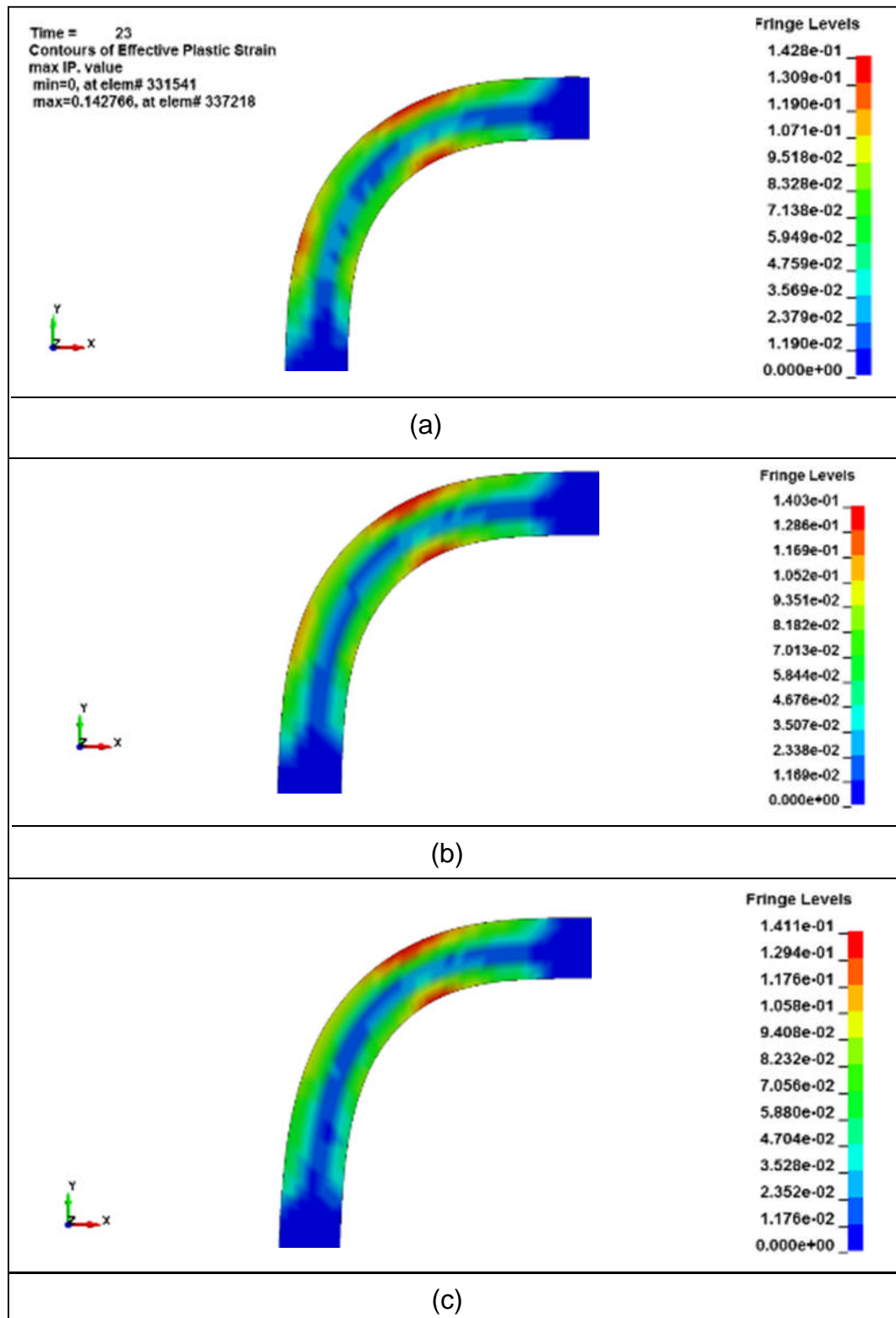


Figure 6.28 The effective plastic strain distribution on the DP600 blank for three different clearness (a) 0.2mm (b) 0.4 mm and (c) 0.9 mm

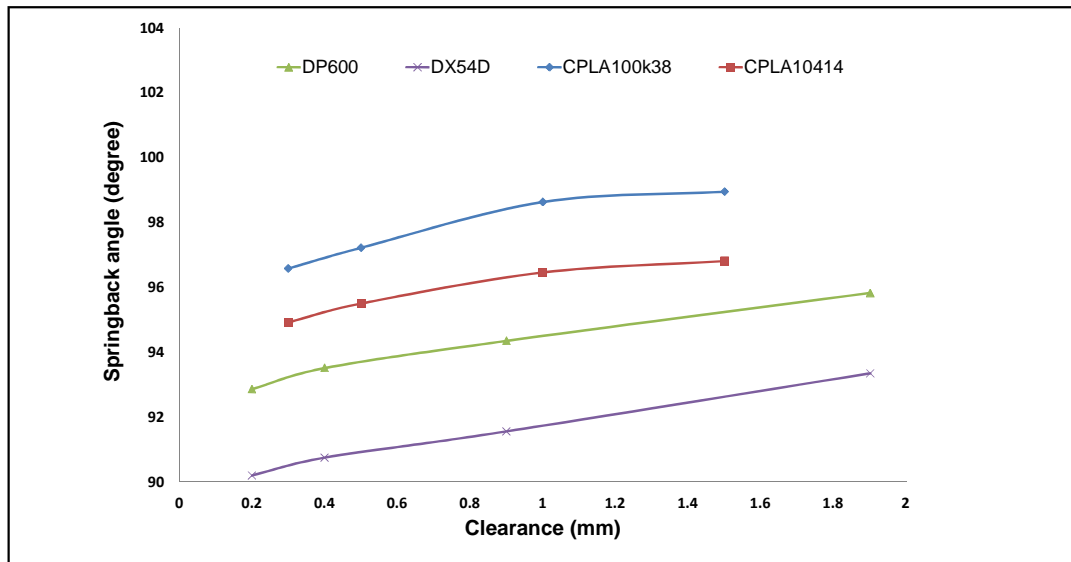


Figure 6.29 The effect of the clearance on the springback angle after L-bending for the different materials

6.4.3 The effect of the punch radius

Four punch radii were considered in the current investigation: 4, 6, 8, 10 and 12 mm. Figure 6.30 shows that the effect of the punch radius is relatively small, with the springback angle increasing only slightly with increase in the punch radius. For instance, by increasing the punch radius from 4 mm to 12 mm, the springback angle increased by only about half a degree for the aluminium materials and by about one degree for the steel blanks.

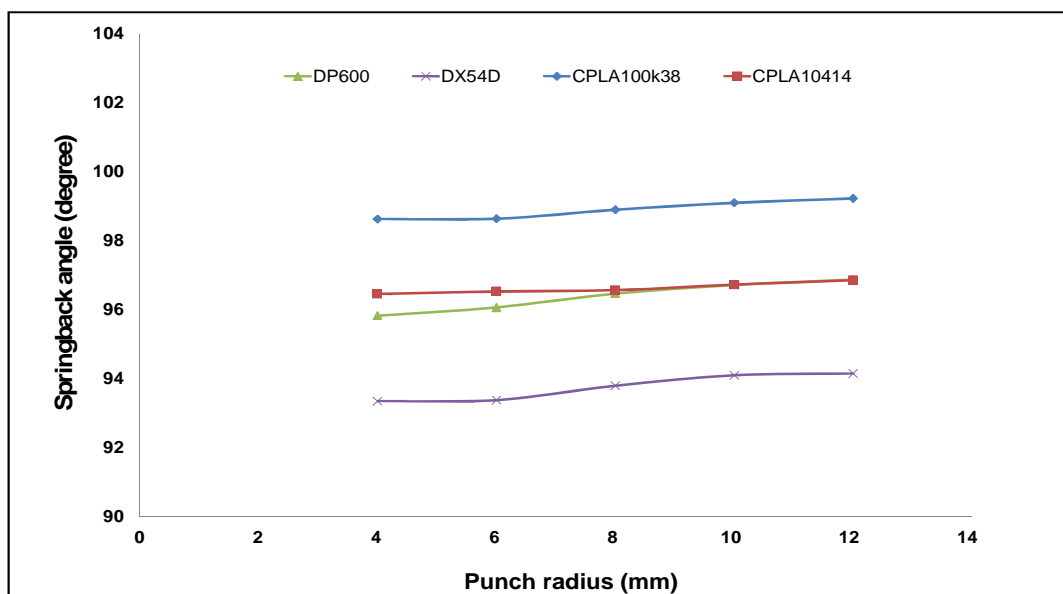


Figure 6.30 The effect of the punch radius on the springback angle after L-bending for the different materials

6.4.4 The effect of the blank holder force (BHF)

In these simulations, four different pressures were applied to the blank holder to simulate total blank holder forces of 0.6, 1.2, 2.4 and 4.8 kN. The influence of the blank holder force on springback was small for all the four blank materials considered. The general tendency was for the springback angle to reduce with increasing BHF except for the low strength DX54D steel where a slight increase in springback was observed with increase of the blank holder force. Figure 6.31 illustrates that the maximum plastic strain increased from approximately 0.12 to 0.14 as the BHF was increased from 0.6 to 1.2 kN for the DP600 blank.

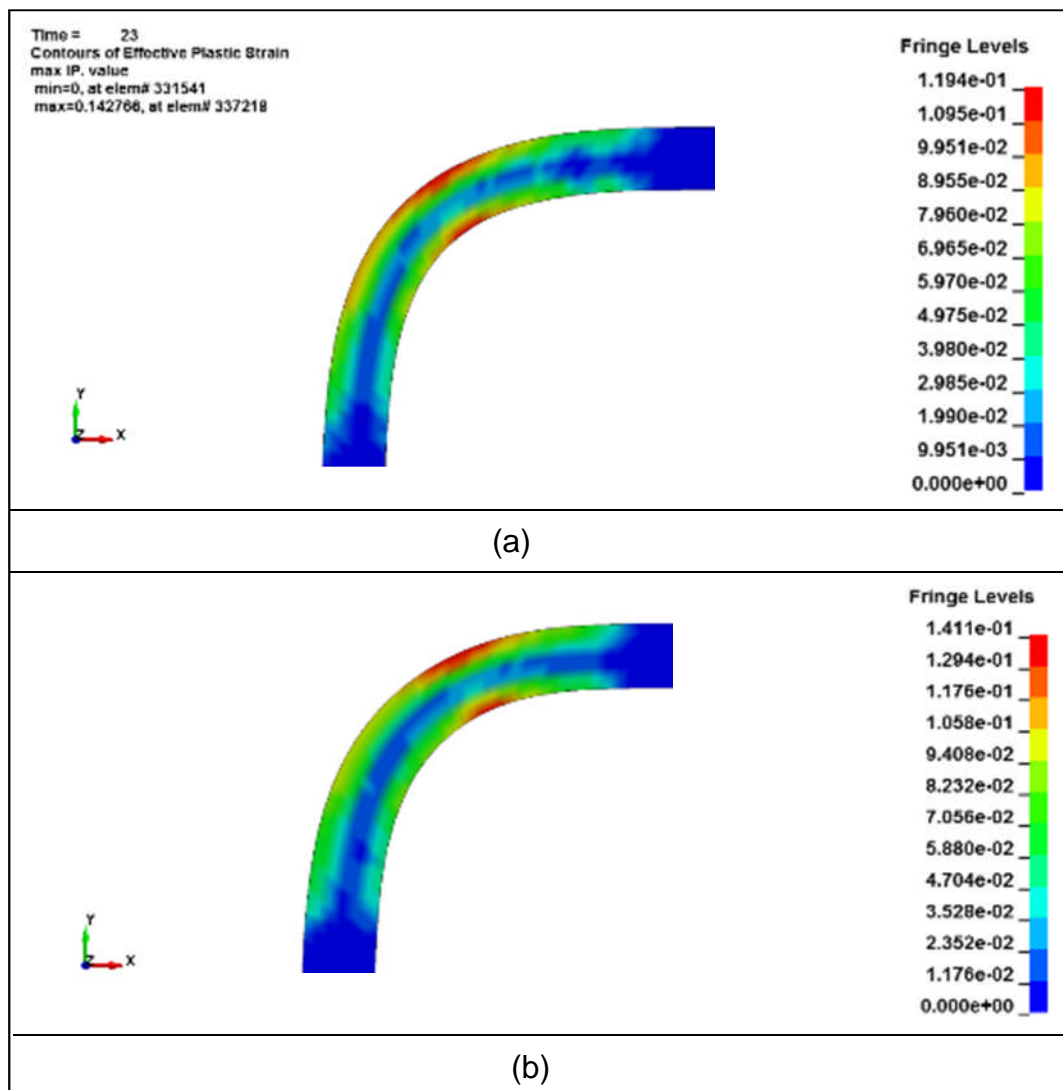


Figure 6.31 The effective plastic strain distribution on the DP600 blank for two different blank holder loads (a) 0.6 kN and (b) 1.2 kN

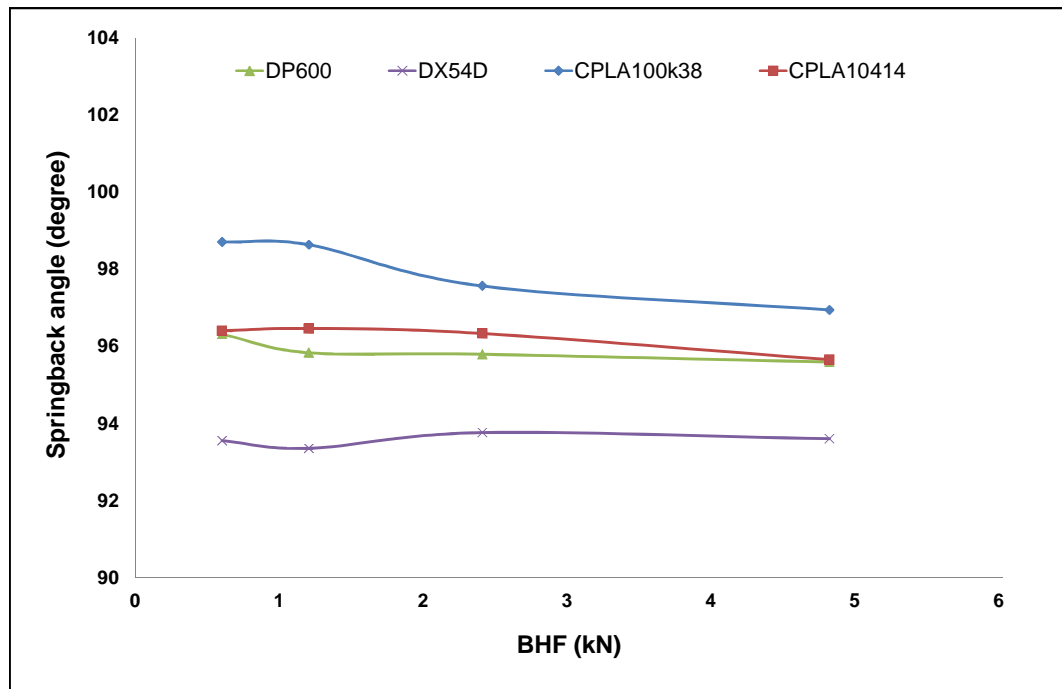


Figure 6.32 The effect of BHF on the springback angle after L-bending for the different materials

6.4.5 The effect of the blank thickness

Three blank thicknesses, 1.6, 2 and 2.5 mm, were used to investigate the influence of the blank thickness on the level of the springback after the L-bending process. Figure 6.34 shows a negative relationship between the blank thickness and the magnitude of the springback. It was found for all materials that the springback decreases for the thicker specimens. Similar observations were made in [72] and [73].

Figure 6.33 shows the plastic distribution contour for the three blank thicknesses of high strength aluminium (CPLA100k38). It illustrates clearly that the highest plastic strains were predicted for the thicker plates, which usually results in lower springback.

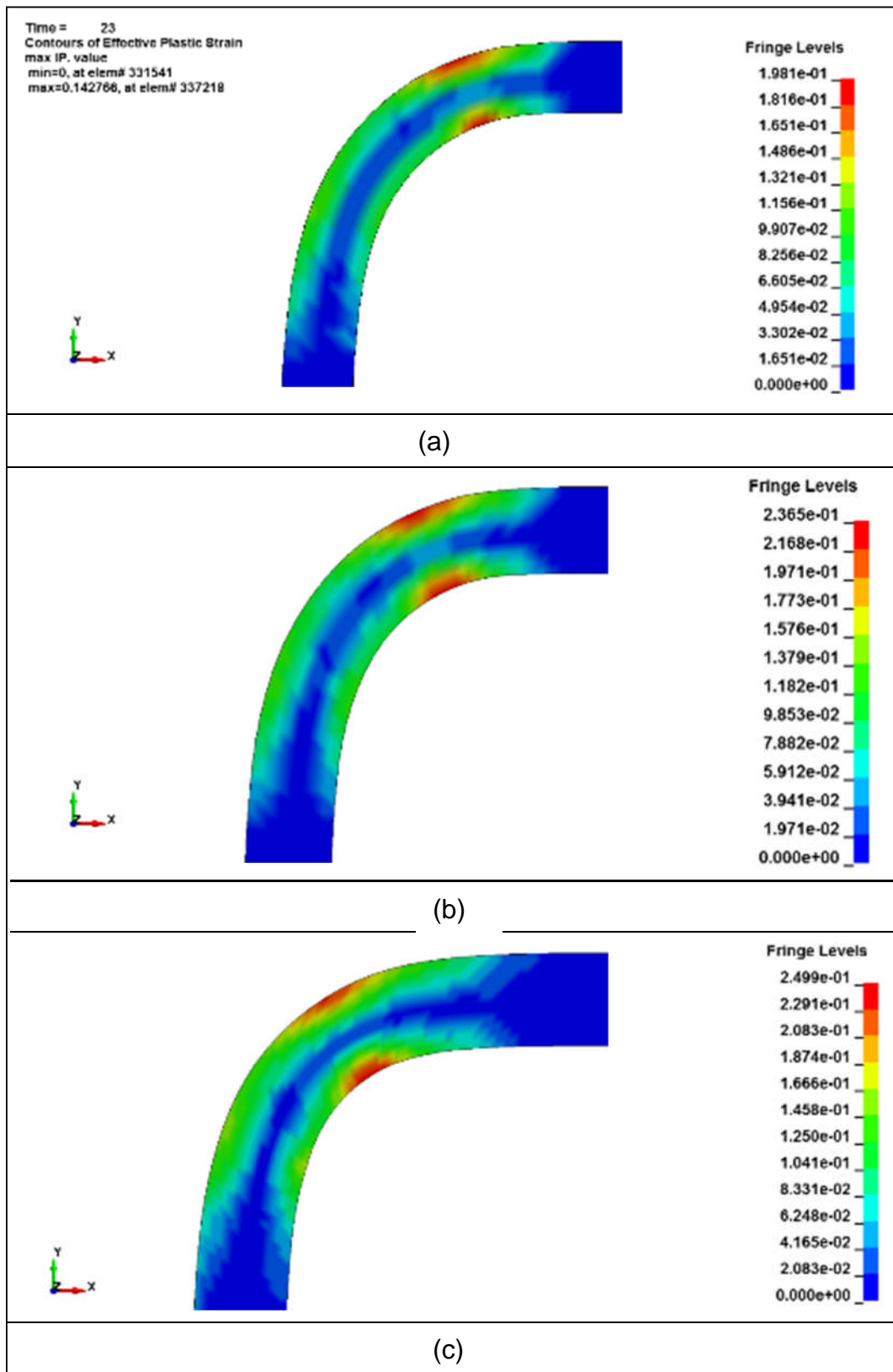


Figure 6.33 The effective plastic strain distribution within the CPLA100k38 blank for three different blank thicknesses (a) 1.6 mm (b) 2 mm and (c) 2.5 mm

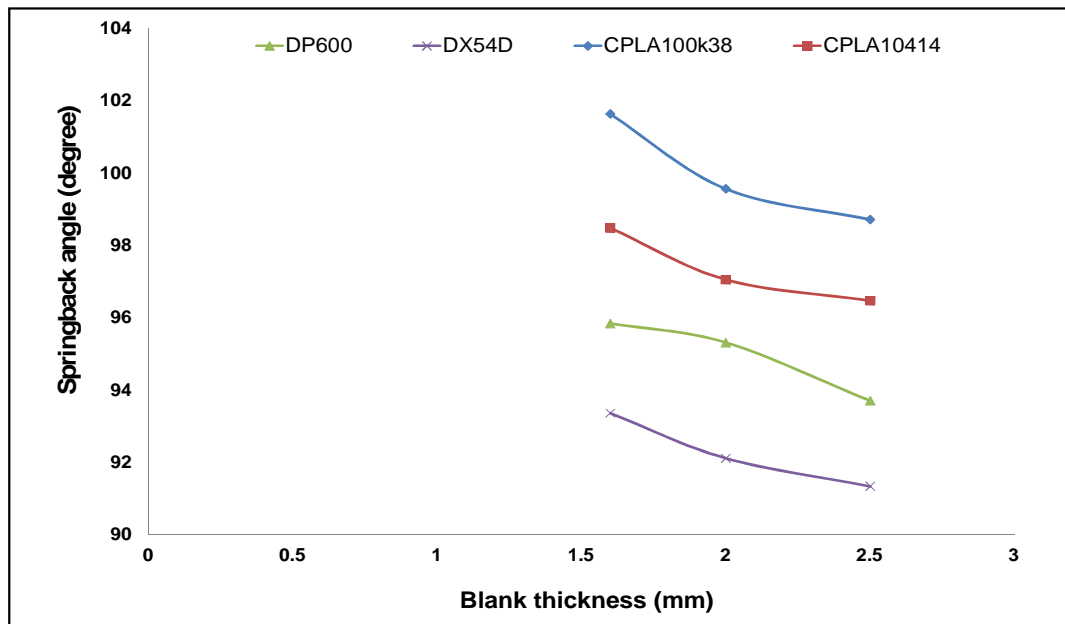


Figure 6.34 The effect of the blank thickness on the springback angle after L-bending for the different materials

6.5 Discussion

To understand more about the behaviour of the blank material during the L-bending process, a cantilever beam subjected to a transverse load at its free end was considered. This load generates a maximum bending moment at the fixed end. The generated moment (M) is the product of the applied load (F) and the length of the beam (l) as shown in equation (6.3):

$$M = F \cdot l \quad (6.3)$$

In the present application, the distance (l) can be considered to represent the sum of the punch and die radii together with the gap between the punch and the die. Therefore, large radii and large gap between the forming tools are associated with a large bending moment. By assuming the same moment is needed at the fixed end to plastically deform the specimen, the force required to achieve that moment is decreased by increasing the distance (l). For example, from Figure 6.35, F_2 is expected to be lower than F_1 to generate the same moment (M) at the fixed end.

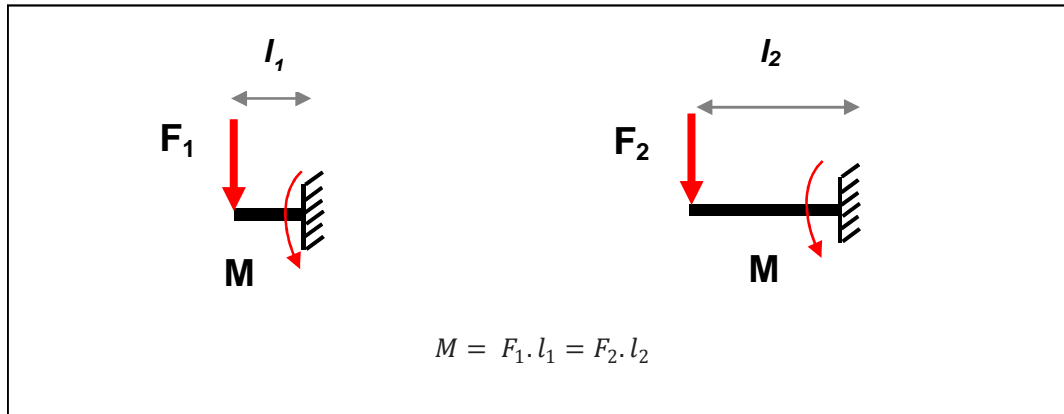


Figure 6.35 Simplified beam model representing the gap and the punch and die radii as distance (l_1 or l_2)

At any point in a plastically-deforming material, the total strain is given by:

$$\varepsilon_t = \varepsilon_e + \varepsilon_p \quad (6.4)$$

in which ε_e , ε_p and ε_t are the elastic, plastic and total strains respectively. Figure 6.36 illustrates 2 points on a general stress-strain curve. From this figure, the following expression (6.5) is always true.

$$\left(\frac{\varepsilon_e}{\varepsilon_t}\right)_1 > \left(\frac{\varepsilon_e}{\varepsilon_t}\right)_2 \quad (6.5)$$

Elastic and plastic strains are greatest within the bent area of the blank specimens. From understanding of the mechanism of the springback, the magnitude of springback that occurs after L-bending is proportional to the ratio of the elastic strain to the total strain. For example, the springback for a deformed blank in which the total strain is at point (1) shown in Figure 6.36 is likely to be larger than the springback from point (2).

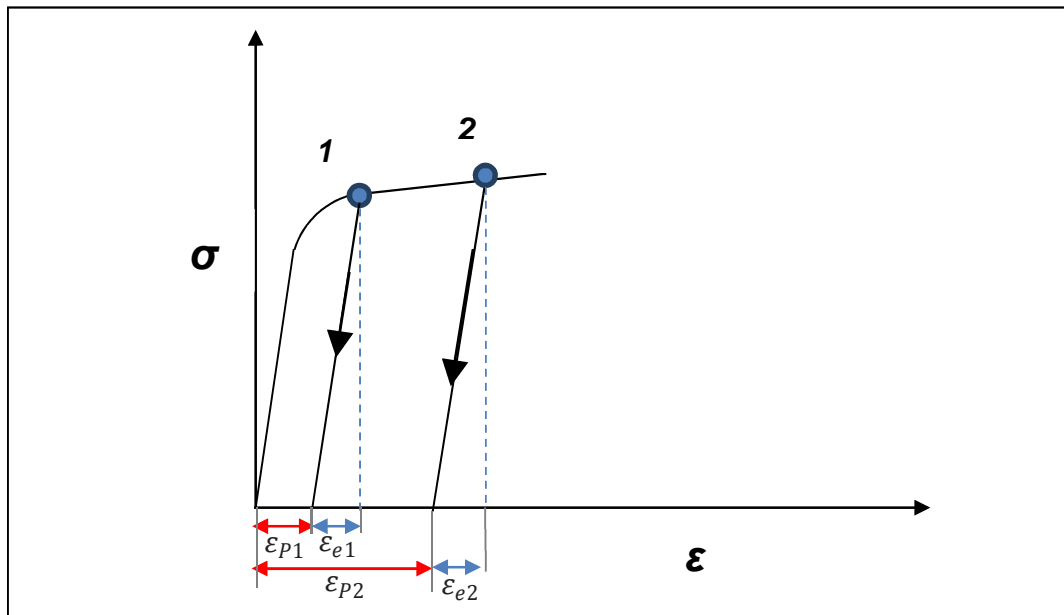


Figure 6.36 A general schematic of elastic-plastic stress strain curve

Figures 6.27, 6.29, 6.32 and 6.34 show the plastic strain distribution in the blank at the end of the L-bending process, particularly around the bent area. It was found that the plastic strain increases with decrease of the die radius and the clearance. Also the strain increases with the increase of the blank holder force and the blank thickness. These results all confirm that the springback decreases when the plastic strain and therefore the total strain increases.

Figures 6.37 and 6.38 show springback angle versus the maximum plastic strain for the high strength steel and aluminium respectively. It can be seen that the springback angle decreases with increase of maximum plastic strain. These results demonstrate the strong correlation between springback angle and maximum plastic strain in the bend area which has not been demonstrated so clearly in the previous work.

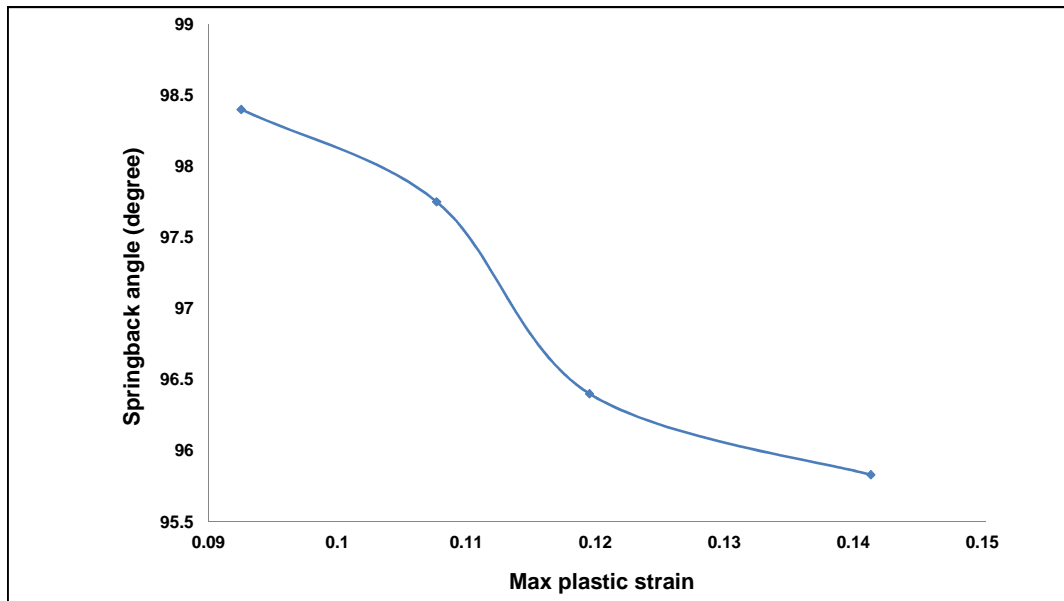


Figure 6.37 Springback angle versus maximum plastic strain for the DP600 steel which were at mixed of different design parameters

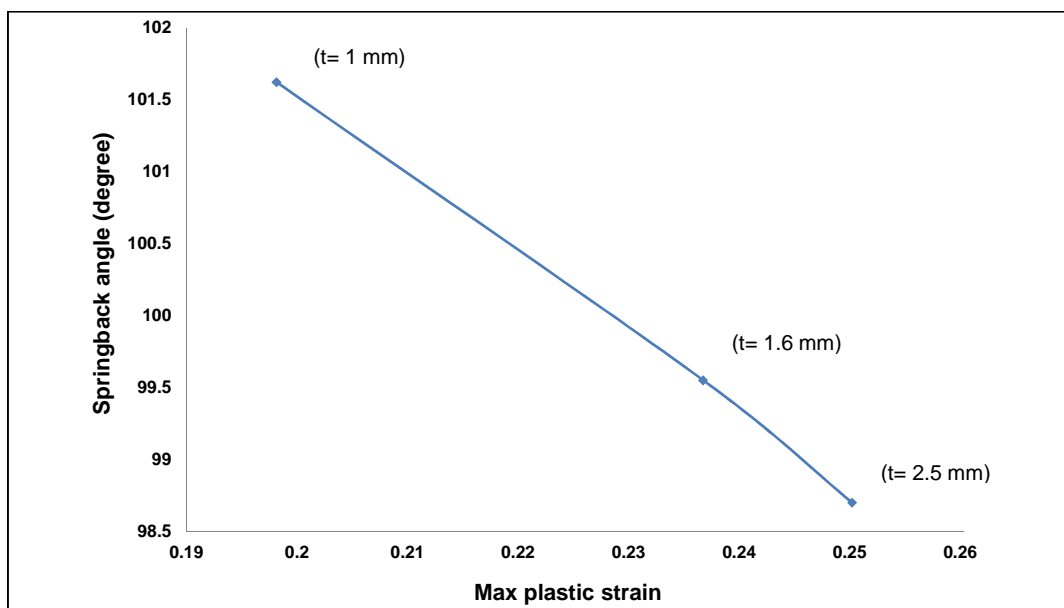


Figure 6.38 Springback angle versus maximum plastic strain for the CPLA100k38 aluminium which were for three different blank thicknesses

6.6 Summary

In this chapter, the experimental set up for conducting L-bending experiments for the four materials studied was outlined. The springback angle, after removing the specimen from the tool, was measured for each specimen using a CMM machine.

A finite element model for the L-bending process was developed and the results showed generally good agreement with the experiment. The material model considered was the Yoshida- Uemori model, available and known as Mat_125 in LS-DYNA, which has seven parameters. The Yoshida material parameters were derived in Chapter 3 for each material. It was demonstrated that there is a clear need to take into account the degradation of the Young's modulus after large plastic strain to achieve accurate springback prediction.

Good predictions of the forming load versus displacement curve and the springback angle were achieved for the low strength steel and both aluminium alloys, while there was a significant error in these predictions for the high strength steel material (DP600) due to the effect of the hot dipped galvanised zinc coating [68-71].

A parametric study was undertaken to investigate the importance of die radius, punch radius, clearance, blank thickness and blank holder load on controlling the springback. Those parameters that have most influence on springback were die radius, clearance and blank thickness. In contrast, there was no significant influence on springback caused by the punch radius or blank holder force variation. A clear inverse correlation between the springback angle and maximum plastic strain in the L-bending process has been established.

CHAPTER 7: U-DRAWING SHEET METAL FORMING EXPERIMENTS AND SIMULATION

7.1 Introduction

This chapter investigates the springback that occurs after the U-drawing sheet metal forming process for the four materials defined in Chapter 3. The main components and concept of the U-drawing process are illustrated in Figure 7.1. The blank is clamped by the blank holder as shown in Figure 7.1(a) followed by the vertical punch movement that draws the blank into the die cavity as illustrated in Figure 7.1(b). Finally the tools are released from the formed specimen which gives rise to the possibility of springback as shown in Figure 7.1 (c).

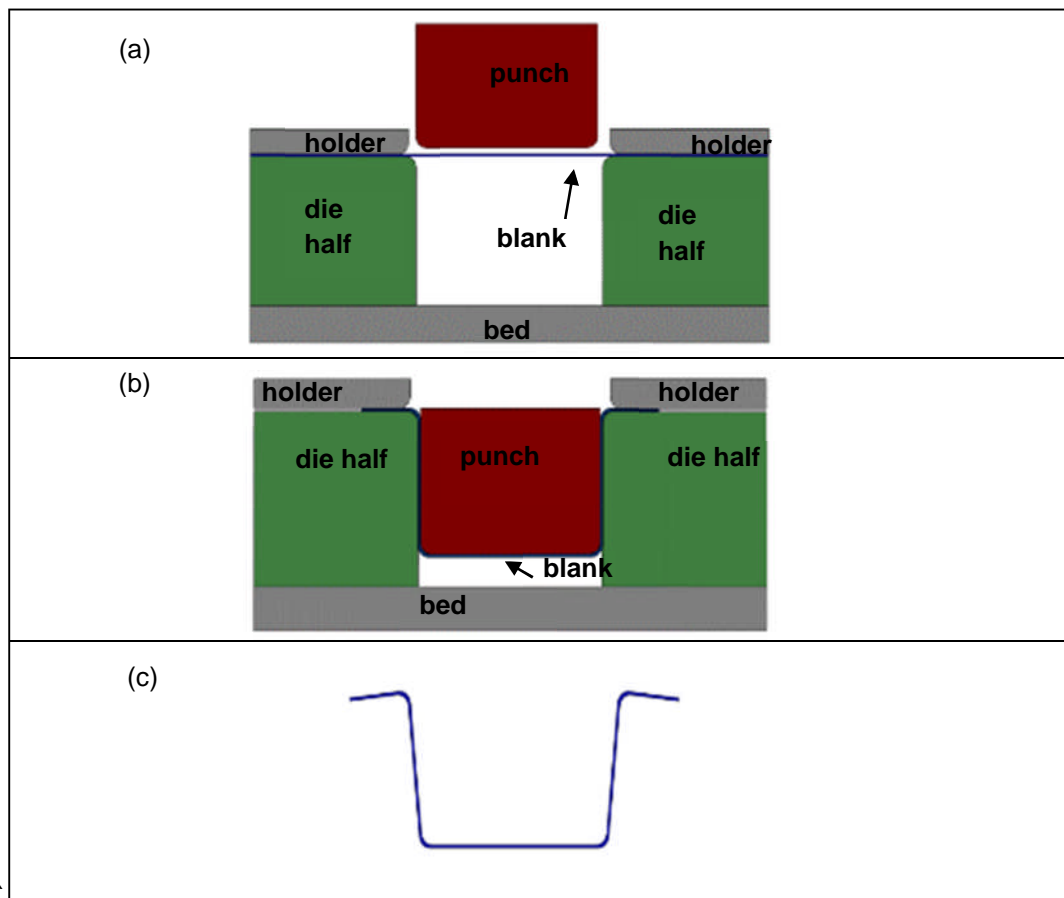


Figure 7.1 U-drawing process: (a) prior to the forming process, (b) end of the forming process and (c) final product with springback

Three identical experiments for each material were carried out using the same methodology and instruments described in Chapter 6 and the forming rig shown in Figure 7.2. The FEA methodology is also very similar to the one described for L-bending in the previous chapter. However, there are some differences such as those associated with the boundary conditions. Also, both 2D and 3D models for the U-drawing process were investigated and the results validated by comparison with experiment. The validated models were used to facilitate further investigation of the different parameters that control springback after the U- drawing process and this work is described in Chapter 8.

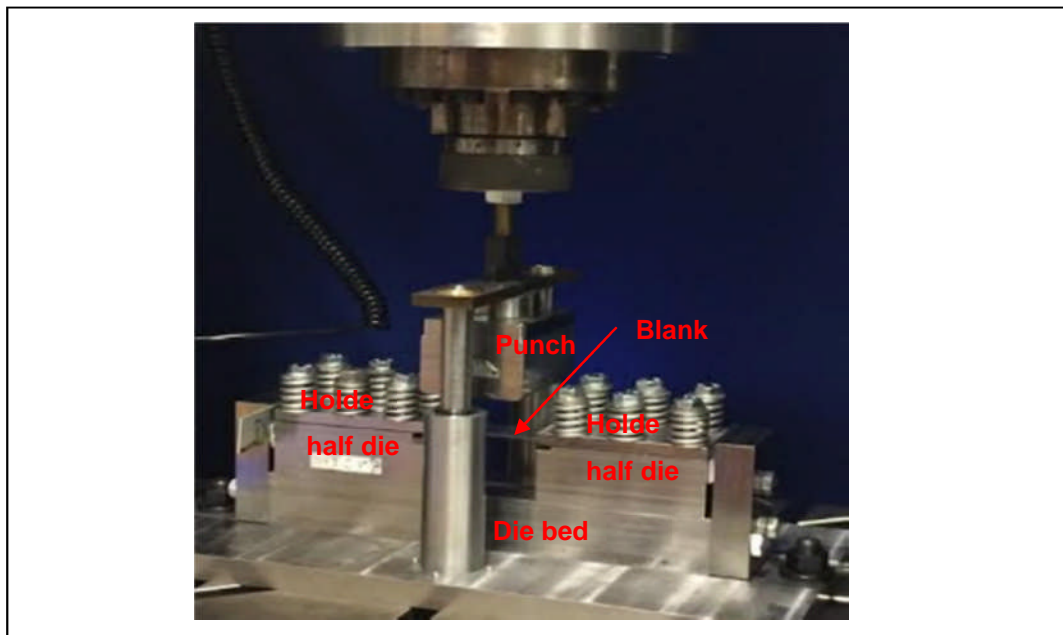


Figure 7.2 U-drawing rig mounted on Instron test machine

7.2 U-drawing experiments

7.2.1 Experimental method

A similar methodology to the experimental procedure for the L-bending process was utilised for the U-drawing experiments. The four blank materials were cut by laser into rectangular strips of 300 x 30 mm as shown in Figure 7.3.

The clearance between the forming tools (punch and die) and the blank as illustrated in Figure 7.4 (c) was set at 0.9 and 1.0 mm for the steel and aluminium specimens respectively due to the difference in blank thickness between the two types of materials.

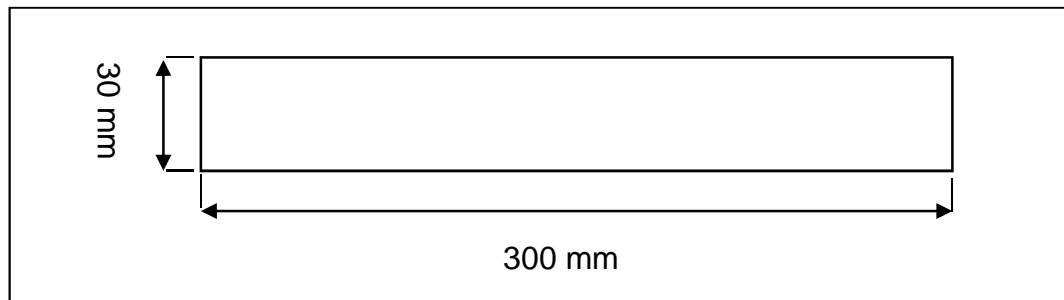


Figure 7.3 Blank dimensions for U- drawing bending process

Figure 7.4 (a) shows the DP600 blank in the clamped position and the punch positioned approximately 4.2 mm above the top surface of the blank. At this position, the Bluehill 2 software mentioned in Chapter 4 was utilised to re-set the load and displacement readings of the punch transducers to zero. This program was also used to specify the punch speed and total punch displacement which were set at 2 mm/s and 48 mm respectively.

The punch was moved down at constant speed to just above the bed of the die to form the U-shape as shown in Figure 7.4 (c), and the punch load and displacement were continuously recorded. The punch was then returned to its original position. Figure 7.4 (d) shows the DP600 specimen following the return of the punch and there is clear evidence of springback occurring. The test was carried out three times for each material under the same conditions to assess the repeatability of the results.

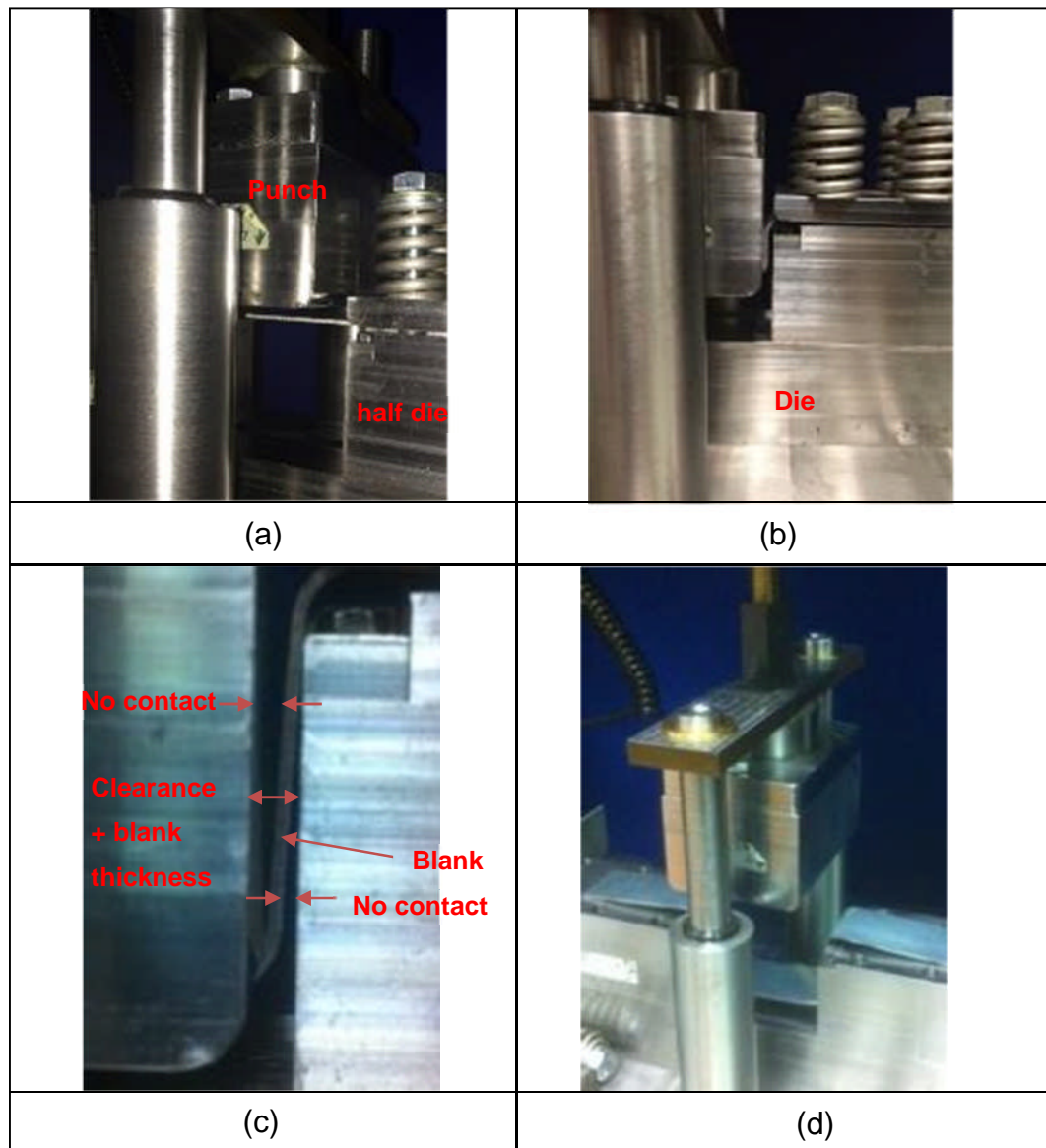


Figure 7.4 The experimental U-drawing process (a) prior to forming (b) during the forming (c) fully formed part (d) after removing the tools (showing springback)

7.2.2 Punch load behaviour during the U- drawing process

Figures 7.5 to 7.8 show the punch force versus displacement curves as recorded by the Bluehill software for the four materials. Similar trends of the punch force versus displacement curves can be seen for all four blank materials.

Also, the results of the three experiments for each material confirm the consistency in the blank behaviour with only the high strength aluminium showing any significant difference between the three repeated experiments. Therefore, the punch force behaviour is explained in detail with referral to the DP600 high strength steel only.

Figure 7.5 (a) shows the punch force versus displacement curves for the DP600 blank. It can be seen that the punch force increases sharply at the commencement of the process at 3 mm of punch displacement to a maximum load of 13.2 kN at almost 20 mm of punch displacement. Subsequently, the punch load decreases by about 1 kN and then levels off until the end of the process as the blank material is drawn further into the die. There is unusual behaviour of the punch load in that two peaks are apparent as shown in the zoomed-in section of Figure 7.5 (a). As mentioned in Chapter 4 the distribution of the blank holder force relies on the position of the bolts and it was found that the blank holder produces enhanced pressure in the vicinity of the bolts as would be expected. Also, the contact area between the blank holder and the blank reduces as the blank is pulled under the blank holder resulting in increasing contact pressure between the blank holder and the blank as the total bolt load remains the same. Consequently, the punch requires more load to maintain the blank drawing process. As the free end of the blank passed the furthestmost two bolts as shown in Figure 7.5 (b), the punch load dropped by about 1 kN due to the reduction in the total clamp load.

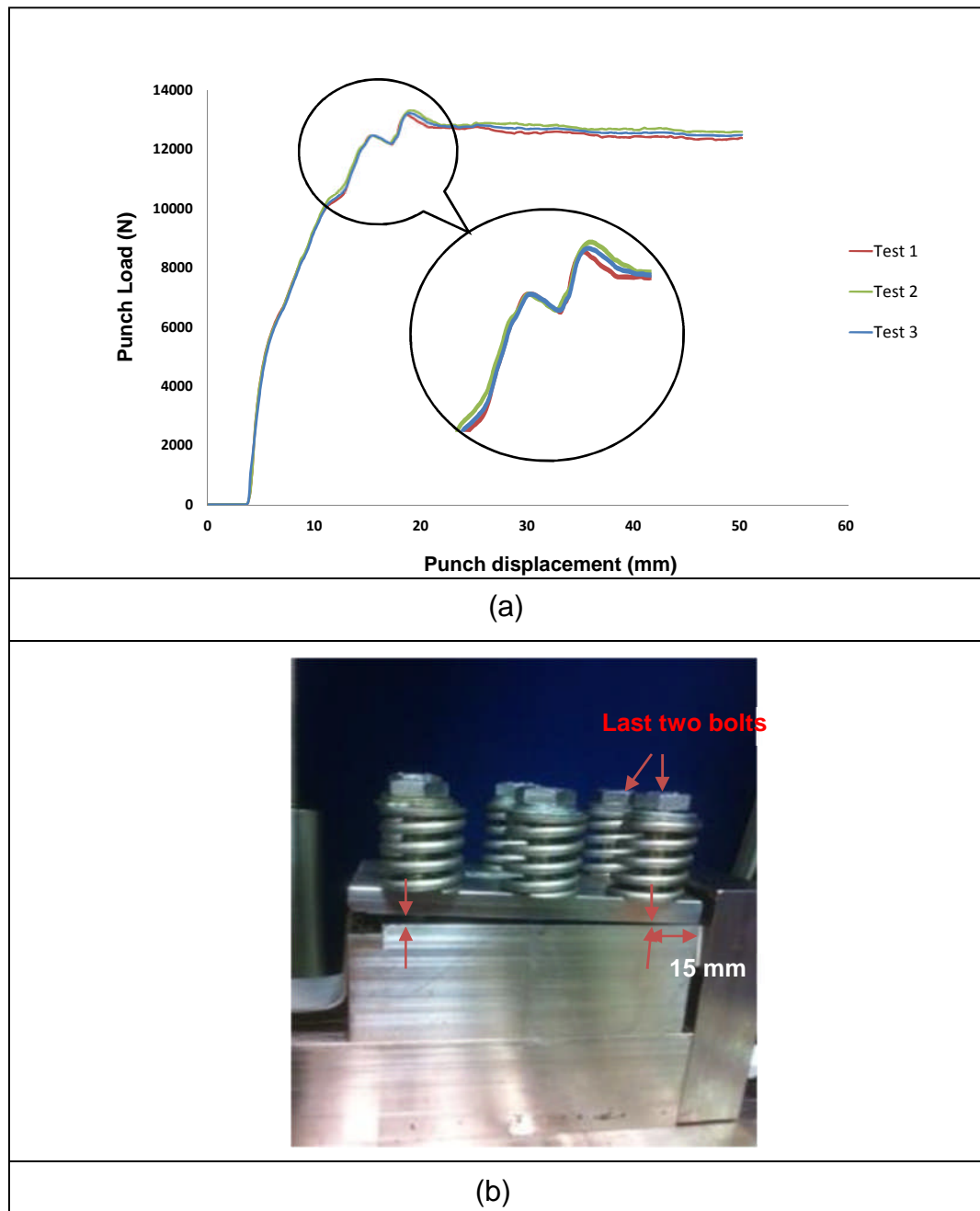


Figure 7.5 (a) Punch load versus displacement for the high strength steel (DP600) during U-drawing (b) the forming tools at the end of the forming process

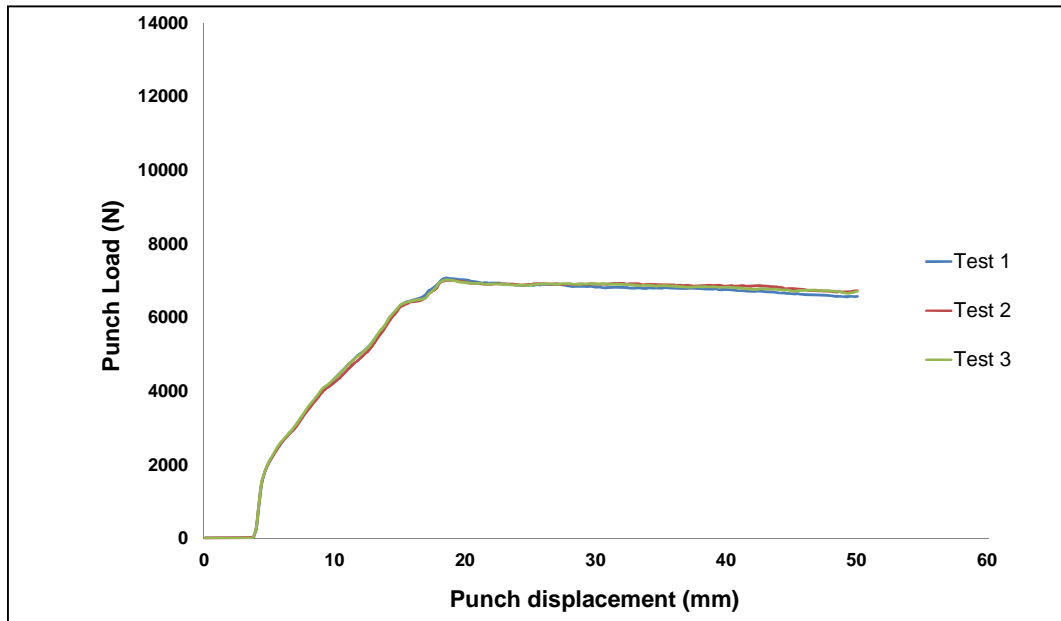


Figure 7.6 Punch load versus displacement for the high strength steel (DX54D) during U-drawing

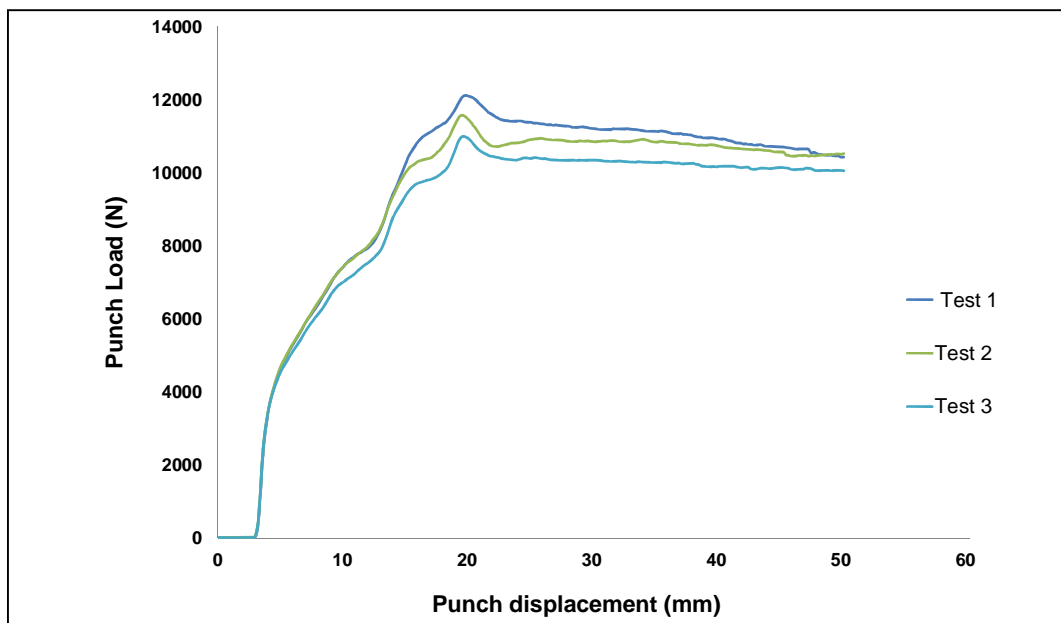


Figure 7.7 Punch load versus displacement for the high strength aluminium (CPLA100k38) during U-drawing

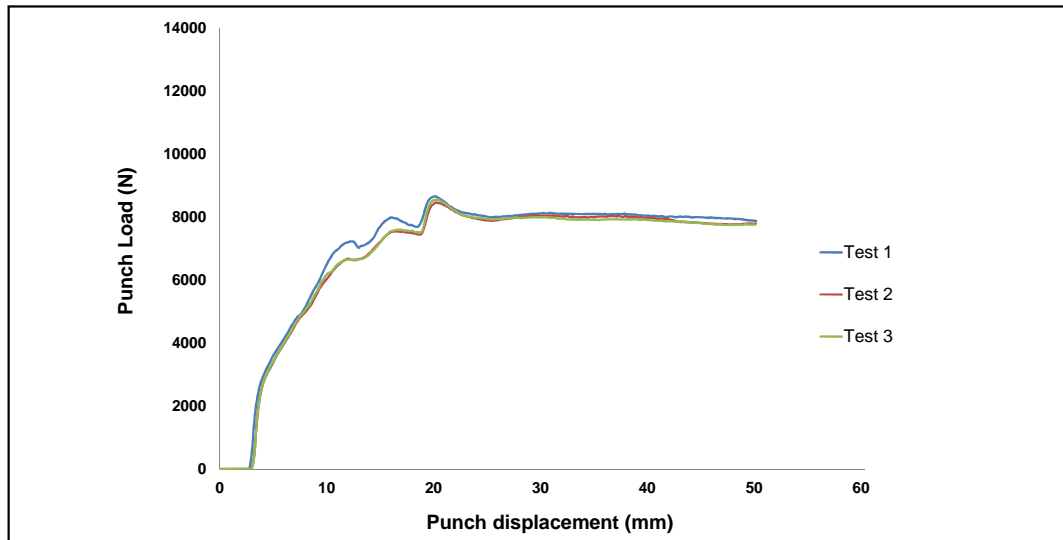


Figure 7.8 Punch load versus displacement for the low strength aluminium (CPLA10414) during U-drawing

There is a significant difference in the magnitude of the punch load required to form the high and low strength materials. Despite the relative complexity of the U-drawing process, Figures 7.9 and 7.10 show that the differences are again much higher between the two steel materials than between the aluminium alloys. This was also noticed for the L-bending process and the main reason is that the difference between the yield and ultimate stresses of the high and low strength steel materials is much larger than for the aluminium alloys as shown in Tables 6.1 and 6.2.

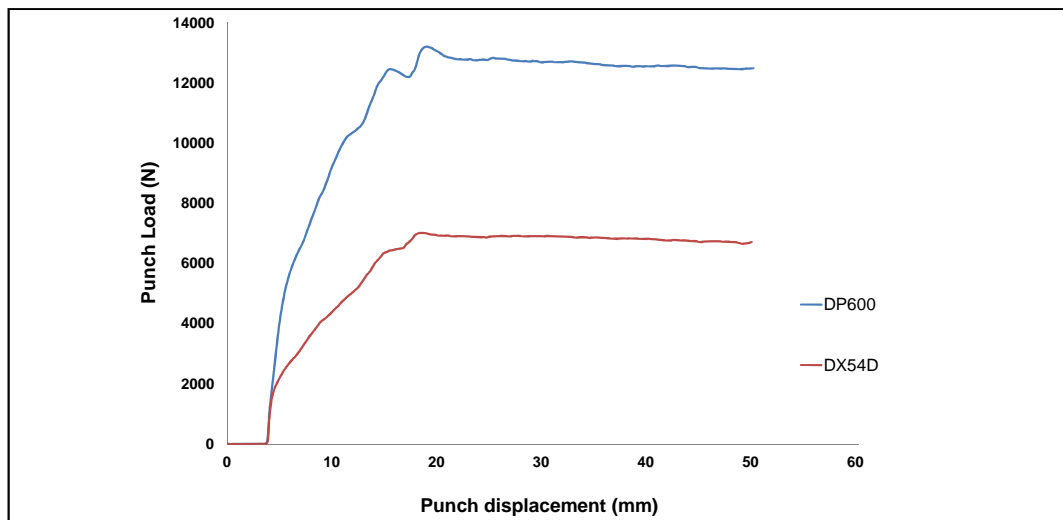


Figure 7.9 Comparison of average punch load versus displacement between the DP600 and DX54D steels during U-drawing

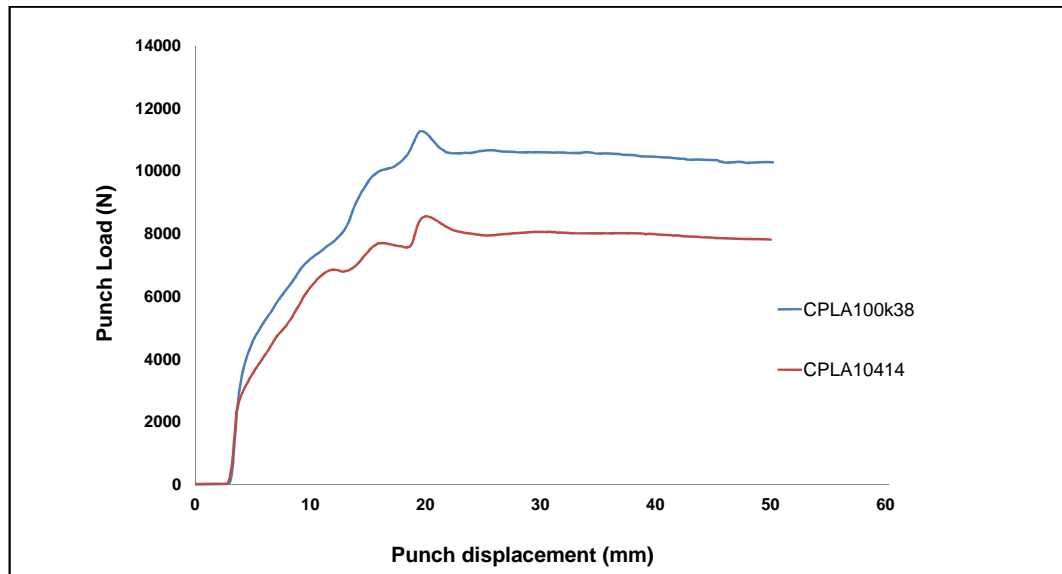


Figure 7.10 Comparison of average punch load versus displacement between the CPLA100k38 and CPLA10414 aluminium alloys during U-drawing

7.2.3 Springback after the U-drawing process

After the completion of each U- drawing experiment, the metal forming tools (the punch and blank holder) were released from the specimen and the deformed blank was removed carefully. Figure 7.11 shows one specimen for each material after extraction from the die. It can be observed from these images that a significantly higher level of springback occurs for the high strength steel compared to the low strength one. However, it seems that there is less difference in the springback between the high and low strength aluminiums which display lower springback than the steels. The same observations were made for the L-bending metal forming process.

The specimens were measured using the same CMM machine used for the L-shape specimens as described in Chapter 6. Figure 7.13 illustrates the location of the measurement points on the deformed specimen and how the straight lines AB, CD and EF were plotted through these points. Subsequently, the θ_1 springback angle was determined as the angle between line AB and line CD whilst the angle between lines CD and EF

defines the angle θ_2 . The springback results for each experiment are presented in Table 7.1.

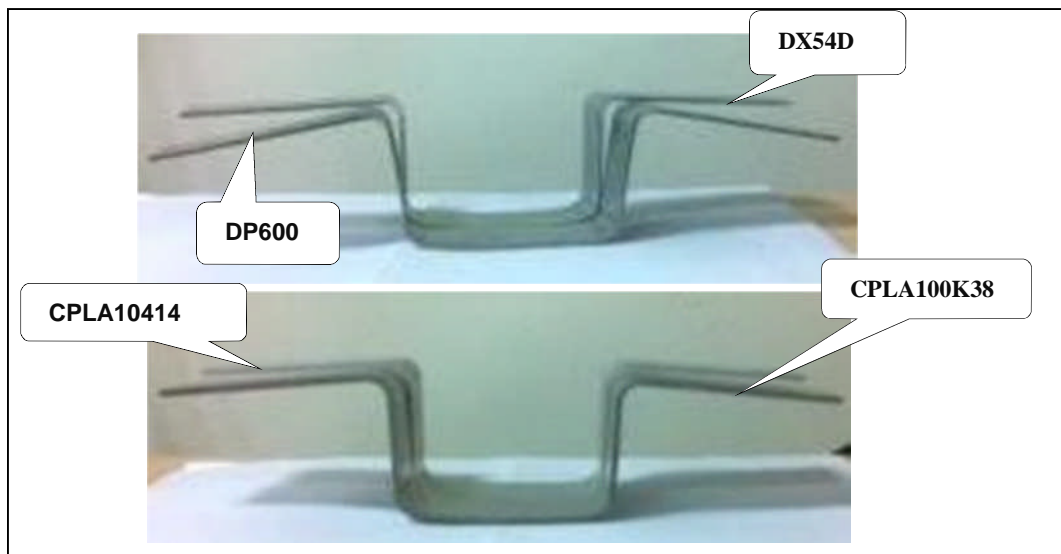


Figure 7.11 The specimens showing springback after the U- drawing process

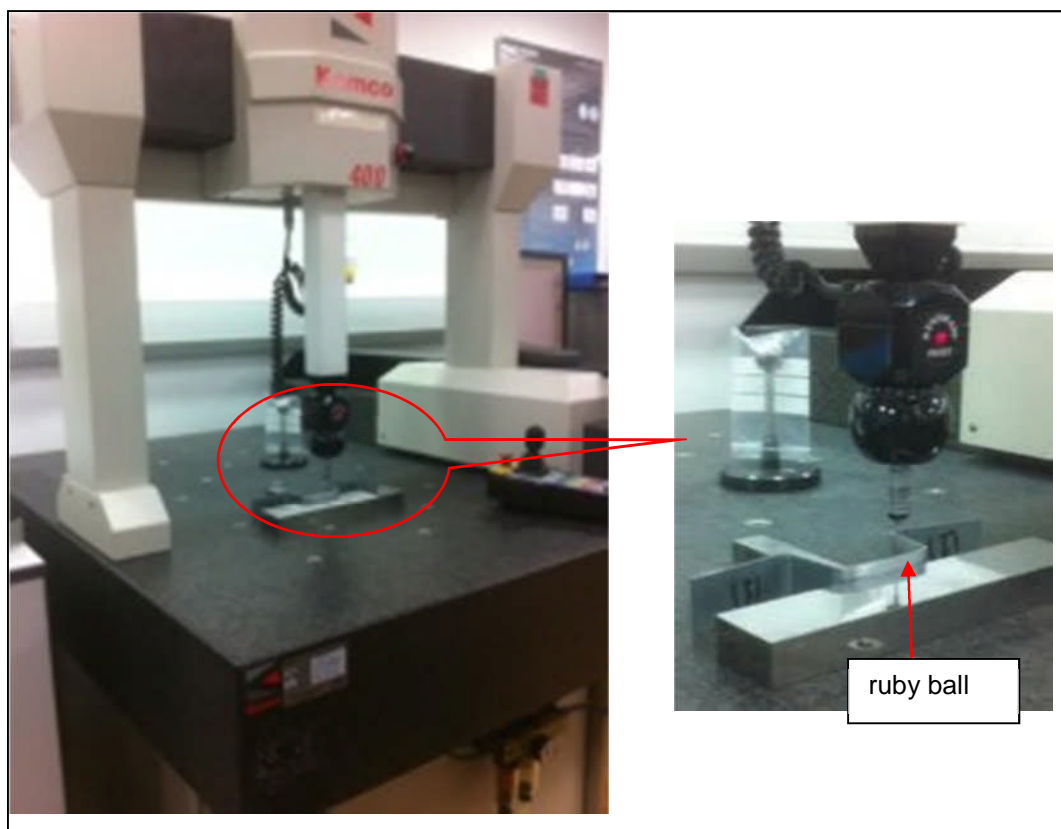


Figure 7.12 Kemco CMM 400 machine set up to measure the U shape profile

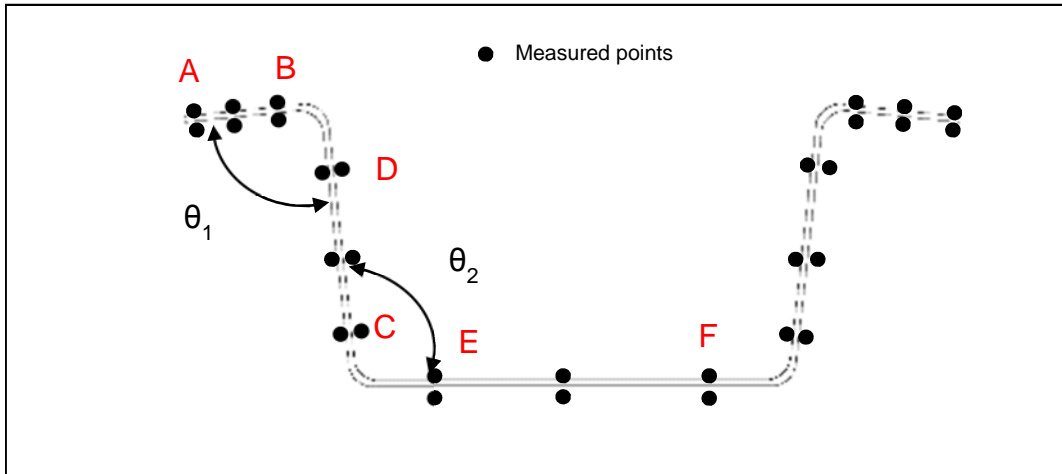


Figure 7.13 Measurement of springback angles after the U-drawing process, showing approximate location of measurement points of a blank

Table 7.1 Experimental springback results for the four blank materials

Materials	Springback Angle (degree)			
	individual		Average	
	θ_1	θ_2	θ_1	θ_2
DP600	88.0	98.1	88.0	98.2
	88.2	98.6		
	87.9	97.8		
DX54D	88.5	91.5	88.5	91.7
	88.4	92.2		
	88.7	91.3		
CPLA100k38	88.3	93.8	88.4	93.5
	88.4	93.3		
	88.6	93.5		
CPLA 10414	88.4	91.1	88.4	91.5
	88.4	91.8		
	88.4	91.6		

7.3 Numerical analysis of U-drawing process and subsequent springback

7.3.1 Finite element model

The method of modelling the U-drawing process was very similar to that employed for the L-bending process reported in the previous chapter. As before, Hypermesh software was used as the pre-processor and Ls-Dyna as the solver and post-processor. Therefore, only the main differences are illustrated in this section.

The basic model is defined in Figure 7.14; note that symmetry boundary conditions were applied to the central plane so that only half of the blank has been modelled. The geometric parameters are defined in Table 7.2. The whole assembly was modelled using firstly 2D plane strain quadratic elements as shown in Figure 7.15 and secondly 3-D quadratic thin shell elements as shown in Figure 7.16. For both element types the explicit solution algorithm of the Ls-Dyna solver was used for the forming analysis and the implicit solution algorithm was used for the prediction of springback.

The Y-U material model was used in each case taking into account the reduction of the Young's modulus. The punch, die and blank holder were considered to be rigid bodies, while the blank was considered to be a deformable body. A one way surface-to-surface contact regime was used to define the interaction between the punch, die, blank and blank holder components. In this contact definition, the blank holder, punch and die were considered to represent the master surface and the blank surface was considered to be the slave surface. The static and dynamic coefficients for all four materials were as listed in Table 6.5.

7.3.1.1 2D Modelling

The assumptions for the 2D plane strain model shown in Figure 7.15 were as follows:

1. The punch is constrained in all rotations and translations in the X-direction only.
2. The blank holder is constrained in all rotations and displacements in the X-direction only.
3. The die is fixed in all degrees of freedom.
4. The blank is fixed along the symmetry line in the X-direction for translation and all rotations.
5. Plane strain conditions are assumed i.e. the strain in the out-of-plane (Z) direction is negligible.

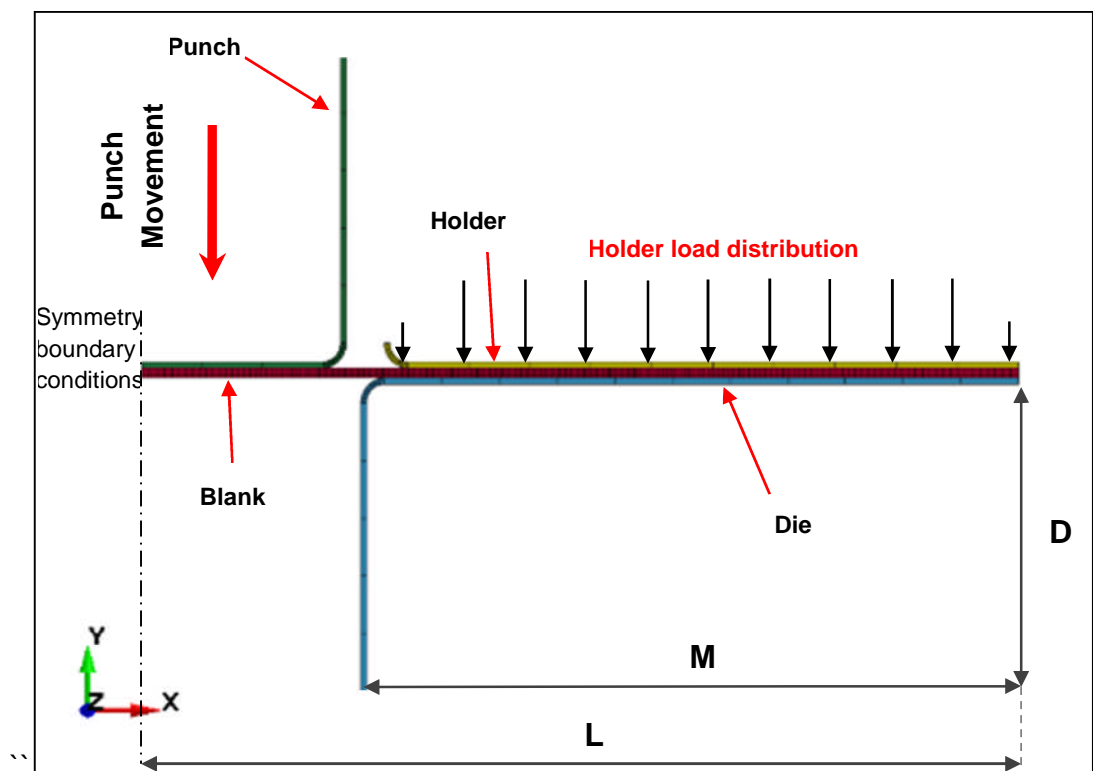


Figure 7.14 Theoretical model of U-drawing process

Table 7.2 Dimensions of the U-drawing finite element model

Geometrical Parameters	L	D	M	Die and punch radii	Blank thickness	Clearance	Material
Dimension (mm)	150	50	112	4	1.6	0.9	Steel
					2.5	1.0	Aluminium

The mesh sensitivity study was very similar to that carried out for the L-bending process. However, during the U-drawing process, the area of the blank that experiences severe stress is much larger than for the L-bending process. Therefore, for the U-drawing process, the blank was divided into three zones designated A, B and C as shown in Figure 7.15. The mesh size in region B was uniform and minimum. Beyond zone B, the element size in zones A and C was increased slowly up to each free end using the 'biasing' option within Hypermesh. The element size in zone B was chosen to be half the minimum element size in the other regions and the biasing ratio used was 1.5 for both regions A and C.

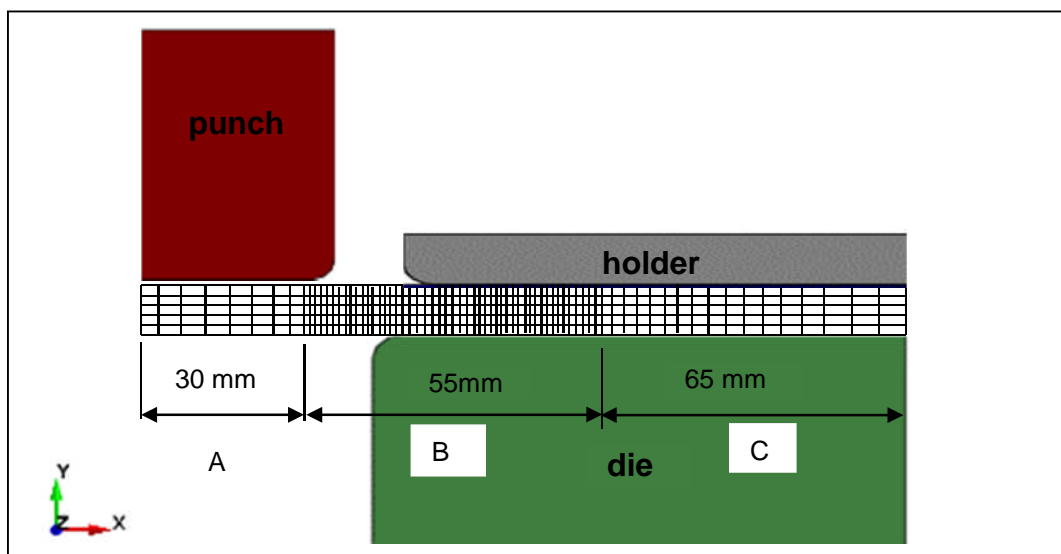


Figure 7.15 Blank discretisation for the U-drawing bending 2D modelling

7.3.1.2 3D Modelling

In the 3D shell element model shown in Figure 7.16, fully-integrated shell elements type ELFORM 16 available in Ls-Dyna were utilised. The element formulation is based on the Reissner-Mindline kinematic assumption where the through-thickness stress is assumed to be negligible [74]. The formulation is used to calculate the shear deformations in the thin shell elements [75, 76]. The following boundary conditions were assumed:

1. The punch is constrained in all rotations and translations in both X and Y-directions.
2. The blank holder is constrained in all rotations and displacements in both X and Y-directions.
3. The die is fixed in all degrees of freedom.
4. The blank is fixed along the symmetry line for translation in X and Y-directions and all rotations.

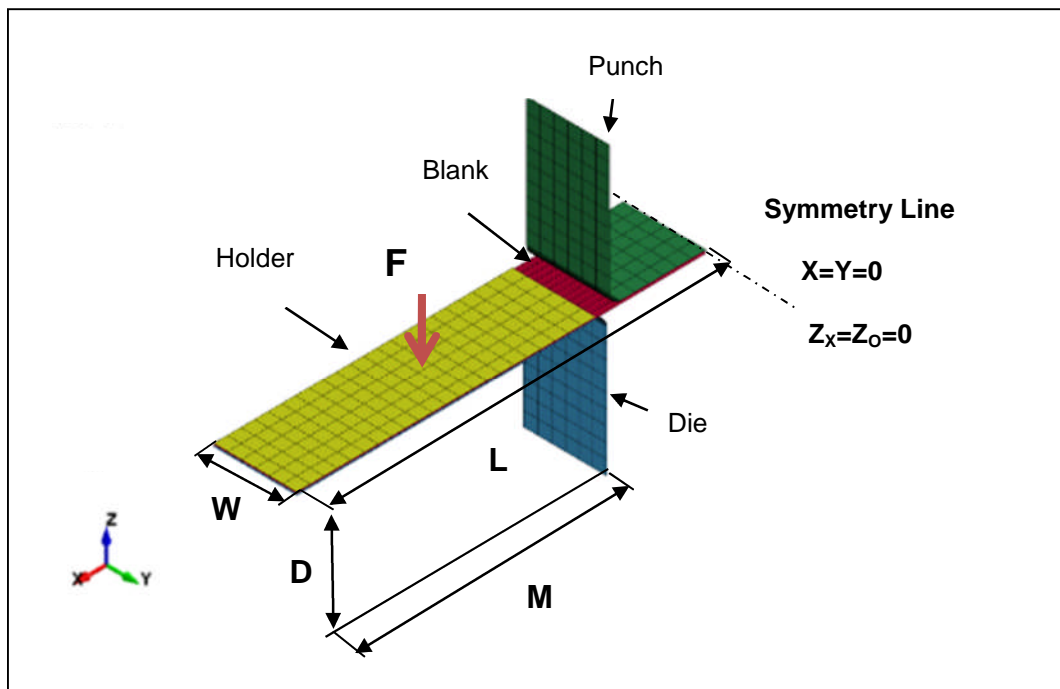


Figure 7.16 The 3D shell element model of U-drawing process

The blank discretisation of the 3D shell element model was similar to that of the 2D plane strain model. The blank was divided into three zones

designated A, B and C as shown in Figure 7.17. The mesh size in region B was uniform and minimum. Beyond zone B, the element size in zone A and C was increased linearly up to each free end using a 1.5 biasing ratio. Moreover, as the blank width is much larger than its thickness, the effect of changing the mesh in the Y direction was considered negligible. The aspect ratio element l : W was set to 1:2 where l and W are the element length and width respectively as shown in Figure 7.17. Six different meshes were used as shown in Table 7.3.

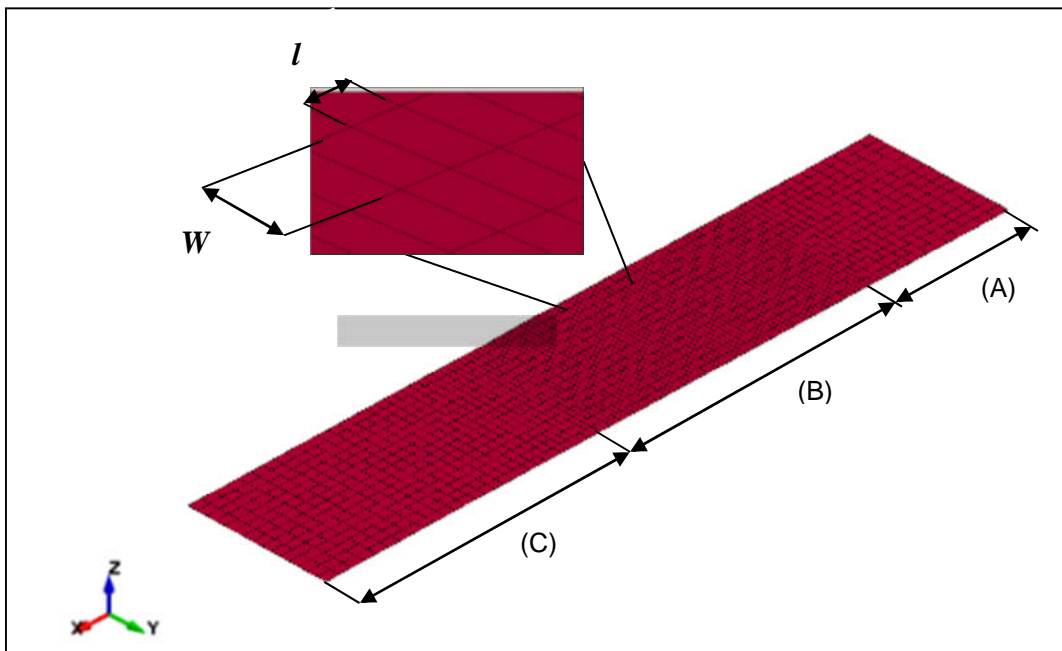


Figure 7.17 Blank discretisation for the 3D shell element model of the U-drawing process

7.3.2 Results of the mesh sensitivity study

The sensitivity of the results to the mesh density of the blank was investigated to achieve a balance between the accuracy of the results and the computation time. The mesh sensitivity study was conducted using the blank mesh model shown in Figure 7.15 for the 2D model and in Figure 7.16 for the 3D model. Also the degradation of the Young's modulus was included in these simulations. The punch force versus displacement was compared for six different mesh sizes for both blank models. Figure 7.18 (a) shows typical results for the 2D model for the DP600 blank for the different mesh densities. It was found that the punch load vs. displacement converged with

an acceptable variation from experiment when the element size in zone B was 0.2 mm for the 2D model, which was mesh 4 as shown in Figure 7.18 (b). Similar results were obtained for the different mesh densities for the 3D model.

Figure 7.20 shows a comparison between the converged mesh results for both 2D plane strain and 3D shell element models and experiment for the DP600 steel. Although both models are able to give acceptable levels of agreement, the 3D model results are generally closer to the experiment and give lower oscillations. Moreover, the 2D model often failed to converge during the prediction of the springback after the forming simulation. Therefore the decision was taken to use the 3D shell element model for all subsequent simulations of springback for the U-drawing forming process.

It was also necessary to conduct a mesh convergence study for the springback prediction using the 3D model and the results of this study are presented in Table 7.3. It was concluded that the results had converged for an element size in zone B of 0.5 mm with 3 hours and 18 minutes of running time, as highlighted by the red box in Table 7.3

Table 7.3 Effect of different element size for the 3D model of the blank in U-drawing springback predictions (red box indicates converged results)

<i>Finite element mesh</i>				<i>Elapse CPU time (hr : min : sec)</i>		<i>Springback angle (degrees)</i>	
Mesh	<i>l</i> (mm)	<i>W</i> (mm)	Number of Elements	Forming (explicit)	Springback (implicit)	θ_1	θ_2
1	1.50	3.0	680	00:07:41	00:00:17	97.95	91.94
2	1	2	1751	00:26:16	00:00:52	87.94	92.38
3	0.7	1.4	3504	01:13:59	00:01:39	88.12	94.51
4	0.5	1	6970	03:15:21	00:03:18	88.78	95.68
5	0.4	0.8	10794	06:07:29	00:06:02	88.80	95.67
6	0.3	0.6	19096	11:14:45	00:10:37	88.79	95.72

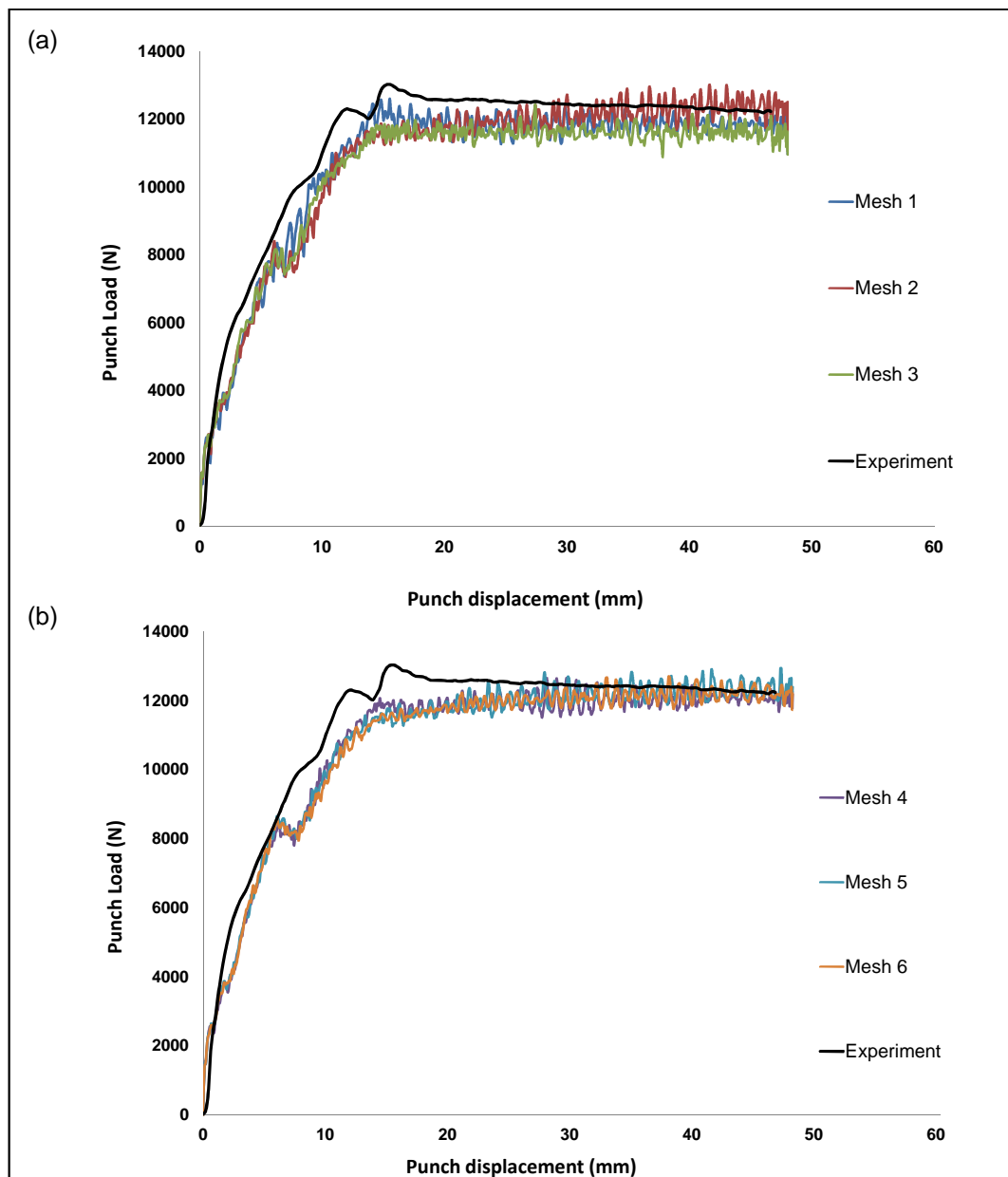


Figure 7.18 Comparison between experimental and 2D numerical modelling of punch force versus displacement curves in U-drawing for different blank mesh densities for DP600 steel

Figure 7.19 shows contour plots of the 3D shell element prediction of the equivalent plastic strain on the DP600 blank during the U-drawing process and after the tools have been removed to give springback. This figure indicates that the analysis of U-drawing is not truly a 2D problem since from Figure 7.19 (f) onwards, the strain is not constant across the width and is noticeably different towards the edges of the blank. This is particularly the

case after springback, Figure 7.19 (i). This is a further indication that the 3D shell element model is more appropriate for the prediction of springback following U-drawing than the 2D plane strain model.

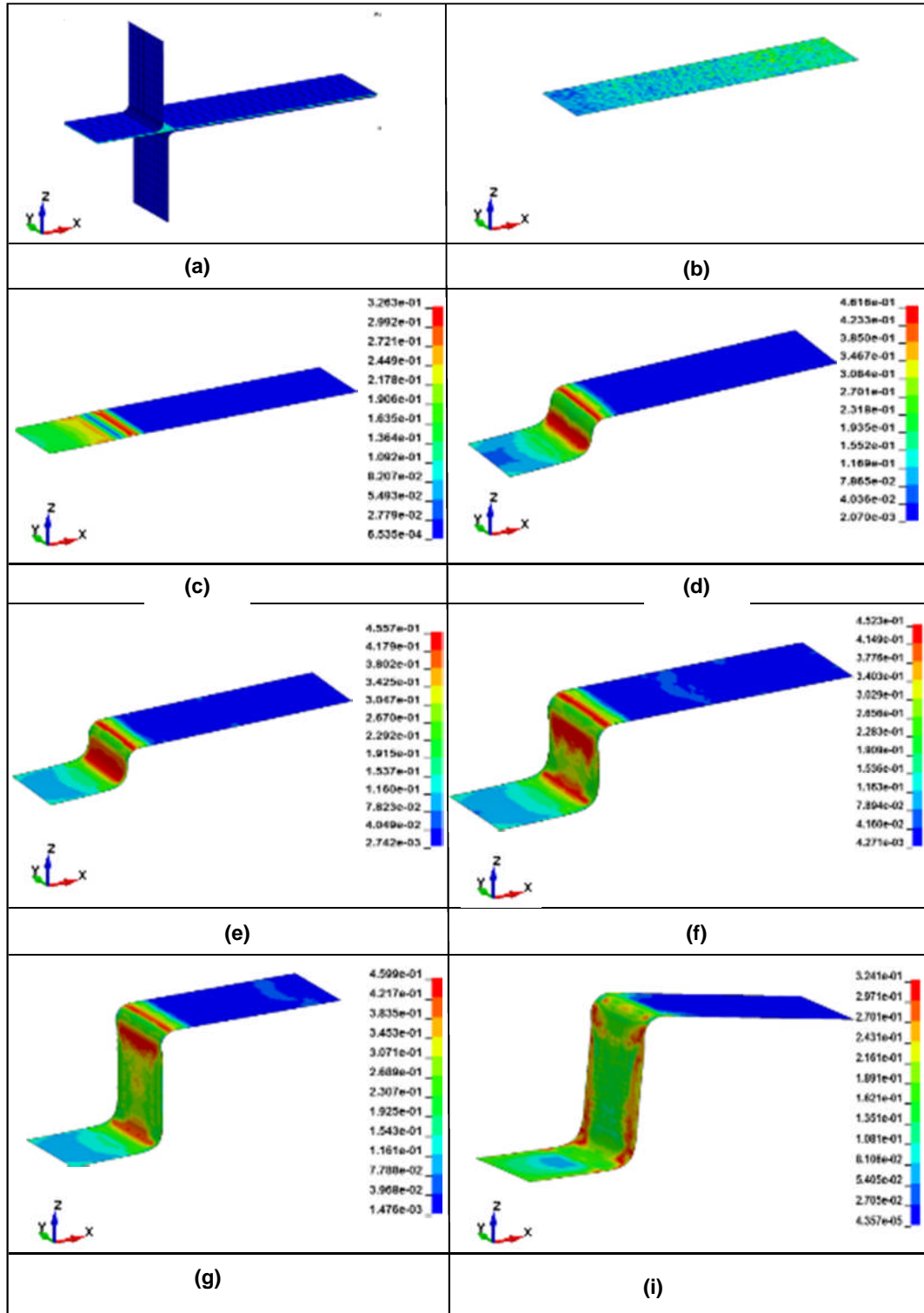


Figure 7.19 3D U-drawing simulation for DP600 and equivalent plastic strain distribution in the blank (a) whole assembly, (b) to (g) snapshots during the process, (i) after springback

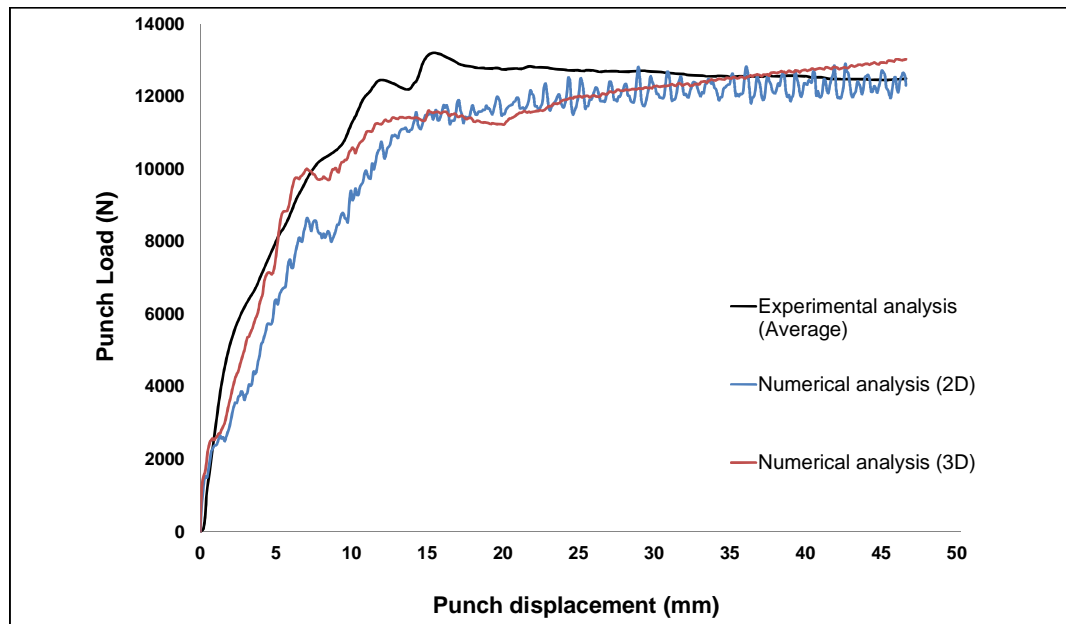


Figure 7.20 Comparison between experimental and numerical punch force versus displacement curves in U-drawing process for DP600

7.3.3 The effect of the degradation of Young's modulus

Figure 7.21 shows the difference in the magnitude of the springback prediction between when the Young's modulus is assumed to be a constant and when it is varied for the four materials for the 3D shell element model. This figure firstly shows good agreement between the experimental and numerical results of the springback for aluminium and low strength steel blanks when the degradation of modulus is taken into account, the exception being the θ_2 results for the DP600 where there is a large discrepancy assumed to be due to the effect of the coating. Secondly, agreement is poor when the Young's modulus reduction following plastic deformation is ignored. Although there was still a significance difference between the experimental and numerical prediction of the springback for the DP600 when the reduction in E was modelled, there was a much greater difference when the reduction of the Young's modulus was ignored. Therefore, the reduction of the Young's modulus was taken into account for all 4 materials in all the subsequent simulations.

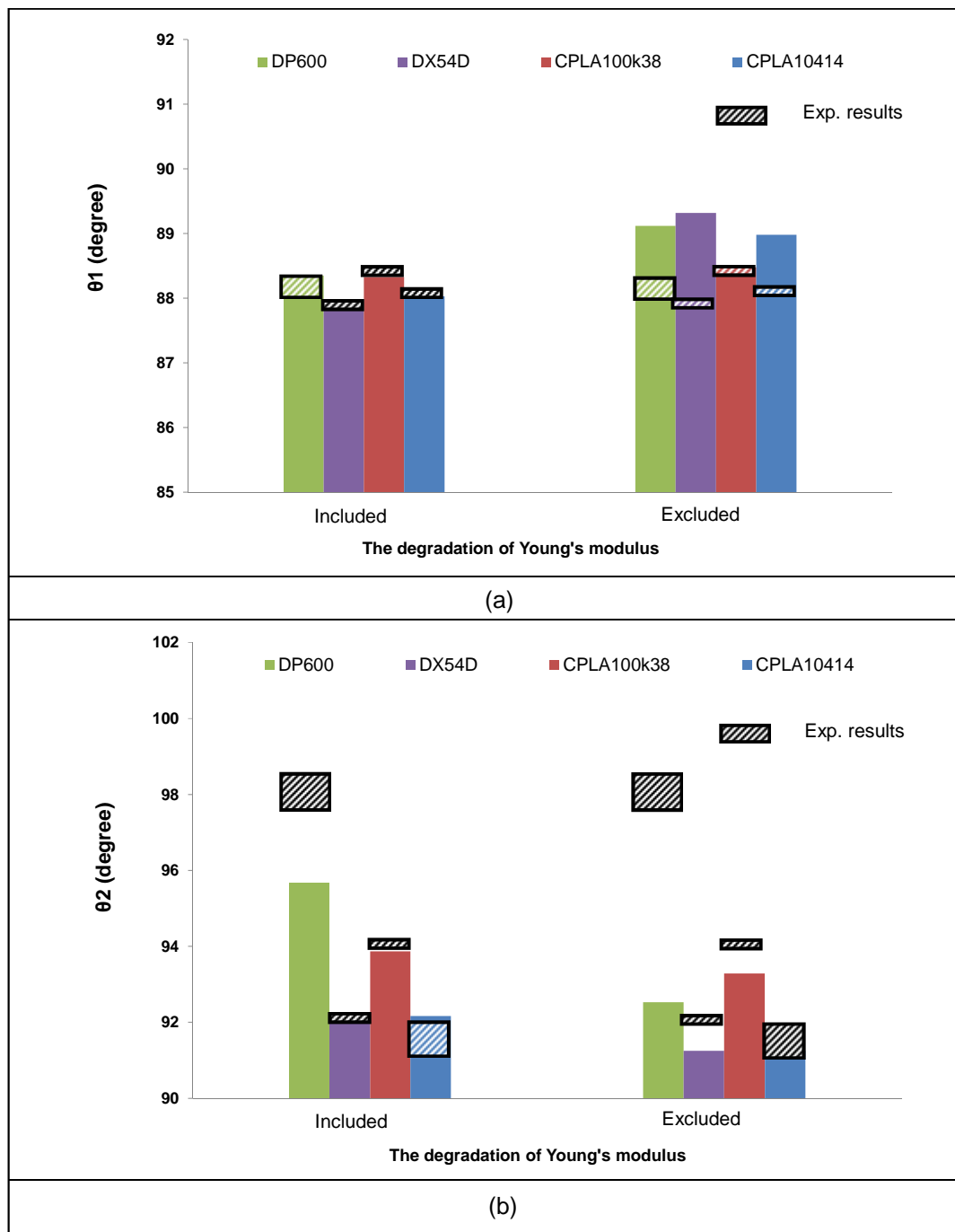


Figure 7.21 Springback after U-drawing process for all materials included and exclude the elastic modulus degradation in comparison with experiment (a) θ_1 and (b) θ_2

7.4 Comparison of numerical and experimental results

As discussed above, Figure 7.20 shows much better agreement between the 3D model load vs. displacement curve and experiment for U-drawing than previously achieved for L-bending for the DP600 steel. Figures 7.22 and 7.23 show the punch force versus displacement numerically and experimentally for DX54D and CPLA100414 blanks respectively. The agreement between the experimental and numerical results is again generally reasonable but the predicted punch load is slightly lower than the experimental measurements until about 20 mm of displacement after which the results were almost the same, especially in terms of the steady state punch load.

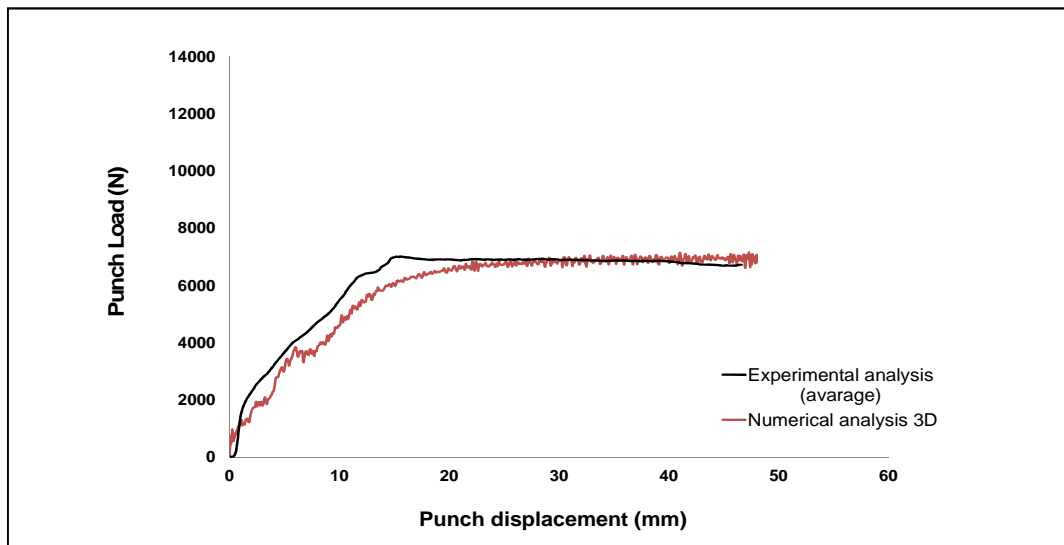


Figure 7.22 Punch load versus displacement for the low strength steel (DX54D) during U- drawing

Figure 7.24 illustrates the punch force versus displacement numerically and experimentally for the CPLA100k38 high strength aluminium blank during the U-drawing process. Here, the punch load calculated numerically by the 3D shell element model is somewhat higher than the experiment especially near the beginning of the process but the steady state results are very similar. The only difference that could contribute to the above variation is

that the blank holder pressure was assumed to be constant for the simulation which was not the case in reality.

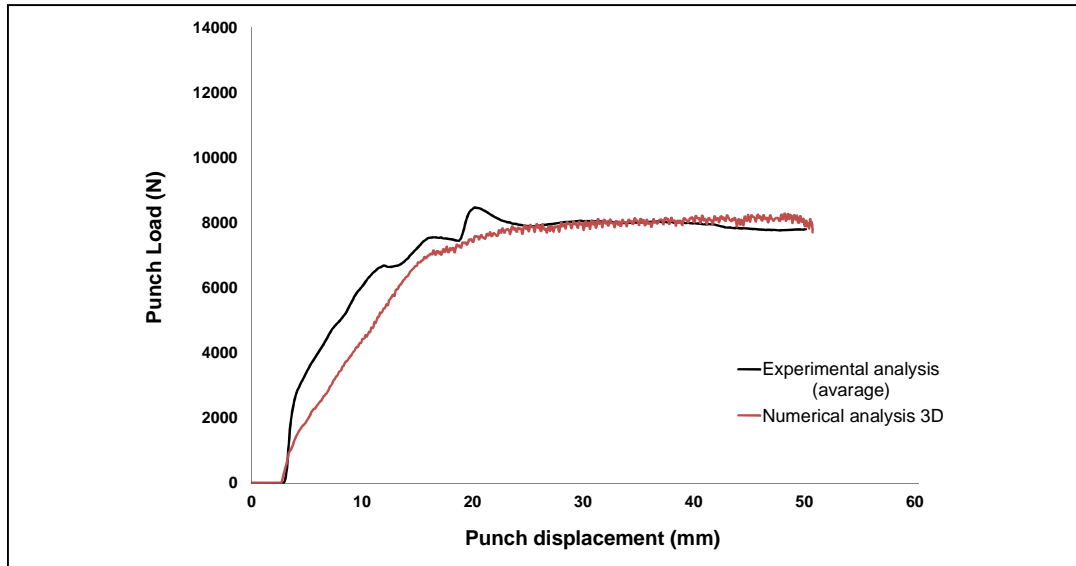


Figure 7.23 Punch load versus displacement for the low strength aluminium (CPLA10414) during U-drawing

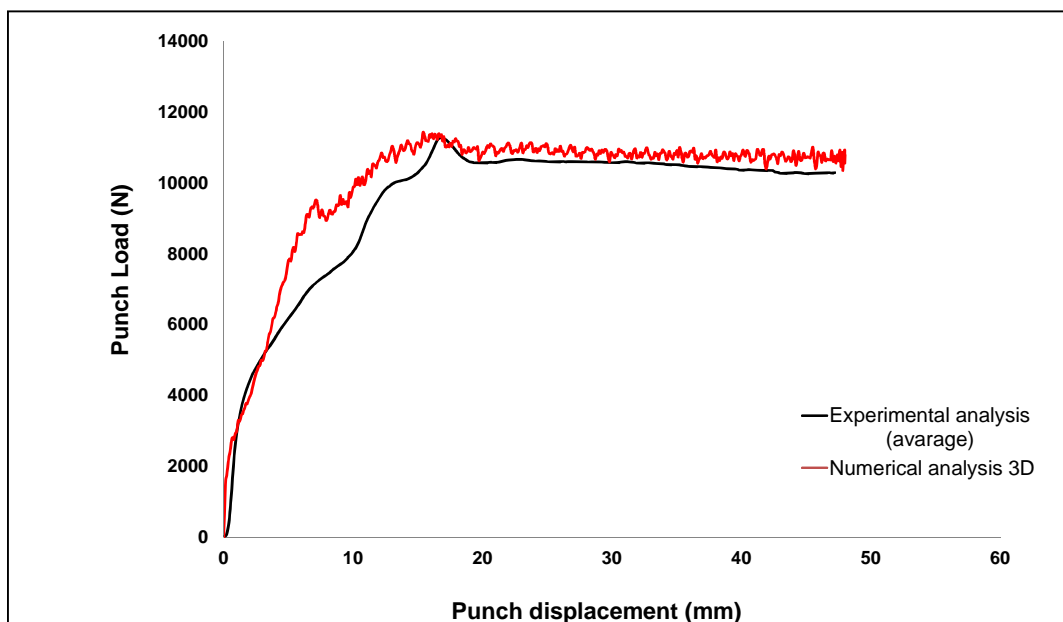


Figure 7.24 Punch load versus displacement for the high strength aluminium (CPLA100k38) during U-drawing process

The numerical analysis of the springback after U-drawing is compared to the experimental results for each blank material in Table 7.4. From this table, it can be seen that the amount of springback was much higher for the high strength materials than the lower strength materials. The highest springback was found for the DP600 (high strength steel), whilst CPLA10414 (low strength aluminium) has the lowest springback. The error between the experimental and numerical results was calculated based on equation (6.2).

It can be seen from Table 7.4 that the maximum error occurs for the high strength steel. Again, as with the L-bending, this is thought to be due to the galvanised coating which is not included in the numerical model. The low strength steel and both aluminium alloys achieved good agreement between the experimental and numerical results, with errors of less than 0.75%.

Table 7.4 Experimental and numerical springback results for the four blank materials

Material	Springback Angle (degrees)				Error (%)	
	Experiment		Simulation			
	θ_1	θ_2	θ_1	θ_2	θ_1	θ_2
DP600	88.0	98.2	88.8	95.7	0.84	2.54
DX54D	88.5	91.7	87.9	92.1	0.73	0.41
CPLA100k38	88.4	93.5	88.1	93.9	0.01	0.52
CPLA 10414	88.4	91.5	88.9	92.1	0.53	0.75

7.5 Summary

In this chapter, the experimental set up for conducting the U-drawing experiments for the four materials has been outlined. The springback angles after releasing the tools from the deformed blanks were measured by the CMM machine. Two finite element models (2D plane strain and 3D shell) for the simulation of the U-forming process were considered and their predictions compared to the experimental results. The material model considered was the Y-U model, available and known as Mat_125 within Ls-Dyna.

The Yoshida material parameters were derived in Chapter 3 for each material. Both 2D plane strain and 3D shell element models were found to give reasonable prediction of the punch load vs. displacement response for all four materials. However, the 2D model was not found satisfactory for the prediction of springback due to convergence problems. On the other hand, the 3D shell model gave generally good predictions of the springback angles. However there was again relatively large errors in the prediction of the springback for the high strength steel DP600 due to the effect of the hot dipped galvanised coating. Also, the influence of the reduction of the Young's modulus on the springback prediction was found to be significant and should be included for accurate springback prediction.

CHAPTER 8: PARAMETRIC STUDY AND MINIMISATION OF SPRINGBACK AFTER U- DRAWING

8.1 Introduction

Using the validated 3D shell element model, a parametric study was carried out to investigate the effect of important parameters such as the die radius, the punch radius, the blank thickness and the clearance on the U-drawing process. The outcome of this investigation was used to develop an optimisation technique that has the aim of minimising the springback angle.

8.2 Parametric study

In this section, the most important parameters found in the literature review were investigated using the validated 3D shell element numerical model of the U-drawing process. These factors are the die radius, punch radius, punch/die clearance and blank thickness. The springback level was determined in this study by evaluating the two angles θ_1 and θ_2 that together characterise the springback after U-drawing as defined in Figure 7.13. The baseline values of the geometric parameters were the same as listed in Table 7.2. Only one parameter was varied at a time with the other parameters remaining as defined in Table 7.2.

8.2.1 The effect of the blank thickness

As most of the automotive industries use metal sheet forms of 1 mm to 2.5 mm for their applications. This study is investigating the influence of the blank thickness varying from 1mm to 2.5 mm. Figure 8.1 illustrates the relationship between the blank thickness and springback angles (θ_1 and θ_2). It can be seen that the springback angle θ_1 increases towards the target angle of 90° with increase of the thickness for all four blank materials as shown in Figure 8.1 (a).

However the rate of increase of θ_1 with respect to the blank thickness is much greater for the high strength steel (DP600), than for the lower strength material (DX54D). In fact, it can be seen from Figure 8.1 (a) that the angle θ_1 decreases slightly when the blank thickness was increased from 1 mm to 1.6 mm for the DX54D low strength steel. For both aluminium alloys, there was a general increase in the angle θ_1 towards the target angle of 90° with increase of the thickness.

Figure 8.1 shows that the θ_2 angle has a negative correlation with the blank thickness and the angle decreases significantly towards the target angle of 90° with increase in the blank thickness. The total reduction in the θ_2 angle varied from one material to another, but it was most significant for the high strength steel (DP600), where the difference between the angle for the thinnest and thickest material was more than 8° , whilst for the low strength steel it was only about 2° . For the aluminium alloys, the total reduction in the θ_2 angle was around 3° as shown in Figure 8.1 (b).

The results show that both angles θ_1 and θ_2 contribute towards a net decrease in the total springback as the blank thickness is increased. Conversely springback increases as the thickness of the blank sheet metal is reduced, particularly for the high strength DP600 steel, and is therefore likely to be a greater problem when forming thin sheets of high strength material.

Figure 8.2 shows the mid-plane cross-section of the blank divided into five regions: I, II, III, IV and V. These sections are used to assist in the description and discussion of the following results. Figure 8.3 shows principal total strains on the upper and lower surfaces of the blank along this cross section for the CPLA100k38 aluminium as an example.

The x-axis in Figure 8.3 represents the length of the blank from regions I to V. It can be seen that the highest total strains occur on the surfaces of the blank in regions II and IV which is coincided with the punch radius and the die radius respectively.

Figure 8.3 (b) shows a magnified view of the critical zones (II, III and VI) to assess the influence of the blank thickness on the magnitude of the strains which have already been shown to control the degree of springback. Although the principal strains are lower for the thinner blanks, the springback has been shown to be generally higher. This is because the elastic strains that cause springback represents a higher proportion of the total strain for the thinner material. However, the principal strains are relatively high with some of numerical noise. Therefore, a reduction in springback was predicted for the thicker blanks.

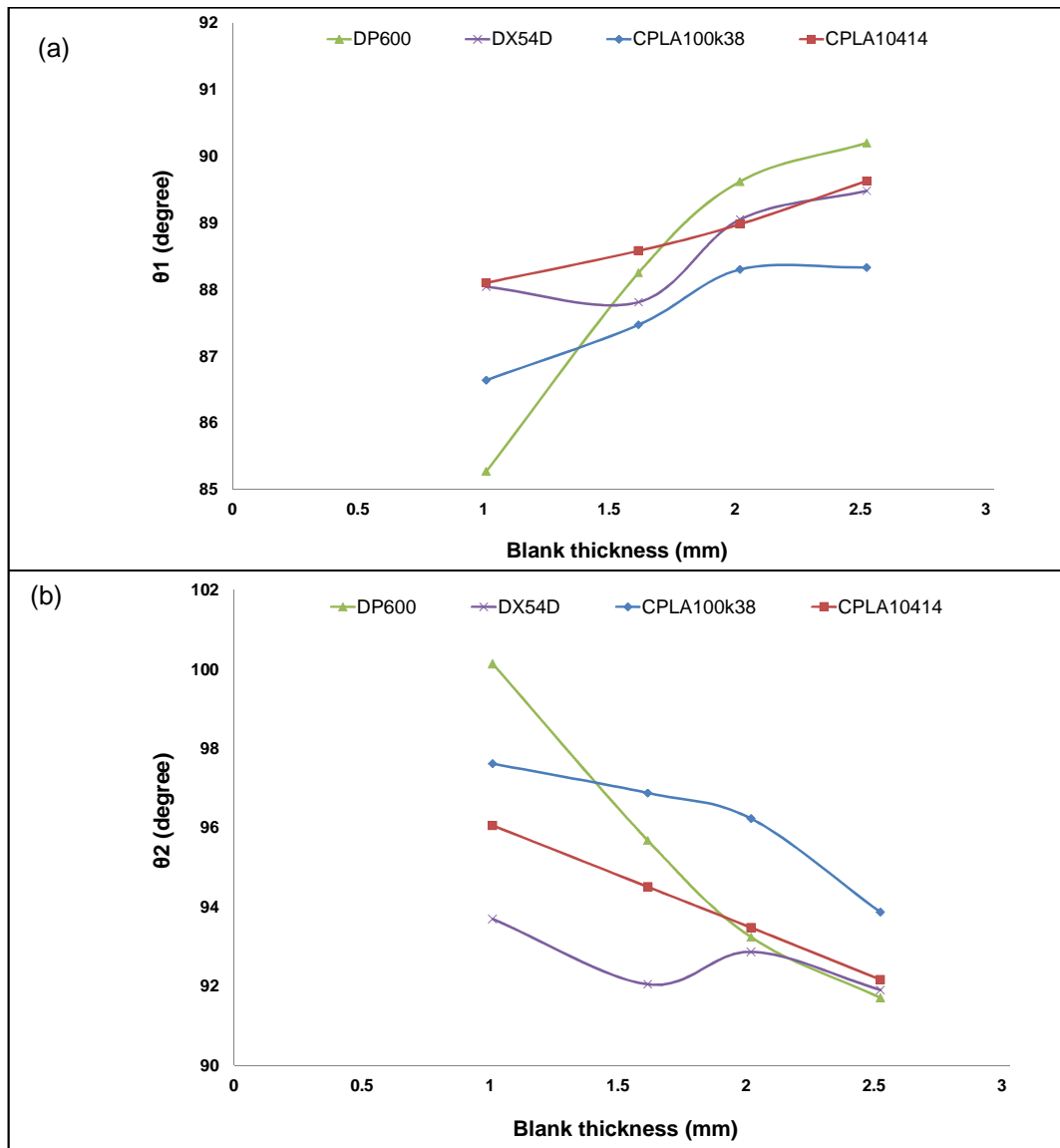


Figure 8.1 Predicted springback after U-drawing for different blank thickness for all tested materials (a) θ_1 and (b) θ_2

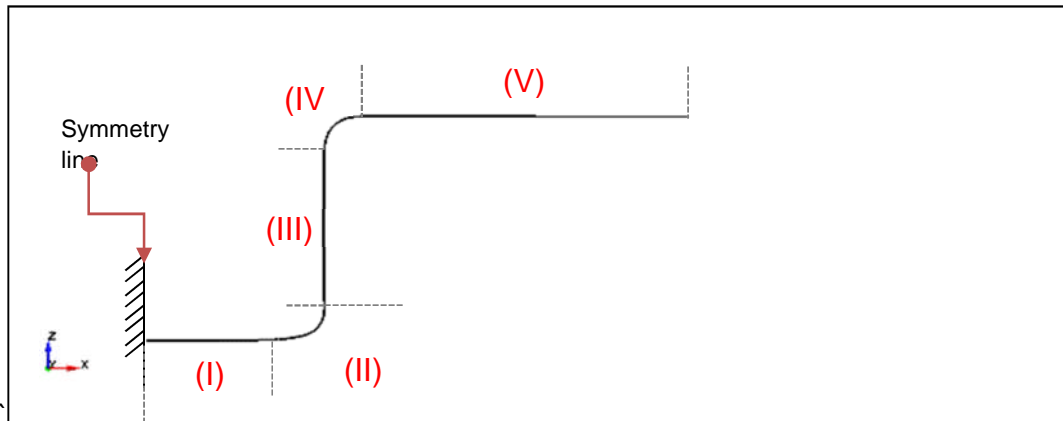


Figure 8.2 A mid-plane cross section for the U-deformed part

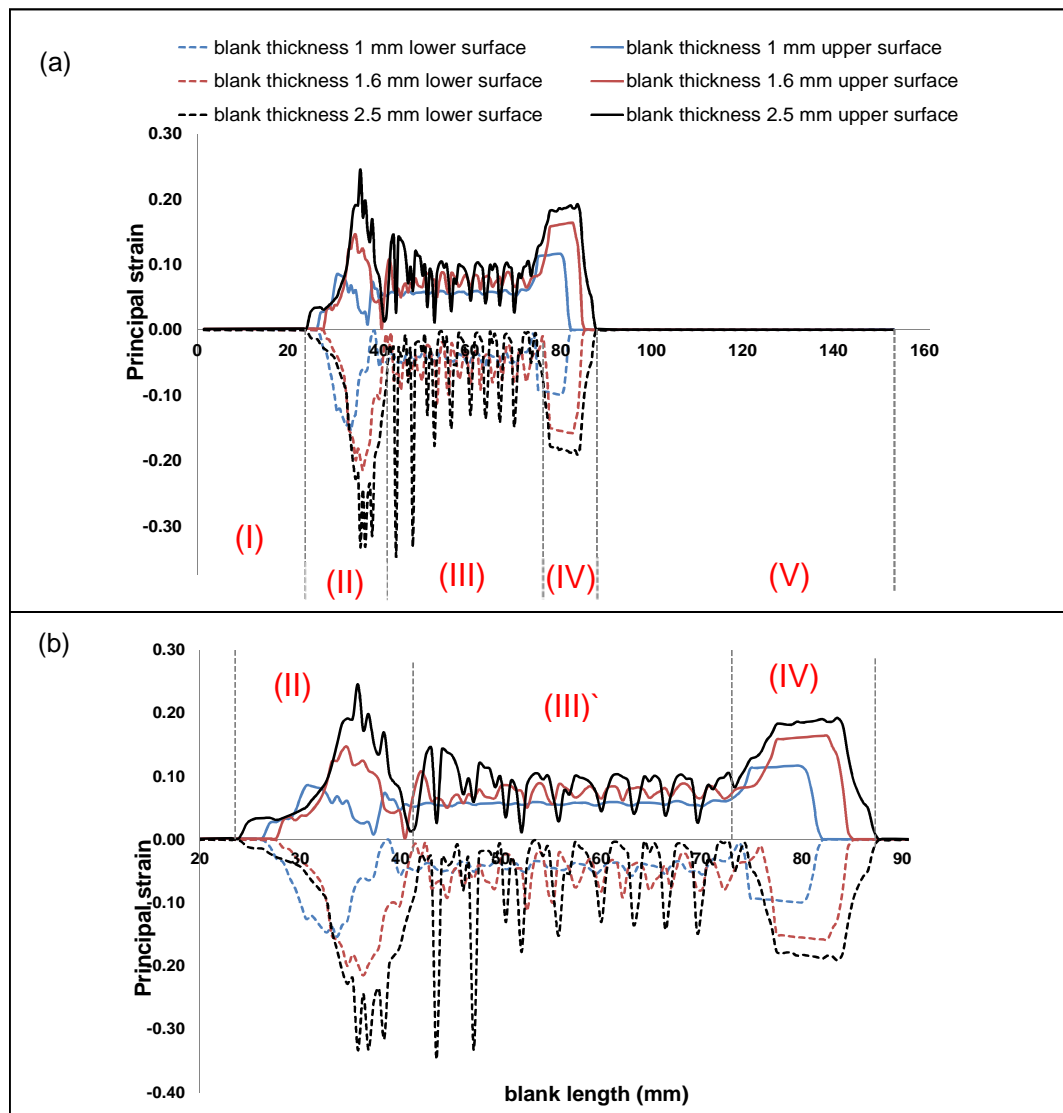


Figure 8.3 Maximum principal strain on upper and lower surfaces for three different CPLA100k38 blank thicknesses (a) full data (b) data zoomed into zones II, III and IV.

8.2.2 The effect of the die radius

The die radius was varied from 4 to 12 mm in 2 mm intervals for all four materials in the 3D shell element simulation of the U-drawing process.

Figure 8.4 illustrates the influence of the die radius on the predicted level of the springback for the four materials. The angle θ_1 was generally slightly increased with increase of the die radius which implies a reduction in the amount of the springback. The large die radius causes more resistance to the blank material flow especially for the relatively high friction coefficient assumed in these simulations as illustrated in Table 6.5. All tested materials seem to have minimum springback angle θ_1 for large die radius except for the CPLA10414 aluminium where there is not much difference in the value of θ_1 when a die radius of 4 mm or 12 mm is used. Based on the results in Chapter 5, the assumed friction coefficient was lowest for the CPLA10414 material (0.27 assumed for both static and dynamic friction coefficients). Therefore, the increase in the die radius has less impact on the springback for these specimens.

Figure 8.4 (b) shows that the angle θ_2 increases with increase of the die radius. This angle increases significantly when the die radius is increased from 4 mm to 8 mm for the high strength DP600 steel. Also, there is a significant increase in the θ_2 angle between die radius of 4 mm and 6 mm for the DX54D material. However, the increase in the θ_2 angle was more gradual for the two aluminium alloys.

Figure 8.5 illustrates principal total strains on the upper and lower surfaces of the DP600 steel for three different die radii. The highest strains occurred in regions II and IV, caused by the punch radius and the die radius respectively. The principal strain in region II was the same for the all three simulations because the punch radius was constant. However, Figure 8.5 shows that in zone IV the highest values of principal strain, along with the shortest deformed blank distance, were predicted for the lowest die radius and vice versa. This can be related to the decreased springback angle θ_2 predicted for the low die radius.

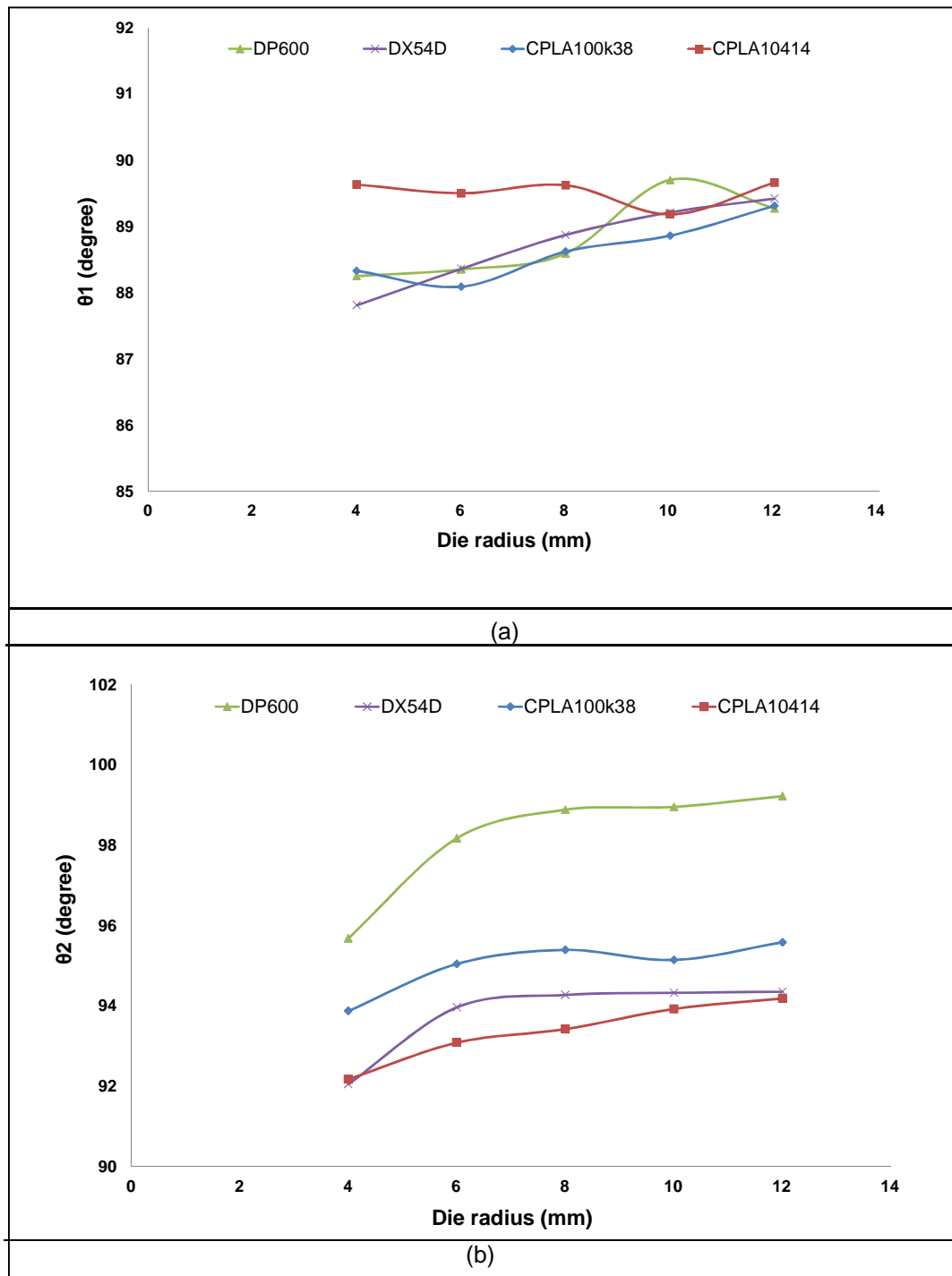


Figure 8.4 Predicted springback after U –drawing for different die radii for all four materials (a) θ_1 and (b) θ_2

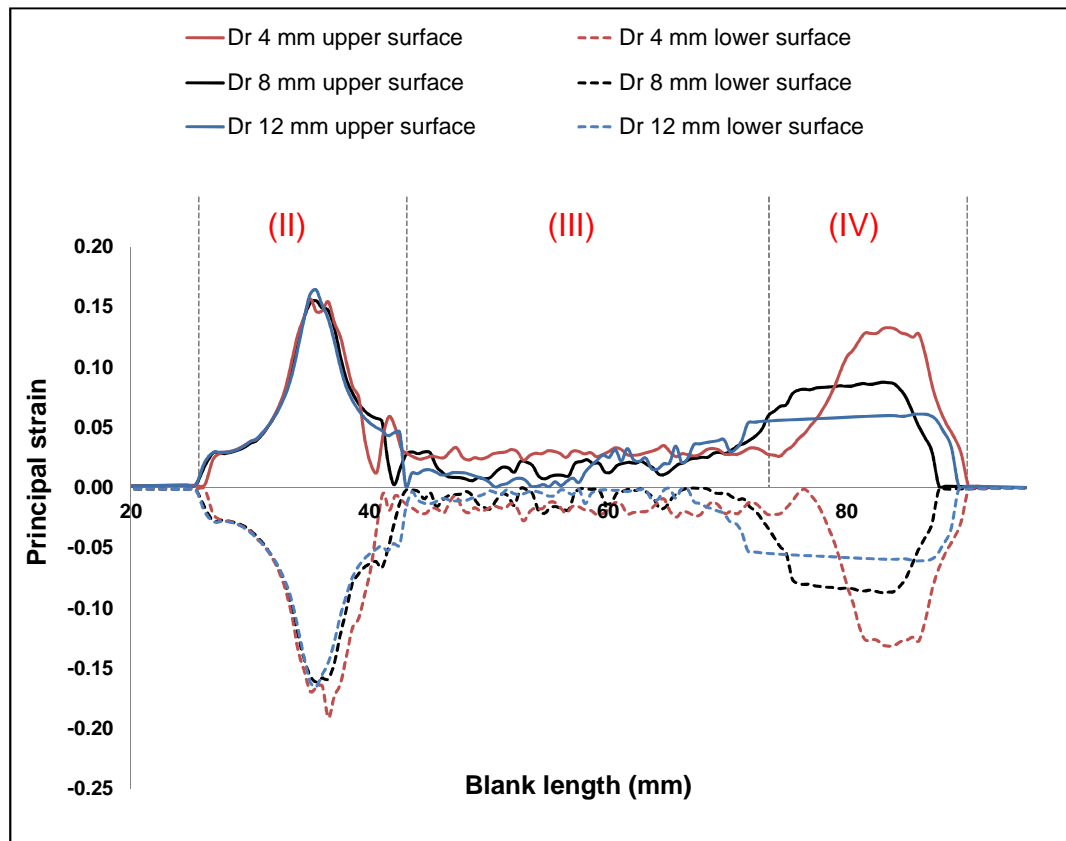


Figure 8.5 Maximum principal strain on upper and lower surface, for three different die radii for DP600 blank

8.2.3 The effect of the punch radius

The punch radius is an important factor since it influences the magnitude of material deformation in the bend region. Therefore, the radius was varied from 4 to 12 mm in 2 mm intervals for each of the four materials.

Figure 8.7 shows the variation of the two angles that determine the degree of the springback after the U-drawing process as predicted by the simulation for the four materials. Figure 8.7 (a) shows only slight increase in the θ_1 angle for all the materials, 1° or less, because the die radius (which largely determines the θ_1 angle) is held constant.

However, Figure 8.7 (b) shows that the angle θ_2 increases significantly with increase of the punch radius for all materials. The most significant increase was for the highest strength steel DP600. On the other hand the increase was also significant for the other materials as the punch radius was

increased from 4 mm to 6 mm after which the angle increases only slightly to the maximum punch radius of 12 mm. The results confirm that as expected the punch radius has more effect on the θ_2 angle than the θ_1 angle because the punch radius influences the strain path in the bottom corner of the formed specimen.

Figure 8.6 plots the principal strain on the upper and lower surfaces of the DP600 steel for the three different punch radii. Although, the die radius was constant at 4 mm for the three simulations, the principal strain path did vary somewhat in region VI due to the punch radius variation. It can be seen that the highest principal strain in region II is for the lowest punch radius of 4 mm which is almost double and triple the highest principal strains for the punch radii of 8 mm and 12 mm respectively. Again the configuration which gives the highest plastic strain also gives the lowest springback as can be seen from Figure 8.7 (b) where the θ_2 angle is minimum for the smallest punch radius of 4 mm.

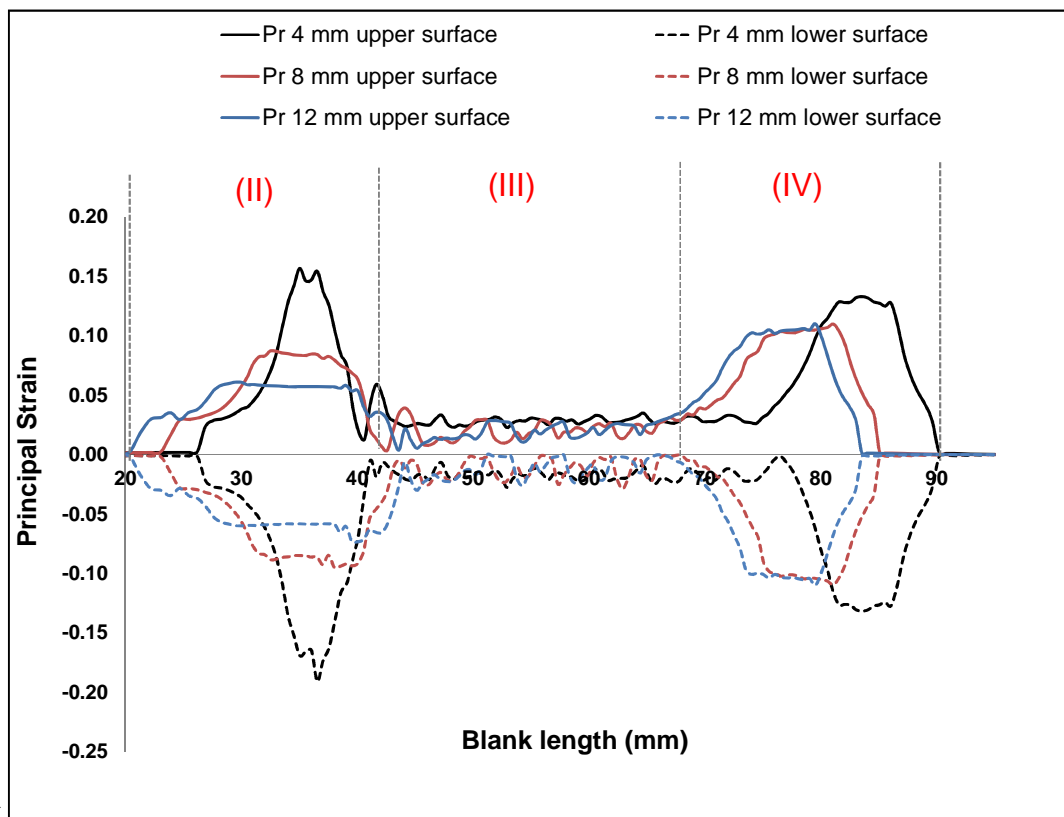


Figure 8.6 Maximum principal strain on upper and lower surface for three different punch radii for DP600 blank

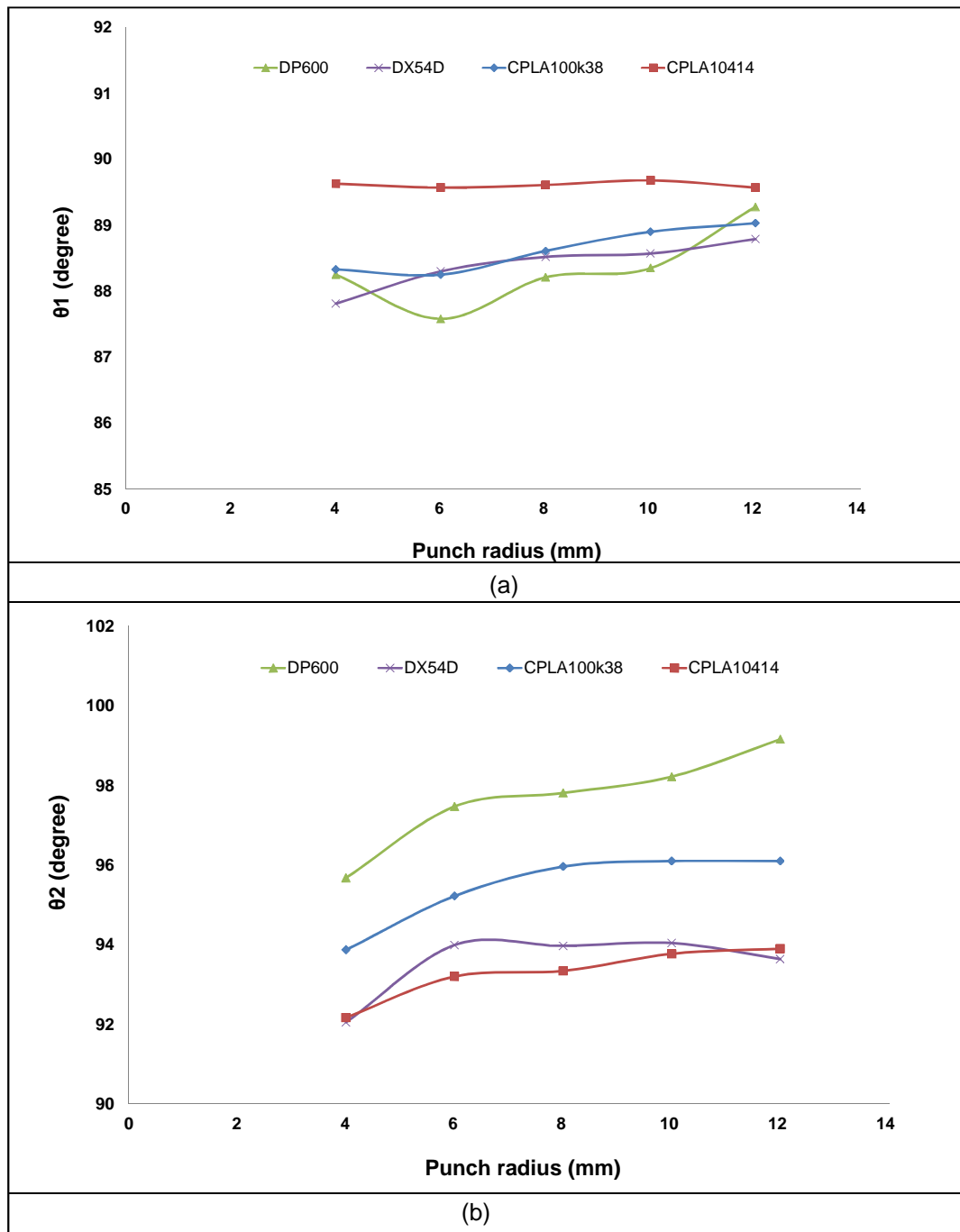


Figure 8.7 Predicted springback after U –drawing for different punch radii for all four materials (a) θ_1 and (b) θ_2

8.2.4 The effect of clearance

The clearance is defined as the difference between the blank thickness and the gap between the punch and the die. It therefore controls the contact area between the blank and the tools (the punch and the die). In this project, the clearance was changed in the Ls-Dyna simulations of the U-drawing process as follows: 0.2, 0.4, 0.6, 0.8, 1.0 and 1.2mm.

Figure 8.8 shows only slight variation of the two springback angles for different clearance values for all the materials considered. All the specimens seem to behave mostly the same with slight variation of the springback angle for different clearance values and the general trend for θ_1 to reduce with increasing clearance and θ_2 to increase (except for the DP600) which is least sensitive to change in clearance.

Increase in clearance will decrease the area of contact between the blank and the tools which means the springback should increase. However, the DP600 seems to behave differently since the springback angles actually decrease only very slightly with increase of the clearance.

Figure 8.9 shows principal total strains on the upper and lower surfaces of the CPLA100k38 aluminium for the minimum and the maximum clearances. It can be seen that there is not much difference in the magnitude and extent of strains along the mid-plane cross section between the two extreme clearances, except small differences in zones III and IV where the minimum clearance gives slightly higher strain than the maximum clearance. This is reflected in the slight decrease of the springback angles θ_1 and θ_2 as shown in Figure 8.8.

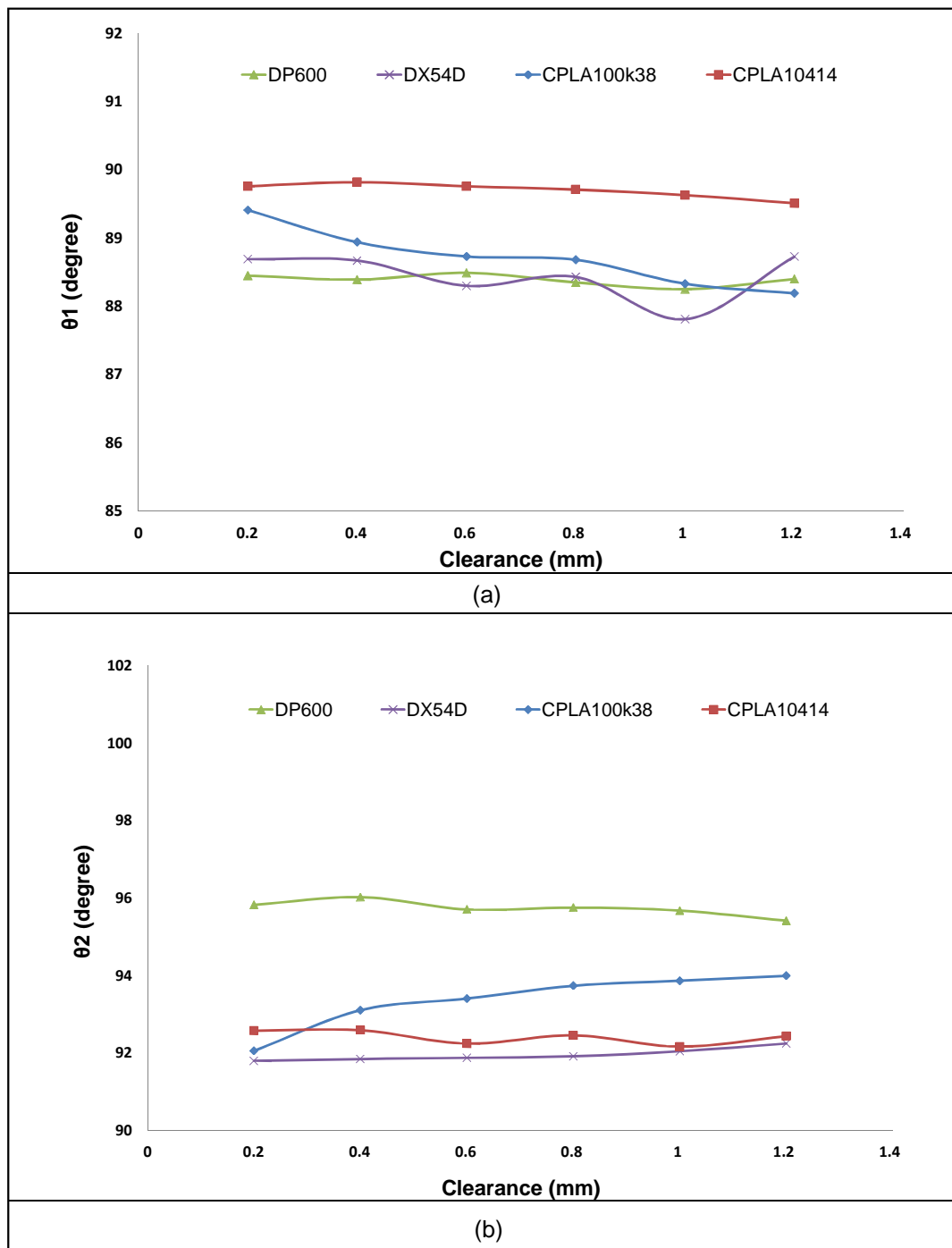


Figure 8.8 Predicted springback after U –drawing for different clearance for all four materials (a) θ_1 and (b) θ_2

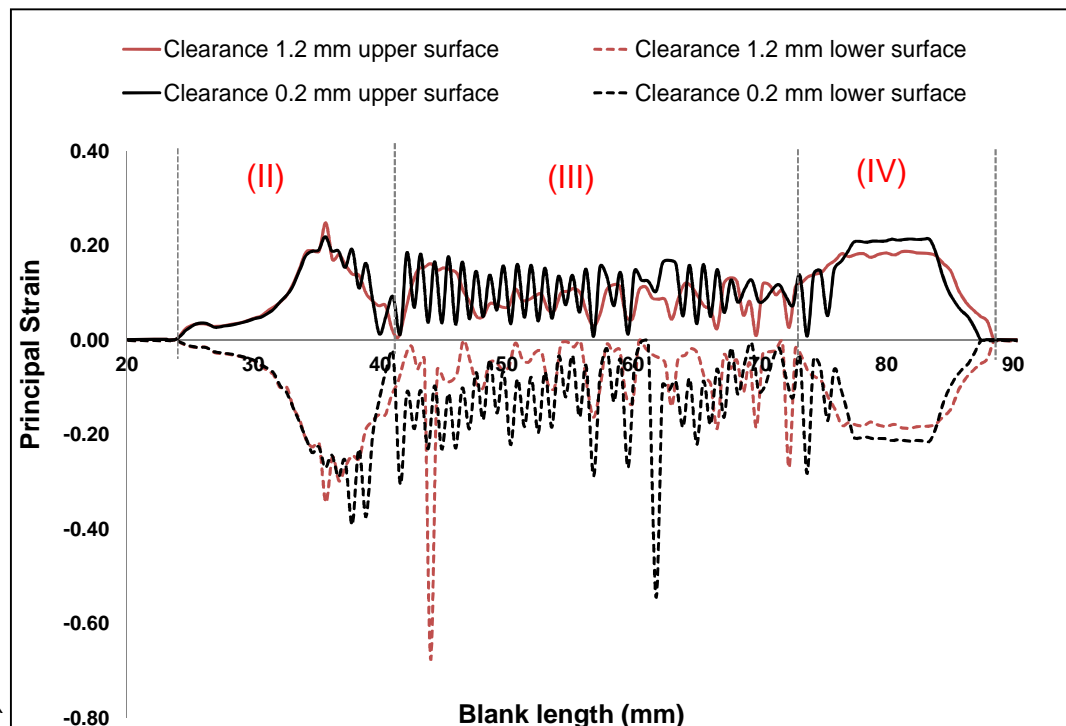


Figure 8.9 Maximum principal strain on upper and lower surface for two different clearances for CPLA100k38 blank

8.3 Design of experiment and optimisation analysis

The blank thickness, die radius and punch radius were all found to have a large influence on the springback magnitude for the four materials used in this study. However, the clearance was found to have an almost negligible effect.

As the blank thickness is most likely to be specified and therefore fixed by the end application, the punch and die radii were varied to find their optimum values to minimise the springback. As the springback was largest for the DP600 blank, This material was selected to be the case study for the optimisation analysis

A Design of Experiment (DoE) approach was utilised to assess the combination of the two selected design variables (the die radius and the punch radius) within a design space. An approximate response surface was used to predict the springback magnitude at points in the design space that

lie between the selected ones at which analysis results were obtained. An optimisation method was developed to find the optimum design variables that give the minimum springback from the predicted response surface. Finally, the optimum design variables were used in a final analysis to validate the optimised solution.

The generic sequence of the optimisation procedures developed in the current study is summarised in Figure 8.10. Each process is briefly explained below:

The DoE is used to select 30 combinations of the two design variables using the Optimal Latin Hypercube (OLH) methodology.

2. Simulations were carried out for the selected points in the design space using the validated 3D shell element numerical model explained in the previous chapter.
3. An approximation response surface using a Moving Least Square (MLS) technique was generated to predict the springback angles within the design space.
4. A Genetic Algorithm (GA) method was used to search for the optimum value of the design variables to give minimum springback.
5. The optimum design variables were utilised in a final numerical simulation for verification of the outcome of the optimisation technique.

Each of these stages are described below in more detail.

In stage one, a Design of Experiments (DoE) process that utilises the OLH methodology, as explained in [77] was used to derive 30 combinations of the two design variables (punch radius and die radius), distributed uniformly through a design space that is determined by an upper and lower limit for each variable as defined in Figure 8.11. The DoE was divided into two parts; one was a build model and the second was a validation model. The purpose of each model was to maximise the uniformity of the design points and to take account of the space-filling properties of the designs.

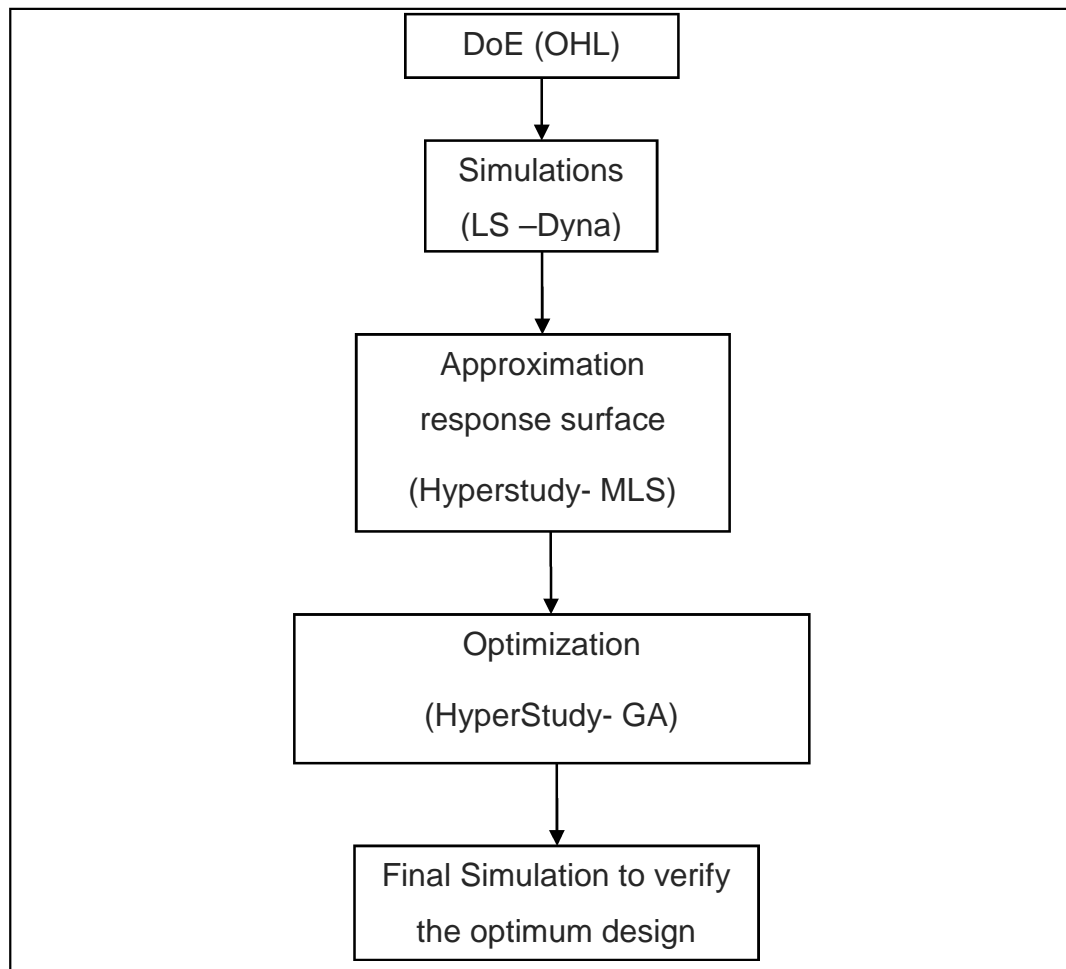


Figure 8.10 stages of Design of Experiment and optimisation procedures

The permutation genetic algorithm (PermGA) reported in [78] was used to generate the OHL build and validation design points as uniformly as possible. The PermGA algorithm works as follows: the design space has points with units of mass and these points apply gravity forces to each other; the potential energy of the system is then minimised. As a result of this process, two non-overlapping distributions of build and validation points were obtained as shown in Figure 8.11.

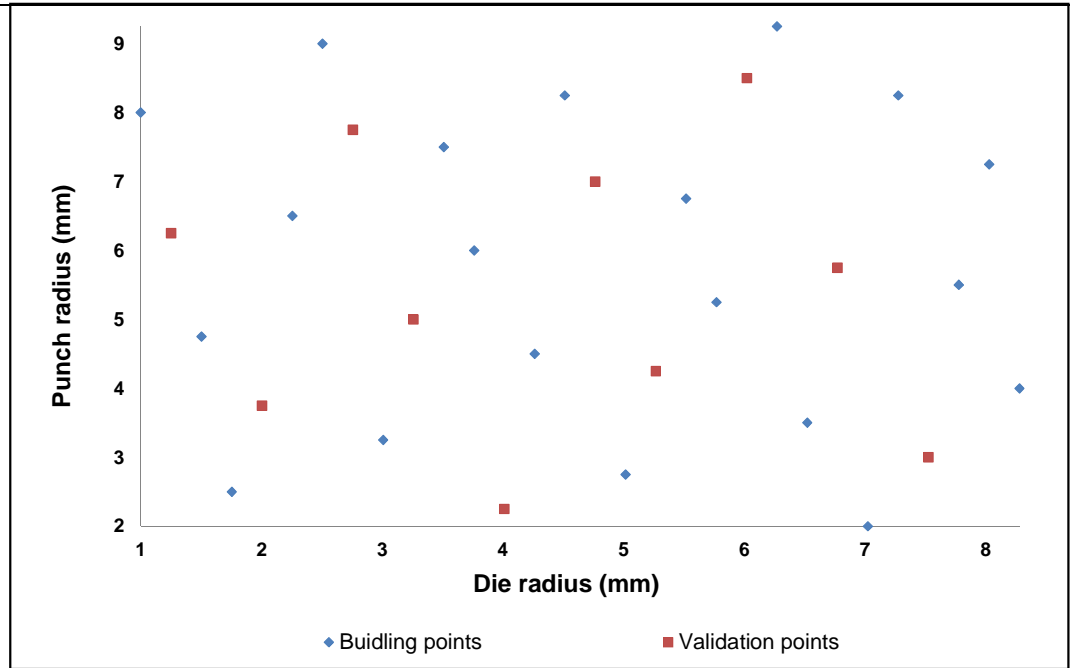


Figure 8.11 Build and validation DoE points

Subsequently, the 3-D shell finite element model for the DP600 high strength steel derived in the previous chapter was used to predict the springback for the 30 selected points using the Ls-Dyna software. The boundary conditions and the other design variables were as specified in Chapter 7. From these results, an approximation response surface of the springback within the design space was plotted using a Moving Least Squares (MLS) approximation method as implemented in HyperStudy version 12 [79].

Figures 8.12 and 8.13 show the response surface for the two angles, θ_1 and θ_2 respectively, which together indicate the level of the springback. Both figures show the predicted angle along the Z-axis plotted against punch radius along the Y-axis and die radius along the X-axis. It can be seen from Figure 8.13 that the θ_2 angle varied significantly through the design space, whilst the θ_1 angle did not as shown in Figure 8.12. Therefore, the objective function is applied to the angle θ_2 only for the subsequent optimisation analysis.

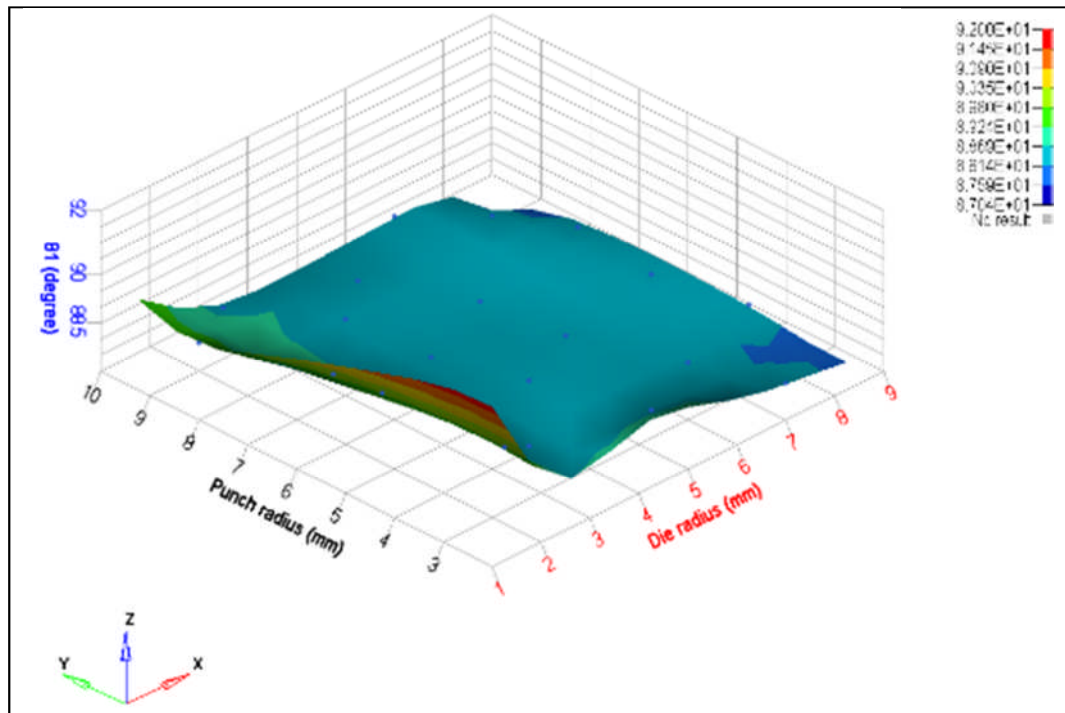


Figure 8.12: Response surface showing predicted θ_1 springback angle for the DP600 blank

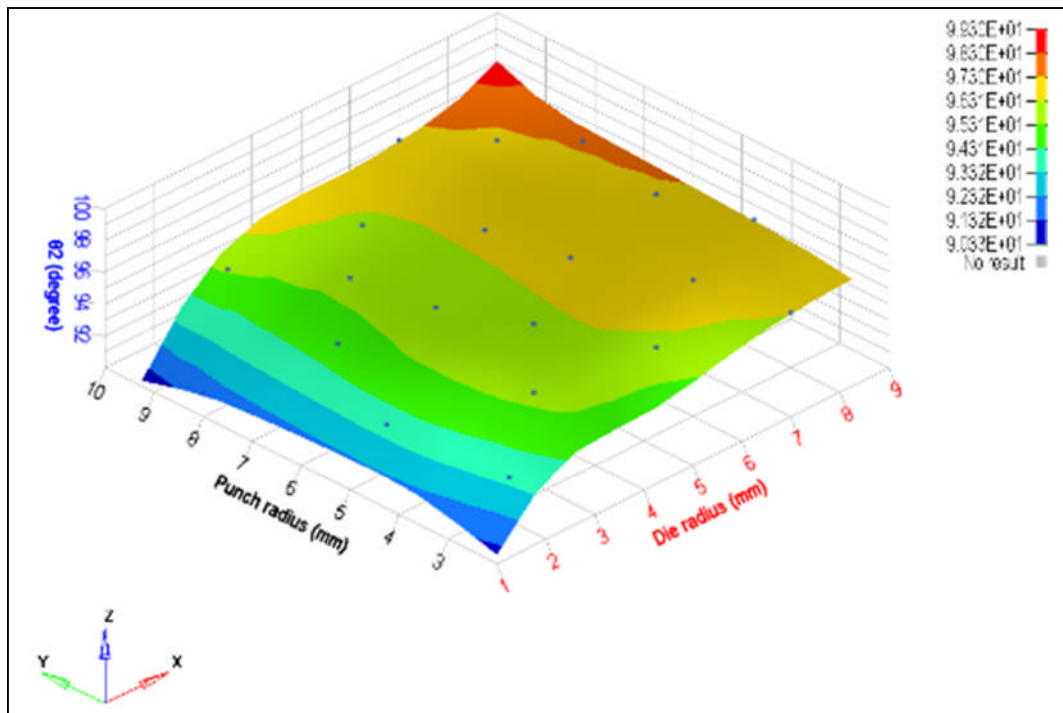


Figure 8.13: Response surface showing predicted θ_2 springback angle for the DP600 blank

For the fourth stage, the genetic algorithm (GA) optimisation technique was employed using Hyperstudy v12 of the Altair HyperWorks package. The main objective was to minimise the angle θ_2 with the following constraints:

$$90 \leq \theta_2 \leq 92 \text{ (degree)}$$

$$88 \leq \theta_1 \leq 90 \text{ (degree)}$$

Table 8.1 shows the optimum design variables found by the GA technique to minimise θ_2 i.e. a die radius of 1 mm and punch radius of 8.25 mm. It can be seen that θ_1 is only 0.66° below the target of 90° and θ_2 only 1.41° above the target.

Table 8.1 Optimum and simulation results of the springback after U-drawing for the DP600 blank for the two design variables

Design variables		(GA) Optimisation prediction		Verification result		Error	
Die radius (mm)	Punch radius (mm)	θ_1	θ_2	θ_1	θ_2	θ_1	θ_2
		(degrees)					
1	8.25	89.34	91.41	89.37	91.52	0.03	0.11

The final stage of the process was to re-run the Ls-Dyna simulation for the optimised design variables (die radius of 1 mm and punch radius of 8.25 mm) to verify the prediction from the optimisation procedure. The resulting springback angles shown in Table 8.1 are in very good agreement with these predicted by the optimisation study.

Figure 8.14 shows the final deformed shape for the initial design variables (which were 4 mm for the punch and die radii) and the optimised ones shown in Table 8.1 . The dramatically reduced springback for the optimised

design is apparent from comparison of Figure 8.14 (a) and (b). In section 8.2 it was shown that the springback increased with increase in both punch and die radii. However, the results of the optimisation show lower springback when the two parameters were varied simultaneously. From Table 8.1, the optimal die radius was the minimum value, whilst the punch radius was close to the maximum limit. This illustrates the power of the optimisation methodology to minimise the springback resulting from the U-drawing process.

Figure 8.15 illustrates the distribution of principal strain on the upper and lower surfaces of the DP600 steel for the initial and optimum design. It can be seen that the principal strain magnitude in zone VI is twice as high for the optimum design when compared to the initial design due to the influence of the small die radius used in the optimum design, and vice versa in zone II. However, the principal strain magnitude in zone III is higher for the optimum design than for the initial one

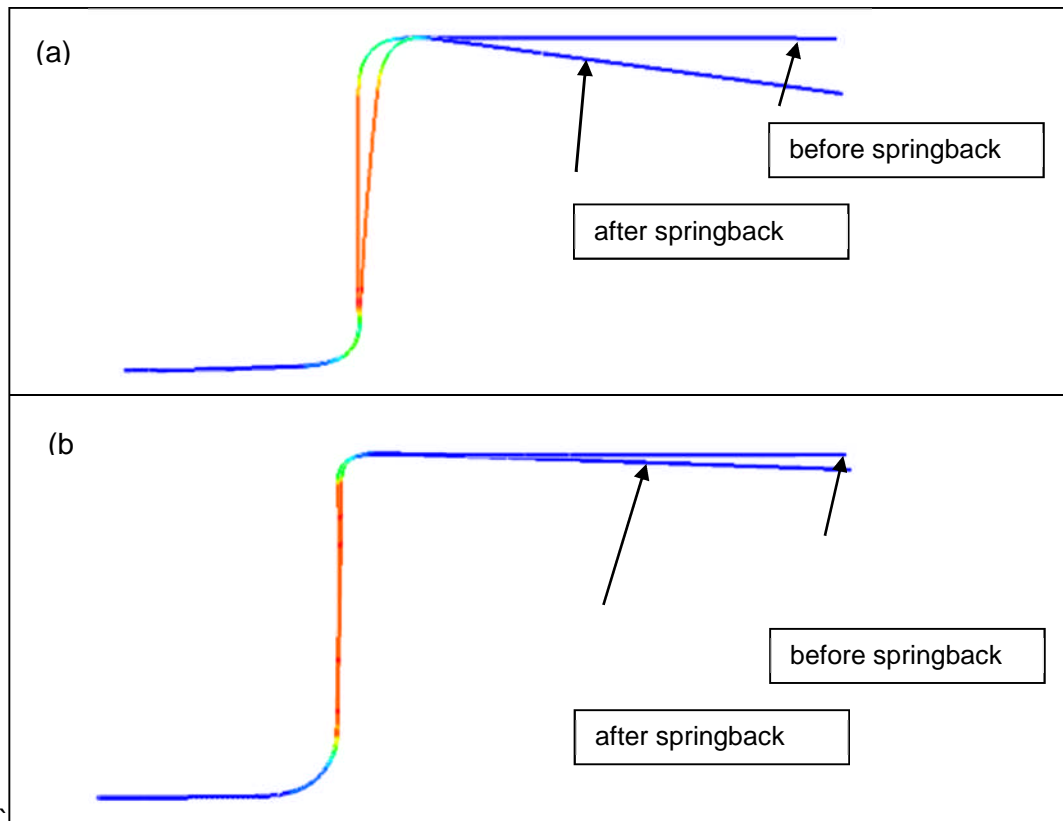


Figure 8.14 Final stage of U –drawing and the subsequent springback for the DP600 blank for (a) the initial design (b) the optimum design

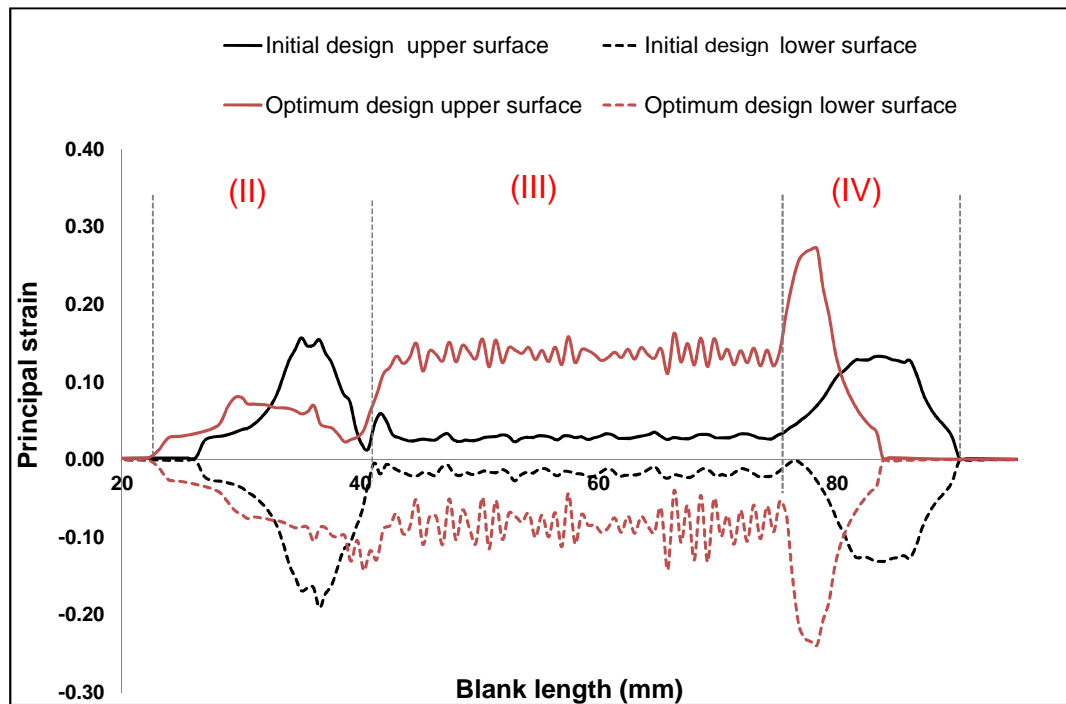


Figure 8.15 Maximum principal strain on upper and lower surfaces for initial and optimum designs for DP600 blank

The same optimum design variables used for the DP600 were utilised in final Ls-Dyna simulations for the other three blank materials. Figure 8.16 shows the predicted springback for the initial and optimum design for the DX54D blank. It can be seen that the springback was reduced using the same optimum design variables that were obtained for the DP600 blank. Figure 8.17 shows principal strains on the upper and lower surfaces of the DX54D for the initial and optimum design which indicates very similar strain behaviour as for the DP600 blank for both initial and optimum designs.

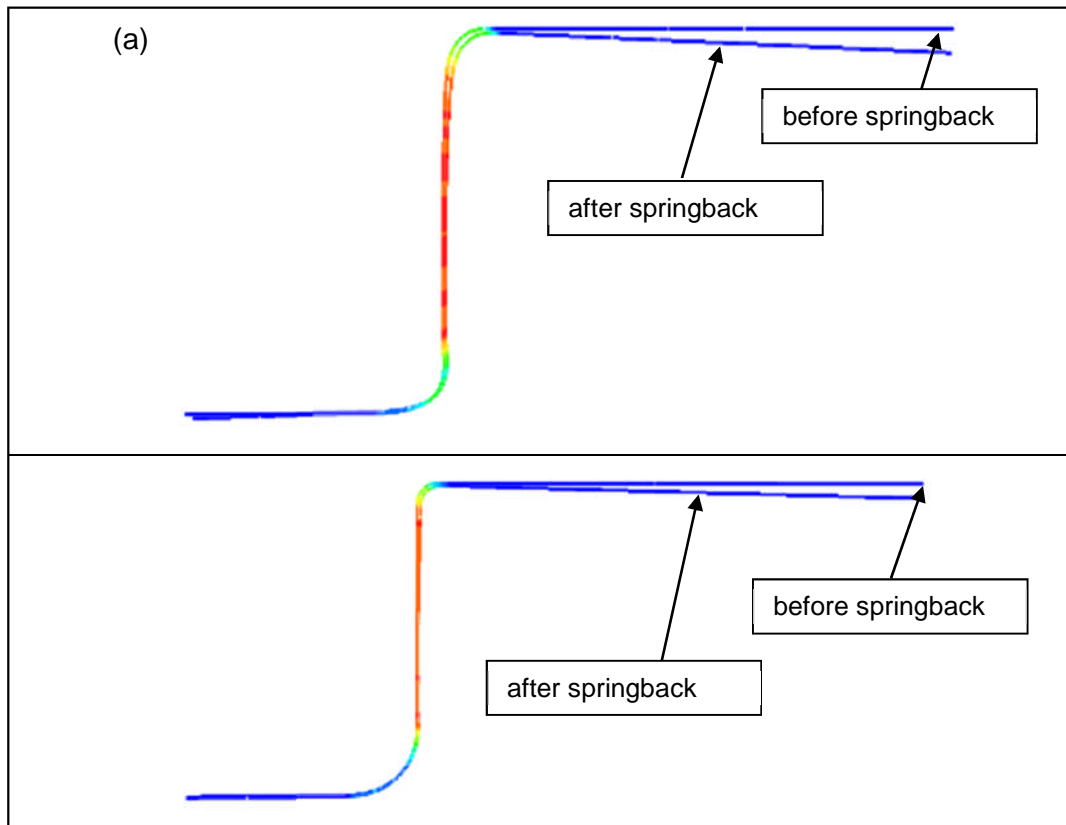


Figure 8.16 Final stage of U-drawing and the subsequent springback for the DX54D blank for (a) the initial design (b) the optimum design

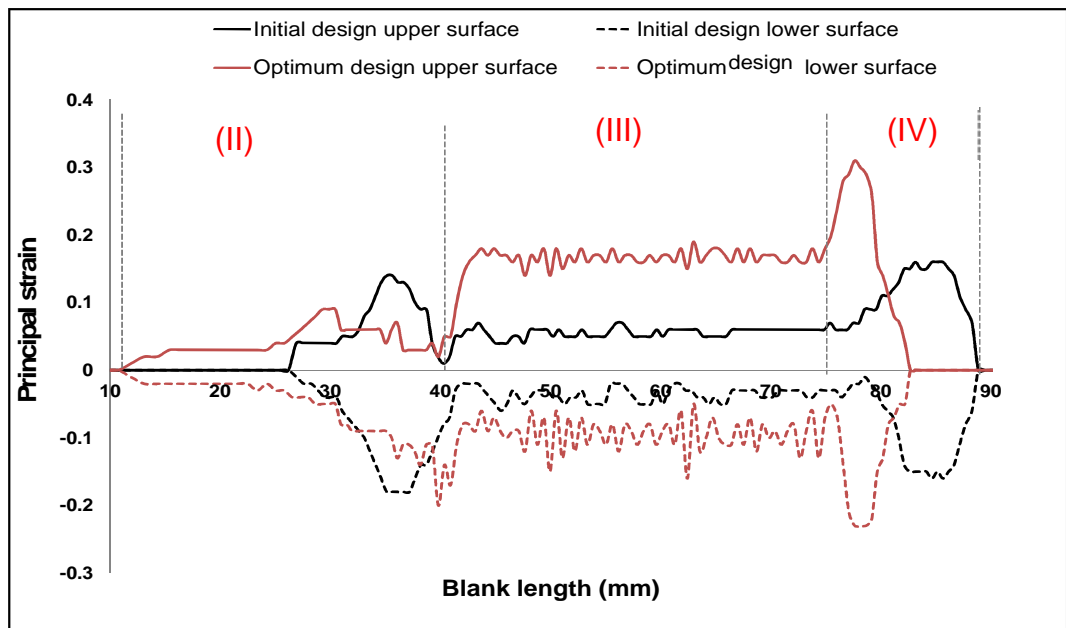


Figure 8.17 Maximum principal strains on upper and lower surfaces for initial and optimum designs for DX54D blank

The optimum design variables were not found appropriate for simulations of the aluminium blank materials since elements of the model started to fold and distort in the vicinity of the die radius region (region IV) as shown in Figure 8.18. It is clear that the elements were inappropriately bent over the die radius which is small for the relatively soft aluminium alloys. In an effect to overcome this problem, element size in the critical region (B) as shown in Chapter 7 was reduced from 0.5 to 0.2 mm but still the above behaviour was observed, despite the huge time consumed for running the simulation. Therefore, the die radius was increased to 2.5 mm whilst the punch radius remained the same at 8.25 mm. Figures 8.19 and 8.20 show the predicted springback for the initial and optimum design with these parameters for the high and low strength aluminium alloys. It can be seen that the springback was significantly reduced using the same optimised punch radius obtained for the DP600 blank but with the die radius now increased to 2.5 mm.

Table 8.2 illustrates springback for the initial and optimum design for all materials used in the current study. The reduction of the springback for the optimum design parameters is clear for all four materials.

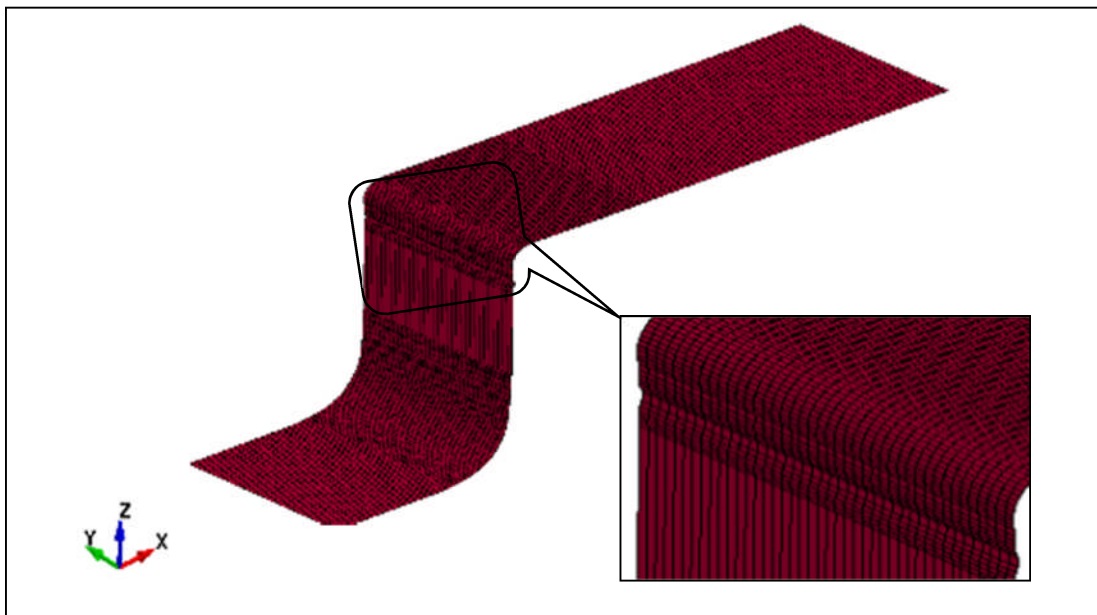


Figure 8.18 Final stage of U-drawing process for CPLA100k38 aluminium blank

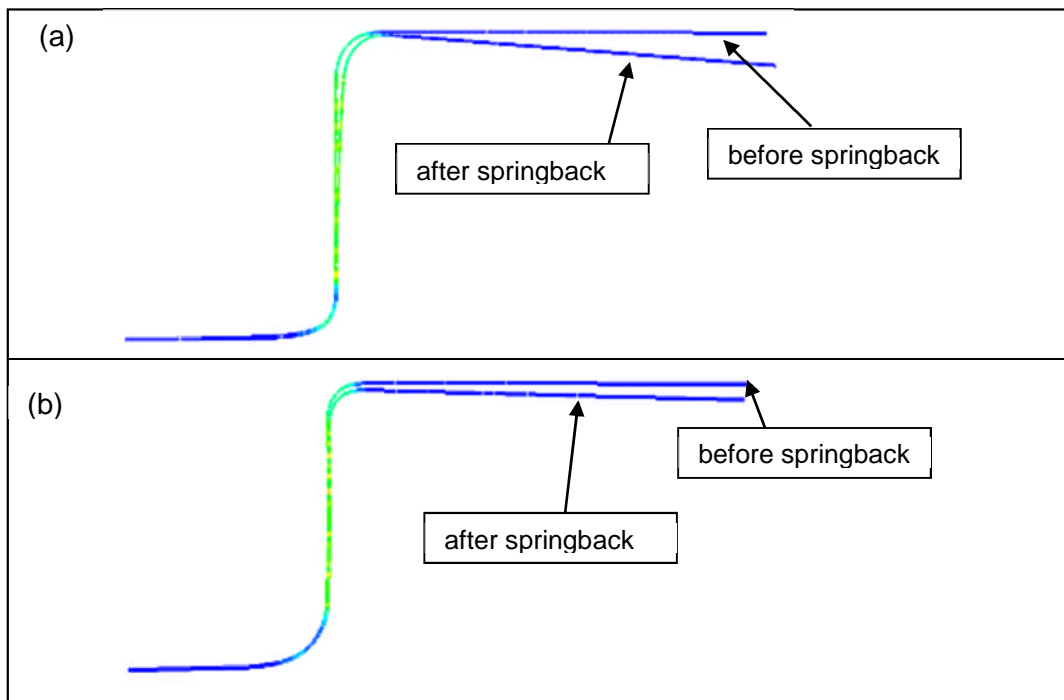


Figure 8.19 Final stage of U –drawing and the subsequent springback for the CPLA100k38 blank for (a) the initial design (b) the optimum design

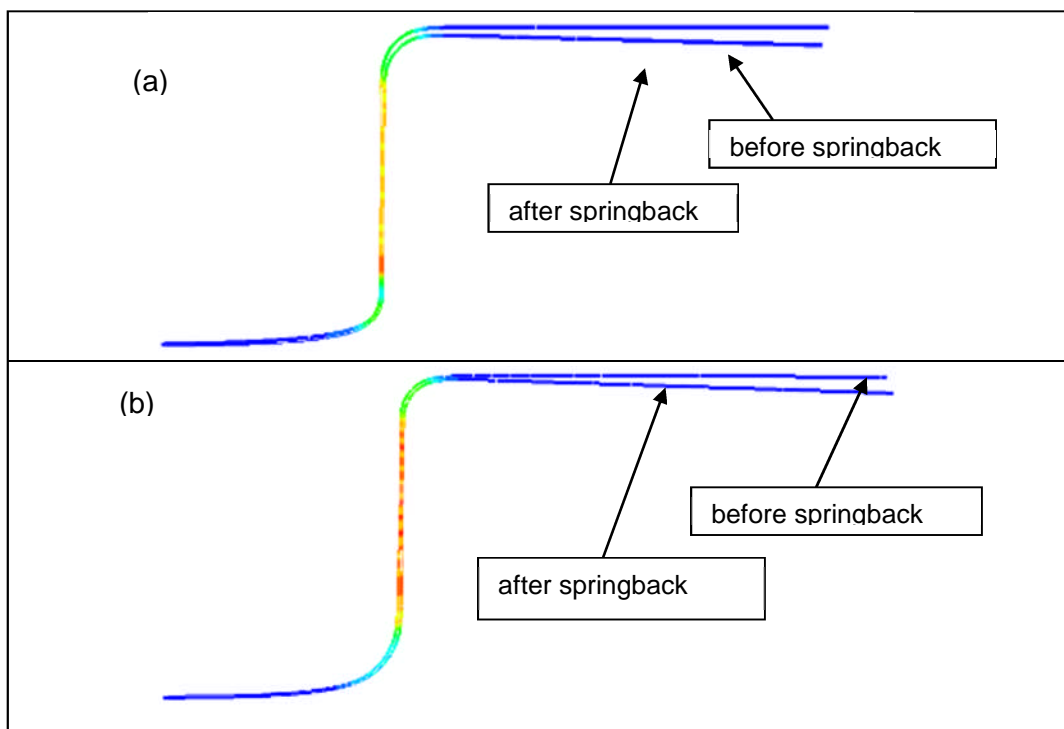


Figure 8.20 Final stage of U –drawing and the subsequent springback for the CPLA10414 blank for (a) the initial design (b) the optimum design

Table 8.2 Springback predictions after U-drawing for all blanks for the initial and optimised designs.

Material	Optimum design variables		Initial design		Optimum design	
	Die radius (mm)	Punch radius (mm)	θ_1	θ_2	θ_1	θ_2
			(degrees)			
DP600	1	8.25	88.78	95.68	89.37	91.52
DX54D	1	8.25	87.89	92.05	89.12	91.05
CPLA100k38	2.5	8.25	88.07	93.87	89.33	91.91
CPLA10414	2.5	8.25	88.85	92.07	89.90	91.95

8.4 Summary

Using the validated 3D thin shell element model described in Chapter 7, a parametric study was undertaken to investigate the importance of parameters such as die radius, punch radius, clearance and the blank thickness on controlling the level of springback. The parameters found to have the most significant influence on the springback were the blank thickness, the punch radius and the die radius. However, there was no significant effect on the springback when the clearance was varied. The

results confirm that springback is likely to be a bigger problem for thinner sheets of high strength material which is the current trend in the automotive industry.

The Optimal Latin Hypercube (OLH) was utilised to construct 30 combinations of the two design variables over which the production engineer has most control (the die radius and punch radius) within a 2D design space for the DP600 blank material. An approximation response surface was generated to predict the springback value at points between the selected ones at which Dyna simulations were conducted. The genetic algorithm optimisation technique within the Hyperstudy v12 of the Altair HyperWorks package was used to find the optimum combination of parameters to minimise springback.

The optimum design variables for the DP600 blank of thickness of 1.6 mm were predicted to be 1 mm for the die radius and 8.25 mm for the punch radius. A final simulation was carried out for these parameters to verify the prediction of the optimisation method. The springback given by the simulation was in very good agreement with that predicted by the optimisation algorithm. The same combination of punch radius and die radius was found to also give very low springback for the low strength steel. However, it was difficult to obtain results for the aluminium blank materials for a die radius of 1 mm. By increasing the die radius to 2.5 mm, the springback was also significantly reduced for the aluminium alloys for the same optimised punch radius of 8.25 mm.

CHAPTER 9: CONCLUSIONS AND FUTURE WORK

9.1 Conclusions

The reduction of vehicle weight to improve fuel consumption and to be more environmentally friendly is a great challenge for the automotive industry. Hence, one of the many steps taken has been to reduce the gauge thickness of sheet metal components and to move to higher strength materials to compensate for the reduction in thickness. However there are problems with higher strength materials because of the change in product shape when the part is removed from the loading due to springback. This is one of the most common defects that can occur as a result of the forming process. Thus, understanding the behaviour of thin sheet products that experience severe deformation during forming processes is a great challenge for designers and researchers.

This thesis has set out to investigate the behaviour of sheet metal materials that are commonly used in the automotive industry. The chosen materials are representative of both high and low strength materials which are known to demonstrate different levels of springback. Two common metal forming processes, the L-bending and U-drawing processes, have been studied in detail using a purpose built forming rig and associated finite element models.

Cyclic tension-compression experiments were conducted for the four materials used in this study. The Bauschinger effect was observed for all the tested materials. Furthermore, work-hardening stagnation was more visible in both aluminium alloys and the low strength steel than in the high strength steel. Also, there was a clear degradation of the Young's modulus following cyclic plasticity loading for all tested materials.

In a metal forming process, the workpiece experiences friction forces due to contact between the workpiece and tool surfaces. In this project, especially during the U-drawing process, the blank was subjected to friction forces which resist the movement of the blank into the die cavity. This could influence the punch load required to form the part and also the resulting springback. Also the surfaces of the tools and of the formed part could be affected by the amount of friction that occurs during the process. Therefore, the friction coefficient was experimentally measured against a representative steel surface for the four blank materials used in this project. Subsequently, the results were utilised in the numerical analysis for the more precise simulation of the metal forming process.

The friction coefficient was found to be different for the four different blank materials. Under dry conditions, the steel blanks produced static and dynamic friction coefficients of approximately 0.3 and 0.25 respectively. However, the static and dynamic friction for the aluminium alloys were difficult to obtain under dry conditions because the differences in hardness of the materials in contact that are thought to cause the hard material asperities on the steel counterface to plough into the soft blank material. This leads to plastic deformation of the asperities, which contributes to the generation of frictional force. Therefore, the current study used an appropriate lubricant on the aluminium surfaces to enable the friction coefficients to be measured. For the high strength aluminium, values of 0.37 and 0.34 were observed for the static and dynamic friction coefficients respectively. The low strength aluminium recorded lower and equal static and dynamic friction coefficients of 0.27 under lubricated conditions.

A baseline experimental set of parameters was used for L-bending and U-drawing processes with the same die radius (4 mm), and punch radius (4 mm). The gap between the blanks and tools for all four materials was 3.5 mm throughout for L-bending but for the U-drawing process it was set at 2.5 mm and 3.5 mm for the steel and aluminium blanks respectively. The influence of the mechanical properties of the blank material during the

forming process (punch force vs. displacement) and after the process (the springback) was investigated.

Consistent results between samples of the same material were found which demonstrates the robustness of the metal forming rig design methodology for both processes. Also, it was found that the differences of the punch load versus displacement curves were much higher between the two steel materials than between the aluminium alloys. Furthermore, it was observed for both L-bending and U-drawing processes that a significantly higher level of springback occurs for the high strength steel compared with the low strength one. However, it seems that there is not much difference in the springback between the high and low strength aluminium materials which both display lower springback than the steels. Furthermore, the springback that occurs for the aluminium alloys are much higher after the L-bending process than after the U-drawing process.

Implicit and explicit finite element methods were utilised to simulate the two forming processes and the subsequent springback. The blank materials were modelled using the Yoshida-Uemori model. HyperMesh v11.0 was used to build the model (creating the geometry, the mesh, specifying the material properties and the boundary conditions). Subsequently, the explicit version of Ls-Dyna_971 was used to simulate the forming process. It was found that the simulated punch force for all tested materials was in good agreement with the experimental results except for the DP600 steel where the simulations predicted much lower punch force than obtained from the experiments. Furthermore, an accurate prediction of the springback was achieved for the aluminium parts and low strength steel, while there was a notable under-prediction of the springback for the coated steel material (DP600) due to the effect of the hot dipped galvanised zinc coating as explained in Chapter 6. Also, it was demonstrated that there is a need to take into account the degradation of the Young's modulus in both processes to achieve an accurate springback prediction except when the springback after L-bending for the DX54D low strength steel was simulated where there was no notable difference when the Young's modulus reduction was ignored.

Serrated stress-strain curves were obtained for the CPLA10414 (Al Mg) aluminium alloy due to the so-called PLC effect which is undesirable as it affects the formability of the material as explained in Chapter 3. However, there was no significant effect on the springback prediction where the error between the experiment and numerical were less than 1% in both L-bending and U-drawing processes.

Both 2D plane strain model and 3D thin shell finite element models were used to simulate the U-drawing process and the subsequent springback prediction were compared with experiment. Although both models give acceptable levels of agreement on the punch load versus displacement behaviour, the 3D model results were generally closer to the experiment. Moreover, the 2D model often failed to converge during the prediction of the springback after the forming simulation. Therefore the 3D model is considered to be preferable for these kinds of simulations because it is both accurate and efficient.

Parametric studies were conducted using the validated numerical models to investigate the importance of die radius, punch radius, clearance, blank thickness and blank holder force (BHF) on controlling the springback. The parameters that have more dominant influence on the springback after L-bending were the die radius, the clearance and the blank thickness. However, there were no significant effects on the springback caused by variation of the punch radius or blank holder force. On the other hand, for the U-drawing process, the parameters found to have greatest impact on the springback were the blank thickness, the punch radius and the die radius.

The Optimal Latin Hypercube (OLH) method was utilised to study 30 combinations of the two design variables (the die radius and punch radius) within a design space for the U-drawing process. Using the 3D shell element model of the U-drawing process, an approximate response surface was created to predict the springback values between the selected design points. The genetic algorithm optimisation technique within Hyperstudy v12 of the Altair HyperWorks package was employed to find the optimum combination of parameters to minimise springback. The optimum design variables were

found to be 1 mm for the die radius and 8.25mm for the punch radius for both types of steel blank materials whereas for the aluminium, the die radius needed to be increased to 2.5 mm for the same punch radius (8.25 mm).

The overall aim of this thesis was to develop and evaluate advanced computer aided engineering analysis techniques that could be used both to predict springback following common metal forming process and to minimise it. The thesis has demonstrated the importance of utilising a suitable material model such as the Yoshida-Uemori model that accurately models the Bauschinger effect and the reduction in Young's modulus following plastic deformation. The work has also developed a novel method of measuring friction between the blank sheet material and the tooling. Explicit FEM analysis followed by implicit analysis have been demonstrated to give generally good prediction of forming loads and springback for both L-bending and U-drawing processes. However, agreement between numerical predictions and experiment were not as good for the coated high strength steel which demonstrates the important of explicitly considering the coating in future studies. A novel set of optimisation procedures has been developed to optimise certain parameters to minimise springback. These methods have been demonstrated to give significant reduction in springback for all material considered. The application and verification of these advanced CAE techniques represent an important contribution to the study of sheet metal forming processes.

9.2 Recommendations for future work

The work described in this thesis, together with the conclusions that have been drawn, suggest that there are a number of areas of further work that will lead to further understanding of the subject. These are summarised below.

The impact of a lubrication regime on the forming test rig should be investigated by ensuring the lubricant remains on the blank during the forming process to assess the effect of the lower friction coefficient on the forming process and the springback phenomenon.

More realistic friction models should be investigated for use in the simulation of metal forming process, where the contact pressure between the tools and the specimen varies during the process and it is much higher around the tool corners. In the current study the friction coefficient was assumed to be constant; however, in reality this is unlikely to be the case.

There is a need for an investigation into the role of a coating on the blank and its impact on springback prediction. This can be done by explicitly modelling the coating using representative mechanical properties for the zinc coating. Also, the influence of the coating process and how it could change the substrate properties should be included. The thickness of the coating seems to have a great effect on the springback; therefore, it might be helpful to include this parameter in the optimisation.

References

1. Rover, J.L. *Jaguar Land Rover Sustainability Report*. 2013 [cited 2014 01/12/2014]; Available from: <http://www.jaguar.co.uk/Images/Jaguar%20Land%20Rover%20Sustainability%20Report%20Interactive%20tcm91-69340.pdf>.
2. Eggertsen, P.A. and K. Mattiasson, *On the modelling of the bending-unbending behaviour for accurate springback predictions*. International Journal of Mechanical Sciences, 2009. **51**(7): p. 547-563.
3. Eggertsen, P.A. and K. Mattiasson, *On constitutive modeling for springback analysis*. International Journal of Mechanical Sciences, 2010. **52**(6): p. 804-818.
4. Mohamad, J.B., *Springback prediction in sheet metal forming : constitutive equations, finite element simulations and experimental validation*, in *Department of design, manufacture and engineering management 2013*, University of Strathclyde.
5. Yoshida, F. and T. Uemori, *A model of large-strain cyclic plasticity describing the Bauschinger effect and workhardening stagnation*. International Journal of Plasticity, 2002. **18**(5-6): p. 661-686.
6. Wilson, D.V. and P.S. Bate, *Reversibility in the work hardening of spheroidised steels*. Acta Metallurgica, 1986. **34**(6): p. 1107-1120.
7. Hasegawa, T., T. Yakou and S. Karashima, *Deformation behaviour and dislocation structures upon stress reversal in polycrystalline aluminium*. Materials Science and Engineering, 1975. **20**(0): p. 267-276.
8. Christodoulou, N., O.T. Woo and S.R. MacEwen, *Effect of stress reversals on the work hardening behaviour of polycrystalline copper*. Acta Metallurgica, 1986. **34**(8): p. 1553-1562.
9. Burchitz, I.A., *Improvement of Springback Prediction in Sheet Metal Forming*. 2008.
10. Wang, C.T., G. Kinzel and T. Altan, *MATHEMATICAL-MODELING OF PLANE-STRAIN BENDING OF SHEET AND PLATE*. Journal of Materials Processing Technology, 1993. **39**(3-4): p. 279-304.
11. Johnson, W. and P.B. Mellor, *Engineering plasticity*. 1983: Horwood.
12. Bower, A.F., *Applied mechanics of solids*. 2009: CRC press.
13. Yu, H.Y., *Variation of elastic modulus during plastic deformation and its influence on springback*. Materials & Design, 2009. **30**(3): p. 846-850.
14. ABAQUS/Standard User's Manual, Version 63.1.
15. Yoshida, F. and T. Uemori, *A model of large-strain cyclic plasticity and its application to springback simulation*. International Journal of Mechanical Sciences, 2003. **45**(10): p. 1687-1702.
16. Firat, M., *U-channel forming analysis with an emphasis on springback deformation*. Materials and Design, 2007. **28**(1): p. 147-154.
17. Dongjuan, Z., C. Zhenshan, R. Xueyu and L. Yuqiang, *Sheet springback prediction based on non-linear combined hardening rule and Barlat89's yielding function*. Computational Materials Science, 2006. **38**(2): p. 256-262.
18. Bouvier, S., J.L. Alves, M.C. Oliveira and L.F. Menezes, *Modelling of anisotropic work-hardening behaviour of metallic materials subjected*

- to strain-path changes*. Computational Materials Science, 2005. **32**(3-4): p. 301-315.
19. Gau, J.-T. and G.L. Kinzel, *A new model for springback prediction in which the Bauschinger effect is considered*. International Journal of Mechanical Sciences, 2001. **43**(8): p. 1813-1832.
 20. Tozawa, Y., *Forming technology for raising the accuracy of sheet-formed products*. Journal of Materials Processing Tech., 1990. **22**(3): p. 343-351.
 21. Hu, Z., E.F. Rauch and C. Teodosiu, *Work-hardening behavior of mild steel under stress reversal at large strains*. International Journal of Plasticity, 1992. **8**(7): p. 839-856.
 22. Ragai, I., D. Lazim and J.A. Nemes, *Anisotropy and springback in draw-bending of stainless steel 410: experimental and numerical study*. Journal of Materials Processing Technology, 2005. **166**(1): p. 116-127.
 23. Verma, R.K. and A. Haldar, *Effect of normal anisotropy on springback*. Journal of Materials Processing Technology, 2007. **190**(1-3): p. 300-304.
 24. Gomes, C., O. Onipede and M. Lovell, *Investigation of springback in high strength anisotropic steels*. Journal of Materials Processing Technology, 2005. **159**(1): p. 91-98.
 25. Geng, L. and R.H. Wagoner, *Role of plastic anisotropy and its evolution on springback*. International Journal of Mechanical Sciences, 2002. **44**(1): p. 123-148.
 26. Eggertsen, P.A. and K. Mattiasson, *On the modelling of the bending-unbending behaviour for accurate springback predictions*. International Journal of Mechanical Sciences, 2009. **51**(7): p. 547-563.
 27. Chongthairungruang, B., V. Uthaisangasuk, S. Suranuntchai and S. Jirathearanat, *Experimental and numerical investigation of springback effect for advanced high strength dual phase steel*. Materials & Design, 2012. **39**(0): p. 318-328.
 28. Chongthairungruang, B., V. Uthaisangasuk, S. Suranuntchai and S. Jirathearanat, *Springback prediction in sheet metal forming of high strength steels*. Materials & Design, 2013. **50**: p. 253-266.
 29. Bathe, K.J., *Finite Element Procedures*. 1996: Prentice Hall.
 30. Prior, A.M., *Applications of implicit and explicit finite element techniques to metal forming*. Journal of Materials Processing Technology, 1994. **45**(1-4): p. 649-656.
 31. Sun, J.S., K.H. Lee and H.P. Lee, *Comparison of implicit and explicit finite element methods for dynamic problems*. Journal of Materials Processing Technology, 2000. **105**(1-2): p. 110-118.
 32. Karafillis, A.P. and M.C. Boyce, *Tooling and binder design for sheet metal forming processes compensating springback error*. International Journal of Machine Tools and Manufacture, 1996. **36**(4): p. 503-526.
 33. Narasimhan, N. and M. Lovell, *Predicting springback in sheet metal forming: an explicit to implicit sequential solution procedure*. Finite Elements in Analysis and Design, 1999. **33**(1): p. 29-42.
 34. Lee, S.W. and D.Y. Yang, *An assessment of numerical parameters influencing springback in explicit finite element analysis of sheet metal*

- forming process*. Journal of Materials Processing Technology, 1998. **80–81**(0): p. 60-67.
35. Lee, S.W., *A study on the bi-directional springback of sheet metal stamping*. Journal of Materials Processing Technology, 2005. **167**(1): p. 33-40.
36. LIU, R.G.D.a.Y.C., *Control of Springback in a Flanging Operation*. APPLIED METALWORKING, 2 January 1984. **3**.
37. Chen, F.-K. and S.-F. Ko, *Deformation Analysis of Springback in L-Bending of Sheet Metal*. Advanced Science Letters, 2011. **4**(6-7): p. 1928-1932.
38. Samuel, M., *Experimental and numerical prediction of springback and side wall curl in U-bendings of anisotropic sheet metals*. Journal of Materials Processing Technology, 2000. **105**(3): p. 382-393.
39. Padmanabhan, R., M.C. Oliveira, J.L. Alves and L.F. Menezes, *Influence of process parameters on the deep drawing of stainless steel*. Finite Elements in Analysis and Design, 2007. **43**(14): p. 1062-1067.
40. Liu, W., Q. Liu, F. Ruan, Z. Liang and H. Qiu, *Springback prediction for sheet metal forming based on GA-ANN technology*. Journal of Materials Processing Technology, 2007. **187–188**(0): p. 227-231.
41. Rao, S.S., *Engineering Optimization Theory and Practice*. 2009.
42. Zheng, Y. and P.K. Das, *Improved response surface method and its application to stiffened plate reliability analysis*. Engineering Structures, 2000. **22**(5): p. 544-551.
43. Mkaddem, A. and R. Bahloul, *Experimental and numerical optimisation of the sheet products geometry using response surface methodology*. Journal of Materials Processing Technology, 2007. **189**(1-3): p. 441-449.
44. Hino, R., F. Yoshida and V.V. Toropov, *Optimum blank design for sheet metal forming based on the interaction of high- and low-fidelity FE models*. Archive of Applied Mechanics, 2006. **75**(10-12): p. 679-91.
45. Gassara, F., R. Hambli, T. Bouraoui, F. El Halouani and D. Soulat, *Optimization of springback in L-bending process using a coupled Abaqus/Python algorithm*. International Journal of Advanced Manufacturing Technology, 2009. **44**(1-2): p. 61-7.
46. SHIMADZU. *datat sheet SHIMADZU tensile test machine*. 2014 [cited 2014 04/02]; Available from: <http://www.shimadzu.com/an/test/universal/ag-xplus/ag-xplus3.html>.
47. Soboyejo, W., ed. *Mechanical Properties of Engineered materials* 2003, Marcel Dekker New York.
48. Abbadi, M., P. Hahner and A. Zeghloul, *On the characteristics of Portevin-Le Chatelier bands in aluminum alloy 5182 under stress-controlled and strain-controlled tensile testing*. Materials Science and Engineering a-Structural Materials Properties Microstructure and Processing, 2002. **337**(1-2): p. 194-201.
49. Klose, F.B., A. Ziegenbein, F. Hagemann, H. Neuhauser, P. Hahner, M. Abbadi and A. Zeghloul, *Analysis of Portevin-Le Chatelier serrations of type Bin Al-Mg*. Materials Science and Engineering a-Structural Materials Properties Microstructure and Processing, 2004. **369**(1-2): p. 76-81.

50. Maziere, M. and H. Dierke, *Investigations on the Portevin-Le Chatelier critical strain in an aluminum alloy*. Computational Materials Science, 2012. **52**(1): p. 68-72.
51. Benallal, A., T. Berstad, T. Borvik, O.S. Hopperstad, I. Koutiri and R.N. de Codes, *An experimental and numerical investigation of the behaviour of AA5083 aluminium alloy in presence of the Portevin-Le Chatelier effect*. International Journal of Plasticity, 2008. **24**(10): p. 1916-1945.
52. Aalco. *Technical Information Aluminium Alloy // Commercial Alloy // 5754 - H111*. 2014 12/02 [cited 2014 12/02]; Available from: http://www.aalco.co.uk/datasheets/Aluminium-Alloy_5754-H111_142.ashx.
53. Opbroek, E.G., *ADVANCED HIGH STRENGTH STEEL (AHSS) APPLICATION GUIDELINES*. 2009.
54. Tokyo Sokki kenkyujo Co, L. *data sheet Strain Gauges 2014* [cited 2014 04/02]; Available from: <http://www.tml.jp/e/download/catalogdownload.html>.
55. Schmid, S.K.a.S.R., *Manufacturing Process for Engineering Materials 2008*
56. Ghaei, A. and D.E. Green, *Numerical implementation of Yoshida–Uemori two-surface plasticity model using a fully implicit integration scheme*. Computational Materials Science, 2010. **48**(1): p. 195-205.
57. *ENTEX STOCK SPRINGS*. 2014 [cited 2014 01/10/2014]; Available from: http://www.entexstocksprings.co.uk/index.php?route=product/product&product_id=1699.
58. INSTRON. *data sheet 5980 Series Dual Column Floor Model*. 2014 [cited 2014 29/01/2014]; Available from: <http://www.instron.co.uk/wa/product/5980-Floor-Model-Systems.aspx>.
59. Wagoner, R.H. and J.-L. Chenot, *Fundamentals of metal forming*. 1997: Wiley New York.
60. Avitzur, B., *Metal forming: processes and analysis*. Vol. 968. 1968: McGraw-Hill New York.
61. Rocol. <https://www.rocol.com/products/ultraform1030-high-performance-forming-lubricant>. 2015 [cited 2015 23/06/2015].
62. bearings, s. <http://simplybearings.co.uk/shop/files/1010.pdf>. 2015 [cited 2015 23/05/2015].
63. Macsteel. http://www.macsteel.co.za/files/080m40_en8_black.pdf. 2015 [cited 23/05/2015 2015].
64. Bowden, F.P. and D. Tabor, *The Friction and Lubrication of Solids-{Part I}*. 1950.
65. Hamrock, B.J., S.R. Schmid and B.O. Jacobson, *Fundamentals of fluid film lubrication*. Vol. 169. 2004: CRC press.
66. Yoshida, F., T. Uemori and K. Fujiwara, *Elastic–plastic behavior of steel sheets under in-plane cyclic tension–compression at large strain*. International Journal of Plasticity, 2002. **18**(5–6): p. 633-659.
67. Chatti, S. and N. Hermi, *The effect of non-linear recovery on springback prediction*. Computers & Structures, 2011. **89**(13–14): p. 1367-1377.

68. Gronostajski, J.Z., *Behaviour of coated steel sheets in forming processes*. Journal of Materials Processing Technology, 1995. **53**(1–2): p. 167-176.
69. Gupta, A.K. and D. Ravi Kumar, *Formability of galvanized interstitial-free steel sheets*. Journal of Materials Processing Technology, 2006. **172**(2): p. 225-237.
70. Srinivasan, R., D. Vasudevan and P. Padmanabhan, *Application of response surface methodology for predicting springback in air bending of electro galvanised steel sheets*. International Journal of Materials Engineering Innovation, 2013. **4**(1): p. 35-56.
71. Chan, K.C. and S.H. Wang, *The effect of a coating on the springback of integrated circuit leadframes*. Journal of Materials Processing Technology, 2001. **116**(2–3): p. 231-234.
72. Özdemir, M., H. Gökmese, H. Dilipak and V. Yilmaz, *Characterization of Microstructure and Bending Response of Sheet Material: Influence of Thickness*. Journal of Advanced Materials and Processing, 2015. **3**(1): p. 3-14.
73. Kazan, R., M. Firat and A.E. Tiryaki, *Prediction of springback in wipe-bending process of sheet metal using neural network*. Materials & Design, 2009. **30**(2): p. 418-423.
74. Andre Haufe, K.S., Paul DuBois. *Properties and Limits: Review of Shell Element Formulations*. 2013 [cited 2015 21/05/2015]; Available from: <https://www.dynamore.de/de/download/papers/2013-ls-dyna-forum/documents/review-of-shell-element-formulations-in-ls-dyna-properties-limits-advantages-disadvantages>.
75. Benson, D.J., Y. Bazilevs, M.C. Hsu and T.J.R. Hughes, *Isogeometric shell analysis: The Reissner–Mindlin shell*. Computer Methods in Applied Mechanics and Engineering, 2010. **199**(5–8): p. 276-289.
76. Bischoff, M., K.U. Bletzinger, W.A. Wall and E. Ramm, *Models and Finite Elements for Thin-Walled Structures*, in *Encyclopedia of Computational Mechanics*. 2004, John Wiley & Sons, Ltd.
77. Park, J.-S., *Optimal Latin-hypercube designs for computer experiments*. Journal of Statistical Planning and Inference, 1994. **39**(1): p. 95-111.
78. Narayanan, A., V.V. Toropov, A.S. Wood and I.F. Campean, *Simultaneous model building and validation with uniform designs of experiments*. Engineering Optimization, 2007. **39**(5): p. 497-512.
79. Hyperstudy, v. 2012 Altair Engineering